Novel Up-Conversion Concentrating Photovoltaic Concepts

Georgios E. Arnaoutakis

Submitted for the degree of Doctor of Philosophy

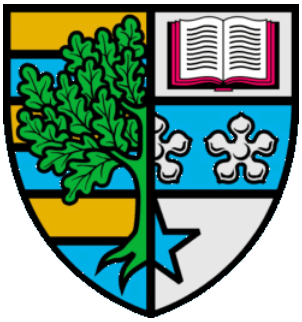

Heriot-Watt University

School of Engineering & Physical Sciences

June 2015

Abstract

This thesis summarises a set of experiments towards the integration of concentrating optics into up-conversion photovoltaics. Up-conversion in rare earths has been investigated here. This optical process is non-linear therefore a high solar irradiance is required. High solar irradiance is achievable by solar concentration. Two concentrating approaches were investigated in this thesis:

The first approach involved the concentration of the incident solar irradiance into optical fibres. An optical system with spherical lenses and dielectric tapers was designed accordingly. A solar concentration of 2000 suns was realised at the end of a single optical fibre. In addition to the total solar concentration, the spectral dependence was characterised to account for the effect of chromatic aberrations. Then, the solar concentration could be transferred into rare earth-doped fibres. For this reason, a series of experiments on double-clad erbium-doped silicate fibres was carried out. Although up-conversion in this type of fibre is minimised, the measured power dependence agrees with up-conversion *via* excited state absorption.

In the second approach, concentrating optics were integrated in up-conversion solar cells. The role of the optics was to couple the photons transmitted by the solar cell to the rare earth up-converter. Therefore, imaging and non-imaging optics were investigated, with the latter exhibiting ideal coupling characteristics; concentration and high transmission of the incident irradiance, but also efficient collection of the up-converted emission. Out of the non-imaging optics, the dielectric compound parabolic concentrator fulfilled these characteristics, indicating its novel use in up-conversion solar cells. Two erbium-doped up-converters were utilised in this approach, beta-phase hexagonal sodium yttrium tetrafluoride (β-$NaYF_4$:25%Er^{3+}) and barium diyttrium octafluoride (BaY_2F_8:30%Er^{3+}). The latter performed best, with an external quantum efficiency (EQE) of 2.07% under 1493 nm illumination, while the former exhibited an EQE of 1.80% under 1523 nm illumination both at an irradiance of 0.02 W/cm^2. This corresponds to a relative conversion efficiency of 0.199% and 0.163% under sub-band-gap illumination, respectively, for a solar cell of 17.6% under standard AM1.5G conditions. These values are among the highest in literature for up-conversion solar cells and show the potential of the concentrating concept that can be important for future directions of photovoltaics.

Acknowledgements

This thesis would not have been made possible without the contribution of several people. First, I would like to thank Prof. T.K. Mallick and Prof. B.S. Richards for giving me the opportunity to pursue this PhD within the Scottish Institute for Solar Energy Research (SISER) and for their guidance and support throughout. Also thanks to Dr. N. Bennett and Dr. J. Marques-Hueso for their guidance, valuable feedback and for putting up with my "too academic" writing style.

For the results presented in this thesis, I would like to thank Dr. K.W. Krämer for providing the β-$NaYF_4$:Er^{3+} up-converter and for his patience with my on-the-rush English. Also thanks to Dr. A. Ivaturi for the preparation of the solid samples that contributed to a great proportion of work in this thesis, as well as Prof. M. Tonelli for the samples of BaY_2F_8:Er^{3+}. Many thanks to Dr. J.C. Goldschmidt and Dr. S. Fischer for making the excellent bifacial solar cells and for their useful comments and suggestions. On the practical aspects, I owe my gratitude to all the workshop technicians at Heriot-Watt University (HWU) and especially Richard, John, Al, Kenny, Mark and Niall who always tried their best to make sense of my ridiculous requests, while trying to carry them out quickly. Also thanks to Alistair and Gordon for the help on the electronics of my setups from the very frustrating beginning. Finally, not forgetting also Paul for his skill on pulling tapered fibres and always gladly reattaching them, the countless times I managed to break them.

I can’t say enough to express my debt to the entire SISER team: Gudrun, Thimio, Dave, Nabin, Gavin, Dalila, Dorothy, Dan, Morgan, Sean, Fateh, Nazmi, Ali, Mandy, Hasan, Jonny, Eliyas, Paolo, Mario, Leonardo, Amber, Ale. I owe to each one of you, at least one of the last two for being the glue of the group and kindly sharing an additional pair of hands, and brains. You all made the work and the breaks enjoyable and possible (!). Either by simply creating the group culture or by dragging me for lunch, coffee, cake or just for a blether and share the burden of everyday problems, you all helped me keep my mental balance. Also thanks to my colleagues at HWU Daniele, Eleonora, Waleed, Christina, Teo, Pano, Luke, Ageel, Odin, Alasdair, Ade, Rosario, Aurora, Kosta, Giorko and also Kosta, Despoina, Sotiri, Rodi, Andrea, Anna, Evi, Giorgo, Mano who offered their friendship on many occasions and shared my exasperation, but also my excitement, during the ups and downs of this PhD. I definitely forget to include many

other people, but you know you were a part of this effort and you have my cordial gratitude.

I wouldn’t have been in the position to write this thesis, of course, without the support of my parents, Manoli and Niki, and my brother, Michali. They always approved my endeavours, no matter how far from them these would keep me. Finally, I can’t express enough on how much I owe to Anastasia, as she would prefer I’d rather not spend more time writing. I certainly owe you twice the time I spent away, and I just hope I can make it up soon.

This thesis received the financial support of the Engineering and Physical Sciences Research Council (EPSRC) and the European Community's Seventh Framework Program (FP7/2007-2013).

For the final steps of this PhD thesis I am also grateful to Dr T.S. O’Donovan and Dr N.J. Ekins-Daukes for their constructive comments, as well as their positive and encouraging attitude.

ACADEMIC REGISTRY

Research Thesis Submission

Name*:*	Georgios E. Arnaoutakis		
School/PGI:	Engineering and Physical Sciences/Photonics & Quantum Sciences		
Version: *(i.e. First, Resubmission, Final)*	Final	Degree Sought (Award **and** Subject area)	PhD in Photovoltaic Engineering

Declaration

In accordance with the appropriate regulations I hereby submit my thesis and I declare that:

1) the thesis embodies the results of my own work and has been composed by myself
2) where appropriate, I have made acknowledgement of the work of others and have made reference to work carried out in collaboration with other persons
3) the thesis is the correct version of the thesis for submission and is the same version as any electronic versions submitted*.
4) my thesis for the award referred to, deposited in the Heriot-Watt University Library, should be made available for loan or photocopying and be available via the Institutional Repository, subject to such conditions as the Librarian may require
5) I understand that as a student of the University I am required to abide by the Regulations of the University and to conform to its discipline.

* *Please note that it is the responsibility of the candidate to ensure that the correct version of the thesis is submitted.*

Signature of Candidate*:*		Date:	June 2015

Submission

Submitted By *(name in capitals):*	GEORGIOS E. ARNAOUTAKIS
Signature of Individual Submitting:	
Date Submitted:	June 2015

For Completion in the Student Service Centre (SSC)

Received in the SSC by *(name in capitals):*			
Method of Submission *(Handed in to SSC; posted through internal/external mail):*			
E-thesis Submitted ***(mandatory for final theses)***			
Signature:		Date:	

Table of Contents

List of Tables

List of Figures

Glossary

List of Abbreviations

AM1.5G	Air-mass 1.5 global
AM1.5D	Air-mass 1.5 direct
AM1.5d	Air-mass 1.5 diffuse
ARC	Anti-reflective coating
ASTM	American Society for Testing and Materials
CAD	Computer aided design
CCD	Charge-coupled-device
CPC	Compound parabolic concentrator
CPV	Concentrating photovoltaic
CR	Cross relaxation
D4σ	Second moment width
DC	Down-conversion
DCPC	Dielectric compound parabolic concentrator
DS	Down-shifting
DSSC	Dye sensitised solar cell
DTIRC	Dielectric totally internally reflecting concentrator
EL	Electroluminescence
ePLQY	External photoluminescence quantum yield
EQE	External quantum efficiency
ESA	Excited state absorption
ETU	Energy transfer up-conversion
FDTD	Finite-difference time-domain
FWHM	Full width at half maximum
GRIN	Gradient index
GSA	Ground state absorption
HPCS	Hard polymer cladding silica
iPLQY	Internal photoluminescence quantum yield
IUPAC	International Union of Pure and Applied Chemistry
I-V	Current-Voltage
LED	Light emitting diode
LSC	Luminescent solar concentrator
MPR	Multi-phonon relaxation
NA	Numerical aperture
NEQE	Normalised external quantum efficiency
NIR	Near infrared
PL	Photoluminescence
PLQY	Photoluminescence quantum yield
PMT	Photomultiplier
PV	Photovoltaic
SC	Solar cell
SNR	Signal to noise ratio
TIR	Total internal reflection
TTA	Triplet-triplet annihilation
UC	Up-conversion
UC-SC	Up-conversion solar cell
UV	Ultraviolet

Vis	Visible
VUV	Vacuum ultraviolet

List of Materials

β-$NaYF_4$	Beta-phase hexagonal sodium yttrium tetrafluoride
Al	Aluminium
Al_2O_3	Aluminium oxide
a-Si	Amorphous silicon
a-SiN_x:H	Hydrogenated silicon nitride
Au	Gold
BaY_2F_8	Barium diyttrium octafluoride
CdSe	Cadmium selenide
CdTe	Cadmium telluride
CIGS	Copper indium gallium selenide
c-Si	Crystalline silicon
Dy^{3+}	Dysprosium (trivalent)
Er^{3+}	Erbium (trivalent)
ETFE	Ethylene tetrafluoroethylene
GaAs	Gallium arsenide
Gd_2O_2S	Gadolinium dioxysulphide
Ge	Germanium
He-Ne	Helium-neon
HgTe	Mercury telluride
Ho^{3+}	Holmium (trivalent)
$LaCl_3$	Lanthanum trichloride
LN_2	Liquid nitrogen
Nd^{3+}	Neodymium (trivalent)
OH	Hydroxyl
PbO_2S	Lead dioxysulfide
PbS	Lead sulphide
PbSe	Lead selenide
PFCB	Perfluorocyclobutane
Pr^{3+}	Praseodymium (trivalent)
PTFE	Polytetrafluoroethylene
QTH	Quartz tungsten halogen
Tb^{3+}	Terbium (trivalent)
Tm^{3+}	Thulium (trivalent)
Y^{3+}	Yttrium (trivalent)
YAG	Yttrium Aluminium Garnet
Yb^{3+}	Ytterbium (trivalent)

List of radiometric quantities

Quantity	Symbol	Units	Expression
Energy	Q	J	
Power / flux	P , Φ	W	$\partial Q/\partial t$
Intensity	I	W / sr	$\partial P/\partial \Omega$
Irradiance / power density	E	W / m^2	$\partial P/\partial A$
Radiance	L	W / (m^2sr)	$\partial^2 P/\partial A \partial \Omega$

All the above quantities can also be used with a spectral distribution either per wavelength λ or frequency ω.

List of physical constants

Constant	Symbol	Value	Units
Planck constant	h	6.626×10^{-34}	J s
Charge of an electron	e	1.602×10^{-19}	A s
Boltzmann constant	k	1.381×10^{-23}	J / K
Speed of light in vacuum	c	2.998×10^{8}	m / s

Conversion of units

Angles: $1^{o} = 17.45$ mrad

Wavelength to wave number: n [1/cm] = 10^7 / (λ [nm])

Wavelength to photon energy: E [eV] = 1.24 / (λ [μm])

Irradiance / power density: E [W/m^2] = 10^{-5} [W/cm^2] = 10^{-3} [mW/mm^2]

Transmission T to absorption coefficient a in thickness l: $T = e^{-al}$

Transmission T to Optical Density D: $T = 10^{-D}$

List of Publications by the Candidate

The following list includes publications in peer-reviewed journals as well as papers presented in international conferences and workshops, related to the subject of this thesis and other projects in reverse chronological order.

Peer-reviewed journal articles

G.E. Arnaoutakis *et al.*, Up-conversion concentrating solar cells based on BaY_2F_8:30%Er^{3+}. *In preparation*.

G.E. Arnaoutakis, J. Marques-Hueso, A. Ivaturi, K.W. Krämer, S. Fischer, J.C. Goldschmidt, B.S. Richards, Enhanced energy conversion of up-conversion solar cells by the integration of compound parabolic concentrating optics. *Solar Energy Materials & Solar Cells,* **140**, (2015), 217-223. doi: 10.1016/j.solmat.2015.04.020

G.E. Arnaoutakis, J. Marques-Hueso, A. Ivaturi, K.W. Krämer, S. Fischer, J.C. Goldschmidt, B.S. Richards. Enhanced up-conversion for photovoltaics *via* concentrating integrated optics. *Optics Express*, 2014, **22**(102), A452-A464. doi: 10.1364/OE.22.00A452

G.E. Arnaoutakis, J. Marques-Hueso, T.K. Mallick, B.S. Richards. Coupling of sunlight into optical fibres and spectral dependence for solar energy applications. *Solar Energy*, 2013, **93**, 235-243. doi: 10.1016/j.solener.2013.04.008

Conference proceedings

G.E. Arnaoutakis, J. Marques-Hueso, K.W. Krämer, J.C. Goldschmidt, B.S. Richards. Up-conversion enhancement in photovoltaic devices *via* non-imaging optics. In *29th European Photovoltaic Solar Energy Conference and Exhibition*. (pp.352–355), Amsterdam, the Netherlands, 2014, September, doi: 10.4229/EUPVSEC20142014-1BV.7.74 (Poster presentation)

Conference proceedings (continued)

G.E. Arnaoutakis, J. Marques-Hueso, B.S. Richards. Up-conversion for Photovoltaic devices: Overview and approaches towards system integration. In *2nd International Symposium on Energy Challenges and Mechanics*. Aberdeen, UK, 2014, August. (Invited presentation)

J. Marques-Hueso, S.K.W. MacDougall, A. Boccolini, J. Morton, **G.E. Arnaoutakis**, B.S. Richards. Up-conversion Photovoltaics: Challenges and Possible Solutions from Nano-photonics. In *2nd International Symposium on Energy Challenges and Mechanics*. Aberdeen, UK, 2014, August.

G.E. Arnaoutakis, J. Marques-Hueso, B.S. Richards. Optimizing integrated optics for up-conversion photovoltaic devices. In *International Workshop on Photoluminescence in Rare Earths (PRE'14): Photonic materials and devices*. San Sebastian, Spain, 2014, May. (Oral presentation)

G.E. Arnaoutakis, J. Marques-Hueso, A. Ivaturi, K.W. Krämer, T.K. Mallick, B.S. Richards. Enhancement of Up-conversion for Photovoltaics with β-$NaYF_4$:Er^{3+} and Concentrating Integrated Optics. In *Optical Nanostructures and Advanced Materials for Photovoltaics,* (pp. PT3C-4). Tucson, Arizona United States, 2013, November. Optical Society of America, doi: 10.1364/PV.2013.PT3C.4 (Oral presentation)

B.S. Richards, J. Marques-Hueso, S.K.W. MacDougall, A. Boccolini, J. Morton, E.D. Mammo, **G.E. Arnaoutakis**, A. Ivaturi. Progress Towards Enhancing the Performance of c-Si Photovoltaic Devices *via* Up- and Down-Conversion. In *Optical Nanostructures and Advanced Materials for Photovoltaics,* (pp. PT3C-1). Tucson, Arizona United States, 2013, November. Optical Society of America, doi: 10.1364/PV.2013.PT3C.1

G.E. Arnaoutakis, J. Marques-Hueso, B.S. Richards, T.K. Mallick. Propagation of white light through optical fibres for CPV systems. In *SPIE 8438 Photonics for Solar Energy Systems IV,* (pp. 843811). Brussels, Belgium, 2012, June. Society of Photo-Optical Instrumentation Engineers, doi: 10.1117/12.922134 (Poster presentation)

Other publications

A. Phinikarides, **G.E. Arnaoutakis**, M. Theristis, G. Kocher. Comparison of a Stand-Alone PV System with a Stand-Alone Hybrid (PV/Wind) System on a Building in Cyprus. In *29th European Photovoltaic Solar Energy Conference and Exhibition*. (pp.3833–3836), Amsterdam, the Netherlands, 2014, September, doi: 10.4229/EUPVSEC20142014-6AV.5.37

M. Theristis, **G.E. Arnaoutakis**, N. Sarmah, T.K. Mallick, T.S. O'Donovan. Solar Spectrum Dependent Thermal Model for HCPV Systems. In 13th *UK Heat Transfer Conference*, London, UK, 2013, September.

Chapter 1 : Introduction

1.1 Motivation

Energy demand in developing, but particularly in developed countries, is increasingly reaching unprecedented levels. The energy demand estimated in 1997 by the International Energy Agency was 8,610 Mtoe, whereas the estimation for 2035 is 13,529 Mtoe [1]. As the units (tonnes of oil equivalent) suggest, oil, coal and gas are still [2] the primary resource for global energy supply. Other than the argument that these resources are the reason behind the anthropogenic global warming [3], the aforementioned fuels are fossils, thus finite in human timescales [4]. It is therefore accepted that if energy supply is not a challenge for humanity today, it will become a major problem at the current rate of energy consumption and if alternative and renewable resources are not sought after.

Energy from the sun is constantly reaching the earth at a rate, which is known as the solar constant, of 1360 W/m^2 [5]. In one hour, this corresponds to approximately the energy the world consumes in a year [6]. One technology able to utilise this resource relies on systems that transfer the solar radiation as heat into liquid media, generally categorised as solar thermal systems. This way, solar radiation is stored in the medium and consequently increases its temperature above the ambient. The stored heat can be subsequently utilised for electricity or direct uses in existing power plants that currently receive the required heat from fossil fuels. Alternatively, solar radiation can be directly converted to electricity in solar photovoltaic systems. Currently, solar thermal technology has an average capacity in the range of 50 W_{th}/m^2, compared to solar photovoltaics with average capacity of 20 W_{el}/m^2 [7].

1.2 Photovoltaics

This thesis will focus on the utilisation of the solar resource by technology based on the photovoltaic/photoelectric effect. The phenomenon involves the separation of electrons from an atom upon absorption of light. Accordingly, the absorbed light needs to possess energy equal or above the energy that holds the whole ensemble together.

If the current trends in solar photovoltaic prices continue with the same exponential decrease [8], photovoltaic technology will be the best alternative to fossil fuels [9]. Despite these positive estimations, the main cost of the technology remains in the module [10] directly related to the abundance of the semiconductor material. Out of the available photovoltaic technologies, crystalline silicon (c-Si) not only embodies 90% of the global market, but also represents the greatest electricity producer among photovoltaic technologies [11]. In addition to the material requirements, another factor driving the cost is the energy conversion efficiency. Although, photovoltaic efficiency improves steadily, the highest single threshold and material solar cell conversion efficiencies are currently not higher than 30% [12]. One reason for this is the low portion of the solar spectrum utilised. This inevitably leads to the search for earth abundant materials [13] that utilise a greater portion of the solar spectrum.

1.3 Up-conversion

The approach followed in this thesis relates to the up-conversion of the sunlight before its interaction with the solar cell. This is an important yet simple, in principle, approach to improve the efficiency of a solar cell. It does that by addition of photons with energy less than the threshold of the solar cell, sub-band-gap photons. This way, photons below the band-gap of photovoltaic solar cells, otherwise lost, can be used to further induce an electric current. Similarly, it constitutes a simple approach because it relies on existing and already developed solar cell technology. It particularly does not interact with the semiconductor material of the solar cell electronically, but merely optically.

Up-conversion involves the addition of two or more low energy photons into one or more of higher energy photons. In fact, the story of up-conversion goes back over 50 years where it was first proposed as a quantum counter [14]. Although the quantum efficiency of the process was expected to be low, this did not prevent the demonstration of the first infrared quantum counters and up-converters [15, 16]. From these very first demonstrations the need to state the power density along with the quantum efficiency was essential due to the nonlinearity of up-conversion. In photovoltaic solar cells, up-conversion was first employed with a rare earth, ytterbium-doped vitroceramic in gallium arsenide (GaAs) solar cells in 1996. Another rare earth, erbium, which will comprise the core of this thesis, was employed for c-Si solar cells. Other rare earths and materials have been proposed but these still remain the most common candidates for

photovoltaics. An up-converter can in practice be an additional layer coupled to the solar cell. Another reason adding simplicity to this configuration is that the two layers, solar cell and up-converter, can be independently, yet concurrently developed.

The main geometry of the device remained the same before the work presented here, as in the first proposed layered configuration. In this thesis, with the intention to gain the maximum out of the solar spectrum with up-conversion, geometries concentrating the incident irradiance were investigated. The relevant bands in the solar spectrum are depicted in Figure 1.1 for c-Si solar cells and erbium up-converters. Absorption of photons at approximately 1500 nm will excite the erbium ion from the $^4I_{15/2}$ energy level to the $^4F_{9/2}$ and $^4S_{3/2}$ to finally emit from the $^4I_{11/2}$ level mainly at 980 nm, above the band-gap of the overlying c-Si solar cell.

The first geometry was inspired by the extended application of rare earth-doped optical fibres. Thus, a novel optical system to concentrate and transfer the required solar irradiance into the core of an erbium-doped optical fibre was investigated. Additionally, up-conversion was studied in erbium-doped optical fibres of low doping concentration.

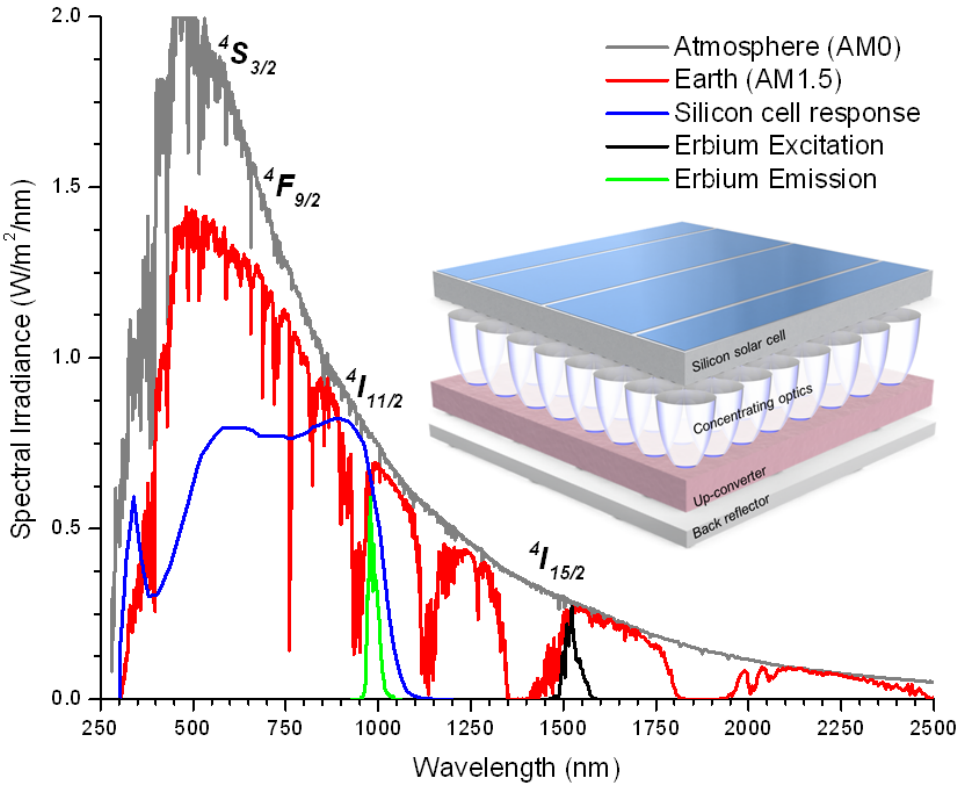

Figure 1.1: The solar spectrum and the main bands responsible for up-conversion in crystalline silicon solar cells. The structure of the device is shown in the inset. The solar cell coupled with the up-converter *via* the optics integrated in the device, first proposed in this work.

In the second investigated geometry, the concentrating optics were integrated into the archetypal layered device structure, as shown in the inset of Figure 1.1. For this purpose, the concentration, transmission and collection properties of several imaging and non-imaging optics were initially investigated. Optimum optical properties were identified for the concentrating optics and further proved the potential of the geometry. Different bifacial solar cells were also assessed according to their optical properties relevant to the performance of the device. Finally, two up-conversion erbium-doped materials realised the devices in this thesis. The first, a so-called up-conversion phosphor, β-$NaYF_4$:25%Er^{3+}, and the second, an up-conversion crystal, BaY_2F_8:30%Er^{3+}. Both rare earth materials are known as two of the most efficient for up-conversion to-date. However, each of them has optical properties that merit the device differently as it will be shown.

1.4 Thesis outline

The thesis is structured as follows. The motivation behind the approaches that I followed to enhance the conversion efficiency of photovoltaic solar cells *via* up-conversion and solar concentration, were introduced in this chapter.

The basic photovoltaic and concentration principles along with the physics behind photo-luminescence and up-conversion are presented in Chapter 2. This includes the theory and the basic models describing the underlying mechanisms that result in the colourful emission from converted infrared photons, invisible to the human eye. A review of the literature of up-conversion in photovoltaics and an outlook of the materials is also given. Finally, Chapter 2 closes with the current approaches and concepts for up-conversion enhancement.

Then, the methods used for calculation, modelling, characterisation and experiments are presented in Chapter 3. This includes the description of the models used for calculation of the three-dimensional distribution of the irradiance in the investigated systems. Also here, the equipment used and the experimental setups, along with a description of the materials used are presented.

The first investigated approach in optical fibres is presented in Chapter 4 with a novel high concentration system, incorporating primary and secondary optics. The essential parameters of the acceptance angle and wavelength for maximisation of the coupling

efficiency and solar concentration are presented in this chapter, along with the regimes for a complete optimisation.

The high solar concentration achieved in the presented system, useful for up-conversion, can be delivered in doped optical fibres. Hence, the study of erbium-doped silicate optical fibres is presented in Chapter 5. The up-converted photoluminescence depending in the length of the optical fibre and the excitation power density were studied in double-clad optical fibres.

The second investigated approach is presented in Chapter 6. There, the secondary optics, were integrated between the solar cell and an up-converting layer used for conversion of the transmitted sub-band-gap photons. The UC layer in this case was multi-crystalline β-$NaYF_4$:25%Er^{3+}, one of the most efficient rare earth phosphors applied in photovoltaics. A comparative study between imaging and non-imaging optics achieving different solar concentrations is presented. Figures of merit to achieve significant enhancements are also provided.

Chapter 7 further focuses on non-imaging optics and particularly dielectric compound parabolic concentrating (DCPC) optics. The effect of the acceptance angle of the DCPC on the excitation profile of the up-conversion layer is presented. Here, the conversion efficiency of the up-conversion solar cell (UC-SC) was also quantified by means of current-voltage (*I-V*) characteristics, a characterisation that is rarely presented for UC-SC.

The DCPC integrated UC-SC were investigated *via* the characterisation of devices based on a different class of up-conversion materials, the BaY_2F_8:30%Er^{3+} in Chapter 8. The latter is a monocrystalline material characterised by high transmission and negligible scattering in the wavelengths of interest.

Finally, in Chapter 9 overall conclusions are drawn from the approaches followed during the course of this thesis and suggestions for future directions are discussed, where potential for further research is identified.

Chapter 2 : Photovoltaics and photoluminescence in rare earths

2.1 The solar spectrum

The ultimate goal throughout this thesis is the efficient conversion of energy from the sun. Being the central star of our planetary system, the sun continuously creates nuclear fusion reactions of hydrogen into helium. This results in emission of electromagnetic radiation from its surface, the photosphere, at a temperature in the region of 6000 K and an energy or spectral distribution following Planck's law. As light from the sun travels through space, it will interact with matter and may thus be transmitted, absorbed, scattered, reflected, refracted or diffracted. Sunlight in the atmosphere and before reaching the earth will mainly undergo the first three interactions, while the three last will be analysed in section 2.6.

Depending on the zenith angle φ as the sunlight reaches the earth, it will be transmitted through path lengths of various air-masses (AM) according to

$$AM = 1 / cos\varphi \qquad (2.1)$$

This angle is of interest as it directly refers to the available solar resource that can be exploited on earth. The AM term has been standardised by the American Society for Testing and Materials (ASTM) and is widely used for photovoltaic applications. The irradiance at top of the atmosphere is AM0, while at $\varphi = 48.2^{o}$ is referred to as the global AM1.5G with an integrated intensity of 1000 W/m^2. The latter has become the standard for the characterisation of solar and photovoltaic devices [17, 18]. Both spectral irradiances are presented in Figure 2.1.

The radiation may be directly transmitted through the atmosphere and corresponds to the direct component of the solar spectrum, denoted as AM1.5D. Part of the radiation is scattered in the atmosphere, especially in cloudy days, and finally reaches the earth as the diffuse component in the spectrum, referred as the AM1.5d. Absorption from O_2, O_3, H_2O and CO_2 in the atmosphere permits negligible irradiance on the earth in the parts of the spectrum around 250 nm, 1300 nm and 1900 nm. Once the light of this spectrum reaches the earth, it is available to be converted into other forms of energy, including electricity.

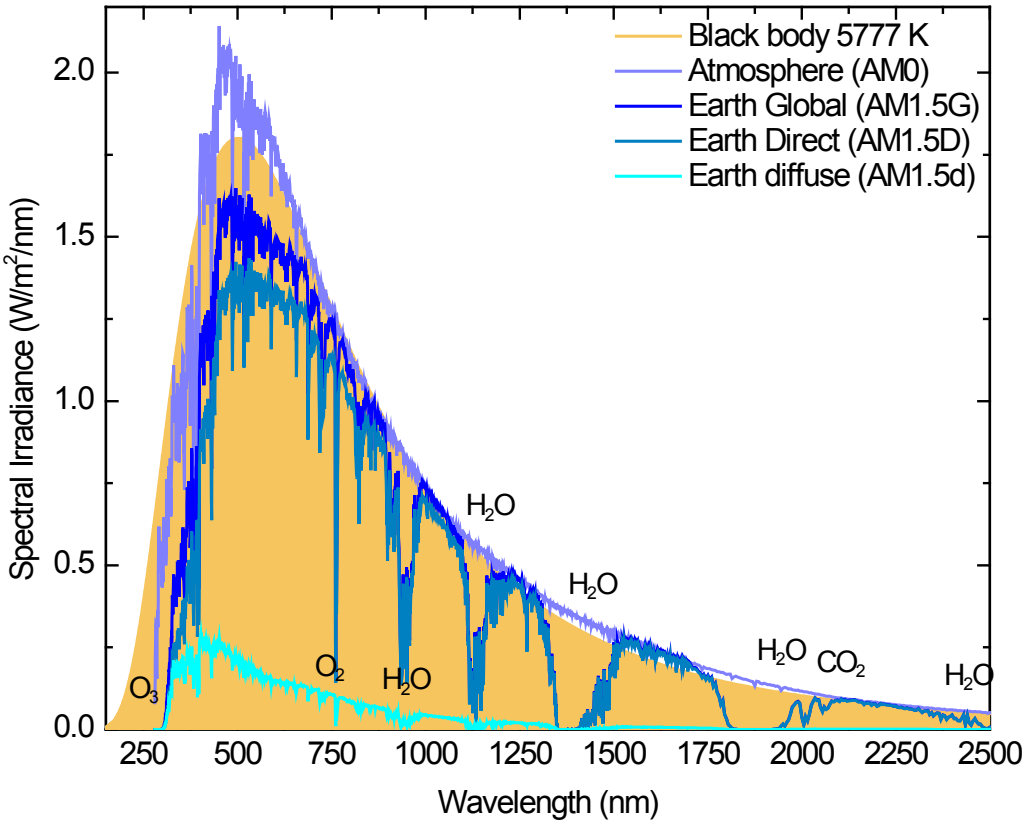

Figure 2.1: The spectral irradiance of the solar spectrum for the extra-terrestrial incident at top of the atmosphere (AM0), the global (AM1.5G), the direct (AM1.5D) and the diffuse (AM1.5d) components. [17, 18].

2.2 Brief photovoltaic history

The story of the conversion of light into electricity goes back to the discovery of a photocurrent from illuminated platinum electrodes immersed in water by A.E. Becquerel [19, 20]. It was later discovered that photocurrent could be obtained from selenium by W. Smith [21] and W.G. Adams [22] and later led to the first solar cell, made of a thin layer of gold on selenium with an efficiency of 1% [23].

The induction of an electrical current by ultraviolet light was further studied by A. Stoletow [24, 25]. The action of light on matter, later dubbed as the photoelectric effect, was explained by A. Einstein, triggered by the idea that light comes in packets, quanta of energy [26], today called photons. The idea further led to the rethinking of the then accepted classical mechanics, being today described by quantum mechanics.

It was not until 40 years later that the first solar cell was made from silicon by R. Ohl at Bell Laboratories [27, 28]. This initiated further research on positive (*p*) and negative (*n*) junctions and the concentrations of impurities in semiconductors. The theory of diodes [29] and the transistor [30] was concurrently developed by W. Shockley. Based on this theory, more efficient solar cells were made [31, 32] that later drove one of the first satellites in orbit around the earth [33]. For the development of the solar cell technology since then, the interested reader may refer to recent literature by the "grandfathers" of photovoltaics for a detailed review [34, 35].

A straightforward differentiation of photovoltaics into three generations is generally made based on industry trends. The 1st generation covers the solar cells widely used at present, based mainly on silicon wafers. Silicon still remains the predominant photovoltaic material. On one hand this is primarily attributed to its abundance on the earth's crust [13]. On the other hand to the extended use of silicon by the microelectronics and the information technology [36], which inevitably leads to the exchange and transfer of knowledge between the industry sectors.

With the 2nd generation, the reduction in costs by the use of less semiconductor material is represented by thin-film technologies. Candidate materials under this generation include cadmium telluride (CdTe), copper indium gallium selenide (CIGS) and amorphous silicon (a-Si).

All the currently pursued approaches fall under the 3rd generation [37] and namely include: tandem multi-junction solar cells [38], quantum well solar cells [39], intermediate band or impurity [40, 41], hot carrier solar cells [42, 43], high solar concentration [44] and spectrum splitting approaches [45-47], spectral conversion [48] that includes down-conversion (DC), down-shifting (DS) and up-conversion (UC), dye-sensitised solar cells and very recently perovskites [49, 50].

One may differentiate further each of the 3rd generation approaches into more categories. It is generally accepted, however, that every approach has its merits and drawbacks. Nonetheless, it may additionally provide new insights into the physical understanding of the technology. Two 3rd generation approaches were followed during the course of this thesis, solar concentration and up-conversion. The two approaches are directly interconnected and merit a parallel investigation. A more detailed review of the two approaches follows.

2.3 Photovoltaic efficiency limits

According to the detailed balance model [51] of a solar cell, the upper limit of the conversion efficiency of a solar cell based on a single threshold *p-n* junction is 30% at 1.12 eV. For silicon, this adjusts to 29.8% [52] by further considering Auger recombination losses and to 29.43% [53] under the AM1.5G spectrum and realistic material parameters.

The main mechanisms that affect the maximum conversion efficiency of a *p-n* junction solar cell are schematically depicted in Figure 2.2. In this schematic the horizontal axis refers to the depth in the *p-n* junction and the vertical axis to charge carrier energy. The conduction E_C and valence E_V bands are indicated, separated by the energy band-gap E_g between the bands.

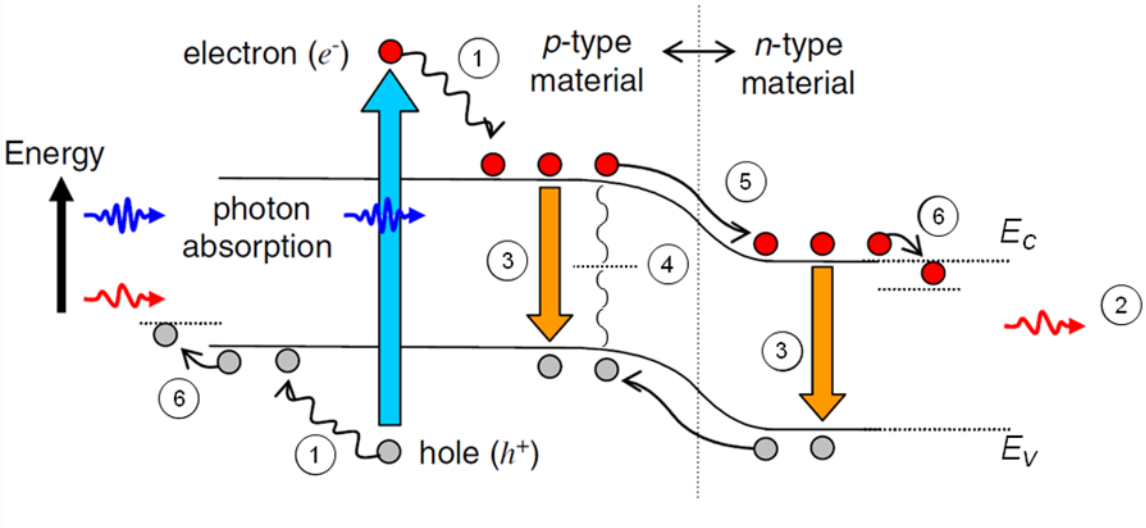

Figure 2.2: Model of a *p-n* junction solar cell and main mechanisms upon absorption of photons. ① Above band-gap/thermalisation, ② below band-gap/transmission, ③ radiative recombination, ④ non-radiative recombination, ⑤ diffusion across the junction, ⑥ voltage drop at the contacts. (Adapted from [48]).

Following the detailed balance model, photons incident on a solar cell can be ① above or ② below the band-gap of the material of the solar cell. Photons above the band-gap will be absorbed by the solar cell and give their energy to an electron in order to move it to the conduction band. However, as these electrons have energy higher than the band-gap at equilibrium, they quickly lose the excess energy as phonons. Similarly, photons

with energy equal to the band-gap will rise to the conduction band and across the junction, ⑤ in Figure 2.2, resulting in photo-current. Finally, photons with energy less than the band-gap will be transmitted through the solar cell. In Figure 2.2 three additional mechanisms are depicted as ③, the radiative recombination of an electron in the conduction band into a hole in the valence band, ④ the non-radiative recombination of an electron into an intermediate state (Shockley-Read-Hall) or another electron (Auger), and ⑥ the voltage drop at the contacts.

2.4 Up-conversion photovoltaic limits

Up-conversion is a promising third generation photovoltaic approach for overcoming the Shockley-Queisser limit [51] of single junction silicon solar cells, that is 29.43% [53]. Among the spectral conversion approaches [54, 55] to overcome the efficiency limit for single-junction solar cells, up-conversion aims to recover sub-band-gap photons otherwise transmitted through a solar cell.

Utilisation of these sub-band-gap photons has been predicted to enhance the conversion efficiency limit of a silicon solar cell to 40.2% and 53.0%, under solar concentration of one and 46,200 suns, respectively [56]. In this model, significant improvements were predicted under high solar concentration and especially by restricting the solid angle of emission. However, zero relaxation of the intermediate level of the up-converter was assumed in this model, underestimating the efficiency under low concentration.

It has been further estimated in extensive models that consider light trapping *via* optical design and non-radiative recombination, that up-conversion can provide a relative efficiency increase of approximately 25% [57, 58] on an overlying silicon solar cell with band-gap $E_g = 1.12$ eV. There, the refractive index of the up-converter was assumed equal to that of the solar cell that is $n = 3.6$. However, for real up-converters of refractive index lower than the solar cell, higher conversion efficiency is expected [59].

2.5 Photovoltaic characteristics

The conversion efficiency of a solar cell η is defined as the ratio of the output power from the solar cell P_{out} to the incident power P_{in}, as:

$$\eta = P_{out} / P_{in} \tag{2.2}$$

Conversion implies the utilisation of the solar resource, so the integrated irradiance of the AM1.5G spectrum is considered as P_{in}. P_{out}, the electrical power, is given by the product of the voltage V between the terminals of the solar cell and the current I. For photovoltaic operation a solar cell should operate under certain regimes to obtain the maximum power, and hence maximum efficiency. These regimes lie between short-circuit and open-circuit conditions. In short-circuit conditions all the photo-generated carriers flow through the diode and the current I_{SC} is maximised. In open-circuit conditions, the photo-generated carriers are equal to the injected carriers and no current flows, but the voltage V_{OC} is maximised. The maximum current and voltage, I_{MP} and V_{MP} respectively, will be extracted a few mV before the V_{OC} as a result of a small potential difference at the contacts [60]. As shown in the current-voltage (I-V) characteristic of a solar cell in Figure 2.3, the current and the voltage at maximum power give rise to the fill factor (FF), defined as,

$$FF = I_{MP}\, V_{MP} / I_{SC}\, V_{OC} \tag{2.3}$$

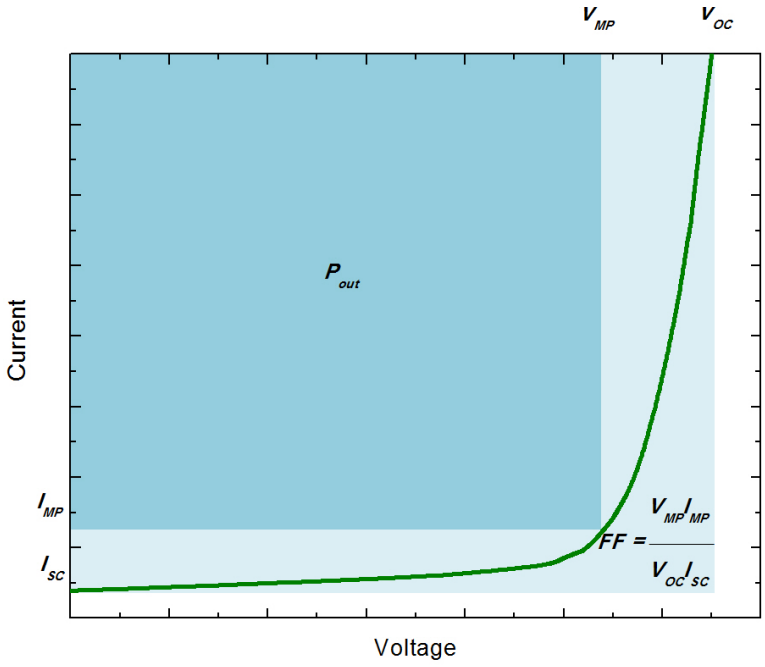

Figure 2.3: I-V characteristic of a generic solar cell and photovoltaic parameters I_{SC}, V_{OC}, I_{MP}, V_{MP} and FF.

2.6 Concentrating optics and photovoltaics

The Shockley-Queisser limit and the up-conversion photovoltaic models consider one sun concentration but also maximum concentration. In the sun-solar cell system, maximum concentration can either mean the restriction of the solid angle of absorption-emission between the sun and the cell, *i.e.* 0.267°, or the extension of the solid angle to a complete hemisphere extending over 2π. Both conditions may practically translate to a change in the solid angle by means of geometrical optics as shown in Figure 2.4.

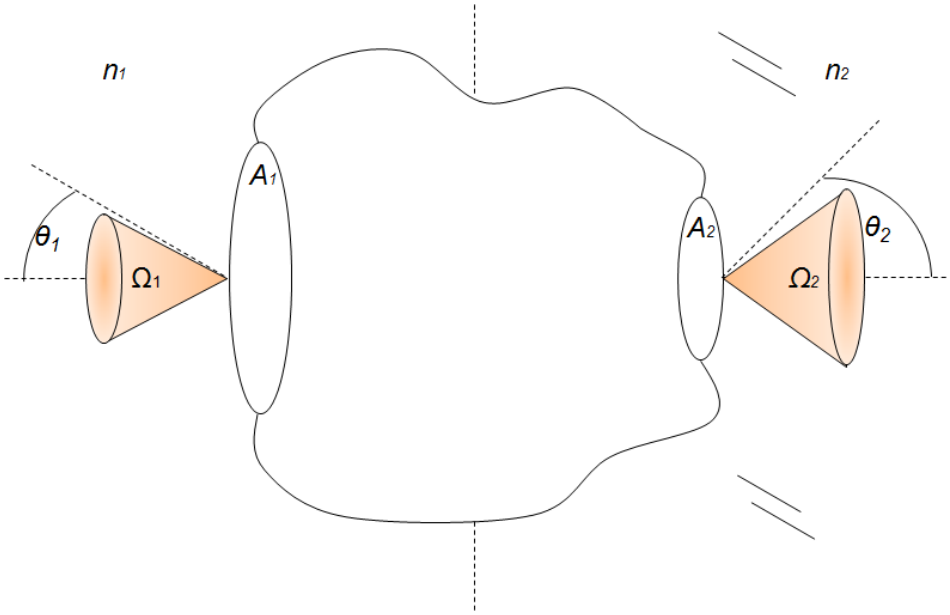

Figure 2.4: Geometrical concentration and *étendue* in a closed optical system. The solid angles Ω, incident angle θ, aperture areas A and refractive indices n are shown.

In this case from conservation of entropy, the generalised *étendue* at the input of the optics should equal the *étendue* at the output, therefore [61]:

$$n_1^2 A_1 \int \cos\theta_1 d\Omega_1 = n_2^2 A_2 \int \cos\theta_2 d\Omega_2 \qquad (2.4),$$

where n is the index of refraction, Ω the solid angle, θ the acceptance angle, and A the aperture of the optics, while indices 1 and 2 refer to input and output, respectively. The concept of *étendue* may also be found as the Lagrange theorem, optical invariant, optical extent, acceptance, throughput or $A\Omega$ product, depending on the context [62].

Additionally, the maximum average solar concentration C in three-dimensional space can be estimated by the angular ratio [61],

$$C = \frac{n_2^2 \sin^2 \theta_2}{n_1^2 \sin^2 \theta_1} \quad (2.5).$$

From Equation (2.5), the upper limit for solar concentration widely used for solar cells on earth is ~46,200×. This implies that the solar cell is surrounded by air with a refractive index of 1. However, if a medium of a higher refractive index is used, this limit raises by a factor equal to the square of the refractive index. The average solar concentration achieved by the optics can be calculated with Equation (2.5). However, the spatial distribution of the concentration, and hence the power density, at the output of the optics will vary significantly from the average and can be modelled *via* ray optics. For an UC-SC, this power density is of particular interest as it relates with the UC luminescence as it will be discussed in section 2.10.

2.6.2 Optics for concentrating photovoltaics

There is a plethora of literature in broadband geometrical optics to transform the solar irradiance. A division between refractive and reflective can be made, *cf*. Figure 2.5(a,b), concentration is obtained *via* a focusing lens or a reflecting mirror, respectively. Solar concentration varies from 2 to 150× in the so-called low to medium range. C-Si solar cells are used in the majority of applications in this range, while thin-film and luminescent approaches are also utilised. To obtain higher solar concentration, the lens or mirror becomes the primary optic and is followed by a so-called secondary optic, see Figure 2.5(c,d).

In systems for high solar concentration up to 1100×, secondary optics are used either to enhance performance, or to ease tracking tolerance [63]. These optics make the system more versatile, especially if one wants to achieve efficient coupling with the solar cells. III-V multi-junction solar cells are utilised in this range. These solar cells currently hold the record for solar energy conversion efficiency, owing to the better spectral matching of the direct band-gap semiconductor alloys, such as GaInP and GaInAs, which are deposited by molecular beam epitaxy on Ge or GaAs substrates.

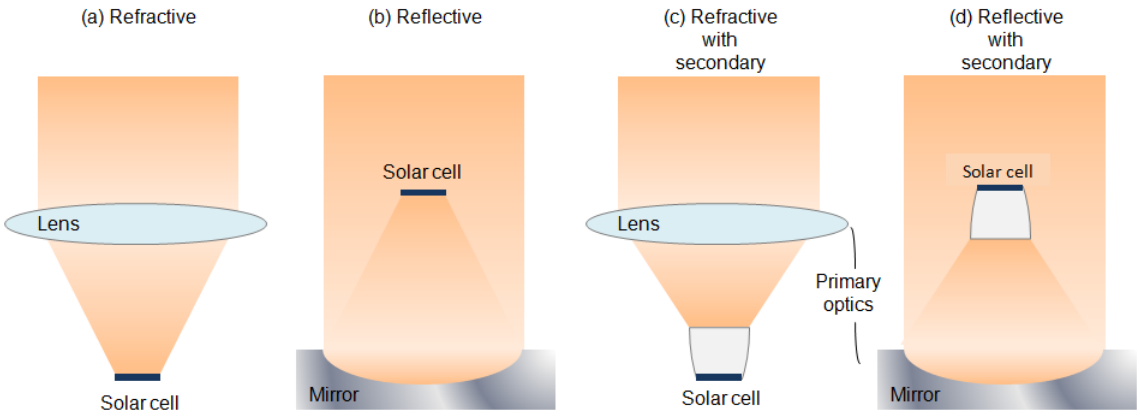

Figure 2.5: Types of concentrating optics for photovoltaics. In (a) refractive and (b) reflective, a lens or mirror is used for low to medium concentration, while for higher concentration secondary optics are used either with (c) refractive or (d) reflective primary optics.

The primary optics currently [63] used for high concentration are Fresnel lenses and parabolic reflectors. The optical design required that the system follows the sun throughout the day on a two-axis tracking system. However, significant benefits can be obtained from the advent of optics and solar cells in the micro-scale. Solar concentration higher than 300× has been demonstrated in flat plate concentrators with GRIN lenses [64, 65] or micro-lens arrays [66, 67] that are able to track the sun by small lateral movements [68, 69].

Additionally, the optics should conform to additional restrictions posed by the solar cell. The main are uniform irradiance at the exit aperture and reduced chromatic aberrations that affect the performance of the solar cell [70, 71]. To this end, primary optics such as non-imaging Fresnel lenses [72], tailored prisms in parallel [73] or arrays of refractive and TIR prisms [74] have been proposed. Additionally, the secondary optics or so-called "homogenisers" are commonly used to transform the irradiance into a uniform profile. For an extensive presentation on the various classes of concentrating optics the reader may refer to [75] and references therein. However, for the purposes of this thesis, the review will be limited to totally internally reflecting (TIR) with a focus on non-imaging optics.

2.6.1 Totally internally reflecting and non-imaging optics

As the term implies, non-imaging optics do not form an image at the end plane as the imaging optics do. This enables an additional degree of freedom towards higher concentration, since transmission of an object through the optic is not a requirement. Consequently, the maximum solar concentration for imaging optics, is by a factor between 2 and 4 lower than what is achieved by non-imaging optics [61, 76]. Since, high solar concentration is one of the purposes of this thesis, non-imaging optics seem to have a great advantage over their imaging counterparts.

The optical path length, defined by the product of the refractive index and the distance elapsed by a ray or wave as [77], $\Sigma n_i d_i$, of all rays between entry and exit planes. It can be seen that the optical path length is equal to the physical path length d_i used in the Beer-Lambert law, only in the case of $n = 1$. One can say that in imaging optics all rays have the same number of interface interactions, as for example when refracting through an imaging lens. However, in non-imaging optics some rays may undergo more than one reflections or refractions.

For TIR to occur between two media of refractive index n_1 and n_2, the input angle θ_1 should be equal or above a critical value, the critical angle, according to Snell's law of refraction,

$$n_1 \sin\theta_1 = n_2 \sin\theta_2 \qquad (2.6).$$

From this, it follows the critical condition for the output angle θ_2 should be equal to $\pi/2$. The incident ray or wave is mainly reflected in medium n_1. But a small fraction, the evanescent wave, is transmitted and propagates in medium n_2 with an exponential decay [78]. This makes optics undergoing TIR more promising for photovoltaics than reflective coatings, such as aluminium, silver or gold, that are also absorbing. Albeit the reflectance of these coatings is higher than 0.95 across the solar spectrum, it falls short compared to TIR in dielectrics. Dielectric media, such as glasses and polymers, are commonly used materials for optics. This also provides broadband transmission of the optics and makes them attractive for application in photovoltaics. Further details on the optical properties of these materials will be given in Chapter 3.

Several non-imaging designs relying on TIR have been investigated with the simplest being the cone, or otherwise called tapered light-pipe in solid [79], hollow [80] and other geometries [81]. First documented by Williamson [82], who also presented a

method for ray-tracing, see Figure 2.6(a), the cone was applied in one of the first attempts for a solar pumped laser [83], see Figure 2.6(b). Although intuitively simple, the cone preserves the *étendue* for adiabatic solid cones which tend towards infinite lengths, *i.e.* approximating a cylindrical light-pipe.

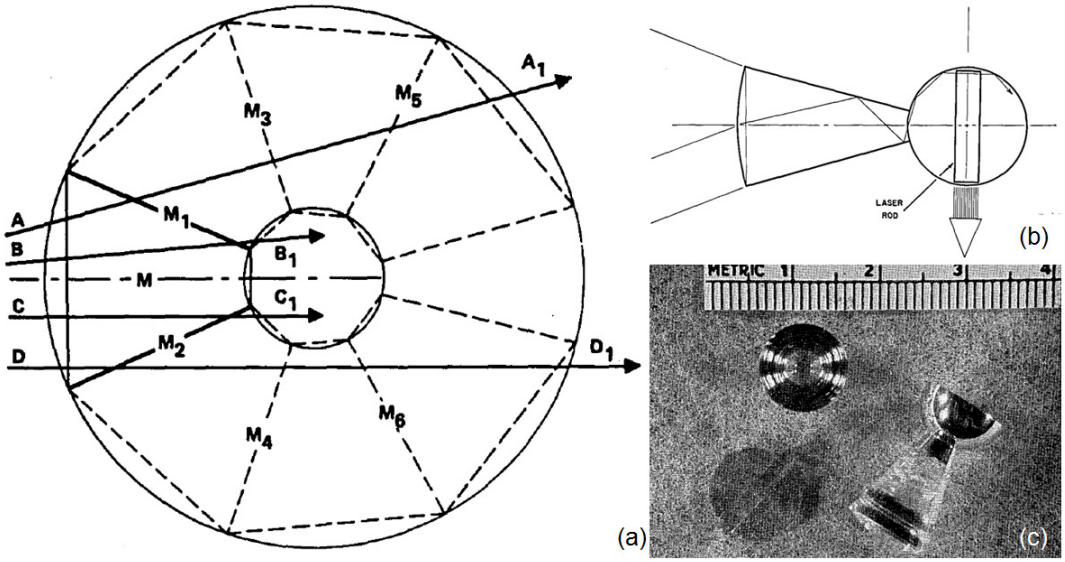

Figure 2.6: (a) Ray-tracing method for a Williamson cone. Rays are transmitted through the cone, if they end inside the inner circle [81]. (b) Schematic of a cone geometry for application in a solar-pumped laser, and (c) photographs of the optics made of strontium titanate [83].

A geometry that has received attention due to its higher angular transmission and concentration than the cone, is the dielectric compound parabolic concentrator (DCPC), shown in Figure 2.7. Investigated extensively by R. Winston [84], was initially used in Cerenkov counters [85]. It can be seen that the DCPC has a higher acceptance angle than a hollow CPC of the same parabola and collects more skew rays [86, 87]. A variation is the DCPC with frustrated TIR that has some advantage over the traditional DCPC for high flux applications [88].

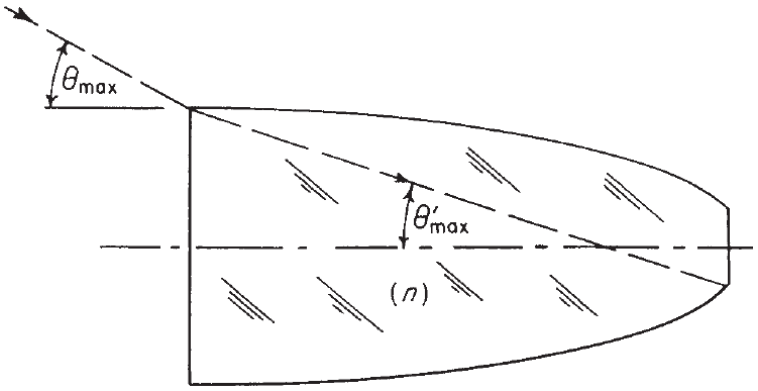

Figure 2.7: Schematic of a dielectric compound parabolic concentrator [61]. The acceptance angle increases compared to the hollow CPC, in proportion to the refractive index of the dielectric material.

A shortcoming of the DCPC, generally common within other non-imaging optics, *e.g.* the elliptical or trumpet concentrator [89], is that for narrow acceptance angles the length of the optics becomes increasingly long. This length can be reduced by using an additional optic as a primary form of concentration. Such designs have been investigated for CPC-DCPC [90] and prism coupled compound parabola [91] shown in Figure 2.8, lens-DCPC and lens-trumpet combinations, see Figure 2.9, where it was shown that shorter lengths by a factor of √C were required for the latter design [92].

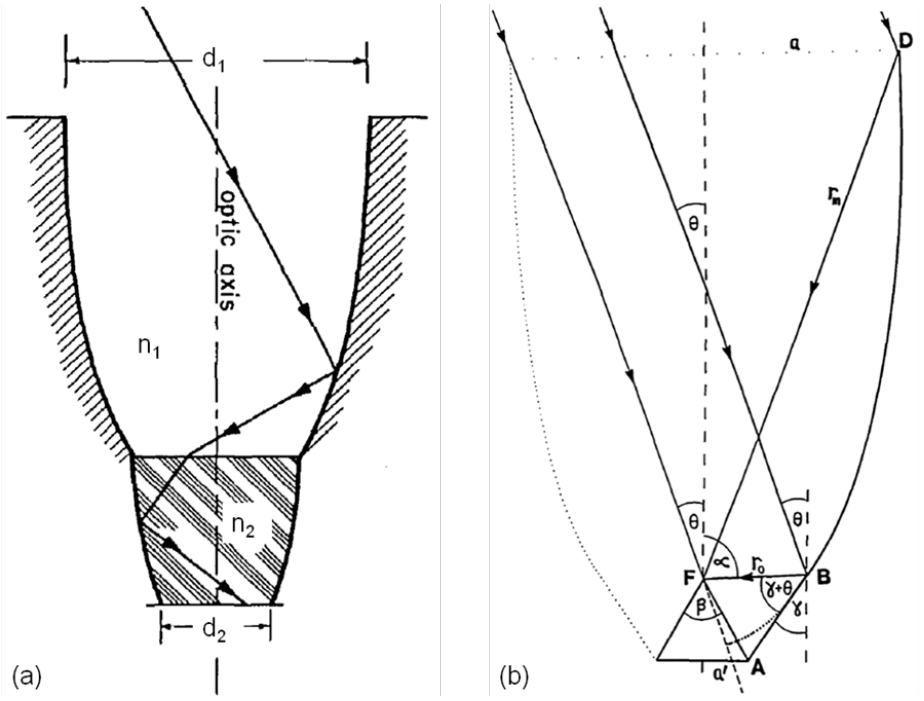

Figure 2.8: Two modifications of the CPC that achieve reduction of the required length, (a) CPC-DCPC and (b) prism-coupled compound parabola. (Adapted from [90, 91]).

Reduced lengths were further demonstrated for TIR optics with a dielectric totally internally reflecting concentrator (DTIRC) [93], see Figure 2.9. By increasing the angle of the arc of the entry aperture, the required length is reduced. Interestingly, while maintaining TIR, the reflective profile of the optic transforms from parabolic to hyperbolic. Certain advantages of this geometry can be applied when there is a restriction in the exit angle of the optic, as for example in optical fibres and will be discussed in the following section 2.6.3. A reduction of the dielectric material of the DCPC can be achieved with prism geometries as has been reported for use with bifacial solar cells [94, 95]. A review on prisms and TIR optics for solar energy applications was given by A. Rabl [96]. Additionally, reduced complexity in applications such as building integrated photovoltaics (BIPV) is achieved by rectangular apertures, matching with the dimensions of solar cells [97-99].

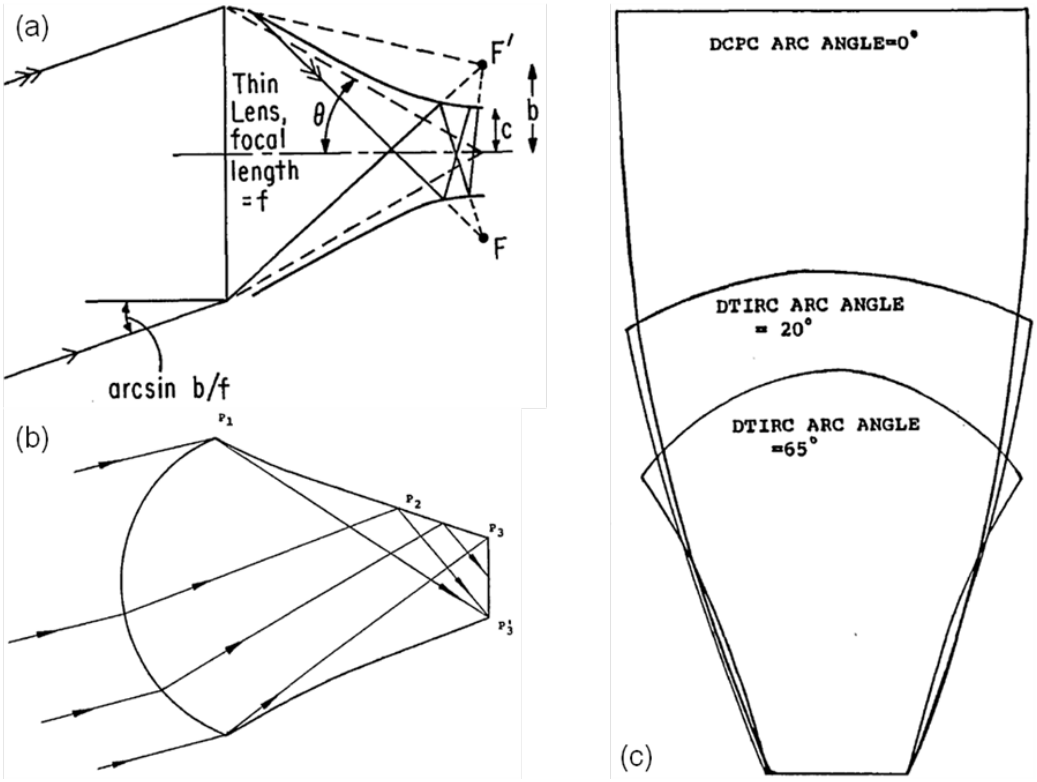

Figure 2.9: Optics with ideal concentration and reduced length, (a) lens-trumpet or flow line [92], (b) DTIRC. (c) Significant length reductions are obtained by increasing the angle of the arc of the entry aperture [93].

On a similar rationale but for illumination in the inverse direction, half-sphere TIR concentrators have been investigated [100]. Different designs for illumination and concentration were investigated by altering the divergence of the source, albeit a figure of merit of the overall optical efficiency was not reported. The half-sphere designs shown in Figure 2.10(a) were oriented towards dense source elements, such as filaments. However, with minor design modifications a similar design can be used into planar surface sources, see Figure 2.10(b), such as light emitting diodes (LED) and diode lasers. These have been investigated in TIR paraboloid optics with truncated and spherical output surfaces [101, 102].

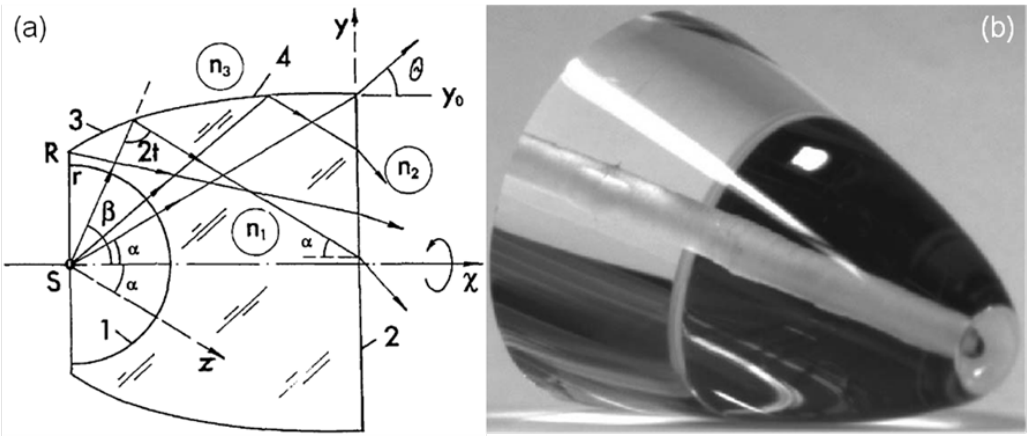

Figure 2.10: (a) Schematic of the half-sphere element designed for reduction of divergence [100]. (b) TIR paraboloid made of glass with truncated spherical exit surfaces [102].

A graphical comparison of the performance between the non-imaging optics investigated in this thesis, the cone and the CPC, can be seen in Figure 2.11. The transmission of the optics of acceptance angle 10^{o} with equal area of entry and exit aperture, hence equal concentration ratio, is displayed. It can be seen that the CPC has unity transmission below 8^{o} compared to the cone that after 4^{o} the transmission is reduced significantly. In other words, a sharper cut-off in the transmission-angle graphs, also observed for a range of acceptance angles around 10^{o} in the Figure, is an indication for best performing concentrators.

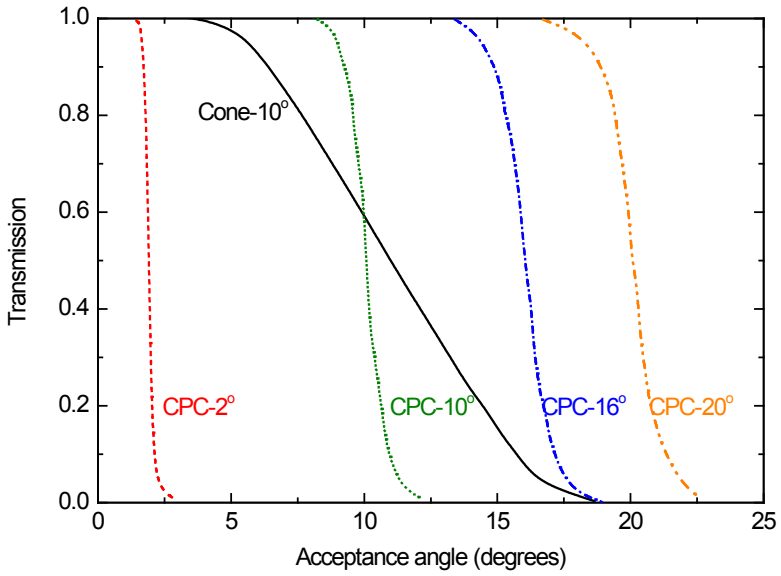

Figure 2.11: Transmission of (a) the 3D CPC for different acceptance angles and (b) the cone for 10° acceptance angle. (Adapted with permission by [61]).

The above review covered geometrical optics at the *étendue* limit that fulfil a single purpose. That is, either the transfer of radiation at the maximum concentration from the input to the output, or the collection of radiation from a finite source. Radiative emission from solar cells and phosphors is well defined as isotropic. Therefore, in the case that coupling is required between the two, as for example in the UC-SC, the optics are to serve a dual function: i) the transfer of the solar radiation at either maximum concentration or optical efficiency, and ii) the collection of the isotropically emitted radiation. As presented above, the CPC was shown to fulfil these functions, and will be further investigated in Chapter 6, 7 and 8.

2.6.3 Optical fibres and coupling

While tapered light-pipes are used for concentration, cylindrical light-pipes can transfer radiation by TIR. This wave-guiding geometry has been extensively studied, developed and expanded into the field of optical fibres. Optical fibres offer numerous advantages and new possibilities to the exploitation of solar energy. By trapping light in optical fibres, the waveguides essentially become cables that transfer concentrated light to the desired application distant from the source. These cables of light may then transfer sunlight for a wide range of applications such as solar lighting in the built environment

[103], solar-pumped lasers [104], solar furnaces [105] or Stirling engines [106], solar-powered photo-catalysis [107], photonic networks that incorporate self-powered sensing and monitoring [108] and high concentrating photovoltaic (CPV) systems [109, 110]. The reader that is interested in an extended review of applications and systems for solar energy *via* optical fibres may refer to [111] and references therein.

To guide light in a fibre, the condition for TIR needs to be fulfilled in the third dimension, giving rise to the numerical aperture (*NA*). The *NA* of an optical fibre is related to the sinus of the acceptance half-angle θ and is described by the following expression:

$$NA = \sqrt{n_1^2 - n_2^2} = n \sin\theta \qquad (2.7),$$

where n_1 and n_2 the refractive indices of the core and the cladding respectively, see Figure 2.12(a). Combining the sine law with the restriction in an optical fibre of given *NA*, Equation (2.5) becomes:

$$C_{of} = (NA/\sin\theta)^2 \qquad (2.8),$$

which implies the proportionality of solar concentration with the *NA*. The primary figure of merit for systems based on optical fibres is the coupling efficiency η_{coup}, which describes how well light is coupled into and out of an optical system, and is simply defined as the ratio of the power output P_{out} over the input power P_{in} as,

$$\eta_{coup} = P_{out} / P_{in} \qquad (2.9).$$

The challenge of coupling solar energy in optical fibres has been analysed in the past for static systems and solar concentrations up to 10× [112], while tapers made of Plexiglas and gradient index (GRIN) rods attached to the tapers, see Figure 2.12(b), were proposed with theoretical coupling efficiency above 90% for incidence angles below 65^o [113].

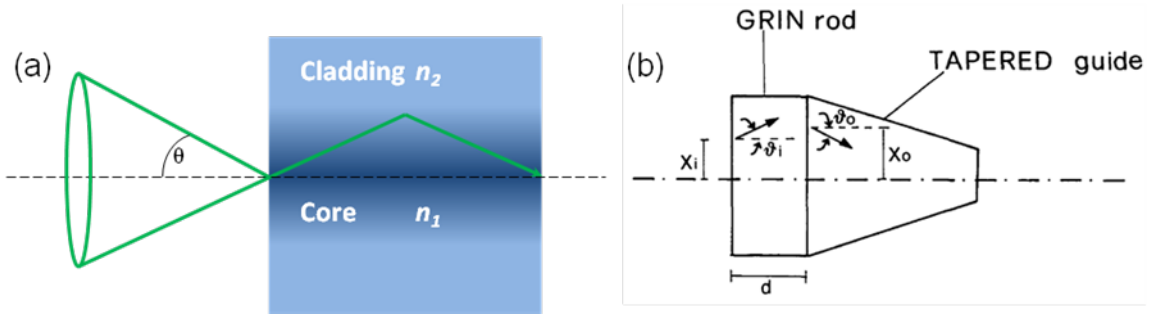

Figure 2.12: (a) Acceptance cone depending on the refractive indices of core and cladding of an optical fibre. (b) Geometry based on GRIN rods and tapered guides as analysed for coupling in optical fibres in reference [113].

Combinations of all-reflective, all-refractive and both reflective and refractive optics for infrared fibre applications were theoretically analysed by ray-tracing with coupling efficiencies between 77% and 100% [114], the highest being for all-dielectric combinations, although lacking experimental validation. Ideal 3D concentrators have been also proposed as angular transformers for optical fibre applications, which consist of a hyperbolic concentrator and plano-spherical lenses, see Figure 2.13, with coupling efficiency between 87% and 100% at *f/5* and *f/50* of the lens, respectively [115, 116].

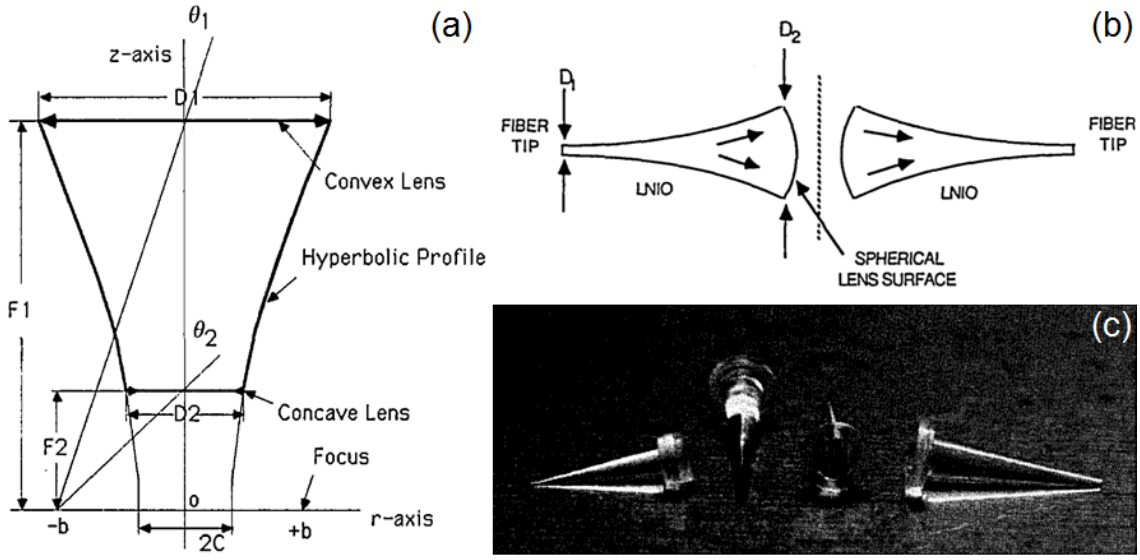

Figure 2.13: Angular transformers for optical fibre applications. (a) Design of a θ_1/θ_2 transformer consisting of a convex lens, an optic of hyperbolic profile and concave lens [115]. (b) Schematic of the coupling between optical fibres, and (c) photo of plastic injection-moulded fibre couplers of dimensions D_1 = 400 µm and D_2 = 2 mm [116].

Despite that previously presented designs were able to reach maximum efficiency or concentration, the experimental demonstrations have obtained significantly lower efficiencies. The highest reported coupling efficiency under the sun is 60% [104], which was measured with a bundle of 19 fibres side-polished and fused together, see Figure 2.14.

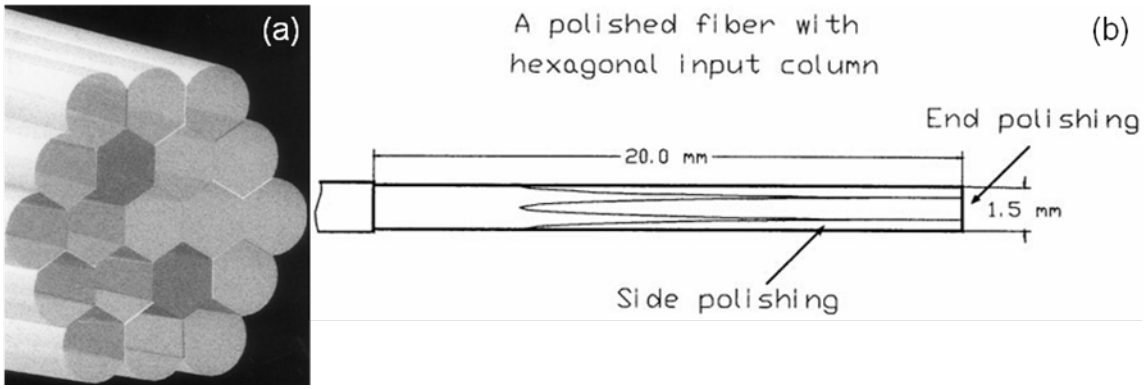

Figure 2.14: (a) Optical fibre bundle consisting of 19 fibres and resulting in the highest sunlight coupling efficiency. (b) The sides of the optical fibres have been polished, with the central fibres of the bundle having hexagonal cross sections. (Adapted from [104]).

For systems comprised of a single fibre, the coupling efficiencies have not exceeded 38% [117]. Whereas a bundle may couple light more easily and transfer more power by considering a good packing fraction [118], a single fibre can be applied in a wider range of applications due to higher solar concentration [119, 120]. In addition, the practical advantages for potential fibre applications worth examining the benefit between ideal and practical, while verifying it in a real system. Such advantages are simple fabrication, inexpensive manufacturing techniques and ease of outdoor installation and cleaning [63]. These aspects are important for coupling sunlight into an optical fibre and are investigated further in Chapter 4.

The discussion so far described optical fibres that were passive. Interesting phenomena occur though, when the optical fibres are doped with luminescent species. When a luminescent substance absorbs light of a defined wavelength and energy, it may emit at a wavelength of higher or lower energy. Rare earth doped fibres have been intensively used as signal amplifiers as they constitute simpler alternatives to electronic repeaters. This way, all optical amplification was made possible. A few examples are optical

fibres doped with erbium (Er^{3+}), which is used to amplify a signal around 1.53 μm, with praseodymium (Pr^{3+}) at 1.3 μm, and ytterbium (Yb^{3+}) at the range between 0.98 and 1.15 μm. By co-doping fibres with Er^{3+} and Yb^{3+}, amplification at 1.55 μm is possible by exciting at 0.98 μm, whereas fibres doped with thulium (Tm^{3+}) and thulium/terbium (Tb^{3+}) provide gain at 0.8, 1.4 and 1.65 μm. The next section will provide more details on how these wavelength conversions, or transitions, occur in rare earths.

2.7 Atomic and crystal structure of rare earths

Rare earth elements consist of the lanthanides, presently renamed lanthanoids by the International Union of Pure and Applied Chemistry (IUPAC) [121], and the metals scandium and yttrium (Y^{3+}). One reason for this categorisation owns to their distinctive photoluminescence properties. Following the accepted terminology, photoluminescence is distinguished into i) phosphorescence and ii) fluorescence. The first occurs on longer lifetimes than the second, implying a change in spin for the first [122, 123]. Throughout this thesis, the term photoluminescence will be used as a synonym for fluorescence.

Trivalent lanthanoids have an electronic configuration $5s^2\ 5p^6\ 4f^n$, where n is the number of electrons in the unfilled shell. The photoluminescence originates from the transitions between the unfilled *4f* electrons. The electronic structure of the rare earth ions, with the electrons in the incomplete *4f* shell screened by the filled *5s* and *5p* outer shells, results in the well-defined characteristic spectra of the rare earth ions, with a small influence of the surrounding solid (crystal or glass) structure.

Two widely studied and applied rare earth examples, Er^{3+} and neodymium (Nd^{3+}), are shown in the energy level diagrams of Figure 2.15 with the main optical transitions. The probability of these transitions to occur and the selection rules can be tracked in the Judd-Offelt theory. For the interested reader, an overview of the theory is given in the appendix.

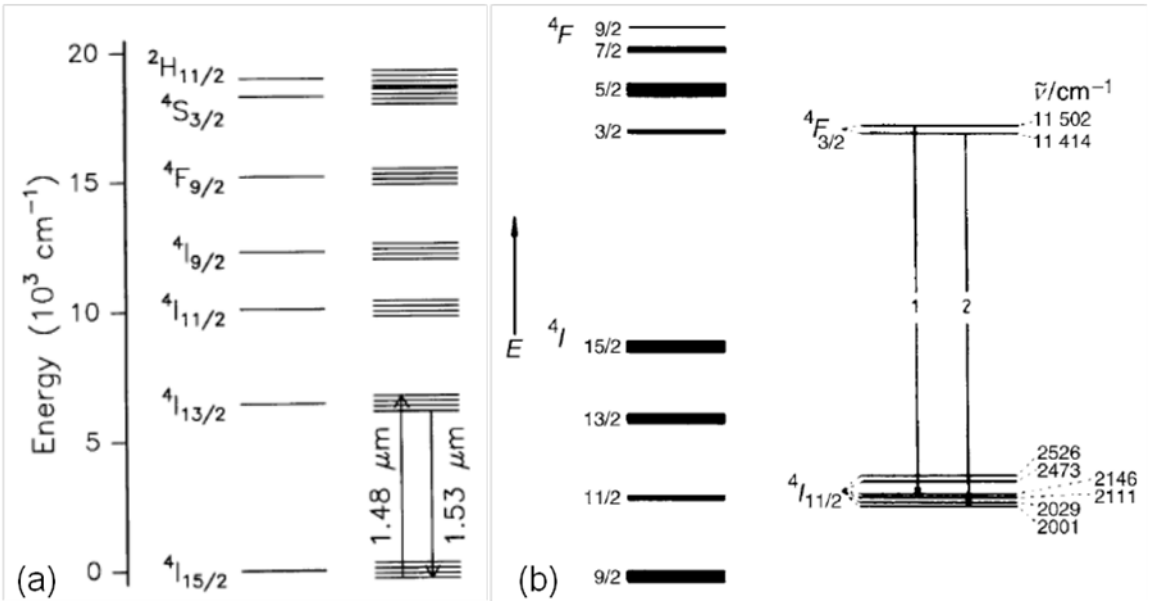

Figure 2.15: Energy levels of trivalent lanthanoid free ions embedded into a solid host. From left to right: Er^{3+} free ion, in solid [124], Nd^{3+} free ion and in solid [125]. The main transitions responsible for 1530 nm amplification in Er^{3+} and 1060 nm lasing in Nd^{3+} are also depicted.

2.8.1 Energy levels of rare earths

Figure 2.16 shows the observed and calculated transitions of trivalent lanthanoids in lanthanum chloride ($LaCl_3$) for energy levels up to 41,000 cm^{-1} [126, 127], while the energy levels in the vacuum ultraviolet (VUV) spectrum have also been calculated and observed [128, 129]. Also known in the literature as the Dieke diagram, it includes energy levels for wavelengths up to 250 nm inherent in the solar spectrum and applying to spectral conversion for photovoltaics, thus can be used for considerations throughout this thesis.

Despite that $LaCl_3$ was used as the host crystal of the rare earth ions, the observed energy levels can still serve as a basis for other crystalline environments with a variation in the order of 10^{-2} wave-numbers [130, 131]. In the diagram (*cf.* Figure 2.16) the thickness of each line corresponds to the magnitude of the Stark level splitting, while more probable transitions to the ground state are indicated by half circles.

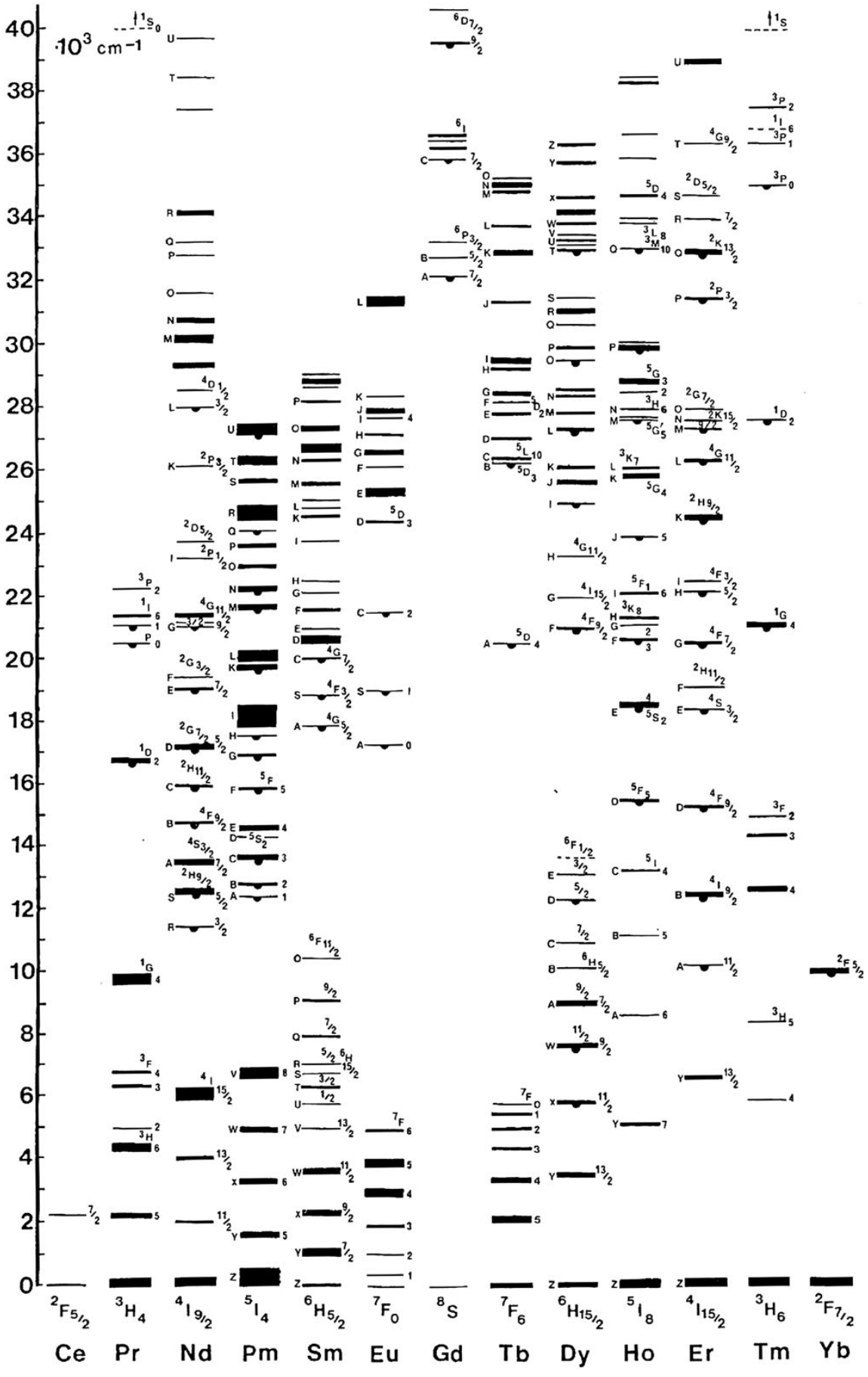

Figure 2.16: Energy levels of trivalent lanthanoids observed in $LaCl_3$ after Dieke *et al*. [126, 127].

2.8 Up-conversion mechanisms in rare earths

With the multiple metastable levels existing in rare earth ions (*cf.* Figure 2.16), the two-level simplified system (see appendix) becomes more complex. Additional kinetics between energy levels become probable and lead to non-linear processes. These radiative processes have been experimentally observed in several rare earths and are presented in Figure 2.17. In order of decreasing relative efficiency these processes are: energy transfer up-conversion (ETU), excited state absorption (ESA), cooperative sensitisation (CS), cooperative luminescence (CL), second harmonic generation (SHG) and 2-photon absorption (2PA). It can be seen that the relative efficiency of processes that rely on excitation of virtual levels, as is for CL, SHG and 2PA, is considerably lower than for processes using real energy levels. This is attributed to the zero lifetime of the virtual levels and the low oscillator strengths that reduce the probability for emission from these levels [132]. In addition, the relative efficiency of three-centre processes, CS and CL, is lower than two- and one-centre processes. In this thesis, I will focus on the first two mechanisms that occur by addition of two or more low energy photons into at least one high energy photon.

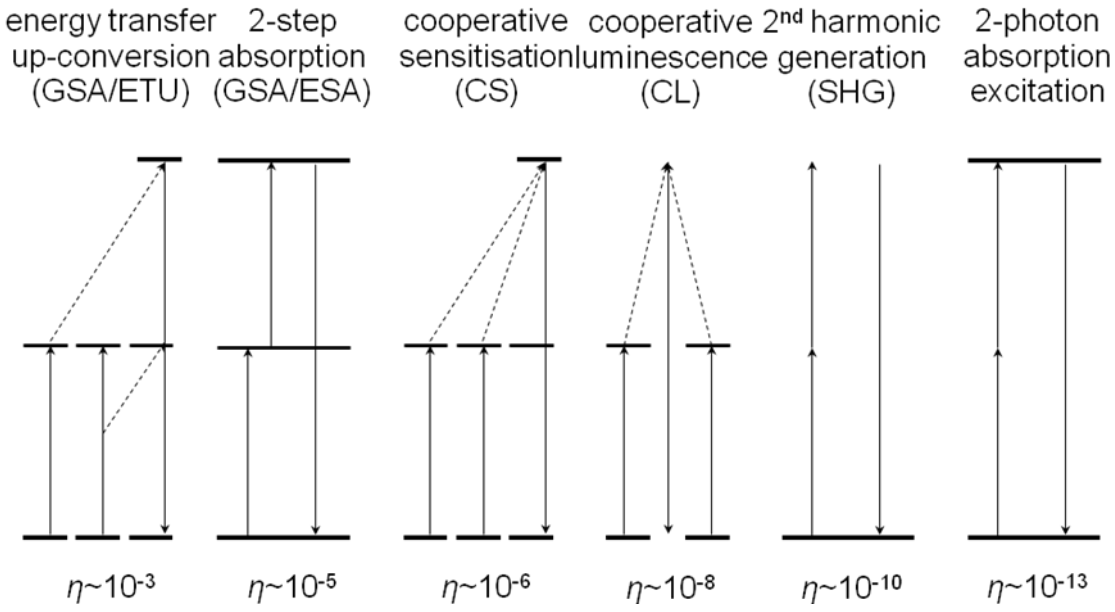

Figure 2.17: Energy level schematic of observed two-photon processes and relative efficiency normalised to the incident power of 1 W/cm^2 (adapted from [133]). Horizontal lines are real energy levels, solid and broken lines represent radiative and non-radiative steps, respectively.

2.8.1 Ground and excited state absorption

The simplest up-conversion mechanism may occur by sequential absorption events in a single ion. In a three level system, *cf.* Figure 2.17, the ion may be in the ground state where upon absorption of photons will be promoted in an excited state *via* ground state absorption (GSA). Alternatively, the ion may be already in an excited state, therefore it will get to a higher excited state upon absorption (ESA). The probabilities G and E for GSA and ESA respectively would depend on the power density of the excitation ρ and the absorption cross section σ_α of the respective state as,

$$G = \rho\, \sigma_{\alpha 01} \qquad (2.10), \qquad \text{and} \qquad E = \rho\, \sigma_{\alpha 12} \qquad (2.11).$$

2.8.2 Energy transfer

As mentioned, up-conversion *via* GSA/ESA occurs in a single ion. On the other hand, energy can be transferred between ions separated by a distance R, called a donor and an acceptor. In this case the probability of energy transfer up-conversion W_{ETU} between ions would be [133],

$$W_{ETU} = \frac{\sigma_a}{4\pi R^2 \tau_D} \int g_D(\omega) g_A(\omega) \partial\omega \qquad (2.12),$$

with σ_α the absorption cross section, τ_D the lifetime of the donor, while g_D and g_A the normalised line shape of the donor and the acceptor per unit angular frequency ω, respectively. Naturally, a critical distance R_C for energy transfer to occur can be distinguished, that can be approximated by considering a unit cell of volume V with critical concentration χ_C and N number of ion sites per unit cell as [134],

$$R_C \approx 2\left(\frac{3V}{4\pi\chi_C N}\right)^{\frac{1}{3}} \qquad (2.13).$$

The spatial parameters of the unit cell can be calculated once the crystal structure is known *via* crystallographic means, such as X-ray and neutron diffraction. Alternatively, the critical distance can be estimated from the theory of the interaction between electric dipole-electric dipole, developed by T. Förster [135] and extended by D.L. Dexter [136]. A semi empirical formula stems from this theory based on the oscillator strength f of the transition, the energy E of the maximum spectral overlap, and

the normalised spectral line shapes of the excitation of the acceptor $g_A(E)$ and the emission of the donor $g_D(E)$ as follows [137],

$$R_C^6 \approx 3\times10^{12}\, fE^{-4}\int g_D(E)g_A(E)\partial E \qquad (2.14).$$

The resonant energy transfer between donor and acceptor implies both energies being equal, *i.e.* $\Delta E=E_D-E_A=0$. Otherwise, energy transfer can still occur between ions of different energy $\Delta E\neq0$, where in this case the energy gap is bridged by phonons in a phonon-assisted energy transfer [133]. The latter has been proposed [138] as the dominant mechanism for energy transfer in β-$NaYF_4$:20%Er^{3+}, one of the most efficient UC phosphors applied in PV, as it will be analysed in following chapters.

2.8.3 Non-radiative processes

It is possible for an ion in the exited state to transfer its energy non-radiatively. The energy can then be transferred to: i) a passive (non-emitting) ion in the host, ii) another active ion in a lower state *via* cross relaxation (CR), or iii) the host lattice by emission of phonons *via* multi-phonon relaxation (MPR). Energy transfer *via* the first two processes is also known as concentration quenching at high doping levels. For the third process, the rate of MPR to the *f* level $A_{nr\text{-}f}$, often referred to as the energy-gap law [139, 140], has been experimentally observed and is approximated by the relation [141, 142],

$$A_{nr\text{-}f} = A_{nr\text{-}i}\, e^{-a\Delta E} \qquad (2.15),$$

where a is an empirical constant dependent of the host material, and ΔE is the energy gap between levels i and f. Since the maximum energy of a phonon $\hbar\omega_{max}$ is known for a particular host, the integer number of the so-called effective phonons can also be estimated from the energy gap ΔE. This has been empirically confirmed to be in the range of 4-6 phonons for oxide, fluoride and chloride hosts [140] and in fact is used as a rule of thumb for *f*-electron systems to distinguish if the dominant process is radiative when above, or non-radiative if below 5 phonons [143]. An example can be found at the lowest two crystal field levels of the $^2F_{5/2}$ multiplet in Yb^{3+} with a ΔE of 39 cm^{-1} in the system of $NaYF_4$:Er^{3+},Yb^{3+} with 350 cm^{-1} maximum phonon energy [144]. In order of decreasing phonon energy, common hosts for lanthanoids are: oxides < fluorides < bromides < chlorides. However, bromides and chlorides are less stable than oxides and

fluorides that have been more widely studied. Taking into account the non-radiative transition rate A_{nr}, the lifetime can be reformulated (see Equations A.5, A.6) to [145],

$$1/\tau_{fi} = \Sigma(A_r + A_{nr}) \quad (2.16),$$

and the quantum efficiency η_{fi} between the two levels i and f can then be defined as,

$$\eta_{fi} = A_{fi} / \Sigma (A_r + A_{nr}) \quad (2.17).$$

2.9 Rate equations and power dependence

Non-linear processes such as UC are in general complex to analyse due to the number of metastable excited states (see Figure 2.17). However, reasonable agreement with experimental results can be obtained by simplified three-level systems. For levels i=0 to 2 the rate of the population as a function of time would be, [146, 147]

$$dN_0 / dt = -GN_0 + (A_{r-10}+A_{nr-10}) N_1 + (A_{r-20}+A_{nr-20}) N_2 + W_{ETU} N_1^2 \quad (2.18),$$

$$dN_1 / dt = GN_0 - EN_1 - (A_{r-10}+A_{nr-10}) N_1 + (A_{r-21}+A_{nr-21}) N_2 - 2W_{ETU} N_1^2 \quad (2.19),$$

$$dN_2 / dt = EN_1 - (A_{r-20}+A_{nr-20}+A_{r-21}+A_{nr-21}) N_2 + W_{ETU} N_1^2 \quad (2.20),$$

where N_i the population density of the corresponding level, G, E, A_{r-if}, A_{nr-if}, W_{ETU} the probabilities of GSA, ESA, radiative or non-radiative transfer and ETU, respectively. Certain assumptions are included in this three-level model such as that the population is achieved only by pumping *via* GSA (one colour excitation), a homogeneous spatial distribution of ions [146] and negligible ground-state bleaching, *i.e.* $N_0 \approx$ constant [148].

Depending on the influence of the up-conversion mechanism, the predominant decay route and the fraction of absorbed power that relates to the path-length in the crystal, Equations (2.18)-(2.20) can serve as a simplified model [148]. Consequently, the slopes of the dependence as a function of excitation power can be systematically derived from the exponents and are presented in Table 2.1. The slopes apply for energy transfer up-conversion in systems of an acceptor without a donor ion, while on the opposing case the slopes level to 1 at the high-pump regime as has been observed in several rare earth/rare earth systems [149].

Table 2.1: Up-conversion mechanism corresponding to the double-logarithmic slopes of the excited-state population densities [148].

Up-conversion mechanism	Predominant decay level	Absorbed pump power	Power dependence
Small ETU or ESA	n-1 or 0	small/large	$N_i \sim P^i$
Large ESA	n-1	small	from level i=1,...,n
Large ETU	n-1	small/large	$N_i \sim P^{i/n}$
Large ESA	n-1	large	from level i=1,...,n
Large ETU	0	small/large	$N_i \sim P^{1/2}$ from level i=1,...,n-1
Large ETU	0	small/large	$N_i \sim P^1$
Large ESA	0	small/large	from level i=n
Large ESA	0	small/large	$N_i \sim P^0$ from level i=1,...,n-1

It can be seen from Table 2.1 that the presented up-conversion mechanisms may result in emission of photons with either the same energy or the same exponent in respect to the excitation power. In this case the question therefore arises, as to whether the underlying up-conversion mechanism is ESA or ETU. One way to distinguish between the two mechanisms is through the temporal evolution of the luminescence decay upon nanosecond pulsed excitation. As shown in Figure 2.18(a), the decay starts immediately after the excitation and indicates that the ion is pumped solely from within, as is the case for GSA/ESA.

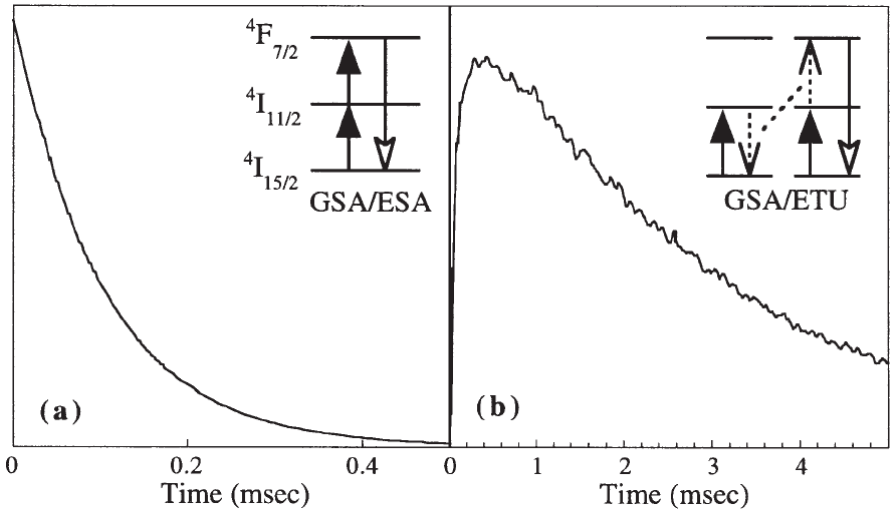

Figure 2.18: Temporal evolution of the $^4F_{7/2}$ to $^4I_{15/2}$ luminescence of 1% Er^{3+}:$RdGd_2Br_7$ upon 10 ns pulsed excitation at (a) 10290 cm^{-1}, and (b) 10172 cm^{-1}, indicating the different up-conversion mechanisms (Adapted from [146, 150]).

On the contrary, in Figure 2.18(b) the much longer decay time is shown upon excitation of a peak of lower energy. This clearly demonstrates that luminescence takes place long after the duration of the pulsed excitation and is a signature of the GSA/ETU process. In addition, for an ETU process involving n photons, the excitation spectrum from $n = 1$ to 5 would have progressively narrower peaks (*cf.* Figure 2.19) indicating the Stark structure of the $^4I_{15/2}$ to $^4I_{13/2}$ transition [133]. This effect would make a distinction between ETU and cooperative processes, as for the latter the convolution of the excitation spectrum would be observed from the absorption of all the involved pair levels. As discussed in section 2.8, the excitation will depend on the coupling between the crystal host and the active ion, resulting in a distinctive Stark structure for each host.

Another way to distinguish between ESA and ETU is through the excitation spectrum. Features additional to the absorption spectrum would be observed if ETU is involved in the luminescence. This has been observed for 1% Er^{3+}:$RdGd_2Br_7$ where excitation peaks above 10245 cm^{-1} corresponding to transitions between the levels $^4I_{11/2}$ to $^4F_{7/2}$ [150].

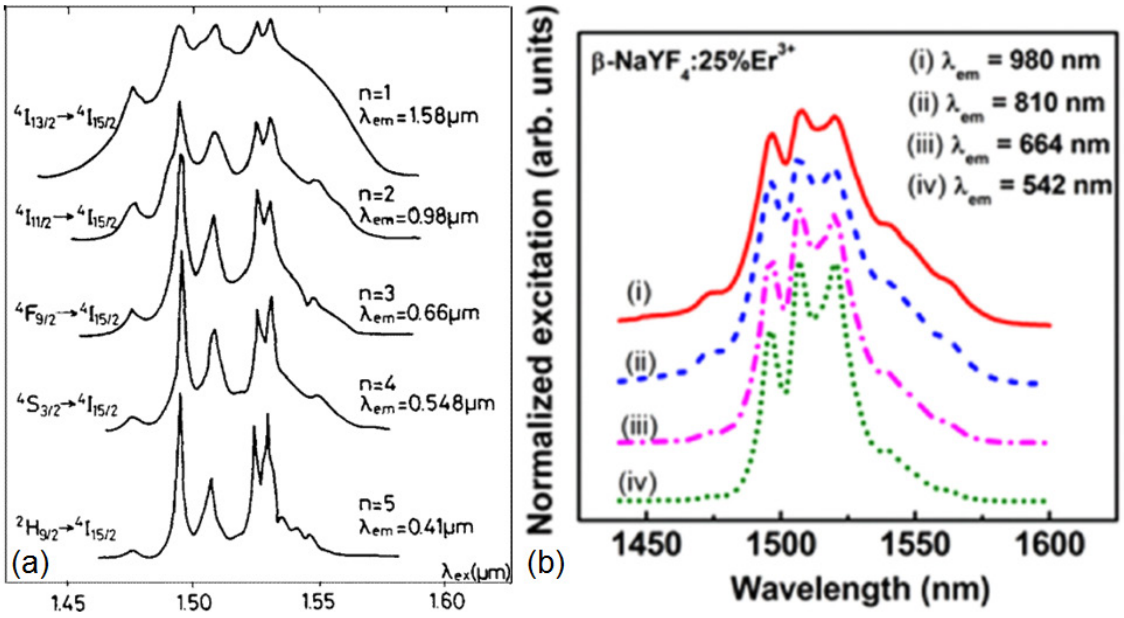

Figure 2.19: Excitation spectrum of (a) YF_3:Er^{3+} and (b) β-$NaYF_4$:25%Er^{3+} for n-photon up-conversion (Adapted from [133, 151]). The narrowing of the excitation spectrum is evident, occurring with higher order up-conversion.

2.10 Up-conversion materials for photovoltaics

The use of rare earths in photovoltaics dates back to 1982, where an increased photovoltaic yield was obtained by insertion of a rare earth-doped layer between the metallic contact and the solar cell [152]. A year later the use of Tb^{3+}-doped lanthanum fluoride and Tm^{3+}-doped calcium tungstate phosphors was proposed as a wavelength converter for solar cells [153]. Since then, a wealth of available materials and hosts has been investigated for photovoltaic applications and can be found in extensive recent reviews [54, 154, 155]. Here, the rare earth materials that exhibit up-conversion and match with photovoltaic solar cells will be reviewed. As a first requirement for a considerable improvement of the conversion efficiency of a solar cell *via* the spectral conversion approach, the up-conversion emission of the rare earth should be matched with the response of the solar cell. Depending on the band-gap of the solar cell, different rare earths can be used.

For high band-gap solar cells such as a-Si, GaAs, CdTe or DSSC, Er^{3+} co-doped with Yb^{3+} is commonly used to extend the absorption range around 980 nm. This results in efficient up-conversion emission around 550 nm also due to the larger cross-section of Yb^{3+}. This combination was actually the first UC-SC device in literature by P. Gibart *et al.* [156], based on a GaAs solar cell after etching the substrate. This allowed for sub-band-gap photons to be transmitted and absorbed by a 100 µm thick Er^{3+},Yb^{3+} vitro-ceramic. An efficiency of 2.5% has been reported under illumination of 891 nm at 1 W and more recently an output power of 0.339 µW under illumination of 973 nm at 145.65 W/cm^2 [157]. Assuming that the reported values refer to quantum efficiency, an estimation of η was unfortunately not given in any of the reports.

For a-Si, J. de Wild *et al.* measured an EQE of 0.03% with an excitation of ~980 nm at 3 W/cm^2 [158]. Under the same conditions the UC-SC exhibited an I_{SC} of 6.2 µA and a V_{OC} of 0.6 V. Interestingly, one third of this EQE has been attributed to sub-band-gap absorption from the a-Si due to a continuous density of localised states. An EQE of 0.14% with an illumination of 980 nm at 1100 mW/mm^2 was reported for $NaYF_4$:Er^{3+},Yb^{3+},Gd^{3+} nanorods with Au nanoparticles applied on the front side of a-Si cells [159]. Under the same illuminating conditions the highest I_{SC} was 1.16 mA. A considerably lower V_{OC} of 0.4 V was reported for these devices, but the voltage difference was not discussed. For high band-gap solar cells, photochemical up-conversion *via* triplet-triplet annihilation (TTA) [160] is an approach that receives

increased interest lately. Relatively low required irradiance levels were reported [161], while a maximum of 49% conversion efficiency is predicted under 1 sun of the AM1.5G spectrum [162].

For c-Si and lower band-gap solar cells, the absorption of Yb^{3+} around 980 nm will compete with the absorption of c-Si extending to approximately 1200 nm. Therefore singly doped Er^{3+} is predominantly the rare earth applied as a post solar cell up-converter. Er^{3+} at its ground state has a configuration of the form $[Xe]4f^{12}5d^{0}6s^{2}$ [163]. Up-conversion occurs between the intra *4f-4f* transitions in Er^{3+} *via* the following possible routes depicted graphically in Figure 2.20. Long wavelength photons (1450-1590 nm) are absorbed *via* ground state absorption (GSA) from the $^4I_{15/2}$ level to the $^4I_{13/2}$ metastable level in the Er^{3+} ion. From this level, two up-conversion processes are possible. Firstly, after absorption of a second photon *via* excited state absorption (ESA), the ion reaches the $^4I_{9/2}$ level where due to the low lifetime relaxes non-radiatively to the $^4I_{11/2}$ level.

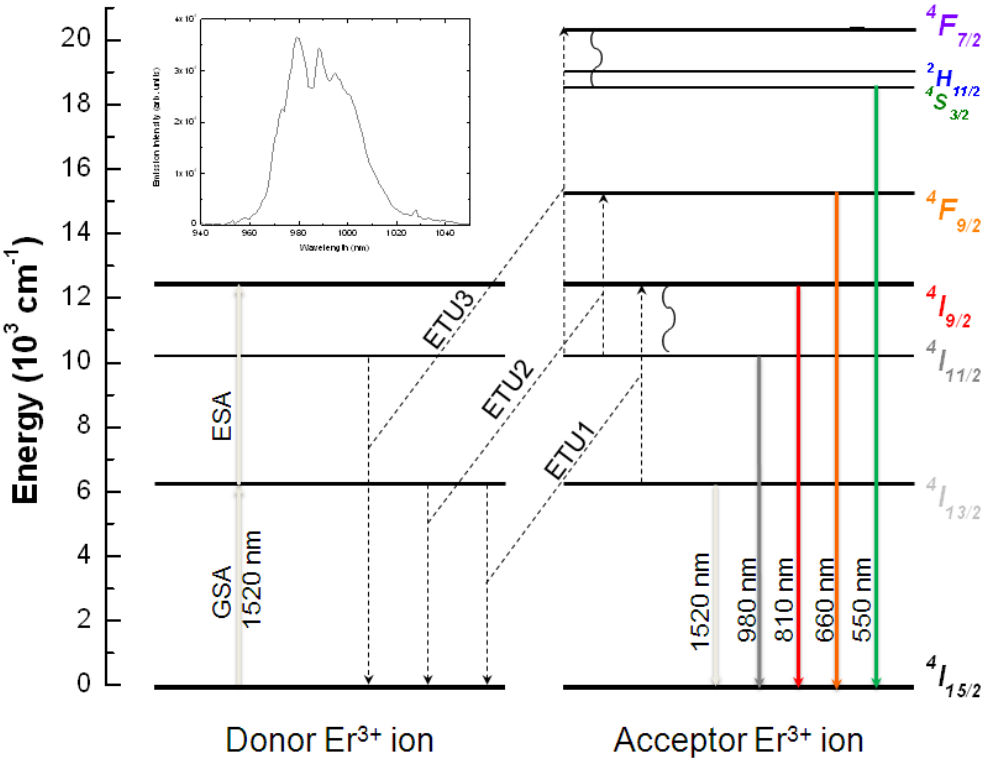

Figure 2.20: Transitions in Er^{3+} responsible for up-conversion for photovoltaics. Upward solid lines represent absorption, downward solid lines represent emission, dotted lines represent energy transfer up-conversion and non-radiative relaxation is depicted by curved lines. The inset shows the spectrum of the main emission around 980 nm upon 1523 nm excitation in β-$NaYF_4$:25%Er^{3+}.

A second, and more probable process, occurs after GSA at the $^4I_{13/2}$ level between two neighbouring Er^{3+} ions where the energy from one ion is transferred to the other, leading to energy transfer up-conversion (ETU) to the $^4I_{9/2}$ for the high energy ion, and to the ground state for the low energy ion. Again, the $^4I_{9/2}$ level relaxes non-radiatively to the $^4I_{11/2}$ level. From this level the ion relaxes radiatively to the ground state *via* emission of a photon with energy equal to the ΔE (980 nm peak wavelength emission in the inset of Figure 2.20). The energy spacing between the levels of Er^{3+} and the phonon energy of a fluoride host, allow for the majority of transitions to result in emission from the $^4I_{11/2}$ to $^4I_{15/2}$ in this material. At low power densities this translates up to the 97% of the total emission to radiate from this level [164].

This was the first rare earth reported by A. Shalav *et al.* and applied for use with bifacial silicon solar cells [165, 166]. Since then, in parallel to the research of materials, systematic effort has also been dedicated to the development of the characterisation methods [167, 168]. This included standardisation of the figure of merits for materials and devices thereof.

For a luminescent material, the primary figure of merit is the photoluminescence quantum efficiency or yield (PLQY) defined as the ratio of emitted photons φ_ε to either a) absorbed photons φ_α for internal PLQY (iPLQY) or b) incident photons φ_i for external PLQY (ePLQY), that is:

$$iPLQY = \frac{\int \phi_\varepsilon(\lambda)d\lambda}{\int \phi_\alpha(\lambda)d\lambda} \quad (2.21), \qquad ePLQY = \frac{\int \phi_\varepsilon(\lambda)d\lambda}{\int \phi_i(\lambda)d\lambda} \quad (2.22).$$

A relation similar to the PLQY follows for the external quantum efficiency (EQE) of an up-conversion solar cell (UC-SC) with power, as

$$EQE \propto \frac{P^n}{P} \propto P^{n-1} \quad (2.23),$$

where P is the power density and n the integer number of low energy photons required to create one high energy photon. Although the exponent n follows the theoretical value at low irradiance, from experimental studies [165, 169] it has been observed to be considerably lower at high irradiance. The most efficient hosts for Er^{3+} to-date for use in conjunction with c-Si have been:

- 25% Er^{3+}-doped hexagonal sodium yttrium fluoride (also referred to as β-$NaYF_4$:25%Er^{3+} or $NaEr_{0.25}Y_{0.75}F_4$) with 8.4±0.8% iPLQY and 6.5±0.7% ePLQY under 1523 nm excitation at 970±43 W/m^2 [151]

- 10% Er^{3+}-doped gadolinium oxysulfide (Gd_2O_2S:10%Er^{3+}) with 12.0±1.0% iPLQY at 700 W/m^2 and 6.5±0.5% ePLQY under 1510 nm excitation at 1100±250 W/m^2 [170].

- 30% Er^{3+}-doped barium diyttrium octafluoride (BaY_2F_8:30%Er^{3+}) with 10.1±1.6% iPLQY and 9.5±0.7% ePLQY under 1520 nm excitation at 4740±250 W/m^2 [171].

Nd^{3+} in fluorochlorozirconate ceramics has been proposed as an up-conversion model for Er^{3+} [172]. With the main absorption at 800 nm however, application of Nd^{3+} links better with higher band-gap solar cells. Other rare earth materials that match with c-Si are the trivalent holmium (Ho^{3+}) and Tm^{3+}. The latter was investigated for up-conversion and down-conversion, due to its peak absorption at 1220 nm and 468 nm and emitting at 976 and 808 nm, respectively [173].

In an attempt to sensitise Er^{3+}, co-doping with dysprosium (Dy^{3+}) represents another scheme [174]. Indeed, co-doping can be a promising approach where additional absorption bands were observed in the $BaCl_2$:Er^{3+},Dy^{3+} system, whereas the additional absorption in the solar spectrum can provide a maximum photocurrent of 0.8 mA/cm^2 [175]. Ho^{3+}, with absorption around 1170 nm and emission at 910 and 650 nm, has been investigated by several research groups [176, 177]. It has been also proposed as an up-conversion with Er^{3+} in a dual layer system at the back of a solar cell and constrained by a back reflector.

Finally, spectral conversion, or otherwise called spectral concentration, can be accomplished by other down-conversion or down-shifting species to complement the absorption bands of rare earths. In this approach, the species shift the solar spectrum from energy bands out of the excitation band of Er^{3+}. Possible candidates include cadmium selenide (CdSe) [145], mercury telluride (HgTe) [178], lead selenide (PbSe) [179] and lead sulphide (PbS) [180] quantum dots with broadband absorption and high PLQY that can be tailored with photonic structures [181].

For the majority of photonic applications, singly doped materials have seen extended application where single wavelength conversion and sharp cut-off bands are required.

Unfortunately for photovoltaics, this constitutes an additional challenge due to the broadband character of the application. The extension of the absorption range, either by co-doping or external layers of materials such as other rare earths and quantum dots, should not interfere with the emission. Especially at wavelengths where the solar cell already responds well, for c-Si this is 980 nm, the extended absorption should not induce re-absorption of the up-conversion emission.

2.11 Concepts for up-conversion enhancement

The two-photon nature of the up-conversion process leads to the non-linear behaviour of up-conversion devices with incident power. Reports in the literature on UC-SC devices based on $NaYF_4:Er^{3+}$ have been characterised for monochromatic power densities in the range of 1000 W/m^2 [169, 182]. It is clarified that this power density does not correspond to 1 sun, which is the integrated power density over the air-mass 1.5 global (AM1.5G) solar spectrum [17]. To achieve this, with the monochromatic power density per wavelength at the range 1450-1600 nm available in the AM1.5G solar spectrum (~0.28 W/m^2/nm), a system of approximately 3,500× the available power density is required. Alternatively, encompassing more photons in the spectrum by broadening and by concentrating the incident spectrum could provide significant enhancements at a lower concentration.

2.11.1 Broadband excitation

Despite the fact that the solar spectrum exhibits a broad bandwidth, up-conversion materials have been usually characterised with monochromatic or narrow bandwidth sources, such as lasers. Along with the application in photovoltaics, this has been addressed recently by the development of methods for broadband characterisation [167, 183]. Under a broadband spectrum, the excitation bandwidth is increased. Consequently, a higher total irradiance can excite the material without increasing the monochromatic irradiance. One of the most efficient up-conversion phosphors, *β*-$NaYF_4$:25%Er^{3+}, has recently been reported with an ePLQY of 6.6±0.7% under broadband excitation of 1.97 MW/m^2 [184]. This up-conversion phosphor exhibits saturation at a power density above 10^4 W/m^2, which agrees well with extrapolated

iPLQY under monochromatic excitation [185]. The equivalent solar concentration can be defined as,

$$C_{exc} = \frac{\int_{\lambda_1}^{\lambda_2} P_{exc}(\lambda)d\lambda}{\int_{\lambda_1}^{\lambda_2} P_{AM1.5D}(\lambda)d\lambda} \quad (2.24),$$

where P_{exc} is the excitation power density or irradiance at the respective wavelength, $P_{AM1.5D}$ the spectral irradiance of the air-mass 1.5 direct (AM1.5D) solar spectrum [17], between λ_1 and λ_2, the integration limits corresponding to the absorption band of the up-conversion phosphor. For β-$NaYF_4$:25%Er^{3+} with an absorption between 1450-1590 nm and the power density of 10^4 W/m^2 as mentioned above, this scales to a solar concentration of more than 350× the integrated solar irradiance in this range (28 W/m^2). This clearly presents an order of magnitude difference in comparison to the monochromatic excitation.

2.11.2 Geometrical concentration

Up-conversion as a non-linear process will benefit from a high solar concentration that will maximise the emission of high energy photons from each pair of low energy photons. For an ideal up-conversion process this emission has a quadratic relation to power. However, due to conservation of energy it will saturate at a high power depending on the dominant mechanism of depopulation [148] leading to a non-linear relation with power.

The incident power relates to the concentration of the solar spectrum which can be quite different between the solar cell and the up-conversion phosphor. Therefore, it would be useful to distinguish between the C_{exc} and the more widely known concentration factor C_{inc} defined by the incident irradiance on the operating wavelength range of the solar cell P_{inc}, as:

$$C_{inc} = \frac{\int_{\lambda_1}^{\lambda_2} P_{inc}(\lambda)d\lambda}{\int_{\lambda_1}^{\lambda_2} P_{AM1.5D}(\lambda)d\lambda} \quad (2.25),$$

To obtain the concentration incident on the solar cell, from Equations (2.24) and (2.25) it would be:

$$C_{inc} = \frac{\int_{\lambda_1}^{\lambda_2} P_{exc}(\lambda)d\lambda}{C_{geo}\int_{\lambda_1}^{\lambda_2} P_{AM1.5D}(\lambda)d\lambda} \quad (2.26),$$

where C_{geo} is the required concentration between the solar cell and the up-conversion material. This additional concentration C_{geo} can be bridged with secondary optics and is commonly calculated by the aperture ratio between input and output as:

$$C_{geo} = A_{in}/A_{out} \quad (2.27).$$

Solar concentration levels equivalent or higher than 350× required for up-conversion are currently utilised in high concentration photovoltaic (CPV) systems [44]. These systems are designed to operate in the range of 500-1,200 suns [186], while a record of 84,000 suns has been experimentally demonstrated on earth [187]. The latter record, although twice the limit of 42,000 suns in air as mentioned in section 2.6, was achieved with sapphire secondary optics having n = 1.76. None of the stated solar concentrations specify the concentration as a function of wavelength and it is noted that this relationship is not always constant, especially for CPV systems with secondary optics which are spectrally dependent [188] due to chromatic or other aberrations. In addition, this concentration is an average value, as the spatial distribution can vary significantly depending on the geometry of the optics, resulting in higher local concentrations useful for up-conversion, but undesirable for the solar cell.

For silicon solar cells the conversion efficiency is maximised at approximately 100 suns [189, 190]. Above this solar concentration, the density of carriers makes Auger recombination more probable, effectively reducing the lifetime [191] with subsequent reduced efficiency as shown in Figure 2.21. In GaAs solar cells, however, a high carrier density does not affect the efficiency until 1000 suns. Above this solar concentration the efficiency drops due to increased series resistance in the emitter, base and contacts of the solar cell [192, 193]. State-of-the-art solar cells are not designed to operate efficiently under such high concentrations due to large series resistance losses that further lead to thermal management issues [109, 194].

As a consequence, the layered device configuration firstly demonstrated by P. Gibart *et al.* on GaAs cells [156] and later on silicon cells by A. Shalav *et al.* [165],

will lead to operation of the cell at a low efficiency regime. For comparison, the highest demonstrated conversion efficiency single junction solar cells is at 92 suns for silicon [195] and at 1004 suns for GaAs [196], see Figure 2.21. Therefore, a mismatch exists between the optimal concentration for the solar cells and that for the up-conversion material. As a direct consequence, an UC-SC with secondary geometrical concentration of the sub-band-gap photons transmitted by the solar cell constitutes a promising approach. The concentration can be achieved either through internal photon management in the material or externally.

Current approaches for optical management include coupling of the localised electric fields *via* plasmon resonance [197-203], photonic crystals [204-206], or the cooperation of both in a solar cell [207] to effectively enhance the local density of optical states in the neighbouring Er^{3+} ions.

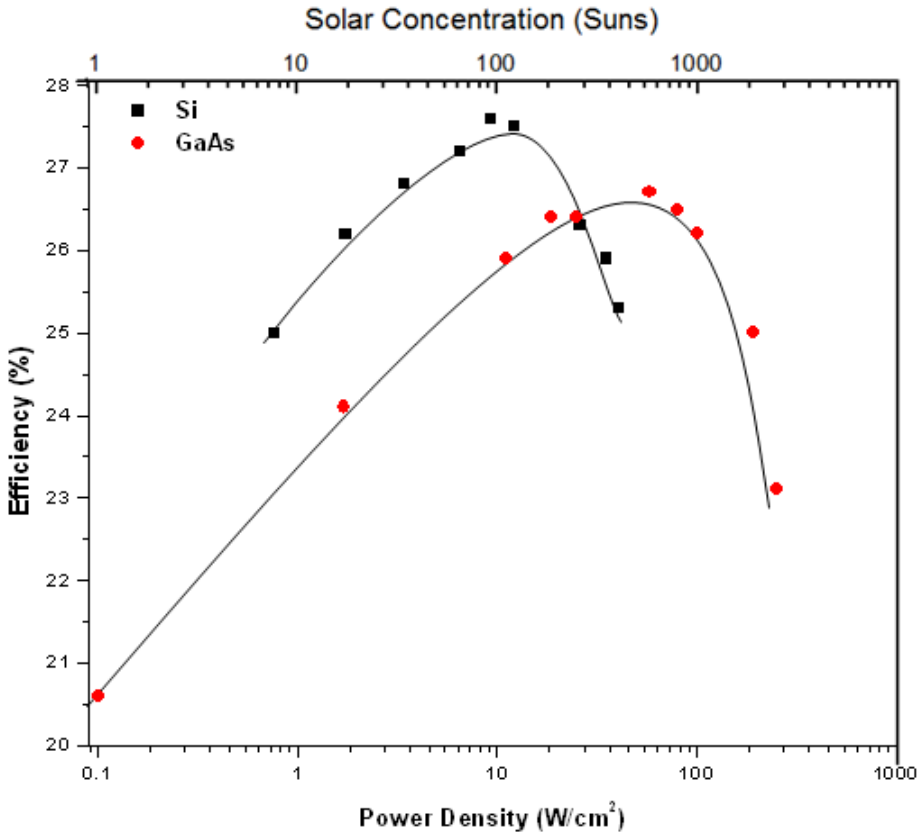

Figure 2.21: Conversion efficiency of c-Si and GaAs solar cells at high solar concentration, with highest efficiency at 100 suns and 1000 suns, respectively. (For Si the data are from reference [195] and for GaAs from reference [196]).

Geometrical concentration can be utilised with integrated macro-scale optics such as slanted metallised back contacts [178], luminescent concentrators [179], or micro-structured back reflectors [208]. To the best of the author's knowledge, three reports were found in the literature relating to concentration directly on the up-conversion material:

The first approach was proposed by C. Strümpel [178] with localised application of up-conversion material at the back of solar cells utilised by slanted metallised rear contacts, as shown in Figure 2.22. With a slant of Lambertian reflection and width b equal to the up-converter, concentration is achieved for angles β greater than 30^{o} as the excitation photons reach the up-converter only for angles greater than 45^{o}, see inset in Figure 2.22.

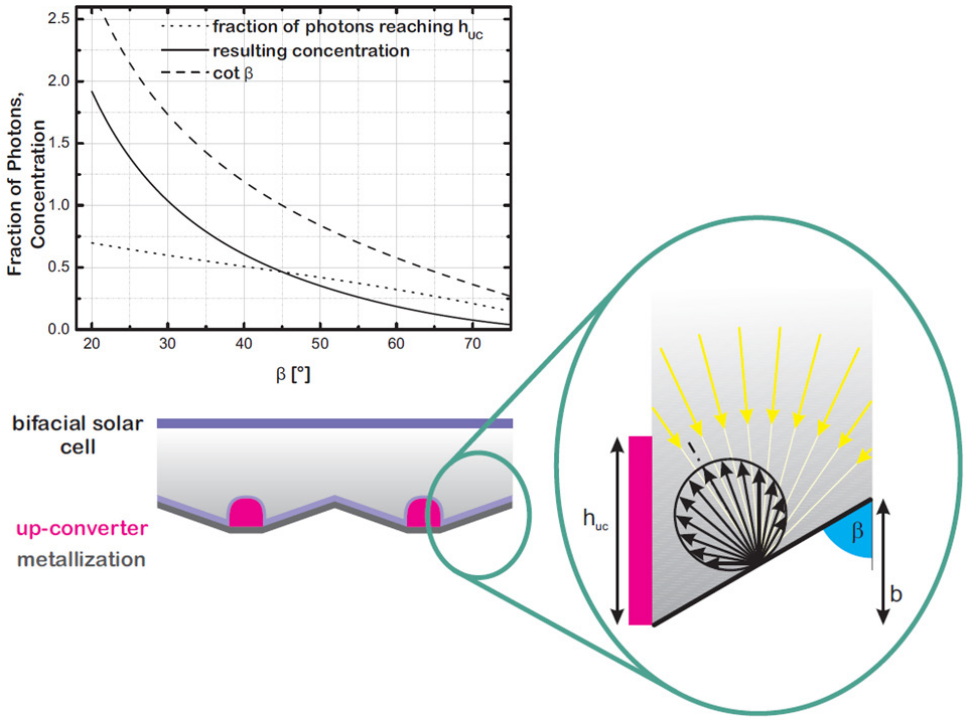

Figure 2.22: Schematic of a localised application of an up-converter at the back of slanted metallised contacts. In the inset, the concentration is displayed as a function of angle β for equal width between the up-converter h_{UC} and the slant b. (Adapted from [178]).

By increasing the height of the up-converter, a higher geometrical concentration can be achieved. This is up to 2.5× when the width of the slant is three times the up-converter, see Figure 2.23(a). The absorption coefficient following a Beer-Lambert law relation with the thickness of the up-converter was also calculated. By further integrating the

excitation from all sides and including the absorption coefficient of the up-converter, a maximum concentration of 2× was estimated at the centre of the up-converter, as shown in Figure 2.23(b).

It can be seen that shading loss from the grid of contacts of the solar cell will occur, however the application of the up-converter needs to be aligned in a way that additional shading by the front contacts is avoided. An additional advantage is the air-tight sealing of the up-converter by the metallised rear contacts that act as the back reflector. At the same time the up-converter is protected by oxidation, which can be deleterious especially for up-converters in chloride hosts [209]. Unfortunately, further implementation of the concept has not been reported. In fact, direct application of rare earths in solar cells [210-212] and semiconductors [213-215] is investigated by many research groups, albeit poses several challenges.

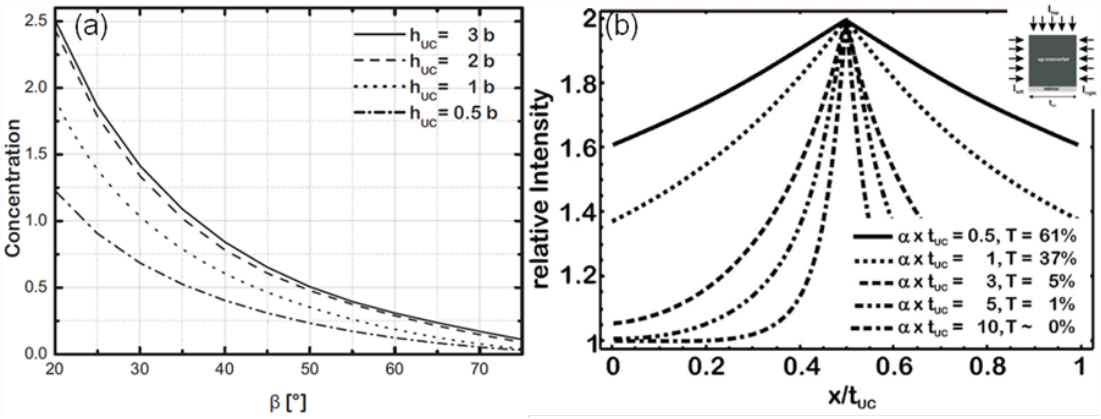

Figure 2.23: (a) Concentration as function angle β of the slant, for different widths of the up-converter h_{UC}. (b) Concentration as a function of relative width in the up-converter. (Adapted from [178]).

The second approach was proposed by J.C. Goldschmidt *et al.* [179] with a fluorescent or luminescent solar concentrator (LSC) at the rear of the up-conversion layer to increase the solar and spectral concentration of sub-band gap photons, see Figure 2.24. In this UC-SC system, a low solar concentration of approximately 10 suns is predicted by the LSC and spectral concentration by incorporation of near-infrared (NIR) emitting quantum dots to broaden the absorption spectrum of the up-conversion layer. One of the strengths of this concept is the incorporation of both geometrical and spectral concentration. However, it can be seen that appropriate coupling of the downshifted

emission from the quantum dots to the up-conversion material is required. If not, the probability for the emission to be reabsorbed would be quite high, since the quantum dots are in a LSC which emits only within the emission cone.

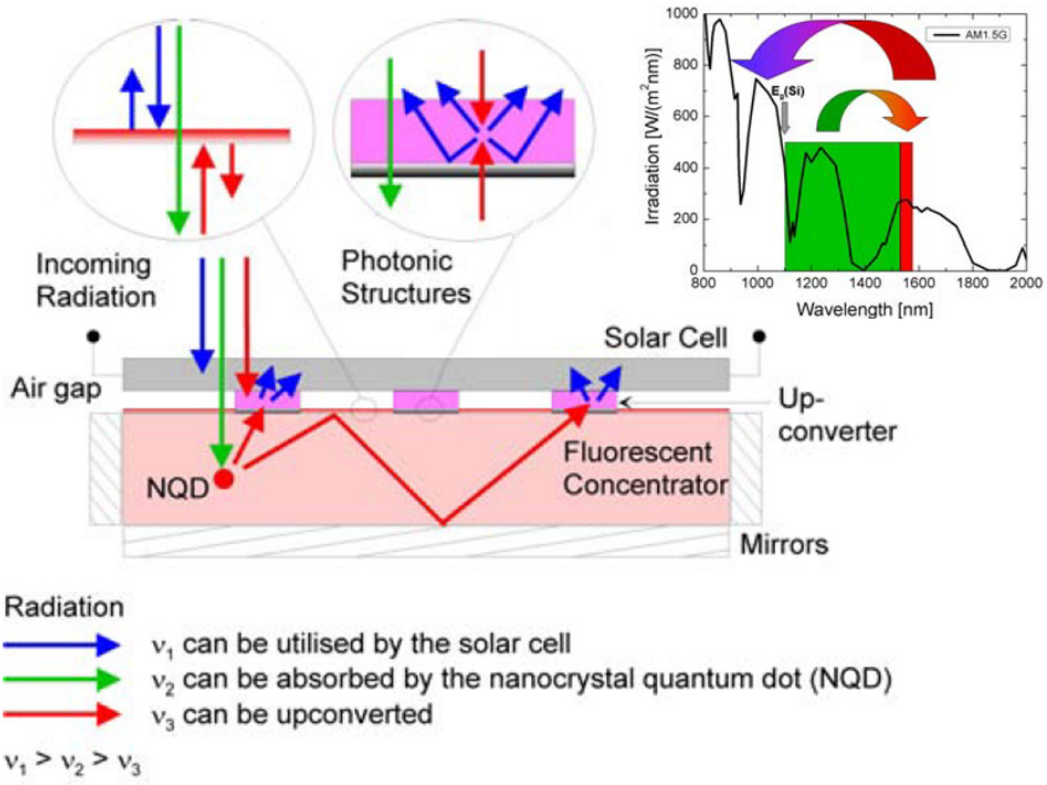

Figure 2.24: Advanced up-converter system with geometrical and spectral concentration. The inset displays the relevant bands in the solar spectrum where the quantum dots aim to shift in order to be further absorbed by the up-converter. (Adapted from [179]).

The third approach, proposed by T.F. Schulze *et al*. [208], consisted of aluminium-coated spherical reflectors at the back of a-Si TTA solar cells. A schematic of the configuration is displayed in Figure 2.25(a), while in Figure 2.25(b) the absorption and emission bands of the organic up-converter are depicted with peaks at 670 nm for the donor (PQ_4Pd) and 550 nm for the acceptor (rubrene), respectively.

A maximum relative enhancement of 20% in EQE was obtained, see Figure 2.26, in comparison to the signal obtained from the flat region of the reflector, shown in the inset. The excitation was calculated to an equivalent solar concentration at 47-55 suns, however a photocurrent of 5×10^{-4} mA/cm^2 at 1 sun was estimated with this

configuration. In addition to the increased up-conversion signal measured directly by the a-Si solar cell, lower volumes of up-conversion material were required when spherical reflectors were utilised. An enhancement of 4.5× was estimated by further optimising the reflector with a material of higher reflectance, and up to 9× with a higher density distribution of embossed spheres.

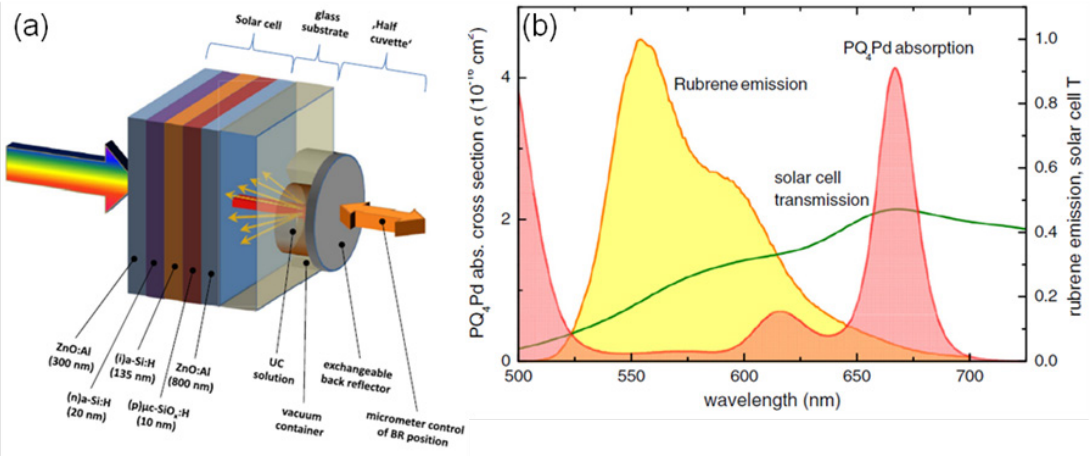

Figure 2.25: Schematic of an a-Si solar cell and configuration for variable volumes of the up-converter. (b) Absorption and emission spectra of the TTA up-converter, overlapped with the transmission of the a-Si solar cell. The up-converter consists of PQ_4Pd as the donor and rubrene as the acceptor. (Adapted from [208]).

It can be seen in the inset of Figure 2.26, that the excitation can be concentrated to desired levels, however parabolic instead of spherical cavities could result in a higher local concentration. Given that this irradiance is not at a saturated power regime for the material, it would further induce a higher photocurrent at the overlying solar cell in comparison to a multi-focusing optic. This way it could also reduce additional re-absorption events in the up-converter.

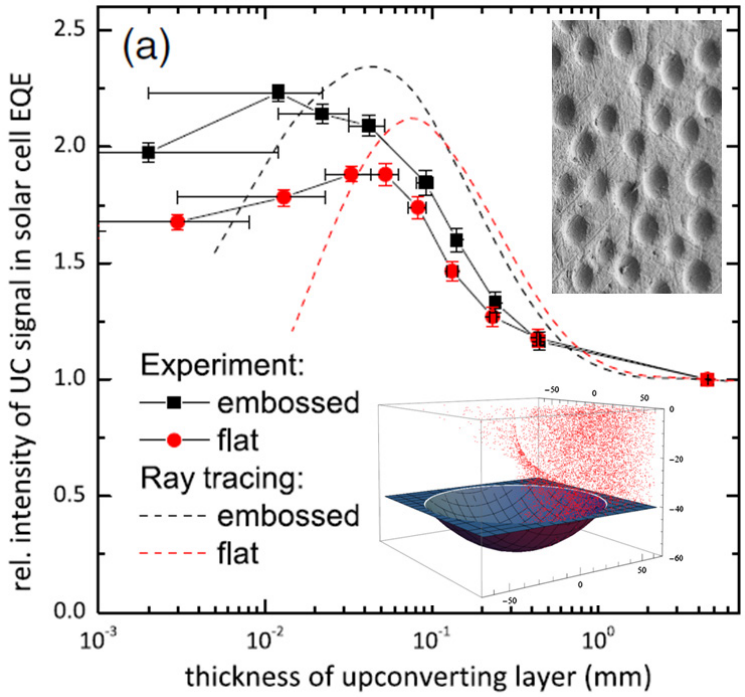

Figure 2.26: Relative EQE of the a-Si TTA solar cell for various up-converter thicknesses, flat and embossed spherical back reflector. The distribution of the spherical cavities and the focusing accuracy of a 20 μm cavity, are displayed in the inset. (Adapted from [208]).

The abovementioned concepts present a simpler approach for the enhancement of up-conversion solar cells. They rely on externally shaping the irradiance of the excitation, without affecting the up-conversion material. In addition, such integrated geometrical optics can potentially bridge the mismatch in concentration between the up-conversion material and the solar cell. It constitutes a promising direction and is one of the main concepts in this thesis, which I will analyse further in Chapters 6, 7 and 8.

Chapter 3 : Methods & materials

3.1 Introduction

In this chapter, the methods used for acquisition of the results in the chapters to follow are presented. First, the method for the calculation and estimation of the irradiance and the coupling efficiency *via* ray-tracing for simulations is presented. Next, a description of the methods for the optical characterisation of up-conversion materials and concentrating optical elements is given. Further details on the electrical characterisation of devices and systems are also presented. Finally, the chapter will close with an overview of UC materials and preparation of the concentrating optical elements used in this thesis.

This chapter expands on material from the following publication: **G.E. Arnaoutakis**, J. Marques-Hueso, A. Ivaturi, K.W. Krämer, T.K. Mallick, B.S. Richards, (2013, November). Enhancement of Up-conversion for Photovoltaics with β-NaYF4:Er^{3+} and Concentrating Integrated Optics. In *Optical Nanostructures and Advanced Materials for Photovoltaics,* (pp. PT3C-4). Optical Society of America.

3.2 Ray-tracing and simulations

The calculations and simulations of the coupling efficiency and the irradiance of the optical configurations presented in this thesis were completed in a non-sequential ray-tracing software package (Optis, Optisworks). This tool is fully integrated with a three-dimensional (3D) computer aided design (CAD) package (Dassault Systèmes, Solidworks). Consequently, all the models of the optical configurations were initially designed in 3D. Each individual optical element was designed at first. Then, the elements required for every optical configuration were incorporated into one assembly. This required the distribution of each element along a virtual optical axis that further allowed for angularly resolved simulations.

The simulations use a non-sequential ray-tracing engine. That is, light emitted from the source can be traced and split several times through the optical configurations, which represents more accurately the physical model. This method of ray-tracing is preferred when studying optics with multiple reflections and scattering, in contrast to sequential ray-tracing. In the latter, rays are traced through one optical element at a time. As the dimension of the optics approaches the wavelength, diffraction becomes more probable and other methods are required to accurately predict the behaviour of diffracted light [216, 217]. At this scale, the propagation of electromagnetic fields by solving the Maxwell equations provides acceptable solutions, implemented in methods such as the finite-difference time-domain (FDTD) [218]. The non-sequential ray-tracing engine is therefore physically valid when the size of the optics is a few orders of magnitude larger than the wavelength [216]. For light throughout this thesis in the range of 1 μm, this translates to 100 μm. Consequently, ray optics and non-sequential tracing is the method that can accurately resolve the studied optics.

A geometrical aspect that affects the ray-tracing and the accuracy of the simulations is the tessellation of an optical element. This can be described either by the magnitude of deflection of a ray interacting with the element, or as the maximum width of the facets comprising the optical element. Decreasing the tessellation increases the computation time. However, the tessellation needs only be smaller than the size of the element. For most configurations throughout this thesis (*cf.* Figure 3.1), 0.02 mm was the minimum facet width used, while 0.05 mm and 1 mm was adequate for most optical elements.

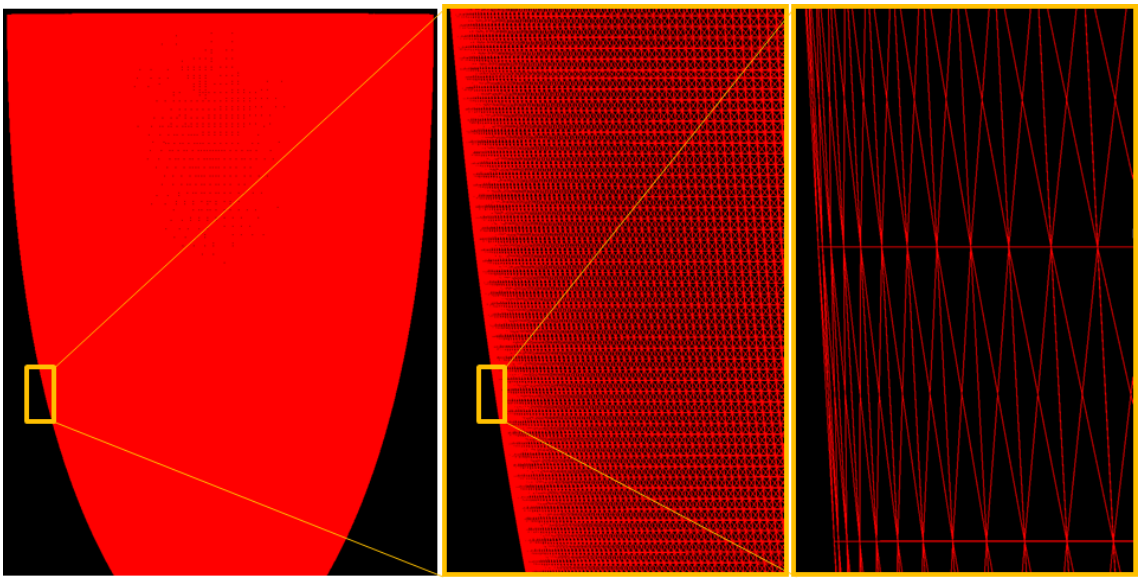

Figure 3.1: Tessellation of the surface of an optical element as implemented in the non-sequential ray-tracing.

3.2.1 Optical material properties

Once the geometrical 3D design was complete, the optical characteristics of the geometries could be set. First, the source of illumination was defined. Based on the illuminating area of the source A, the optical flux Φ was calculated from the desired irradiance E according to, $\Phi = E\,A$. Uniform emittance was used for all the modelled sources. For simulations of optical configurations under the sun, the source was modelled as a solid disk emitting light at a limited half-angle of 0.27^{o}, unless otherwise stated. If the simulated solar spectrum was AM1.5G, the irradiance of the disk was 1000 W/m^2 or 900 W/m^2 if the AM1.5D was used. These irradiance values agree with the proposed irradiance spectra as standardised by ASTM [17, 18]. A summary of the source parameters is given in Table 3.1.

Table 3.1: Summary of the parameters used in the presented optical configurations.

	Broadband coupling model (Chapter 4)	**Up-conversion model (Chapters 6, 7, 8)**	
Source		Excitation	Emission
Irradiance (W/m^2)	900	190	190
Emittance	Uniform	Uniform	Uniform
Intensity	Lambertian	Lambertian	Lambertian
Half-angle (^{o})	0	0	90
Spectrum (nm)	280-4000 (AM1.5D)	1522-1523	930-1060

The surface quality of an optical element is defined by the absorbance $A_{(\lambda)}$, the reflectance $R_{(\lambda)}$ and the transmittance $T_{(\lambda)}$ of the surface. For the configurations and the wavelengths ranges throughout this thesis, optically polished surfaces were assumed. This implies that the light-matter interaction was considered spectrally constant at the surface. For propagation of light in the material however, the spectral variation of dispersion and absorption was fully defined in the material properties. In particular, the refractive index n of the optical materials was calculated with the Sellmeier equation [219-221],

$$n^2 - 1 = \sum_{i=1}^{3} \frac{A_i \lambda^2}{\lambda^2 - l_i^2} \tag{3.1}$$

where λ is the wavelength, A_i the oscillator strength constant and l_i the oscillator wavelength. For most common optical glasses the constants A_i and oscillator wavelengths l_i, the so-called Sellmeier coefficients, are widely tabulated. For example the coefficients for fused silica [222] and BK7 glass [223] are displayed in Table 3.2. For materials that coefficients were not given, the spectral dispersion and absorption coefficients as a function of wavelength were used. All materials were considered as isotropic and non-scattering, unless otherwise stated. The refractive indices and absorption coefficients of the used materials are presented in Figure 3.2.

Table 3.2: Three-term Sellmeier coefficients for materials used in the presented models.

	Fused silica	**BK7**
A_1	0.69617	1.03961
l_1	0.0684	0.07746
A_2	0.40794	0.23179
l_2	0.11624	0.14148
A_3	0.89748	1.01047
l_3	9.89616	10.1765

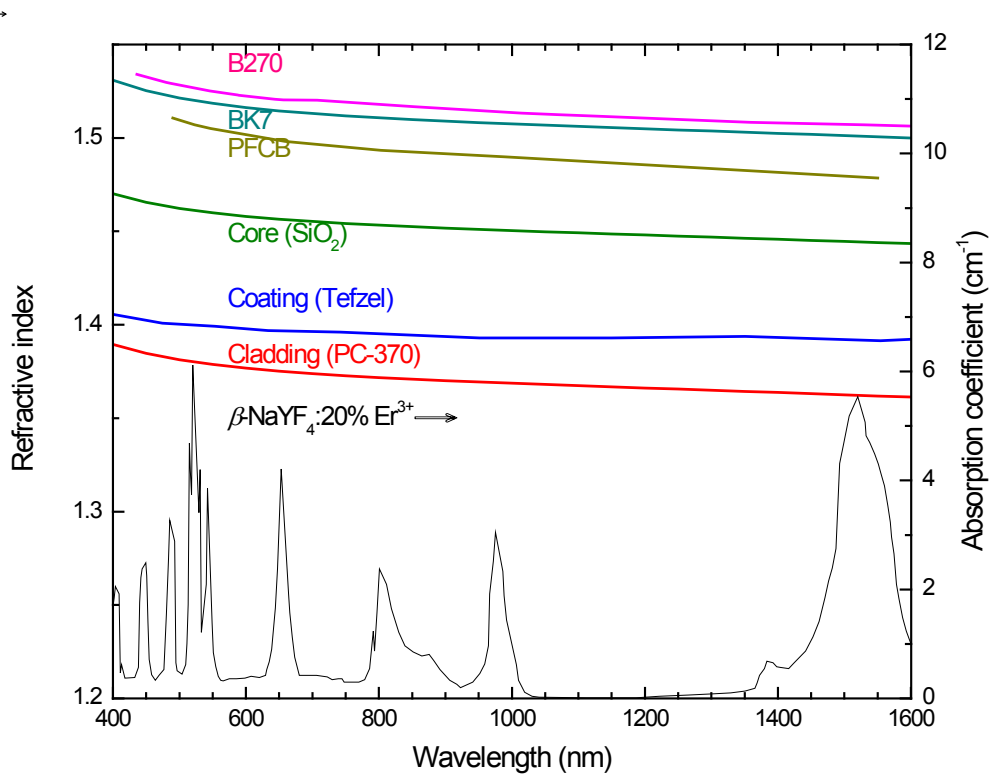

Figure 3.2: Refractive index and absorption coefficients of the materials used for optical modelling.

Finally, irradiance detectors were defined on the optical systems. An irradiance detector, similar to an experimental setup, was defined by rectangular surfaces mapping the apertures of the investigated optics. Consequently, the detector was defined fully by its area and a plane facing the optical element, *i.e.* the side that detects light. This way, the figures of merit could be then quantified. For example, the irradiance and concentration of an optical system was quantified by two detectors, at the entry and exit aperture. Equally, the coupling efficiency of an optical system could be calculated by having knowledge of the illuminated area and the optical power.

3.2.2 Ray-tracing examples

Once all geometrical and optical parameters of the configurations were defined, the ray-tracing and the simulation could be implemented. Ray-tracing was first run to acquire a qualitative account of the coupling and the losses in the optical configuration. Errors in the interfaces due to insufficient tessellation or inconsistency of the optical properties could also be identified. For all simulations an adequate number of rays was used (usually 10^7) to ensure low noise and high resolution.

One example can be seen in Figure 3.3 where configurations for the broadband coupling in optical fibres are displayed. The light coupled in the fibre and guided toward its end can be seen. Stray rays at the end of each taper are visible. It can also be seen that out-coupling occurs especially for rays impinging at more oblique angles, *i.e.* the peripheral rays of the lens. The effect is more pronounced for the lens with a shorter focal length. For this configuration, this first account also allowed for an estimation of the optimum distance between the primary and the secondary optics.

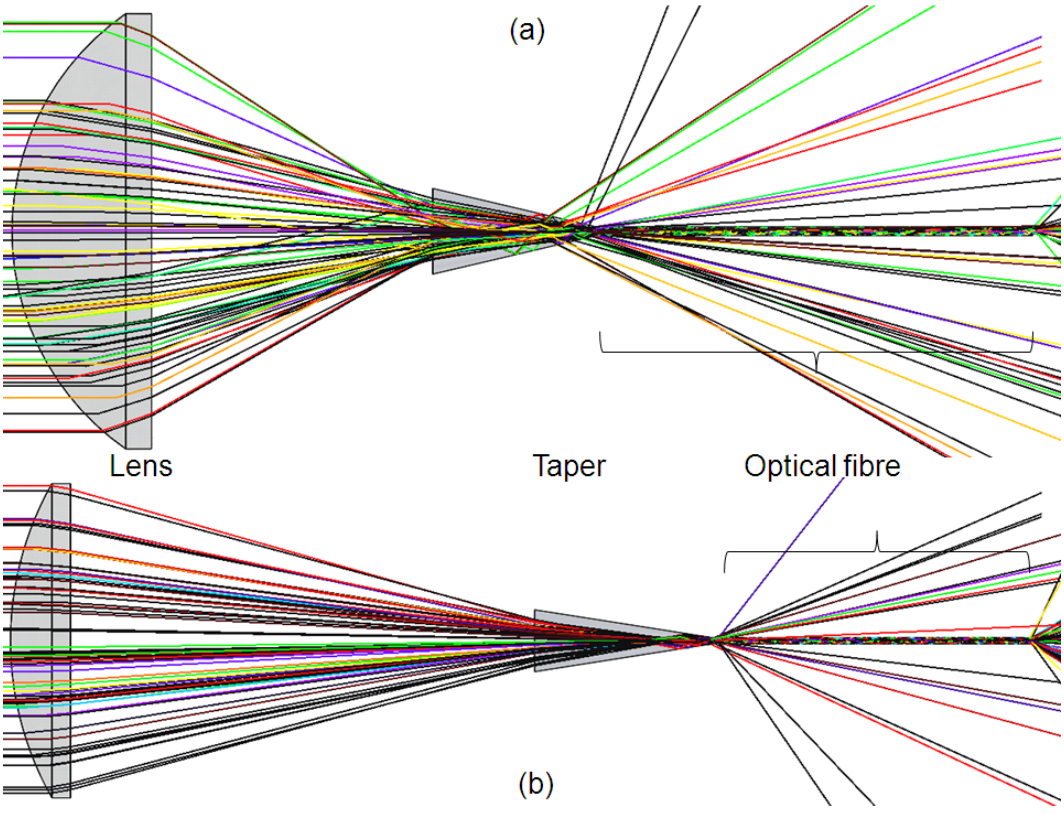

Figure 3.3: Ray-tracing of two configurations for broadband coupling in optical fibres. (a) A *f*/1.31 lens with *a* taper of angle a 14.04° and (b) a *f*/3.28 with a taper of angle *a* 9.46°. The optical fibre of *NA* 0.48 with boundaries marked by broken lines was used in both configurations. In-coupling and out-coupling can be seen as rays guided in the fibre and stray rays at the end of the taper, respectively.

The effect of chromatic aberration of primary lenses could also be examined through ray-tracing. As shown in Figure 3.4, the effect of chromatic aberration when coupling light from an *f*/9.84 lens in a taper of angle *a* 3.18° is clearly displayed. From (a) 300 nm light, the focus shifts to a longer distance as the wavelength increases to (b) 500 nm, (c) 1000 nm and (d) 1700 nm. The same effect is also observed for an *f*/2.19 lens and taper of angle *a* 14.04° for the same wavelengths in Figure 3.5.

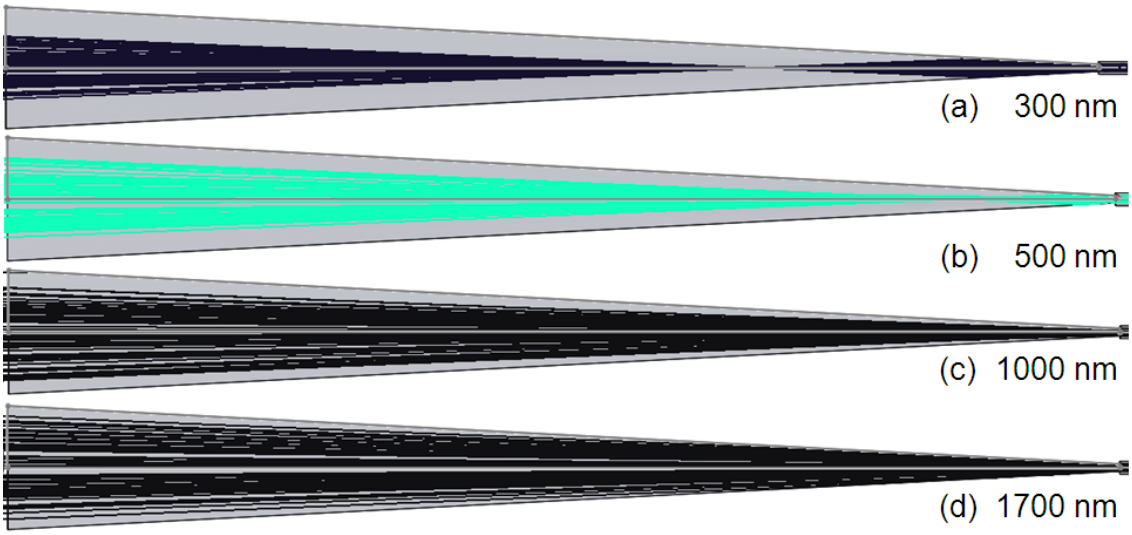

Figure 3.4: Ray-tracing indicating the spectral dependence of the coupling between a *f*/9.84 lens and a taper of angle *a* 3.18°. The effect of the chromatic aberration of the lens is shown for the wavelengths (a) 300 nm, (b) 500 nm, (c) 1000 nm and (d) 1700 nm.

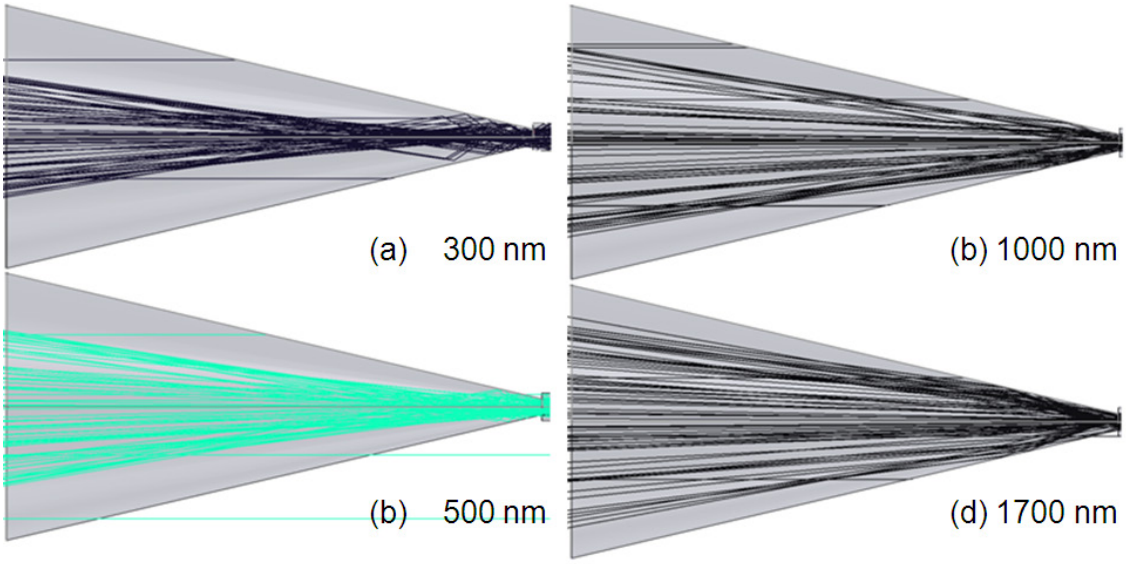

Figure 3.5: Ray-tracing indicating the spectral dependence of the coupling for a *f*/2.19 lens and taper of angle *a* 14.04°. The effect of the chromatic aberration of the lens for the wavelengths (a) 300 nm, (b) 500 nm, (c) 1000 nm and (d) 1700 nm is displayed.

3.3 Characterisation methods

This section is dedicated to the optical configurations and setups used for characterisation of the devices and systems investigated in this thesis. The sources of illumination are presented first, followed by the characterisation of the photoluminescence quantum yield (PLQY) of up-conversion materials. Then, the setups for characterisation of optical fibres are presented closing with the setup for electrical characterisation of the up-conversion solar cells.

3.3.1 Monochromatic excitation

A Fabry-Pérot tunable laser was used as a source for monochromatic excitation. This type of laser is based on an InGaAsP diode as the active medium. The diode is placed in a resonator arrangement, formed by a diffraction grating in Littrow configuration, *i.e.* with equal incident and diffraction angles, and the diode itself (*cf.* Figure 3.6). The diffraction grating is used for wavelength selection in addition to a Fabry-Pérot interferometer (*étalon*) [224]. The selection of the wavelength in this system is achieved by adjusting the resonant modes of the diode with the reflectance maxima of the *étalon* and the diffraction grating. By mechanically controlling the tilt of the diffraction grating and the *étalon*, the reflection angles can be adjusted. The output of the resonator is further coupled into a fibre pig-tail with 9 μm angled ends and *NA* of 0.1. This results in a source with a FWHM of 0.1 nm [225], tunable between 1450-1590 nm.

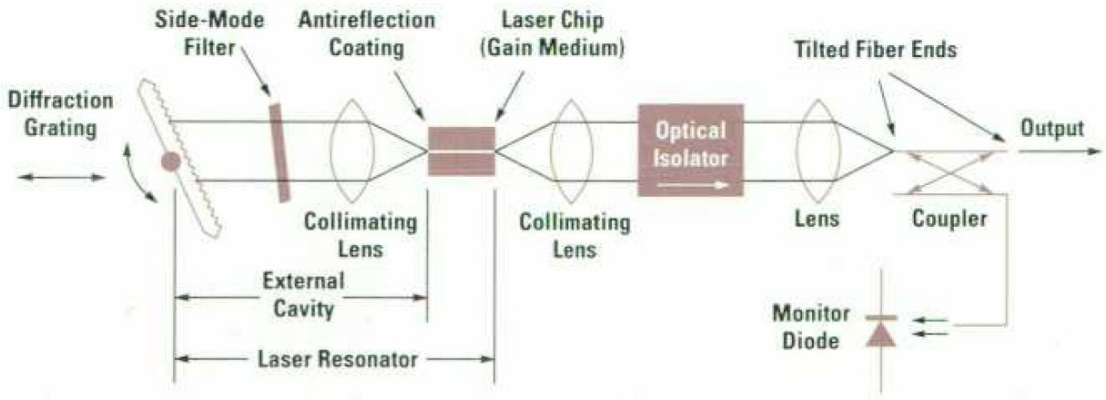

Figure 3.6: Schematic of optical elements required for wavelength selection in a tunable laser (Adapted by [225] with permission of the Hewlett-Packard Company).

The output of the tunable laser was coupled into an optical fibre (Thorlabs, P3-1550A-FC-1) supporting single mode propagation over the entire wavelength range and again collimated with a lens of *NA* 0.15 (Thorlabs, F280APC-1550). The beam width was determined according to the second moment criterion ($d4\sigma$). The standard deviation of a cross section x of the beam with centre of gravity x_0 along the direction of propagation is given by [226],

$$\sigma_x^2 = \frac{\int_{-\infty}^{\infty}\int_{-\infty}^{\infty} I(x,y)(x-x_0)^2\,\partial x\partial y}{\int_{-\infty}^{\infty}\int_{-\infty}^{\infty} I(x,y)\partial x\partial y} \qquad (3.2).$$

Since the width of a Gaussian beam w is well approximated by twice the variance σ, the $d4\sigma$ width of the beam can be calculated for the cross section of the beam. The horizontal and vertical cross sections of the beam, characterised by a NIR camera (Electrophysics, Micronviewer 7290A), can be seen in Figure 3.7. The camera uses a lead-oxysulfide (PbO_2S) detector of area 9.5×12.7 mm in a vidicon tube configuration [227]. Contrary to charge-coupled-devices (CCD) that detect in distinct elements or pixels, in this configuration the beam is imaged on a photoconductive film. The image on the film is then scanned by an electron beam emitted by the detector and the voltage difference is used to reproduce the image [228]. A continuous profile was therefore scanned with a resolution of 240 lines per mm. The detector has a broad spectral response from 400 nm to 2000 nm. The profile of the laser beam was characterised for different wavelengths across the range 1450 – 1590 nm and at the available flux between 0.1 – 6 mW. At a flux higher than 2 mW, neutral density filters (Thorlabs, NEK01S) were used to avoid saturation of the detector above its damage threshold of 1 mW/cm^2.

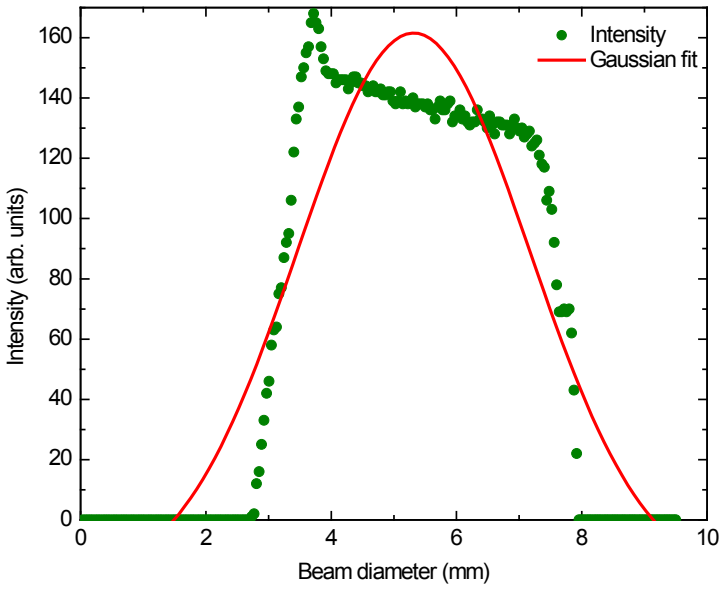

Figure 3.7: Irradiance profile of the monochromatic tunable laser at 1523 nm after collimation.

From Equation (3.2) the $d4\sigma$ width was calculated as $w_x = 3.82$ mm and $w_y = 4.54$ mm. It can be seen that the profile of the beam is asymmetric along the axis of propagation. Consequently, the $d4\sigma$ diameter of 4.20 mm was taken as the best approximation for calculations of the illuminating area. The irradiance of the laser in the range of the available flux for the wavelengths 1493, 1522 and 1523 nm is shown in Figure 3.8.

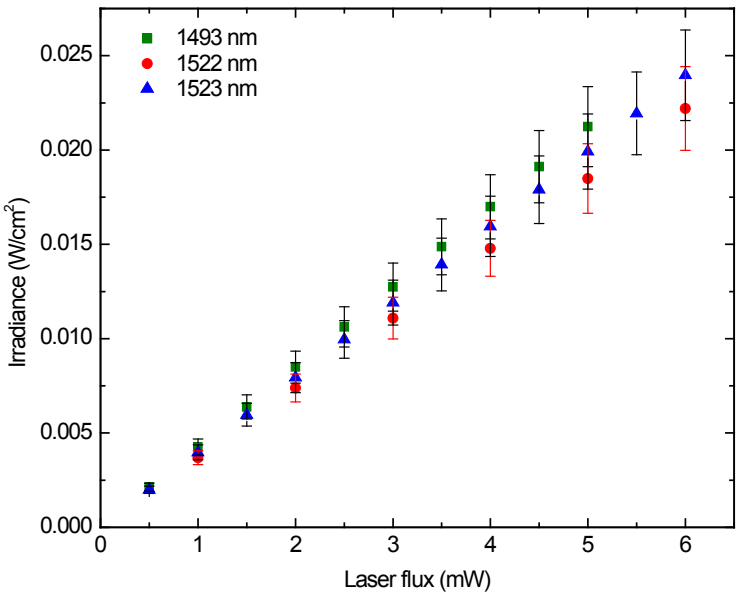

Figure 3.8: Irradiance of the laser in the range of the available flux. The irradiance is shown for the wavelengths of the peak response of the up-conversion materials used in power dependent measurements.

In configurations where the beam was focused, the irradiance at the focus of the beam was calculated with the equation [229], $E = P\, w_0^2\, \pi\, \lambda^{-2}\, f^2$, where P is the total flux and w_0 is the waist of the unfocused beam, λ the excitation wavelength and f the focal length of the lens. The calculation assumes that the beam illuminates 99% of the aperture of the lens and the *1/e* criterion with 86% of the power within the focused spot. The divergence of the collimated beam was also characterised. The profile was measured at 10 intervals between 10 cm and 90 cm from the collimating lens. This range covered the length of illumination of the setup for electrical characterisation of the solar cells presented in section 3.3.5. Consequently, the degree of divergence was calculated from the tangent of the hypotenuse in the half triangle between two profiles in a maximum half-angle of 0.02^{o}.

3.3.2 Broadband excitation

The optical setup used to characterise the PLQY of the up-conversion materials under broadband excitation can be seen in the schematic of Figure 3.9. A 1000 W quartz tungsten halogen (QTH) lamp (Oriel, 66187) was used as the excitation source. The output of the QTH lamp was collected by a spherical mirror and plano-convex lenses. The collected light was guided into a fluorescence spectrometer *via* a multimode optical fibre (Thorlabs, BFL48-1000) and collimated with an *f*/1 plano-convex lens (Thorlabs, LA1951-C). A series of short and long wave-pass filters (Edmund Optics) have been used to adjust the desired spectral windows in Figure 3.10. In addition, a 300 µm thick silicon wafer and a long wave-pass filter centred at 1200 nm were used to block wavelengths below 1100 nm.

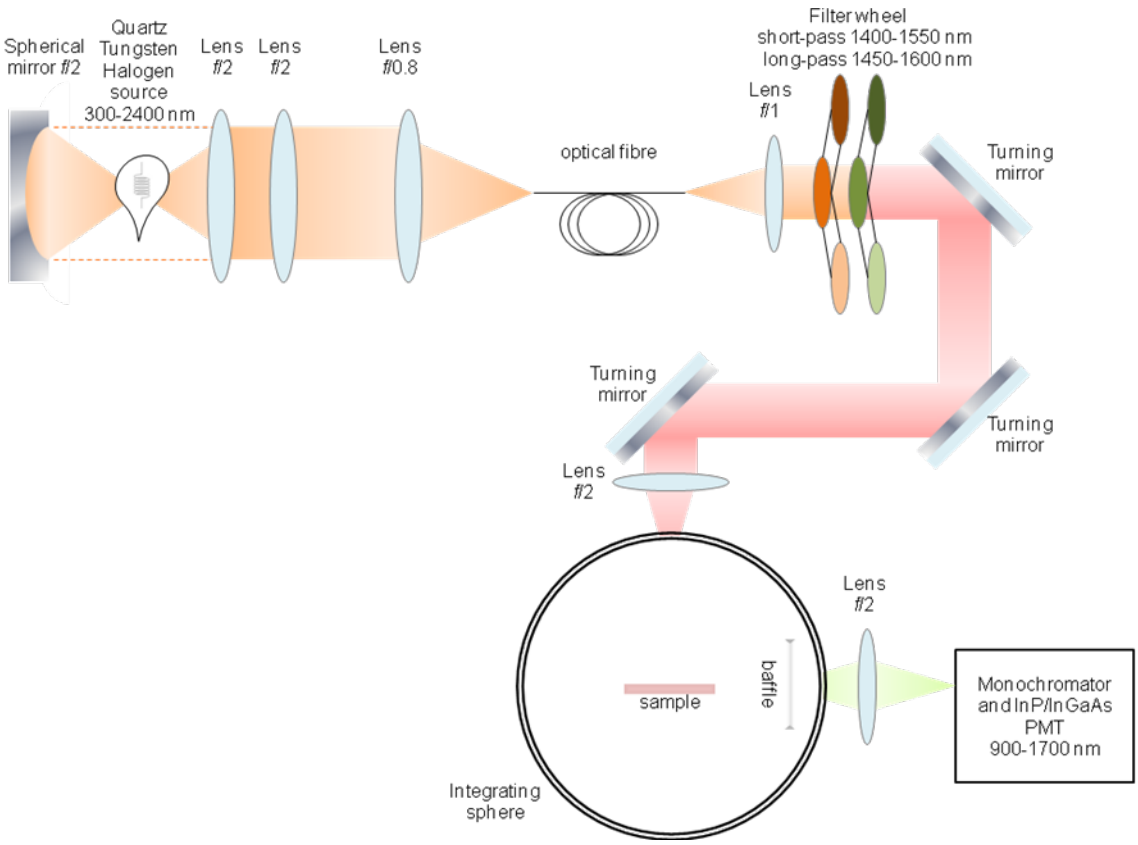

Figure 3.9: Schematic of the optical setup for characterisation of up-conversion materials under broadband excitation.

Fluorescence measurements were performed in a fluorescence spectrometer (Edinburgh Instruments, FLS920) equipped with a Jobin-Yvon integrating sphere, Czerny-Turner monochromators and liquid nitrogen (LN_2)-cooled NIR photomultiplier tube (Hamamatsu, R5509-72).

The integrated power was measured with a thermal detector (Thorlabs, S302C) of maximum calibration uncertainty ±5% and the focused beam diameter of 1.86 mm was characterised by a NIR camera (Electrophysics, Micronviewer 7290A).

Figure 3.10 shows the excitation spectrum of Er^{3+} in β-$NaYF_4$ on the right vertical axis and the power density on the left vertical axis as a function of wavelength. The spectral windows were selected in order to investigate the cumulative effect of the broadband excitation on wavelengths other than the main resonant peaks at 1508 and 1523 nm.

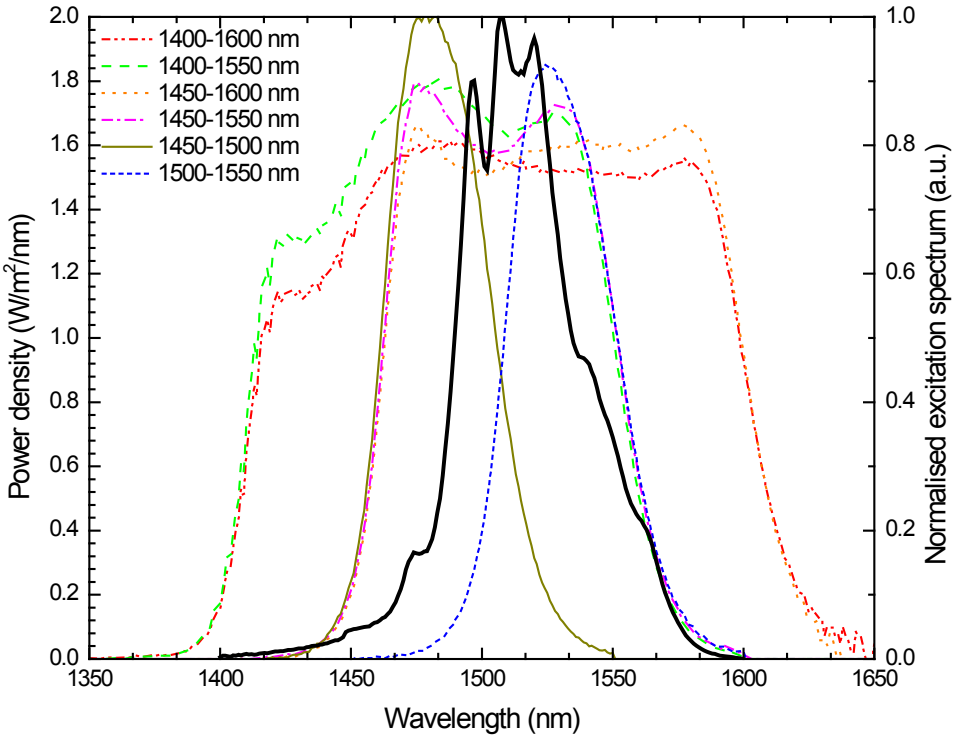

Figure 3.10: The excitation spectrum of β-$NaYF_4$:25%Er^{3+} under monochromatic excitation (black solid line) resulting to the $^4I_{11/2} \Rightarrow {}^4I_{15/2}$ transition (980 nm emission) and the broadband spectra used to excite the samples for iPLQY measurements.

3.3.3 Photoluminescence quantum yield

A fluorescence spectrometer (Edinburgh Instruments, FS920) was used for characterisation of the photoluminescence and the PLQY of up-conversion materials. The instrument uses single photon counting with sensitivity greater than 750,500 cps. This provides a maximum signal to noise ratio (SNR) of 6000:1 and a maximum resolution of 0.1 nm. The accuracy of the technique has been estimated as ±10%. The instrument is equipped with two gratings at the excitation and three at the emission monochromator. The excitation gratings have peaks at 300 nm and 1200 nm, while the emission at 500 nm, 750 nm and 1200 nm. The single photon counting extended red photomultiplier (PMT) (Hamamatsu, R928) has a detection range of 185 – 900 nm and the analogue liquid nitrogen (LN_2) cooled NIR PMT (Hamamatsu, R5509-72) 900 – 1700 nm. An integrating sphere made of Spectralon, known for its high lambertian reflectance over the entire wavelength range, was used.

Upon excitation of the sample at an angle, a fraction of light is reflected from the surface facing the excitation beam. This amount depends on the quality of the sample's surface and the geometry of the setup. Therefore, an appropriate angle was found to maximise the emission and obtain an adequate SNR. One side of the sample was polished. This side was used for measurements as it consistently resulted in higher emission. Before every measurement, maximum signal was obtained by adjusting the slit size accordingly. The signal rate was set so adequate signal reached the detector, but not more than the upper limit to avoid saturation. After the optimum signal rate is obtained, synchronous, excitation or emission scans could be performed. For an excitation scan, the emission wavelength was set at the emission peak and the measurement range varies along the excitation range. To acquire an emission scan, the excitation wavelength was fixed at the excitation peak (obtained from an excitation scan) and the measurement varied along the emission range. Correction was applied after every scan, in order to obtain pure spectra without effects of the instrument (integrating sphere, monochromator, and detector).

For the calculation of iPLQY four emission spectra were recorded: i) a spectrum of the reference over the excitation range L_a, ii) a spectrum of the reference over the emission of the sample E_a, iii) a spectrum of the sample over the excitation range L_c, iv) the emission spectrum of the sample E_c. By substituting the emitted photons with $E_c - E_a$ and the absorbed photons with $L_a - L_c$ in Equation (2.21), the iPLQY was calculated from the following equation:

$$iPLQY = \frac{\int_{\lambda_1}^{\lambda_2} Ec(\lambda)d\lambda - \int_{\lambda_1}^{\lambda_2} Ea(\lambda)d\lambda}{\int_{\lambda_3}^{\lambda_4} La - Lc(\lambda)d\lambda}, \tag{3.3}$$

with λ_1-λ_2 the emission and λ_3-λ_4 the excitation band. The iPLQY of β-$NaYF_4$:25%Er^{3+} characterised under the broadband excitation in section 3.3.2, see Figure 3.10, are summarised in Table 3.3. The highest iPLQY, 4.27%, is given with the broadest excitation of 200 nm, which covers all the excitation spectrum of Er^{3+} and encompasses more photons per unit area. A decrease by 0.35% is shown by removing the excitation between 1400-1450 nm, and a decrease by 1.66% after removal of the 1550-1600 nm excitation. After reduction to the 1500-1550 nm excitation the iPLQY is reduced by a further 0.65%, which results to 1.61%. An improvement of 0.05% is also observed by

extending the excitation 1450-1550 nm to 1400-1550 nm, indicating the additional emission by exciting the absorption tail of Er^{3+}.

Table 3.3: iPLQY corresponding to the broadband excitation spectra of Figure 3.10.

Spectral range of excitation (nm)	FWHM (nm)	Irradiance (W/m^2)	iPLQY (%)
1400-1600	200	290	4.27
1400-1550	150	235	2.21
1450-1600	150	230	3.92
1450-1550	100	163	2.26
1450-1500	50	93	0.58
1500-1550	50	86	1.61

The iPLQY values in Table 3.3 are comparable with these in references [168, 183]. However, the iPLQY and the integrated broadband irradiance should be taken with care as a correction for the broadband excitation and the mismatch with the AM1.5G spectrum has not been applied. The first correction accounts for the re-emission of the sample from the $^4I_{13/2}$ to the $^4I_{15/2}$ level in the excitation spectrum, presented as a negative absorptance value of the sample. The second correction accounts for the disagreement between the spectrum of the experimental broadband excitation and the solar spectrum at AM1.5G conditions.

3.3.4 Broadband coupling in tapered optical fibres

The optical setup for characterisation of the coupling in tapered fibres is shown in Figure 3.11. A 1000 W quartz tungsten halogen (QTH) lamp (Oriel, 66187) was used as the illumination source. The measured spectrum of this source is shown in the inset of Figure 4.6. It corresponds to the spectrum emitted by a black body of correlated colour temperature 3200 K [118, 230]. A helium-neon (He-Ne) laser (Melles Griot, 25LHR991-249, 632.8 nm, 10 mW) was also used for coupling efficiency measurements and alignment. Double and triple axis linear translation stages were used for accurate alignment within ±0.5 mm for the vertical and horizontal axes and within ±1 mm along the optical axis. Alignment of the optical elements was carried out with a He-Ne laser source and an iris. The He-Ne source was first placed on a 3-axis stage with

pitch and yaw control, aiming at the centre of the optical axis of the system. Then, by traversing the iris along the optical axis, the pitch and yaw of the laser were adjusted to achieve acceptable alignment. Uncoated 2" BK7 plano-convex lenses with 90% clear aperture were used for collimation and focus of the beam through a pinhole of 1 mm. The achieved collimation was measured within ±0.5°.

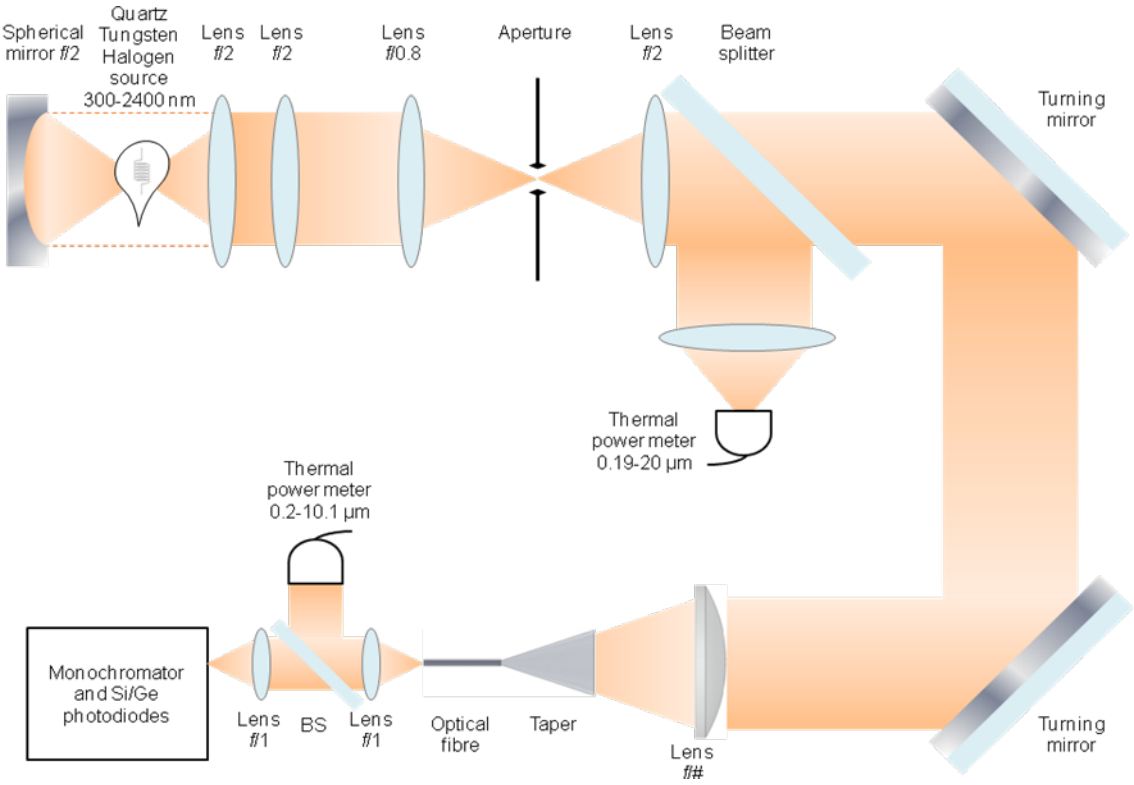

Figure 3.11: Schematic of the optical setup for characterisation of the broadband coupling in tapered optical fibres.

The power at the input of the coupling configurations was measured with a thermal power meter (Ophir, 1000W) of diameter 34 mm and surface area 907.46 mm^2. An additional *f*/2 plano-convex lens was used to allow for the measurement of the input power of the system. For total power measurements at the end of the fibre, a thermal detector was used (Thorlabs, S302C) with maximum calibration uncertainty of ±5%, while for spectral characterisation a Czerny-Turner monochromator with $f = 110$ mm (Spectral Products, CM110) with calibrated silicon and germanium photodiodes (Newport, 818-UV and 818-IR, respectively) were utilised.

3.3.5 Fluorescence spectroscopy in optical fibres

Spectroscopic characterisation of the Er^{3+}-doped optical fibres has been performed in the setup depicted in Figure 3.12. A fibre-coupled tuneable laser (HP-Agilent, 8168-F, 6 mW at 1523 nm) was used as an excitation source. Further details on this source are given in section 3.3.1. The excitation beam was focused with a microscope objective lens of *NA* = 0.4 (Newport, M-20X). Three-axis compact flexure translation stages (Melles Griot, 17AMB003/T) were used for alignment of the pump in the optical fibres.

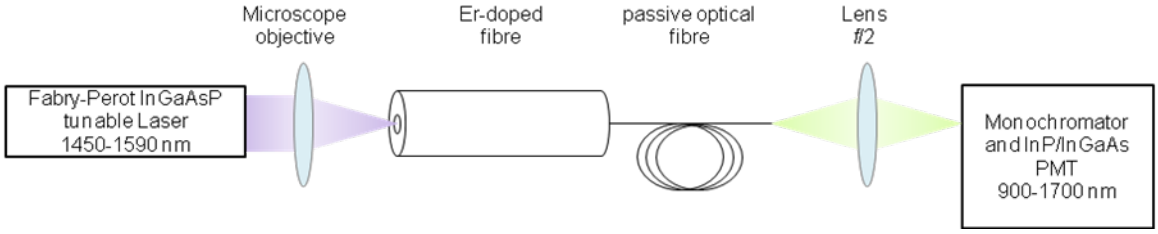

Figure 3.12: Schematic of the optical setup for the characterisation of Er^{3+}-doped fibres.

A portable fibre cleaver (Fitel, S325A) was used to cleave the fibres into the desired lengths. The cleaver enabled 0^o cleaving for fibres with cladding of diameter 0.125 μm and coating from 0.25 μm to 0.90 μm. Supported cleave lengths varied between 3 and 20 mm, while for cleaving longer fibres, the disposal compartment was removed.

The optical fibres were mounted as cleaved on V-grooved flexure stages (Thorlabs, HFF003**)** and the emission was collected from the opposite end of the doped fibre. A multimode fibre (Thorlabs, BFL48-1000) was utilised for collection of the emission, directly butt-coupled to the doped fibre with refractive index matching liquid (Cargille, L-RIA-165). This allowed for a coupling with reduced reflection at the facets of the optical fibres. The emission was finally guided into the emission arm of a fluorescence spectrometer (Edinburgh Instruments, FLS920), equipped with Czerny-Turner monochromators and a liquid nitrogen (LN_2)-cooled NIR photomultiplier tube (Hamamatsu, R5509-72).

3.3.5 Electrical characterisation of up-conversion solar cells

The up-conversion solar cells were characterised in the setup displayed in Figure 3.13. The system was illuminated at normal incidence with monochromatic illumination from the NIR tunable laser (HP-Agilent, 8168-F) covering a wavelength range of 1450-1590 nm as presented in section 3.3.1. The laser was fibre-coupled and collimated, resulting in a beam with a second moment width diameter ($d4\sigma$) of 4.20 mm and a divergence half-angle of 0.02°, characterised with a NIR camera (Electrophysics, Micronviewer 7290A). No additional illumination bias was applied during this characterisation. The entire setup was enclosed to minimise the interference of stray light with the measurements. The level of stray light and noise was measured as the photocurrent from one of the bifacial solar cells in the range of 0.3-0.5 nA.

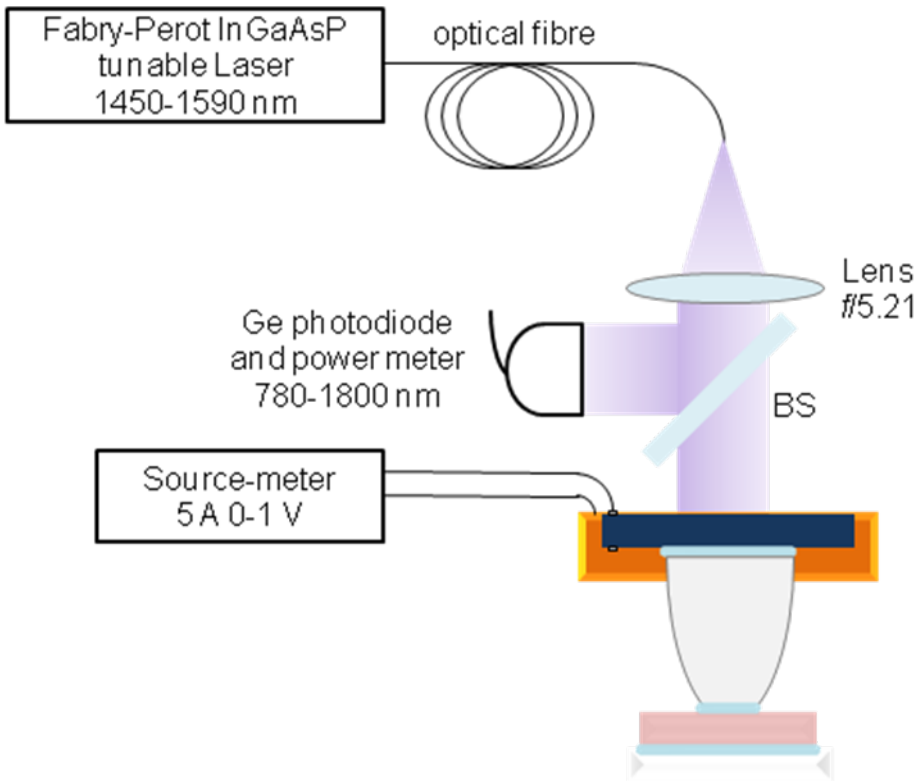

Figure 3.13: Schematic of the optical setup for electrical characterisation of up-conversion solar cells.

The photocurrent generated from the solar cell was measured with a source-meter (Keithley Instruments, 2440-C) and the power incident on the device was measured using a calibrated germanium photodiode (Newport, 818-IR). For the power density at

the up-conversion phosphor, the same illumination system was used, but the phosphor at the output of each optic has been replaced with an integrating sphere attached with the germanium photodiode, both calibrated for the excitation wavelength. By having knowledge of the incident power P_{in} the following relationship was used to determine the external quantum efficiency (EQE):

$$EQE = \frac{hcI_{sc}}{\lambda e P_{in}}, \tag{3.4}$$

where h is Planck's constant in m^2kg/s, c the speed of light in m/s, λ the excitation wavelength in m and e the electronic charge in coulombs. The current-voltage (I-V) characteristics of the solar cell configurations were determined by sweeping the voltage from zero until open-circuit V_{OC}. From these, the FF and the η of the up-conversion solar cell configurations under sub-band-gap illumination could be calculated from Equations (2.3) and (2.2), respectively.

3.3.6 Spectrophotometry

An UV/Vis/NIR spectrophotometer (Perkin Elmer, Lambda 950) was used for transmission measurements, equipped with an integrating sphere to support solid angles up to 2π sr from the exit apertures of each optical element. The absorption, transmittance and reflectance of samples and optical components such as lenses, filters *etc.* were also measured. The photoelectric accuracy of the instrument is ±0.0003A, while a relative uncertainty of less than 0.5% is quoted in the calibration certificate by the manufacturer. The range of measurements for this instrument varies from 175 – 3300 nm and the resolution is between 0.05 – 5 nm for UV/Visible range and 0.20 – 20.00 nm for NIR range. The scan range and step, beam height and width can be selected through software. Depending on the range of measurement (UV, Visible, NIR) the software changes to the suitable detector. The spectrophotometer is equipped with deuterium and tungsten halogen lamps, photomultiplier (PMT) detector for the UV/Visible range and a Peltier controlled PbS detector for the NIR range.

3.4 Materials

In this section, details on the building blocks of the up-conversion solar cells will be given. In particular, the up-conversion materials will be presented after the bifacial silicon solar cells. Finally, further details on the fabrication of tapered optical fibres will close the chapter.

3.4.1 Bifacial silicon solar cells

Three types of silicon bifacial solar cells were utilised for up-conversion measurements in this thesis. The transmittance of the solar cells is shown in Figure 3.14. The increasing performance, possibly associated with the evolution of experience, can be clearly seen. In order of increasing transmittance at 1500 nm, this is 24% for the textured bifacial, which was superseded by 40% for the planar bifacial, finally championed by 84% exhibited by the planar solar cell with optimised ARC. Further details for each of these solar cells will be given next.

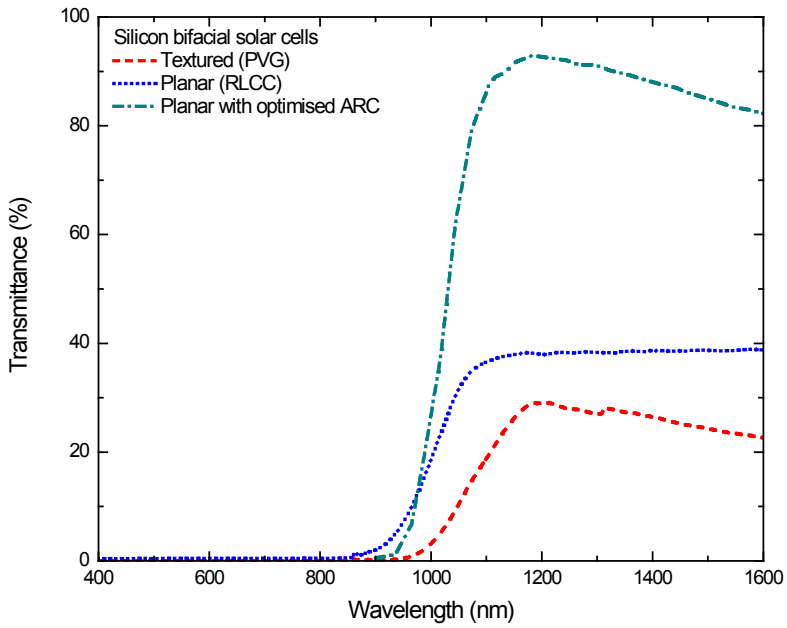

Figure 3.14: Transmittance of the bifacial silicon solar cells utilised in this thesis.

3.4.2 Textured bifacial mono-crystalline silicon solar cells

The first UC-SC during the course of this thesis utilised textured bifacial mono-crystalline silicon solar cells (PVG, Earth-ON190). A single ARC coating of SiN was applied on both sides. Information about the texture geometry of the cells was not available from the manufacturer. The transmittance of the solar cells however, (see Figure 3.14) agrees with this of bifacial cells with V-grooves and inverted pyramids [231]. The EQE of the solar cell between 1450 and 1590 nm with the β-$NaYF_4$:25%Er^{3+} was characterised and is shown in Figure 3.15 and the power dependence at 1523 nm in Figure 3.16.

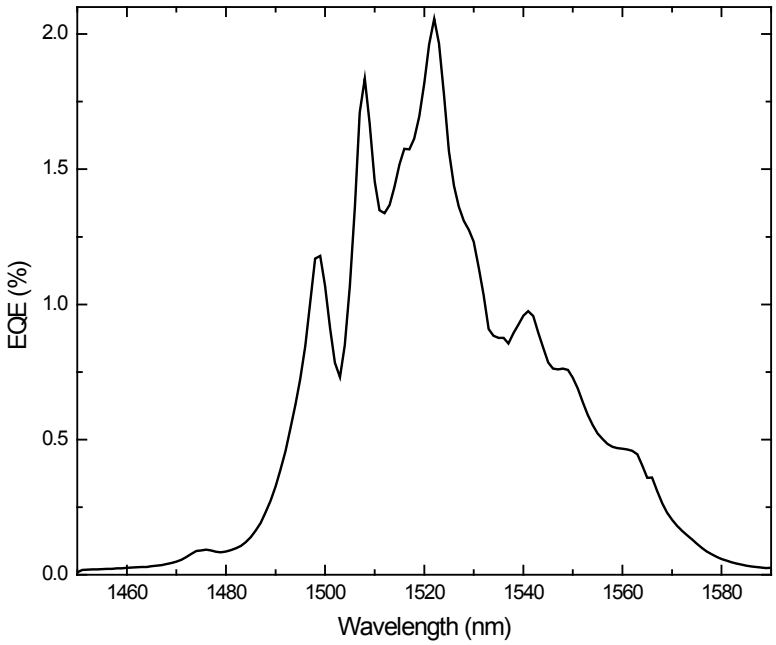

Figure 3.15: EQE of UC-SC at 7.34 W/cm^2 illumination between 1450-1590 nm.

An EQE of 6.93% under 1523 nm illumination at 22.05 W/cm^2 was measured, corresponding to a normalised EQE (NEQE) of 0.31 cm^2/W. The NEQE is commonly used to compare between non-linear devices and materials characterised under different excitation conditions, to allow for comparisons in a linear regime. It can be seen however, that the NEQE is not constant and also follows a non-linear relation at different powers.

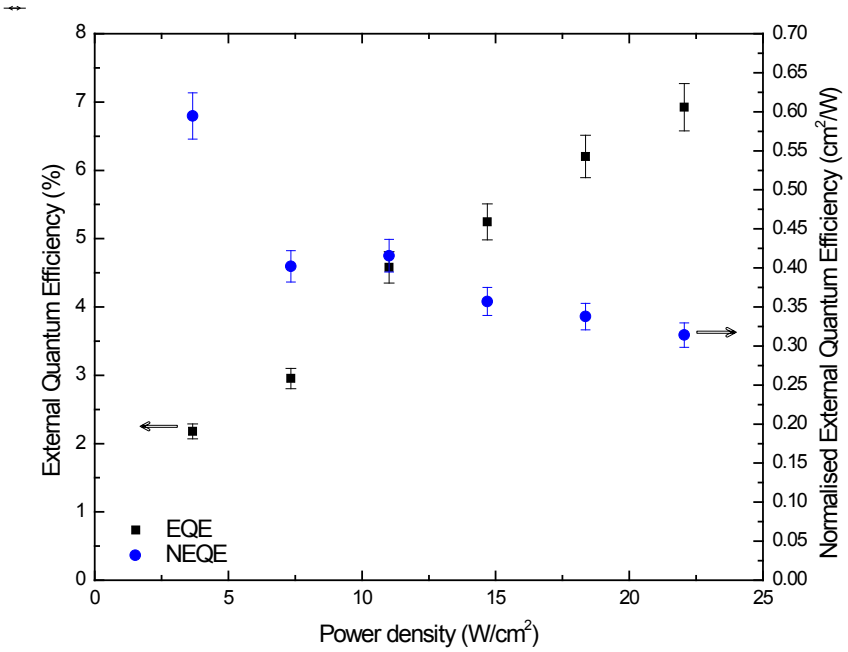

Figure 3.16: Power dependent EQE and NEQE of the UC-SC under 1523 nm illumination.

3.4.3 Bifacial rear-line-contacted-concentrator solar cells

Rear-line-contacted-concentrator (RLCC) solar cells were utilised afterwards. The solar cells are made as back contact-back junction (BCBJ) on one side, allowing minimum shadowing on the other side from a grid of fingers and bus-bars. They were illuminated from the back-side where both contacts are deposited, *i.e.* the grid-free side was facing the up-conversion material. The transmittance of the solar cells is shown in Figure 3.14. For the devices with tapered and parabolic integrated optics, a microscope glass slide was used between the solar cell and the optics by application of an additional layer of matching liquid between the interfaces. This allowed for the mechanical support of the solar cell that could not be accomplished with the small apertures of these optics. The EQE of the devices was finally corrected for the transmittance of the glass slide.

3.4.4 Planar bifacial silicon solar cells optimised for up-conversion

The optimised for up-conversion bifacial silicon solar cells were made in the Fraunhofer Institute for Solar Energy Systems by the group of Dr. J.C. Goldschmidt. A rectangular copper frame of 35 mm width, enabling collection of carriers by the front and back contacts of the bifacial solar cells, was used (see Figure 3.17). The up-conversion layer

or the concentrating optics were attached directly beneath the cell after a thin layer of index matching liquid. Finally, beneath the up-conversion layer a block of PTFE or an Au-coated glass slide was used as a back reflector.

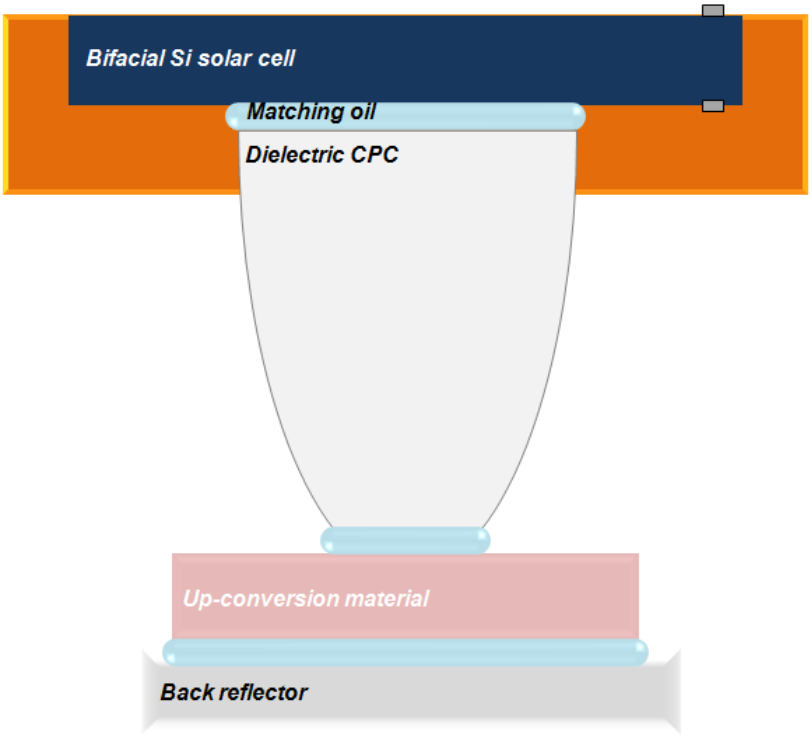

Figure 3.17: Schematic of the up-conversion solar cell devices. A copper frame was used for support and as a back contact, while liquid of appropriate refractive index was used between solar cell, concentrating optics, up-conversion material and back reflector.

3.4.5 Erbium-doped $NaYF_4$

The first up-conversion phosphor used for the UC-SC in this thesis, $NaYF_4$:25%Er^{3+}, was prepared in the department of chemistry and biochemistry of the University of Bern, by the group of Dr. K.W. Krämer. The phosphor can be formed in two phases. The cubic, also called *a*-phase, and the hexagonal, the *β*-phase. The *β*-phase displayed in Figure 3.18(a) exhibits the most efficient up-conversion emission upon doping with lanthanoids by substitution of Y^{3+} [143]. The lattice parameters of the *β*-phase are *a* and *b* 5.97567 Å and *c* = 3.53053 Å [232] shown in Figure 3.18(b), while when doped with Er^{3+} the parameters were reported as *a* and *b* 5.959 Å and *c* = 3.514 Å [233].

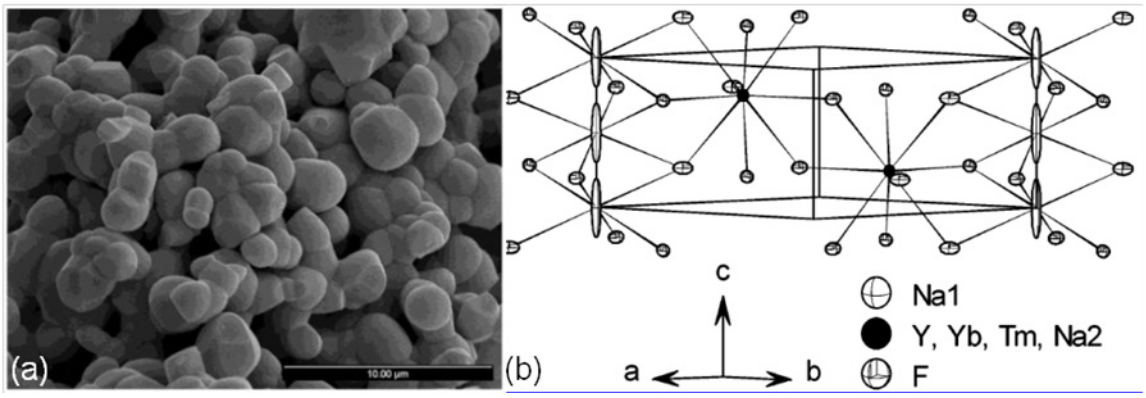

Figure 3.18: (a) SEM photograph of the $NaYF_4$ phosphor with a crystal size ranging between 1-3 µm and up to 200 µm for larger aggregates. (b) Crystal structure determined by x-ray crystallography. (Adapted from [232]).

Before incorporation into the UC-SC, the phosphor in powder form was encapsulated in a solid state layer of perfluorocyclobutane (PFCB). This host was chosen for its matching refractive index and phonon energy, in order to minimise parasitic scattering and absorption of the UC emission. In the literature the refractive index of $NaYF_4$ is taken as 1.482, the same as that of $NaYF_3$ [233]. The average phonon energy of $NaYF_4$ was determined as ~360 cm^{-1} [234] by the weighted average of the three strongest phonon modes of the Raman spectrum shown in Figure 3.19.

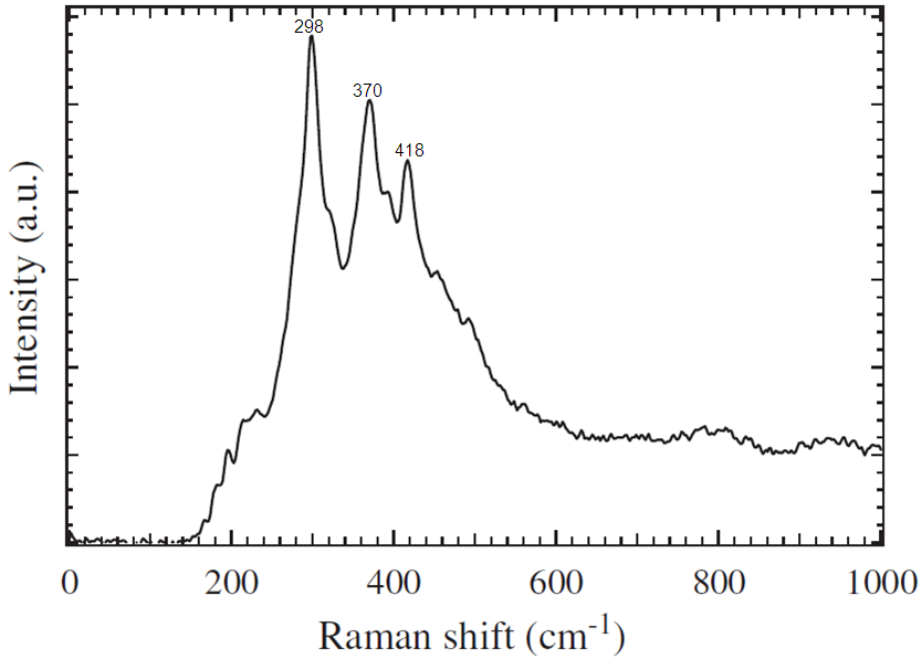

Figure 3.19: Raman spectrum of $NaYF_4$ at room temperature upon 9394.5 cm^{-1} excitation. The strongest phonon modes can be seen at 298 cm^{-1} 370 cm^{-1} and 418 cm^{-1}. (Adapted from [234]).

PFCB is a semi-fluorinated polymer of 1,1,1-tris (4-trifluorovinyloxy phenyl) ethane. A polymer host is preferable in comparison to other solid state hosts such as glass, as it can be processed at a lower temperature. The refractive index of PFCB was determined to be between 1.4785 and 1.5036 at 1550 nm [235]. By Raman spectroscopy, the phonon energy of PFCB was determined as ~1600 cm^{-1} originating from hydrocarbon (C-H) bond vibrations [236, 237]. The solid samples utilised in the UC-SC in Chapters 6 and 7 were cut into discs of 12.5 mm diameter and polished down to a thickness of 1 mm.

3.4.6 Erbium-doped BaY_2F_8

The second up-conversion crystal used for UC-SC in this thesis, BaY_2F_8:30%Er^{3+}, was made at the department of physics "E. Fermi" of the University of Pisa, in the group of Prof. M. Tonelli. The structure of the crystal is monoclinic $C_{2/m}$, with prism angles $\alpha = \beta = 90°$, $\gamma = 99.676°$ and lattice constants a = 6.972 Å, b = 10.505 Å and c = 4.260 Å [238, 239], see Figure 3.20. The refractive index of BaY_2F_8 has been determined as 1.59, while its phonon energy as ~350 cm^{-1} [240].

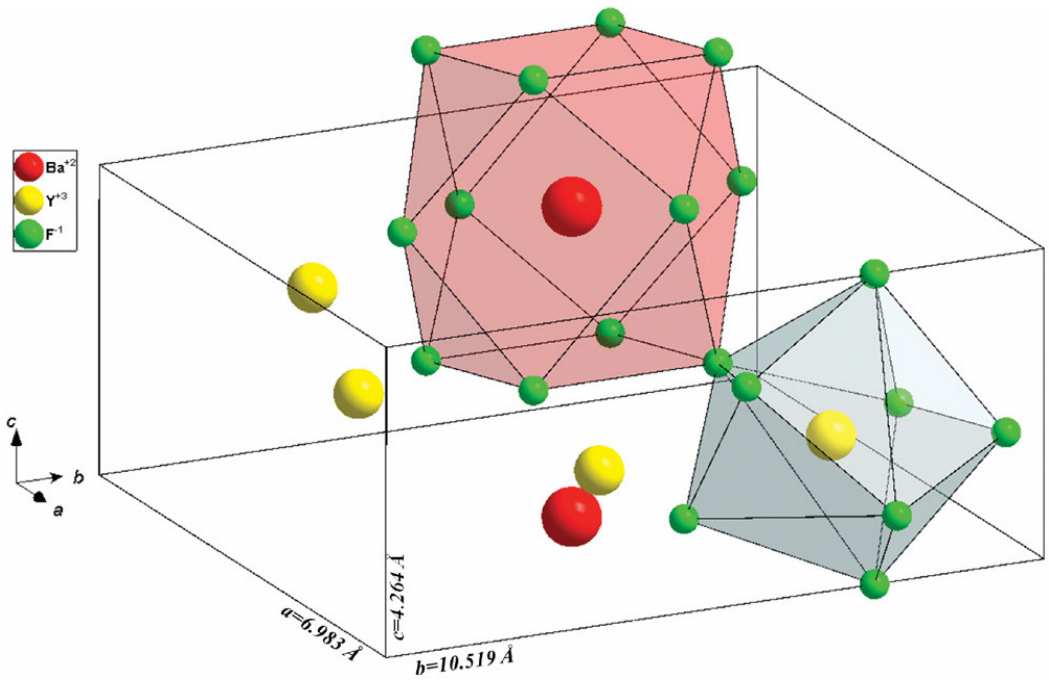

Figure 3.20: A unit cell of the simplified crystal structure of the BaY_2F_8. The 12-vertex polyhedron of BaF_{12} is shown in pink and the 8-vertex YF_8 polyhedron in grey. (Adapted from [239]).

The asymmetric structure of the crystal leads to the extended absorption and emission from the active doping material, in this case Er^{3+}. The crystals were prepared in Argon under low pressure conditions with the Czochralski method. The final crystals were cut in rectangular blocks and polished to optical quality. The dimensions of the up-conversion crystal utilised in the UC-SC in Chapter 8 were $10.08 \times 10.03 \times 2.33$ mm^3.

3.4.7 Tapered optical fibres

The tapers were made in the glass workshop of Heriot-Watt University by P. Allan. The fabrication involved softening and extruding silica rods and attached to optical fibres after removing a short segment of the coating. One end of the silica rods was held on a lathe. Then, heat from a torch was applied, while the other end of the rod was pulled and extended to the required length along the rotation axis of the lathe. By pulling the rod by its ends while heating, the cross-section of the rod was reduced at the centre and a bi-conical geometry was obtained. The pulled rod was then cut at the centre into a pair of frusta and heated again at the narrow end to create a smoother surface. The wide surface of the frustum, later used as the entry aperture, was polished with 0.25 μm abrasive diamond particles. Finally, the optical fibres held through a pipette where attached to the narrow end of the tapers by an additional application of heat. The cladding and the coating of the optical fibres was removed before the connection with the tapers by an appropriate stripping tool (Thorlabs, T28S46).

Vibration during the pulling process resulted in undulations towards the narrow ends of the tapers. These were especially pronounced in the longer tapers of angle 2-3^o. In total six tapers were prepared and attached to optical fibres, all shown in Figure 3.21. The undulations additionally resulted at an off-centre alignment of the optical fibre during the attachment. These tapers as a consequence had a reduced monochromatic coupling efficiency. Upon illumination of a taper of angle a 2.38^o with the He-Ne laser source focused with an f/6.56 lens the coupling efficiency was 37.73%. The theoretical coupling efficiency for the same lens-taper configuration estimated by the model was 87.99%, hence the analysis was performed only for the best three tapers.

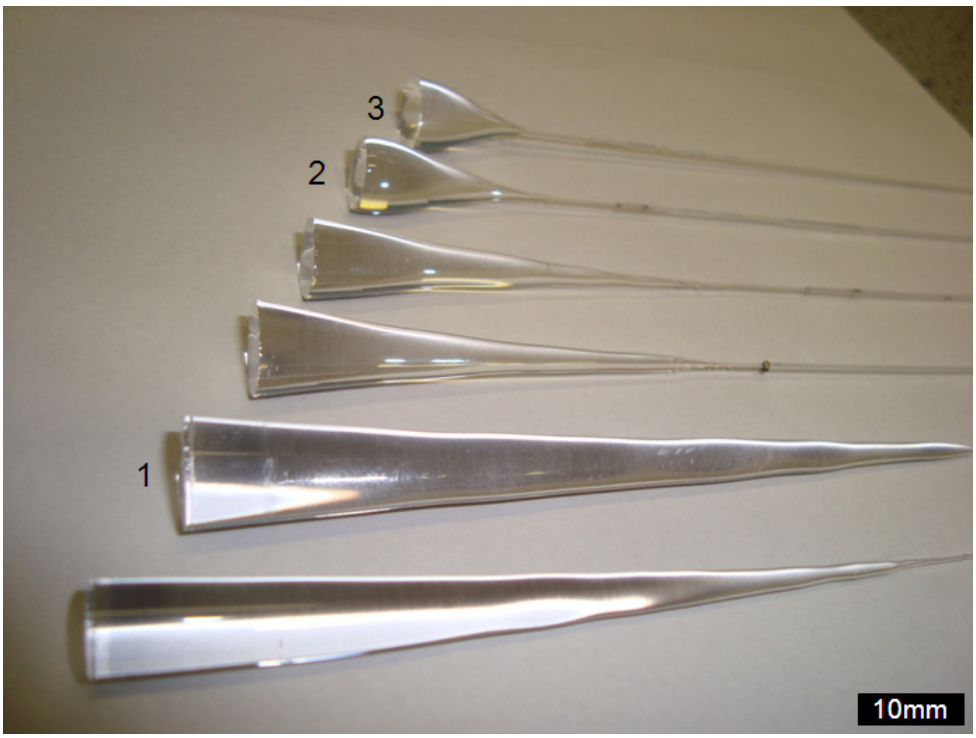

Figure 3.21: Photograph of the tapered fibres prepared in-house during this thesis. Undulations created during fabrication are clearly visible for the longer tapers.

The geometrical specifications of the prepared tapers are listed in Table 3.4. The profile of the tapers 2 and 3 does not suffer from undulations while drawing, but has a hyperbolic profile, the effect of which is discussed in section 4.4. The *f*/# of the focusing lenses was 5.47, 3.28 and 2.19 for tapers 1, 2 and 3, respectively.

Table 3.4: Geometrical specifications of the in-house prepared tapers

Taper	1	2	3
d_{in} (mm)	11.25	10.72	11.62
L (mm)	111.53	28.92	18.81
α (°)	2.89	10.5	17.16

Step index low-OH multimode fibres were used, consisting of silica core 600 µm ±2%, hard polymer cladding 630 µm ±2% and Tefzel coating 1040 µm ±2% (Thorlabs, BFL48-600).

Chapter 4 : Coupling and spectral dependence of primary and secondary optics with optical fibres

4.1 Introduction

The requirements for efficient coupling of sunlight in optical fibres as described in Chapter 2 are optimal matching between primary and secondary optics, while embodying practical advantages for a real system. These requirements are analysed in this chapter for a novel design that consists of spherical lenses as primary concentration optics and dielectric tapers as secondary optics. This results in a simple two-stage concentrator of flexible design able to reach high concentration of 2000 suns at the end of a single optical fibre, as the experiments have shown. In addition, solar concentration as a function of wavelength of the incident light is used for the first time to the best knowledge in the characterisation of a CPV system.

This chapter expands on material from the following publications: **G.E. Arnaoutakis**, J. Marques-Hueso, T.K. Mallick, B.S. Richards, (2013). Coupling of sunlight into optical fibres and spectral dependence for solar energy applications. *Solar Energy*, **93**, 235-243. **G.E. Arnaoutakis**, J. Marques-Hueso, B.S. Richards, T.K. Mallick, (2012, June). Propagation of white light through optical fibres for CPV systems. In *SPIE 8438 Photonics for Solar Energy Systems IV,* (pp. 843811-843811). Society of Photo-Optical Instrumentation Engineers.

4.2 Experimental details

4.2.1 Primary optics – spherical plano-convex lenses

Spherical lenses are used as primary optics for the concentration of incident light. A lens is described by its focal ratio or *f*-number, defined as $f/\#=f/D$ where f is the focal length and D the diameter of the lens. Since the sun is a broadband source of light, chromatic aberration is expected due to dispersion through the lens, resulting in a wider visible focal spot. For this reason secondary optics are also implemented.

4.2.2 Secondary optics – dielectric tapers

Dielectric tapers of circular cross-section directly attached to the optical fibres are used as secondary optics to ease coupling of light into the fibre. Similar tapers were previously proposed by D.E. Williamson [82] to improve the field of view and reduce the active area required for photo-detectors. The large surface of the frontal face of the taper enables the use of low quality lenses as the primary optics. The length of the taper L, confined by entry and exit apertures d_{in} and d_{out} respectively, resulting in an acceptance angle $\alpha = tan^{-1}[(d_{out}-d_{in})/2L]$, define the geometry of the taper.

4.2.3 Step index multimode silicate optical fibres

Hard polymer cladding silica (HPCS) step index multimode fibres offer low attenuation over a broad bandwidth. Common *NA* for HPCS [241] are as high as 0.37 and 0.48, while attenuation is affected by scattering at ultraviolet (UV) wavelengths and vibrational absorption at NIR wavelengths from hydroxyl (OH) groups at 1180, 1400 and 1670 nm, see Figure 4.1. It can be seen that for wavelengths below 400 nm the transmission is reduced due to absorption in the polymer cladding [241], although fibres with high-OH content are used with better transmission in the UV. Apparently, these fibres would be more favourable for applications utilising the UV and visible content such as photo-catalysis and lighting. Conversely, for fibres with low-OH content the UV transmission is sacrificed but transmission is improved in the NIR, allowing for distinct spectral windows to be utilised for applications such as photovoltaics and thermal applications. This is depicted in Figure 4.1 where the transmission per 10 m of a

state-of-the-art HPCS fibre is overlapped with the air-mass 1.5 direct (AM1.5D) solar spectrum as defined by the ASTM G173-03 standard. It can be seen that absorption from OH groups in the atmosphere matches with the absorption in optical fibres, especially at 1180 and 1400 nm.

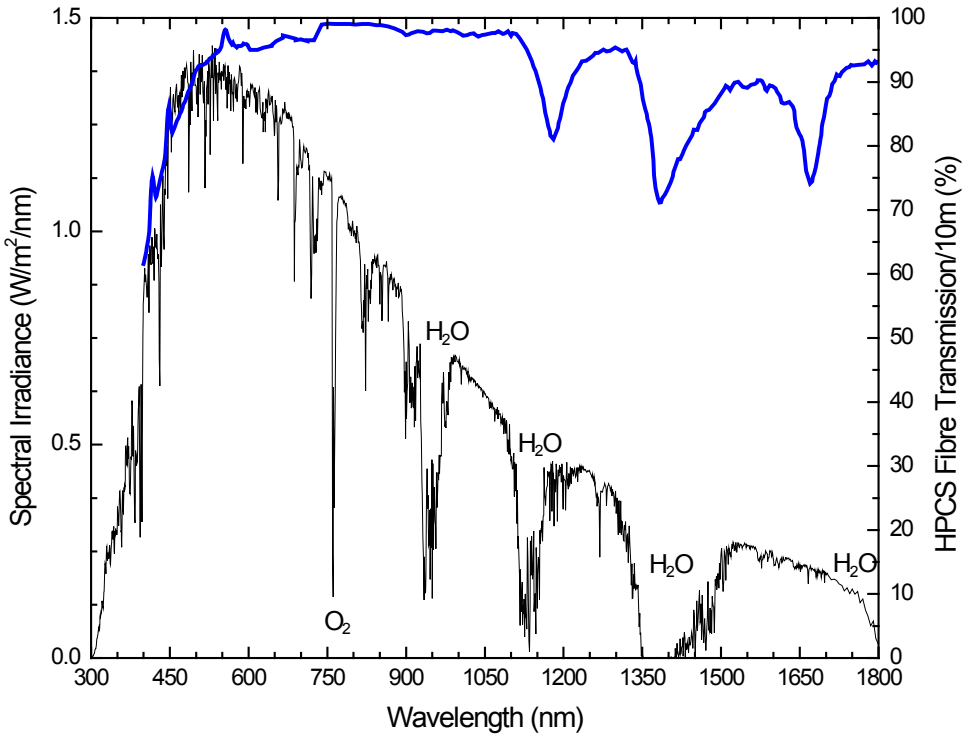

Figure 4.1: Overlap of the AM1.5D solar spectrum with a HPCS fibre displaying the suitability for solar applications. The transmission of the fibre was adapted from reference [241]. The main absorption from H_2O and O_2 is also indicated.

The parameters *f/#* of a spherical lens and angle α of a dielectric taper, related to the *NA* of an optical fibre will serve the basis of this analysis and are displayed in Figure 4.2(a) defined by f and D for a spherical lens, d_{out}, d_{in} and L for a dielectric taper, and θ for an optical fibre.

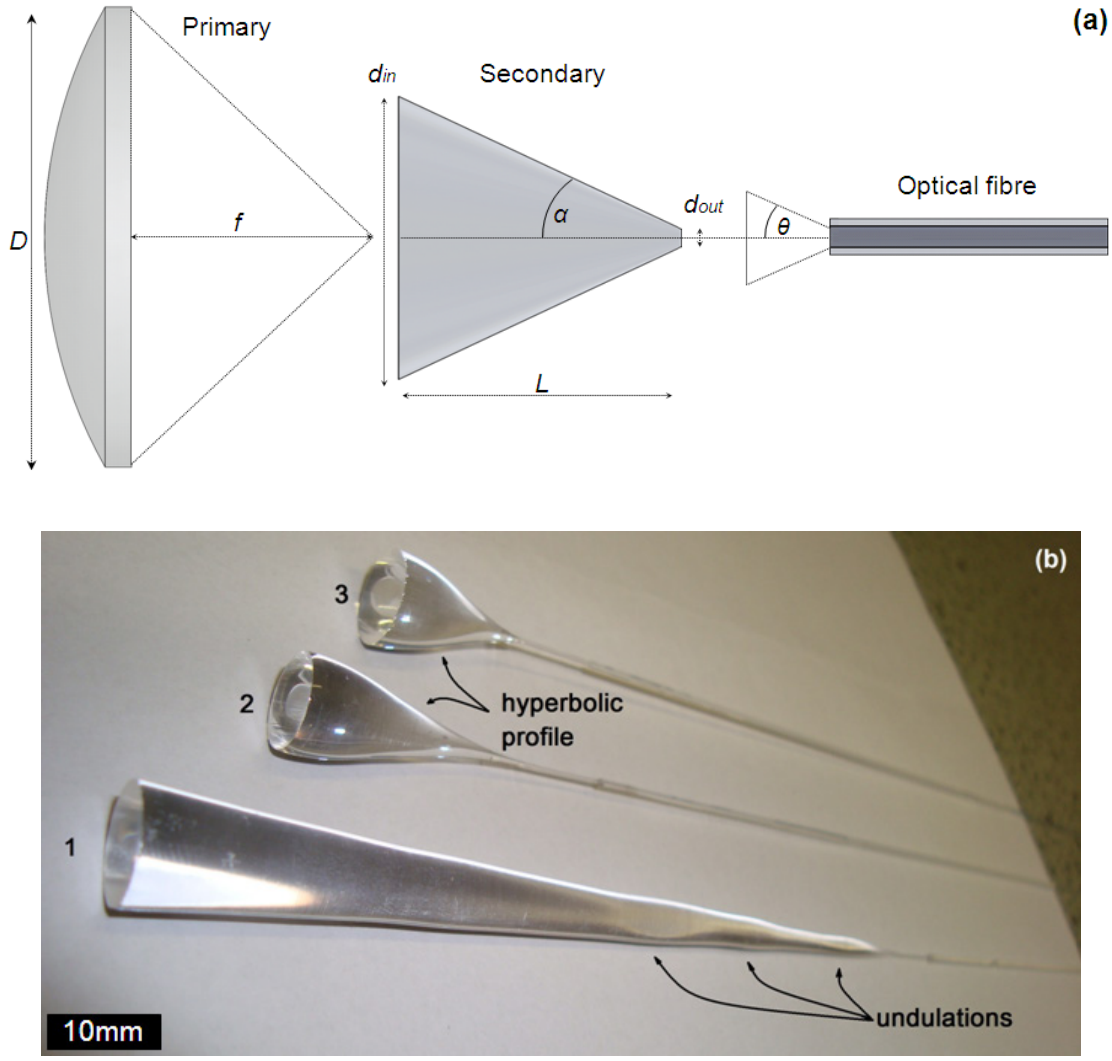

Figure 4.2: a) 2D schematic of the optics used and definition of geometrical parameters of the elements: primary-lens, secondary-taper and optical fibre, (b) Photograph of the tapers prepared in-house and attached to optical fibres. Undulations and hyperbolic profile created during fabrication are indicated.

4.2.4 Monte Carlo simulations and ray-tracing

A 3D model of the system was developed using ray-tracing software (Optis, Optisworks) while the proposed [17] AM1.5D reference spectrum was used with a total integrated intensity of 900 W/m^2. All simulations considered a single 50 mm long fibre (other dimensions given in section 3.4.7) with $NA = 0.48$. The core material was modelled as fused silica with known spectral dispersion [222], while the cladding and coating as fluorinated polymers (Luvantix, PC-370 and DuPont, Tefzel/ETFE) [242].

It is important to have knowledge not only of the limit for maximum performance, but also the region where a compromise in performance can be made in order to maintain

practical advantages. Hence, a simulation matrix was scheduled by varying *f/#* from 1 to 11 in 8 steps and α from 26^{o} to 2^{o} in ten steps. The angle *a*, was chosen as the first integer below an angle of $\theta = 28^{o}$, which corresponds to the *NA* of the used fibre from Equation (2.7). Parameters such as undulations or hyperbolic profile, see Figure 4.2(b), created by simple fabrication techniques of the tapers are not taken into account in the simulations. The undulations result in optical loss as instead of funnelling light towards the fibre, they disrupt TIR. On the other hand, a controlled hyperbolic profile may be desirable as it constitutes an ideal 3D concentrator [115]. Despite that, modelling of both parameters is not within the purposes of this chapter, the effect caused is discussed in section 4.4.

All simulations presented here assumed a perfectly collimated source. In the case of a divergent source the radiation pattern at the end of the fibre changes due to the radial dependence analysed by Y. Qu *et al.* [243] in light pipes made of quartz. This effect is relevant to the uniformity of the beam exiting the fibre and is thus important for photovoltaic applications at high concentrations.

4.3 Ray-tracing and identification of optical losses

An incident ray of light ① is attenuated through the optical system by losses and aberrations shown as secondary rays in Figure 4.3. These may originate from:

- Fresnel reflection on both surfaces of the lens (~8% as uncoated lenses are used) ②, ③
- Reflection at the front surface of the taper (~4%) ④
- Chromatic aberration from the lens (depending on wavelength and leading to losses in the taper) ⑤
- Spherical aberration from the lens (affecting the focus and leading to losses in the taper) ⑤
- Disruption of TIR in the taper (depending on the geometry for matching with the lens) ⑥
- Disruption of TIR in the fibre (expected to be negligible if within the *NA*) ⑦
- Absorption in the fibre (negligible at wavelengths useful for solar energy as shown in Figure 4.1)
- Reflection at the end of the fibre (~4%) ⑧

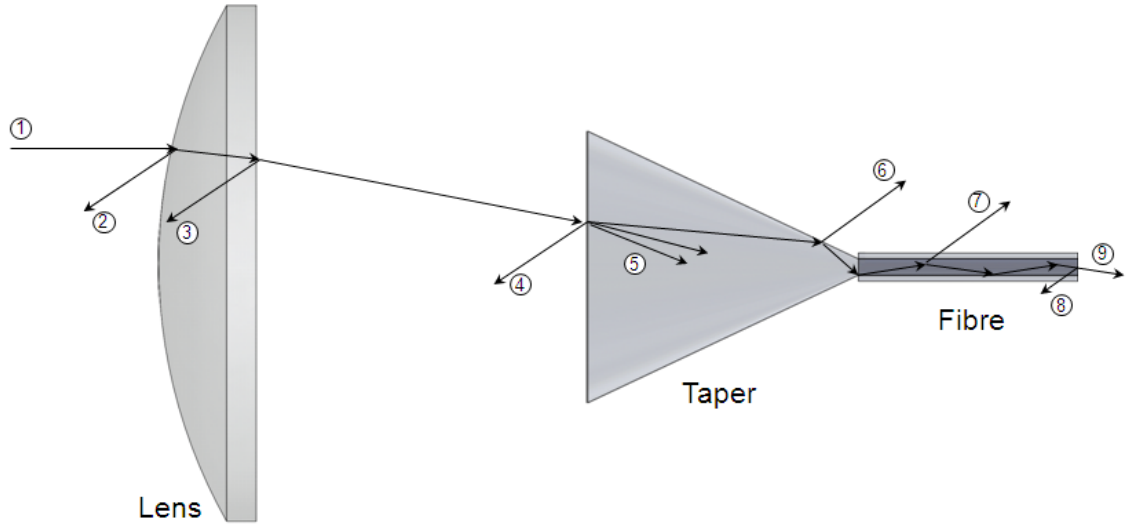

Figure 4.3: Ray-tracing diagram of a lens-taper-fibre system. Incident radiation ① can be reflected in the front ② or back ③ surface of the lens or the front surface of the taper ④, focused on shorter of longer lengths due to spherical and/or chromatic aberration ⑤, if TIR is disrupted in the taper ⑥ or in the fibre ⑦, reflected at the back surface of the fibre ⑧ or be transmitted to the application ⑨.

From the above a figure of around 84% coupling efficiency of the system can be estimated. The losses due to reflection at the lens can be reduced by using antireflective coated (ARC) lenses. Although, due to the limited window of operation (typically a few hundred nanometres) and the intensity exceeding the damage threshold of the ARC, uncoated lenses are preferred.

The estimation for losses due to absorption and reflection is straightforward, but further analysis is needed to quantify for the TIR losses in the taper exceeding the critical angle after a number of reflections in the taper. In this case the losses depend on; a) Matching between primary and secondary optics which is analysed in section 4.4, b) Spherical aberration which is observed for marginal rays important for this system in order to achieve high solar concentration at the end of the fibre, c) Chromatic aberration from the lens which results in focusing at shorter or longer lengths depending on the wavelength of the incident radiation, further discussed in section 4.5. Regarding disruption of TIR in the fibre which is expected to be low if light is kept within the *NA*, this is also further analysed in section 4.4 especially for light approaching the limit of the acceptance cone of the fibre.

4.4 Coupling efficiency simulation and experiment

The effect from the mismatching between primary and secondary optics on the optical performance of the system has been investigated by ray-tracing simulations. In Figure 4.4, the correlation between *f*/# of the primary and the acceptance angle α of the secondary optics is plotted. By keeping the aperture of the lens D constant, the focal length f was varied accordingly. Coupling efficiency below 10% is shown in this regime (coloured as blue in Figure 4.4) for low *f*/# lenses with small α and equally high *f*/# lenses with tapers of large α. In this regime, sunlight converging from the primary lens is refracted through the entry aperture of the taper, while at extreme converging angles associated with high *f*/# it may also be reflected at the front surface of the taper. In addition, sunlight refracted through the entry aperture, is consequently refracted out through the sides of the taper at angles above the critical to maintain TIR in the taper.

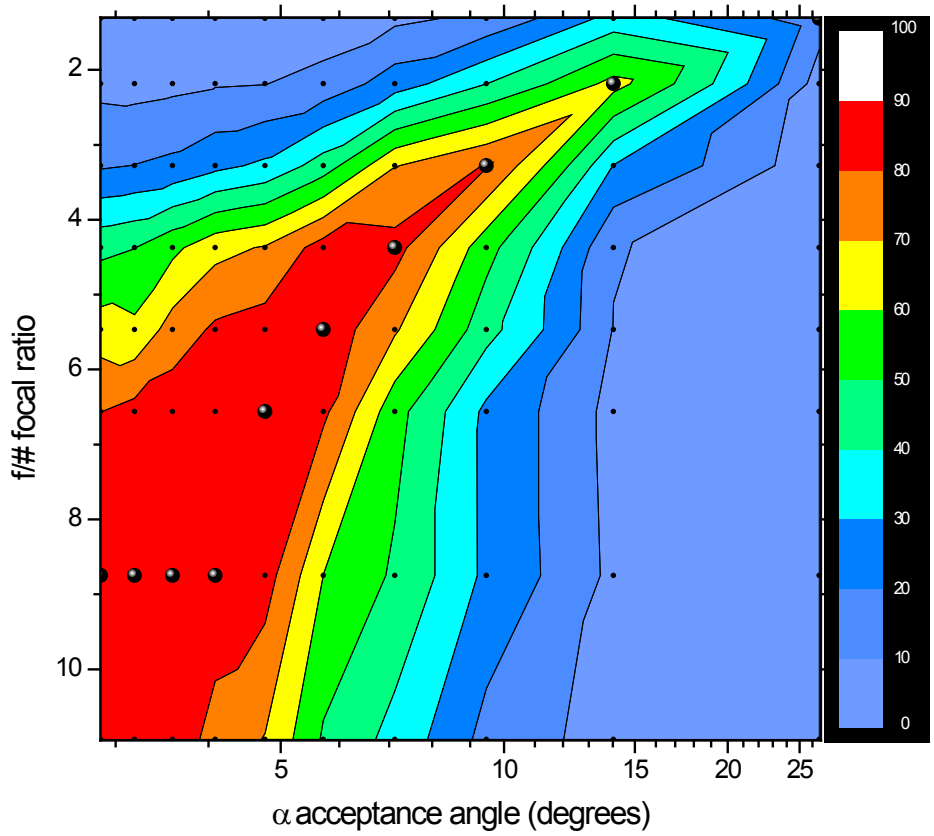

Figure 4.4: Coupling efficiency of the system as a function of acceptance angle α and focal ratio *f*/#. The optimal efficiency region is shown for narrow angles below 10^{o} despite that the optical fibre used in simulations supports incident light up to 28^{o}. The highest coupling efficiency combinations of focal ratio and acceptance angle (black spheres) are used for an element-by-element analysis.

It is shown that the highest coupling efficiency is achieved within narrow acceptance angles α and particularly below 10^{o}. The *f/#* of the primary optics to match these acceptance angles vary between 4 and 11. Higher *f/#* numbers are translated in long focal lengths. It is clear that a compromise is needed for practical reasons in a fixed system of adequate compactness and high coupling efficiency. A spread of high coupling efficiencies is observed towards higher *f/#* and lower acceptance angles α. Although this is true for wide acceptance angles, this trend is saturated for angles below 5^{o} as it is shown for the highest coupling efficiency combinations (black spheres in Figure 4.4).

It is shown that coupling efficiency is far from optimum when the acceptance angle of the taper is approaching that of the fibre (28^{o}). To better understand this constraint in performance, an element-by-element analysis of the system is needed. The highest coupling efficiency combinations from the simulations, shown as black spheres in Figure 4.4, were analysed for each individual element: lens, taper and fibre. Also the total coupling efficiency was measured experimentally to demonstrate the practical value of the proposed design and to identify possible challenges. Figure 4.5 displays the agreement between model and experimental data, as well as experimental data under monochromatic illumination for comparison.

In this element-by-element analysis better than 94% coupling efficiency to the fibre is observed for acceptance angles between 3^{o} and 10^{o}. For angles higher than 10^{o} and approaching the angle restricted by the *NA* of the fibre (28^{o}) the coupling efficiency drops significantly, a result corroborated also by other studies [244-246]. Correlating to the optical fibre's acceptance angle (28^{o}) this accounts for less than 50% the *NA* of the fibre, leading to the decision of under-filling the acceptance cone for maximum performance.

Considering that all rays within the *NA* of the fibre will be transmitted and that the primary optic, if accurately focused, accounts only for reflection and absorption losses, the coupling efficiency of the proposed system relies on the secondary concentrator. This is explicitly displayed in Figure 4.5 for acceptance angles higher than 15^{o} where the efficiency of the taper drops down to 20%.

The measurements with the QTH lamp and the He-Ne laser are displayed in Figure 4.5 with best coupling efficiencies 29% and 72% respectively obtained with taper 1. As mentioned in sections 3.4.7 and 4.3 the prepared tapers are affected by undulations

(taper 1) or hyperbolic curvature (tapers 2 and 3) of the profile which are not taken into account in the simulations. This contributes to a significant difference between simulated (85%) and experimental (29%) coupling efficiency for taper 1.

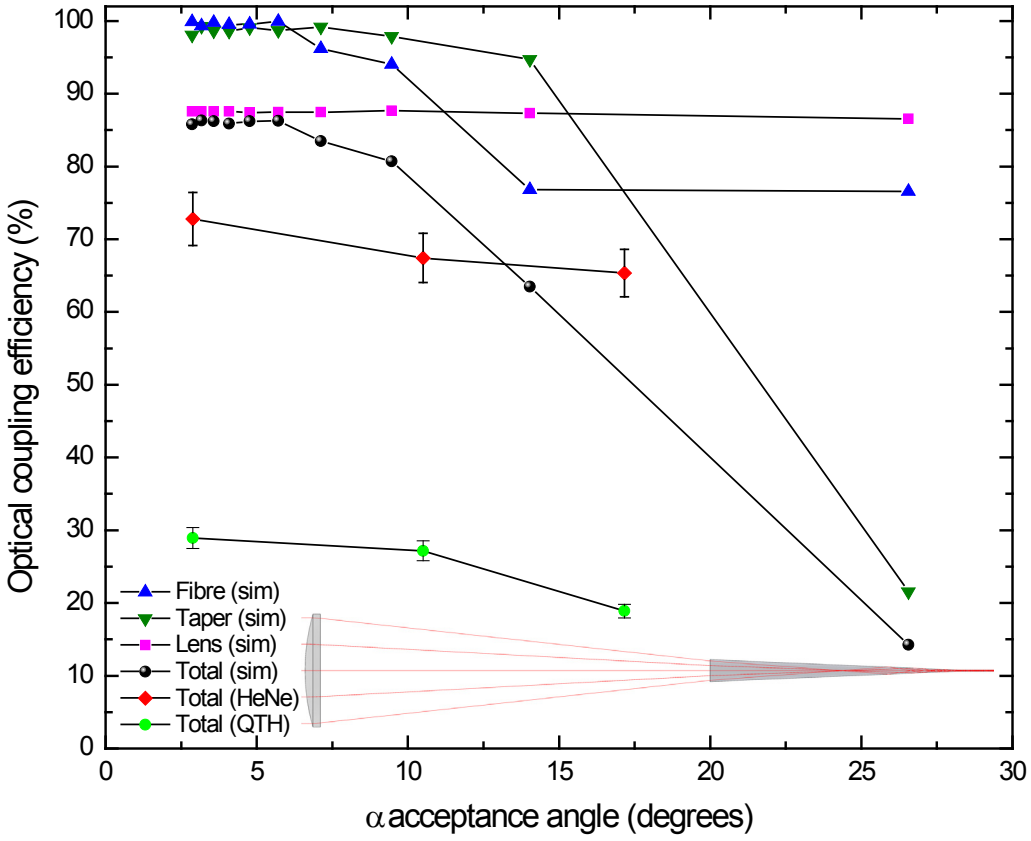

Figure 4.5: Break down of highest coupling efficiency combinations from simulations referred as black dots in Figure 4.4 for each element of the system and total measured with monochromatic (He-Ne laser at 632.8 nm) and white light (QTH lamp) sources for the three tapers of Table 3.4. The discrepancy in total coupling efficiency between simulation and experimental data is due to arbitrary geometrical parameters (see discussion) in the fabricated tapers that were not considered in simulations. The spectral dependence of coupling efficiency is observed as the steeper slope of coupling under white illumination compared to the linear trend of the monochromatic, meaning that for increasing acceptance angles, losses occur faster for white than monochromatic light.

Tapers 2 and 3 have lower coupling efficiency because of the widening of the acceptance angle leading to less light being coupled into the fibre. Despite that, the coupling efficiency of these tapers under monochromatic illumination is higher than expected from the simulated trend. The reason for this dissimilarity is partially the

better performance of the hyperbolic profile compared to the taper [61, 247], Two more reasons are identified for the different slopes between experimental results obtained with illumination from the QTH lamp and the He-Ne laser:

a) The different spectrum of the sources, as the He-Ne laser with a red monochromatic beam is focused with minor chromatic aberration through the lens and is transmitted almost seamlessly through the fibre. On the other hand the focus of the polychromatic white beam of the QTH lamp is varying as it will be explained further in section 4.5. This was observed especially for longer focal lengths, *i.e.* for the *f/5.47* lens used with taper 1, as a wider visible focal spot compared to shorter focal lengths.

b) The size of the beam which is affecting the coupling of marginal rays suffering spherical aberration through the spherical lens in the fibre, as it has been mentioned in section 4.3. Apparently, this is not a problem for the beam of the He-Ne laser which is only propagating around a limited region along the optical axis of the system.

The effect of the chromatic aberration of the lens on the coupling efficiency is further examined quantitatively by a spectral analysis in the next section with taper 1, which has the highest measured coupling efficiency.

4.5 Spectral power output and solar concentration

In this section, the power density and the solar concentration attained with the proposed system are examined for wavelengths 350 to 1800 nm where the solar spectrum has the highest intensity and can be used in CPV with existing solar cells such as silicon, germanium or III-V multi-junction cells. From Equation (2.8), with a fibre of $NA = 0.48$ and semi-angle $\theta_s = 4.7$ mrad [248] the maximum concentration under 1 sun would be approximately 10,400 suns, although with the apertures used in this study from Equation (2.27) the maximum C_{geo} is 7,100 × and the measured C_{geo} is 5,800 × (since the clear aperture of the lens is 90%). The highest concentrations based on ray-tracing simulations in this study were 6200 suns for $\alpha = 3^o$ and 6150 suns for $\alpha = 10^o$. In Figure 4.6 the spectral irradiance at the end of the fibre as a function of wavelength is displayed, while the respective spectral irradiance of the source is given in the inset.

A maximum solar concentration of 2000 suns is measured with taper 1 due to the losses explained in sections section 4.3 and 4.4. This concentration is not constant as one

might expect across the spectrum, but depends on the chromatic aberration. This is displayed in Figure 4.6, where the system has been optimised for two wavelengths by adjusting the taper at shorter and longer focal lengths than the designed (f = 250 mm at 587.6 nm) for 600 nm and 1500 nm respectively. This result reveals the spectral, in addition to the angular dependence, of the performance on this high concentration system. On the other hand, it enables the calibration of the system to acquire the highest solar concentration at the wavelength range of interest, depending on the solar cell response.

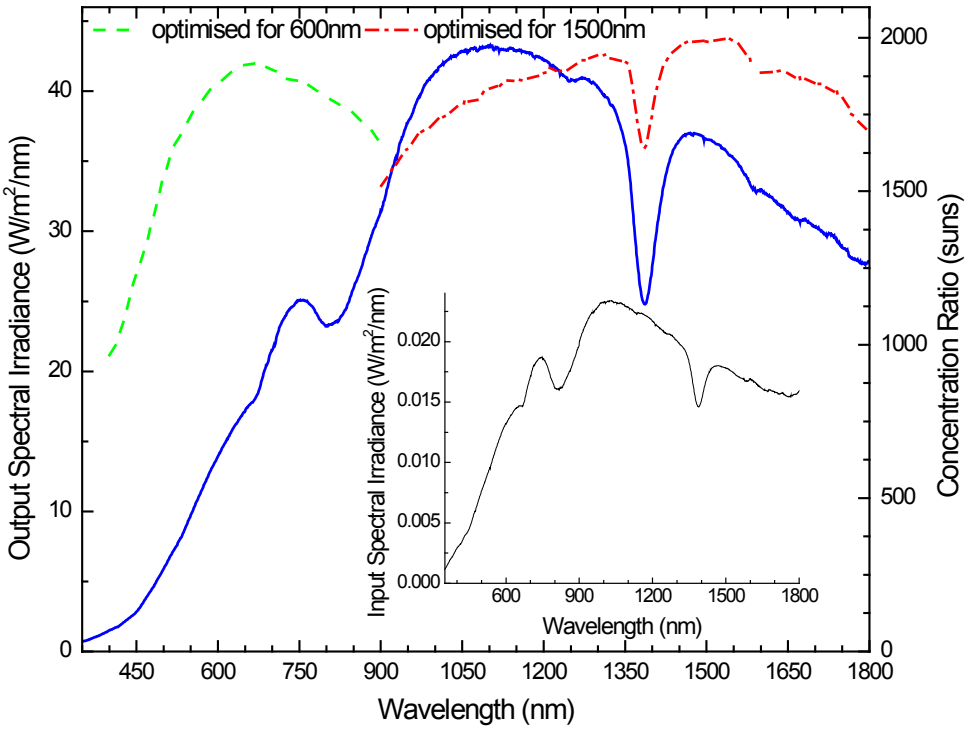

Figure 4.6: Output of the system as a function of wavelength. The system is excited by an incandescent QTH source with spectral irradiance shown in the inset. The concentration ratio from Equation (2.27) as a function of wavelength is displayed on the secondary axis adjusted for two maxima by controlling the chromatic aberration of the primary concentrator.

Additionally, absorptive losses displayed as reduced power density at 670, 1200 and 1400 nm reflect the vibrational absorption of OH that is present both in the fibre and the atmosphere. As mentioned in section 4.2.4 this absorption does not represent a barrier for solar energy applications since the terrestrial solar spectrum at these wavelengths has its lowest intensity. Nevertheless, they are accounted for and are shown as the

reduction of solar concentration at these wavelengths. The spectral effects of the aluminium coated elements of the monochromator used for the measurements are displayed as the valley centred at 800 nm.

The high power density over this range of wavelengths enables the experimentation on non-linear processes, while the high solar concentration can be calibrated through the system, *e.g.* by expanding the output of the fibre before the solar cell, to a flux commensurate with state-of-the-art solar cells. It is also indicative that by measuring the solar concentration as a function of wavelength, aids to a better understanding of the system and is thus proposed as an additional method of characterising CPV systems.

The acquired results can be further improved by reassessing the fabrication method of the tapered optical fibres. One reason for the reduced coupling efficiency of the tapered fibres was identified in the undulations at the profile of the tapers. The undulations were a result of vibration during the pulling process. These were more detrimental for the longer tapers of this study and can be reduced by a vibration-isolated pulling method. Conversely, a more suitable fabrication method could be lathe turning, which is widely applied in bulk optical elements. Highly resolved profiles and reduced surface scattering are obtained with this method by controlling the so-called scratch-dig parameter and any diffractive effects. Another aspect not investigated in this thesis, was the reduced mechanical stability of the fibres after the attachment with the taper. This occurred after removal of the cladding, therefore application of a low index cladding layer followed by a final layer of polymer coating is deemed essential.

4.6 Conclusion

The important parameters behind efficient coupling of sunlight in optical fibres were analysed in this chapter, and the margins for maximum coupling efficiency have been presented with the proposed system. Despite that high *NA* are achievable today in fibres with polymer cladding, best performance for solar applications is found by under-filling the acceptance cone of the fibre. For maximal coupling efficiency, *f/#* between 4 and 11 for the primary optics, and acceptance angles of the secondary optics below 50% of the *NA* of the fibre are shown. In addition, the spectral dependence of the solar concentration was measured to provide a more thorough understanding of the CPV system. A maximum of 2000 suns that can be calibrated to specific wavelengths

depending on the application, has been verified experimentally, allowing to design an efficient high concentration system with present day solar cells. Based on these attributes the proposed system can be tailored to solar energy applications or existing solar cells for CPV systems providing new routes for better exploitation of solar energy.

Chapter 5 : Up-conversion in erbium-doped silicate optical fibres

5.1 Introduction

This chapter is dedicated to the study of erbium-doped silicate fibres and the assessment of the potential for spectral conversion. This type of optical fibre has been extensively used in amplification and lasing applications, as well as up-conversion fibre lasers. Given the extensive development of this technology, it is interesting to investigate the potential of the incorporation with solar-coupled systems, presented in Chapter 4. In particular, photoluminescence from the $^4I_{11/2}$ to $^4I_{15/2}$ transition of Er^{3+} is investigated upon excitation of the $^4I_{13/2}$ level as a function of the optical fibre length. The influence of re-absorption of the photoluminescence along the fibre is also studied analytically and finally as a function of excitation power.

5.2 Erbium-doped silicate optical fibres

Er^{3+}-doped silicate fibres (Liekki, Er60-70/400DC) were utilised for up-conversion studies, with 60 dB/m core absorption and 1.7 dB/m for the cladding at 1530 nm. The diameters of the optical fibres were 70 μm for the core, 400 μm for the inner cladding and 500 μm for the outer cladding. The cladding was made of proprietary low index acrylate, resulting in a *NA* 0.09 and 0.46 for the core and the cladding, respectively. A low *NA* is required to maintain single-mode propagation and consequently good beam quality, essential for fibre lasers [249]. On the other hand, the high *NA* of the cladding and the diameter enable efficient coupling and multimode propagation, as required for the broadband case of sunlight. As seen in Chapter 4, optical fibres of equivalent *NA* enabled adequate broadband coupling around 1500 nm. The coupled sunlight would be consequently required to excite multiple levels in Er^{3+}.

The host is defined as a silica tetrahedron $(SiO_4)^{2-}$ and it is co-doped with Ge and Al. The co-dopants, in addition to the change in refractive index, enhance the solubility of the active Er^{3+} ions [250]. The fibres were originally developed towards applications such as signal amplification and fibre lasers. Consequently, any up-conversion signal is undesired and is kept to a minimum. Usual techniques are low doping concentration and forbidden modes or mode-stripping, thus allowing certain modes to propagate in the

fibre. However, under certain conditions, a small up-converted emission can be detected to allow for a study of the up-conversion dynamics in silicate fibres and its utilisation for photovoltaic conversion.

In this double-clad fibre geometry, only the core is doped (*cf.* Figure 5.1), that is where the signal beam propagates. The core is surrounded by an inner cladding that is used to guide the pump beam [251], required for amplification and population inversion, depending on the end application [252]. Usually, the core is single-mode with low *NA*, while the inner cladding is multimode with *NA* higher than the core. Consequently, the pump propagating in multiple modes overlaps with the core and is absorbed by the active ion. Most of the emitted signal is constrained within the core, owing to its low *NA*.

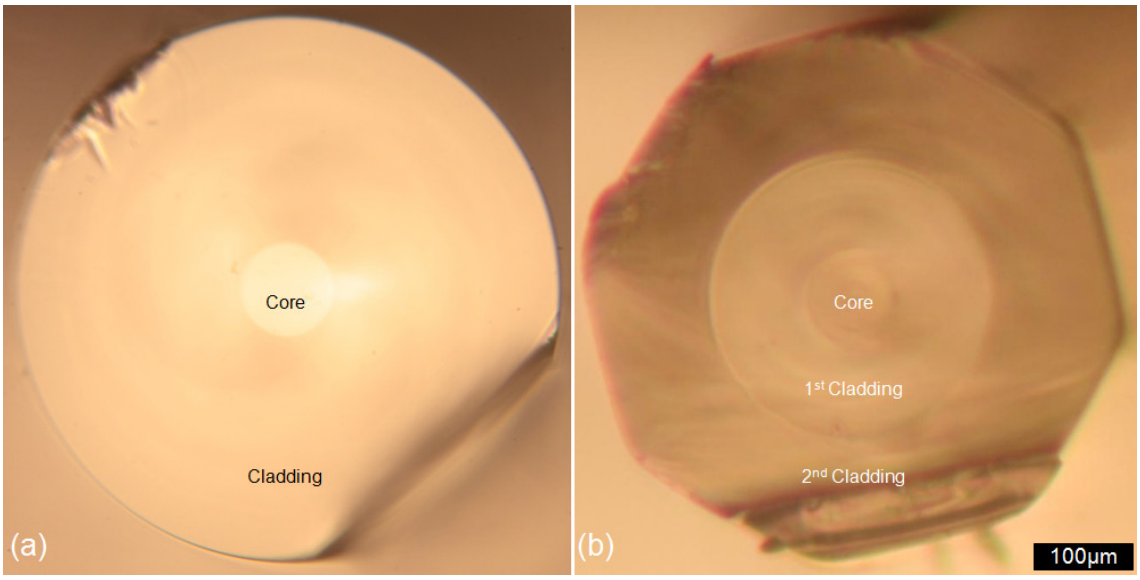

Figure 5.1: Microscope photographs of the cross section of the double-clad optical fibres utilised as cleaved in this study. The transition from the inner to the outer cladding with lower refractive index can be seen in the (a) passive fibre. The octagonal cross section of the second cladding of the (b) active Er^{3+}-doped fibre is shown.

The cladding features an octagonal cross-section owing to a better overlap of the pump with the doped core, and consequently increased absorption, in comparison to circular or other designs [253-255].

5.3 Photoluminescence and fibre length

In Figure 5.2 the up-converted emission is given for different fibre lengths. The fibres were excited at 1523 nm and a constant power of 6 mW.

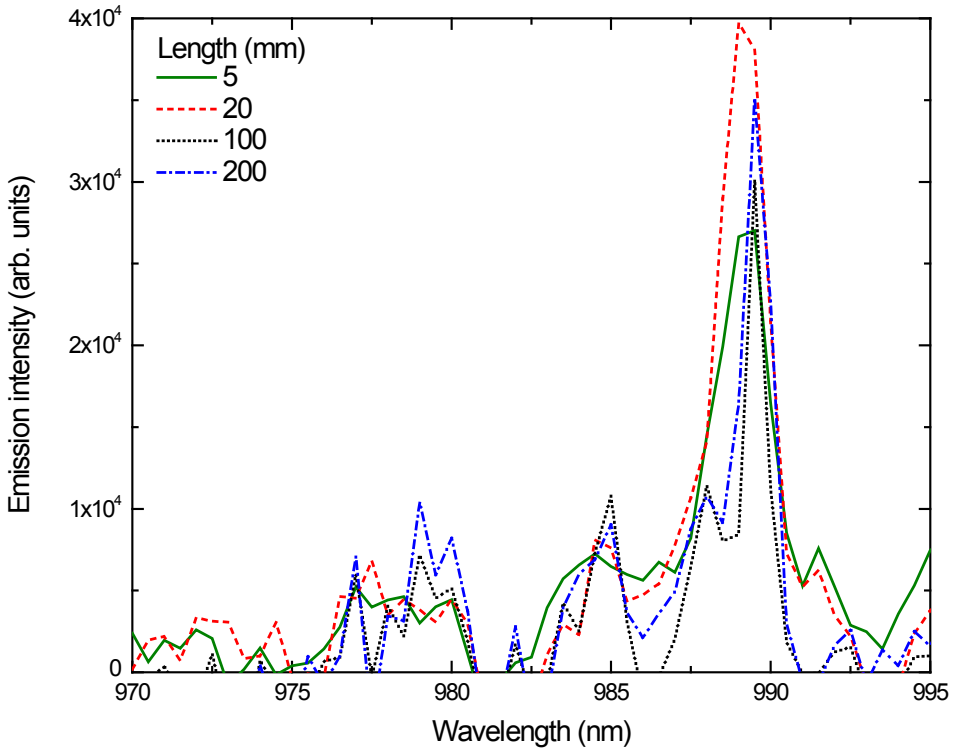

Figure 5.2: Emission from the $^4I_{11/2}$ to the $^4I_{15/2}$ level of erbium for different fibre lengths under 1523 nm excitation at a power of 6 mW.

A clear emission peak is observed, at ~989 nm for all the presented fibres. The most intense emission is observed for the 20 mm fibre, and lower emissions are gradually displayed for the 200 mm, the 100 mm and finally the 5 mm.

After a single excitation-emission event within the doped fibre, the up-converted emission is expected to be re-absorbed and re-emitted until it is guided to the opposite end of the fibre. The absorption and emission events in the fibre are expected to follow an exponential relation according to the Beer-Lambert law, *i.e.* $I_{out}=I_{in}\ e^{-al}$, where I_{in} and I_{out} are the input and output intensities respectively, a is the absorption coefficient and l is the length of the waveguide. It is expected, however, that equilibrium between reabsorption events would be obtained for a single length of optical fibre. This is further analysed in the next section.

5.4 Influence of re-absorption

Attenuation due to absorption is usually measured in fibres *via* the cut-back method. This is accomplished by measuring the transmitted power through a fibre of a fixed length. Then, the fibre is cut to shorter lengths and the transmitted power is measured again. The attenuation a can then be determined as [256],

$$a = 10 \log \frac{I_{in}(\lambda)}{I_{out}(\lambda)} \qquad (5.1),$$

where $I_{in}(\lambda)$ and $I_{out}(\lambda)$ the transmitted intensities through the fibre before and after cutting, respectively. The attenuation in fibres differs by a factor of 2.3×10^{-3} cm^{-1} with the absorption coefficient, since the Beer-Lambert law follows a relation according to the power with base e instead of base 10. By having knowledge of the absorption coefficient α at the excitation wavelength and β at the emission wavelength, and assuming a constant rate of energy transfer between ions η_{ET} along an optical fibre of length L, the probability of the transmitted emission P from the opposite end of the fibre can be estimated as [257],

$$P(\alpha, \beta, L) = \eta_{ET}(\alpha, \beta) e^{-\beta L} (1 - e^{-(\alpha-\beta)L}) \frac{\alpha}{\alpha - \beta}, \qquad (5.2)$$

In Figure 5.3 the probability as a function of fibre length is presented. The absorption coefficient a at 1530 nm, provided by the manufacturer, is 0.138 cm^{-1}. It is noted, however, that much lower values of $1.196\text{-}1.541 \times 10^{-3}$ cm^{-1} have been reported in literature [258] and relate to the pumping technique. The respective values for the energy transfer efficiency η_{ET} and absorption coefficient β were not found in literature, therefore a value of 50% and 0.13-0.21 cm^{-1} were considered in this calculation, respectively.

Equal probability of transmitted emission is found for fibre lengths of 2 and 20 cm with absorption coefficient $\beta = 0.13$ cm^{-1}. The relation for these fibre lengths agrees very well with the photoluminescence measurements. Based on this estimation, the UC emission is expected to be increased at least by a factor of 2 for fibre lengths 6-7 cm.

An ideal two-photon η_{ET} was assumed for the presented calculations. This is expected to overestimate the probability of the transmitted emission, even for the most efficient up-conversion materials based on low-phonon fluoride or chloride hosts [54].

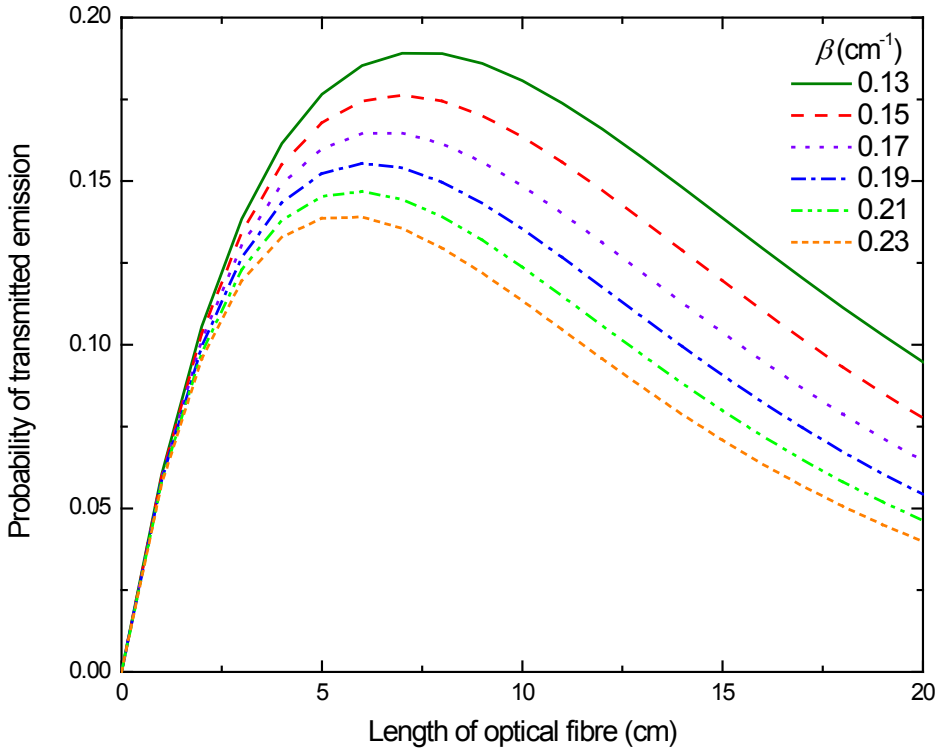

Figure 5.3: Probability of emission transmitted at the opposite end of the fibre as a function of fibre length for different absorption coefficients β at the emission wavelength.

The highest probability is obtained for all absorption coefficients β at fibre lengths between 6-7 cm. The same result was confirmed even for η_{ET} lower by an order of magnitude. The constant energy transfer rate considered here implies a linear relation of the energy transfer between ions. As discussed in Chapter 2, the η_{ET} is affected by the up-conversion dynamics in the material. To further study the up-conversion dynamics in the optical fibre, the emission at different power of excitation is required and is presented in the next section.

5.5 Power dependence

The peak emission corresponding to the $^4I_{11/2}$ to the $^4I_{15/2}$ transition is displayed in Figure 5.4 as a function of excitation power at 1523 nm for the 5 mm and 20 mm fibres.

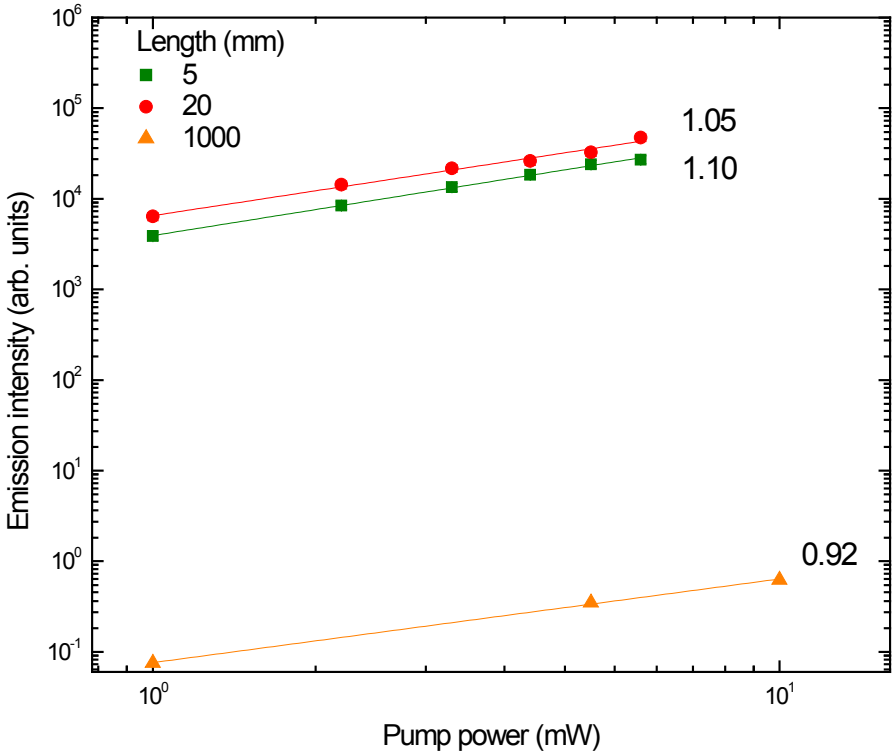

Figure 5.4: Power dependence of the emission for fibre lengths of 5 mm and 20 mm. The emission of a 1 m fibre of 300 ppm Er^{3+} concentration from reference [259] is also included. The slopes of the least square fits are indicated by the numbers for each fibre length.

As shown in the previous section, the 20 mm optical fibre exhibited the highest up-converted emission of all the presented fibres. The slope of the least square fits is 1.05 and 1.10 for the 20 mm and the 5 mm, respectively. For a two-photon process, a slope of 2 is expected. This has been observed in optical fibres of doping concentration 310 ppm, at an excitation power below 0.70 µW [260, 261]. This low level of doping concentration is used to reduce energy transfer *via* ETU and cooperative processes. At higher excitation pump-regimes however, the slope is expected to be reduced due to competing processes. In addition, owing to the low lifetimes of the first excited meta-stable level in silicate hosts in the range of several ms [260, 262], energy transfer between Er^{3+} ions is inhibited. Hence, higher order processes are not expected to contribute as a depopulation mechanism.

On the contrary, ESA from the ground state to the first excited state is a more probable process. This has been observed in 1 m long optical fibres of 300 ppm Er^{3+} concentration [259]. Longer length was used due to the lower absorption at 5±0.5 dB/m

of this optical fibre (Thorlabs, M5-980-125). Since the peak absorption of Er^{3+} is at approximately 1520 nm, strong wavelength dependence was observed in regard to the emission spectrum between 950-1030 nm from the $^4I_{11/2}$ to $^4I_{15/2}$ level. While the highest emission was observed when excited at 1520 nm, reduced emission was observed upon excitation of 1480 nm, 1550 nm and 1580 nm at a constant pump power of 10 mW. The power dependence of the emission in this optical fibre is also plotted in Figure 5.4. A slope of 0.92 is calculated from the least square fit of the double-logarithmic plot and is in reasonable agreement with the slopes of the 5 and 20 mm long fibres. This suggests that ESA is the main mechanism for the 980 nm up-conversion emission in this type of optical fibre and agrees with the low doping concentration.

As seen in Chapter 2, ETU is a more efficient up-conversion process than ESA [133]. Since ETU strongly depends on the inter-ionic distance and further on the molar concentration [263, 264], optical fibres with Er^{3+} doping concentration higher than 1000 ppm [265-267] would be possible candidates for 1520 nm to 980 nm up-conversion. In fact, a doping concentration in the range of 10-30% for Er^{3+}-doped up-conversion materials has been reported in literature, as discussed in Chapter 2. In addition, the radiative lifetime can be significantly extended to facilitate population of meta-stable levels in hosts of lower phonon energy, such as fluorides. For example, one of the most widely applied hosts for up-conversion optical fibre applications [268, 269] is the fluorozirconate glass (ZBLAN).

5.6 Conclusion

In the investigated optical fibres, up-conversion is not optimised since it is undesirable for amplification and laser applications. However, adequate emission has been observed and studied. The emission was measured for optical fibre lengths of 5, 20, 100 and 200 mm, with the 20 and 200 mm long fibres exhibiting the highest UC emission. A definite relation was not observed between the UC emission at all the examined fibre lengths. Good agreement was obtained, between the 20 and 200 mm long fibres with an absorption coefficient β at 980 nm of 0.13 cm^{-1}. The emission, and hence the rate of transitions in the optical fibre, was shown to be influenced by the excitation power. This also confirms that adequate excitation power was available at the investigated pump regimes.

However at higher pump regimes, the length of the waveguide is expected to contribute to the up-conversion component. In order to maximise up-conversion, this would be a trade-off between the re-absorption of the emission and the length of the optical fibre. Nevertheless, the latter aspect does not exclude the feasibility of optical fibres as wavelength converters for solar applications and is further discussed in Chapter 9.

Chapter 6 : Enhanced up-conversion for photovoltaics *via* concentrating integrated optics

6.1 Introduction

In this chapter, concentrating optics were incorporated on the rear side of a bifacial silicon solar cell, with the intention to further concentrate only the sub-band-gap photons useful for up-conversion as shown in the schematic in Figure 6.2. In this manner, the solar cell can operate at a more suitable concentration to maximize its conversion efficiency, while the transmitted light is further concentrated to the high power densities required for efficient up-conversion. After further integration with primary optics, the UC-SC device could be fully associated with CPV systems. This route proposes the research questions of, firstly, what effect does the addition of secondary concentration optics have on the NIR response of an UC-SC device, and secondly how do different concentrator geometries affect the performance of the integrated UC-SC device.

This chapter expands on material from the following publications: **G.E. Arnaoutakis**, J. Marques-Hueso, B.S. Richards, (2014, May). Optimizing integrated optics for up-conversion photovoltaic devices. In *International Workshop on Photoluminescence in Rare Earths (PRE'14): Photonic materials and devices*. San Sebastian, Spain. **G.E. Arnaoutakis**, J. Marques-Hueso, A. Ivaturi, K.W. Krämer, S. Fischer, J.C. Goldschmidt, B.S. Richards, (2014). Enhanced up-conversion for photovoltaics *via* concentrating integrated optics. *Optics Express*, **22**(102), A452-A464. **G.E. Arnaoutakis**, J. Marques-Hueso, A. Ivaturi, K.W. Krämer, T.K. Mallick, B.S. Richards, (2013, November). Enhancement of Up-conversion for Photovoltaics with β-NaYF4:Er^{3+} and Concentrating Integrated Optics. In *Optical Nanostructures and Advanced Materials for Photovoltaics,* (pp. PT3C-4). Optical Society of America.

6.2 Experimental details

6.2.1 Monte Carlo simulations and ray-tracing - UC-optics model

The profile of the concentrating optics was determined in a digital microscope. A description on the modelling of the tapered optics was given in section 4.2.3. The parabolic profiles were recorded by traversing the focus of the camera along the *Z* axis of the microscope. Then, the recorded profiles were converted into continuous Cartesian coordinates by least square fitting an exponential equation of the form: $y = a + b\,e^{cx}$. The fitting parameters were $a = -0.52381288$, $b = 3.31664876$ and $c = -0.16433$. The coordinates could be then introduced in a 3D model to design the concentrating optics.

The forward transmission and the irradiance profile at the exit aperture of the parabolic and tapered optics, exciting the up-conversion phosphor was determined *via* Monte Carlo simulations (Optis, Optisworks). The available power at 1522 nm from the fibre-coupled laser after the solar cell was used to illuminate the entry apertures of the optics.

The backwards transmission was also determined by Monte Carlo simulations. In this case, the isotropic emission at the main wavelength of 980 nm was modelled as a Lambertian source extending over a solid angle of 2π sr as shown in Figure 6.1.

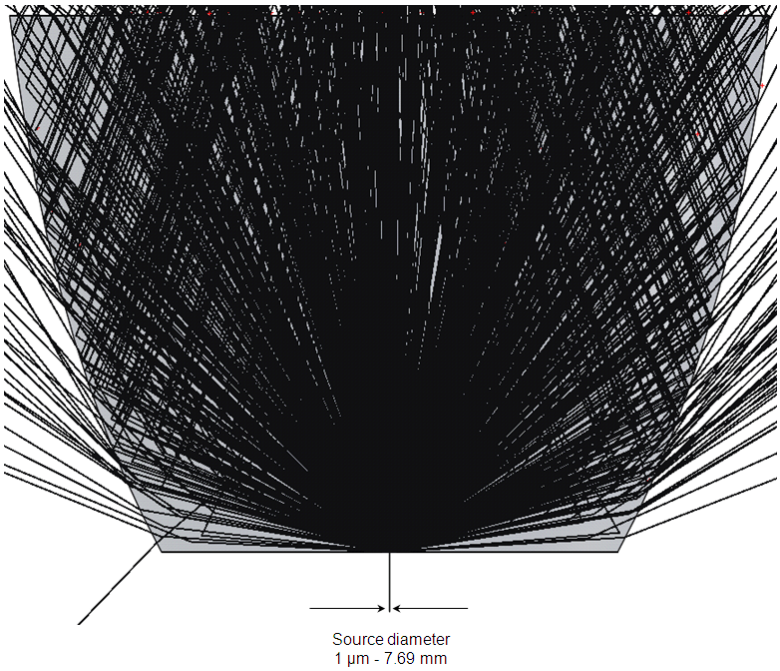

Figure 6.1: Ray-tracing schematic of the parabolic optics illuminated by a Lambertian source of diameter 1 µm.

The diameter of the source was varied between fully covering the exit aperture of the optics. This translates from a diameter of 7.69 mm for the parabolic, 2 mm for the tapered optics and down to 1μm.

6.2.4 Bifacial rear-line-contacted-concentrator solar cells

Rear-line-contacted-concentrator (RLCC) silicon cells were used to realise the UC-SC device. The cells were based on a design originally intended for CPV systems with maximum efficiency optimised at 100 suns [190, 270, 271], however these were modified to be both planar and bifacial. The best cell used in this study had an efficiency of 14% under 1 sun and external quantum efficiency (EQE) of 38% at 980 nm. It should be noted that for future research on the integration of UC-SC devices into systems, solar cells that have been recently specifically designed for this purpose [272] would offer significant advantages.

6.2.5 Concentrating integrated optics

The concentrating integrated optics consist of two different dielectric tapers made of fused silica with refractive index $n = 1.46$ at $\lambda = 589$ nm as described in reference [188] (labelled 2 and 3) with effective acceptance half-angles 10.50^{o} and 17.16^{o}, respectively. Bare (uncoated) tapers were experimented with, as well as applying gold (Au) coatings (~240 nm minimum thickness) on the external surface of the tapers by plasma sputter-coating (Fisons Instruments, Polaron SC502). Additional optical elements used in this study for comparison were an objective lens (Leitz Wetzlar, NPL100) with magnification 100×, numerical aperture (*NA*) of 1.30, entry and exit apertures 28.26 mm^2 and 3.14 mm^2 respectively, and a parabolic concentrator made in-house from fused silica, with entry and exit apertures 107.64 mm^2 and 46.42 mm^2, respectively. A schematic of the configurations is depicted in Figure 6.2(a) and photo of the parabolic concentrator attached with the bifacial solar cell is shown in Figure 6.2(b).

Optical coupling between elements was achieved with refractive index matching liquid (Cargille, L-RIA-766, $n = 1.53$ at $\lambda = 589.2$ nm) applied between the interfaces of the UC-SC device in limited quantity to avoid affecting the wave-guiding properties of the integrated optics.

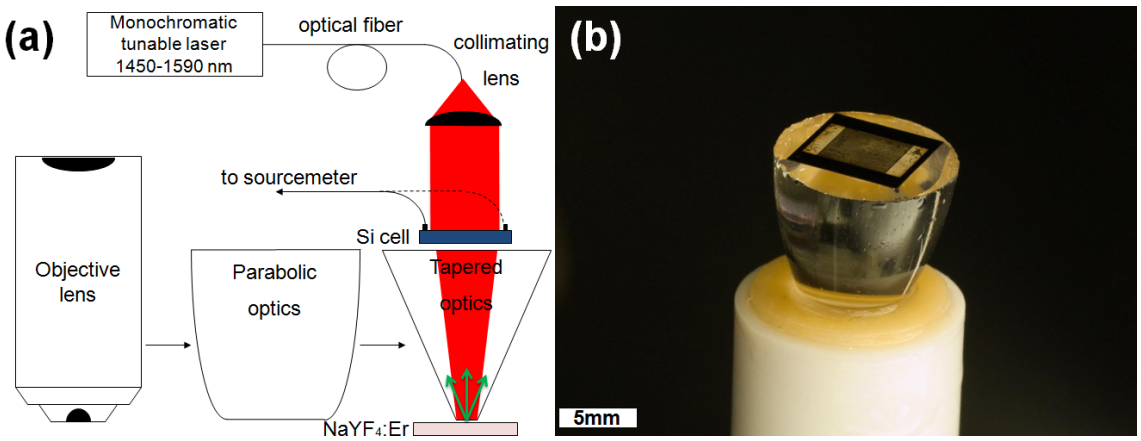

Figure 6.2: (a) Schematic of the UC-SC device with integrated optics behind the solar cell. For detailed characteristics the reader is referred to the section of materials and methods. (b) One of the concentrators used in this study (parabolic) with a bifacial silicon solar cell attached. The up-conversion phosphor is attached on the exit aperture of the parabolic concentrator.

6.2.6 Erbium doped $NaYF_4$

The up-conversion material consisted of β-$NaYF_4$ micro-phosphors doped with 25% Er^{3+} cast in a perfluorocyclobutane (PFCB) polymer (Tetramer Technologies LLC, USA) matrix. The phosphor-to-polymer weight ratio was 84.9% and the material was prepared according to the methods in references [151, 232].

6.3 Coupling of integrated optics with primary optics

As mentioned in Chapter 4, for incorporation of the integrated optics in CPV systems, coupling with primary optics is required. The coupling is analysed in this section, for tapered integrated optics coupled with plano-convex lenses. Figure 6.3 shows a schematic of the system with integrated optics which consists of: a lens of diameter D and focal length f, a bifacial silicon solar cell, a dielectric taper of acceptance angle α and the up-converter, in this case β-$NaYF_4$:25%Er^{3+}.

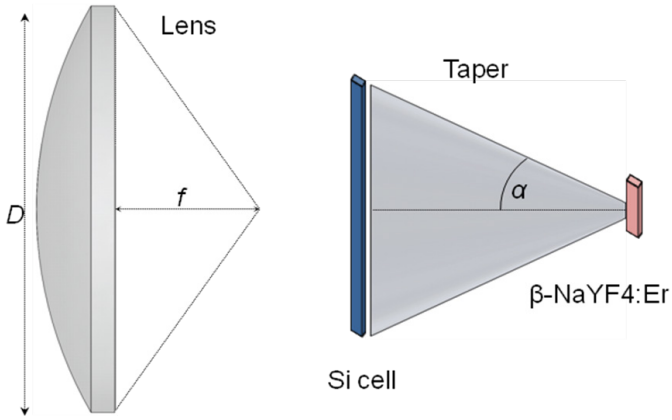

Figure 6.3: Schematic of the UC-SC device with integrated optics coupled with primary optics.

The optical system was modeled to determine the geometrical concentration (C_{geo}) at the end of the taper and consequently at the β-$NaYF_4$:25%Er^{3+}. C_{geo} is defined as the ratio of entrance to exit aperture. As shown in Figure 6.4, C_{geo} can effectively reach values above 6000× for acceptance angles below 10^o and *f*/# above 3. It should be noted that the transmission of the solar cell is not included in these simulations. This is expected to overestimate the solar concentration on the up-converter by a factor proportional to the transmission. Assuming a constant C_{geo} per wavelength, this corresponds to a power density of approximately 1500 W/m^2 under the AM1.5D spectrum at 1500 nm.

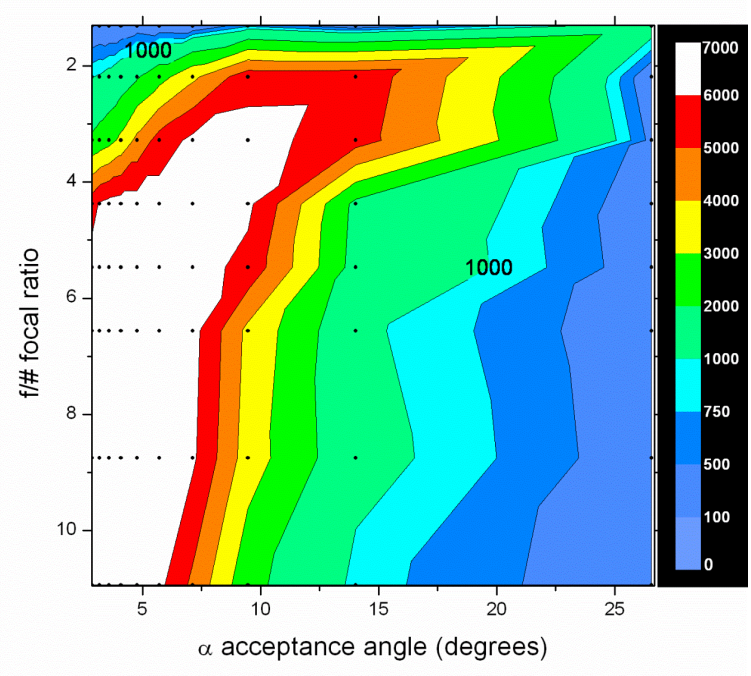

Figure 6.4: Solar concentration of the system as a function of acceptance angle α of the taper and focal ratio *f*/# of the lens. The 1000× solar concentration is indicated, where state-of-the-art CPV systems are frequently designed.

6.4 Selection criteria of the concentrating optics

Each of the optical elements in this study encompasses different concentrating properties and has been selected for the following reasons. The tapered concentrators, although non-ideal compared to the parabolic concentrator, feature higher concentration ratios – 28.7× and 33.7× for tapers 2 and 3, respectively. The parabolic concentrator although having a lower concentration ratio of 2.3×, is considered thermodynamically an ideal concentrator and its angular acceptance is superior to the tapers [273]. This last attribute plays a significant role on high CPV systems which are normally combined with primary optics. Last, the objective lens was also used to obtain a comparison of optics with higher concentration of 100×. As discussed in Chapter 2, the non-linear nature of up-conversion requires an UC-SC system in the range of 3500× solar concentration. With the assumption that silicon solar cells can operate at 100 suns (which is valid with state-of-the-art silicon solar cells [195] if characterised under standard temperature and illumination conditions [12]), the secondary optics should concentrate the transmitted sub-band-gap photons 35× to acquire the required solar concentration for up-conversion. Therefore a range of possible solar concentrations around this value is covered with the selected secondary optics.

6.5 External quantum efficiency

The EQE of the UC-SC devices with five different secondary concentrating optical elements is shown in Figure 6.5 as a function of the excitation wavelength at a power density of 0.007 W/cm^2. The spectra are similar in shape, with the highest EQE observed for all three devices at 1522 nm, while secondary resonant peaks are observed at 1508 nm and 1497 nm. The line shape of the spectra follow also with minor peaks at 1473 nm, 1543 nm, 1551 nm and 1564 nm, resulting from the convolution of the Stark levels with energy between 5500 cm^{-1} and 7500 cm^{-1} [138].

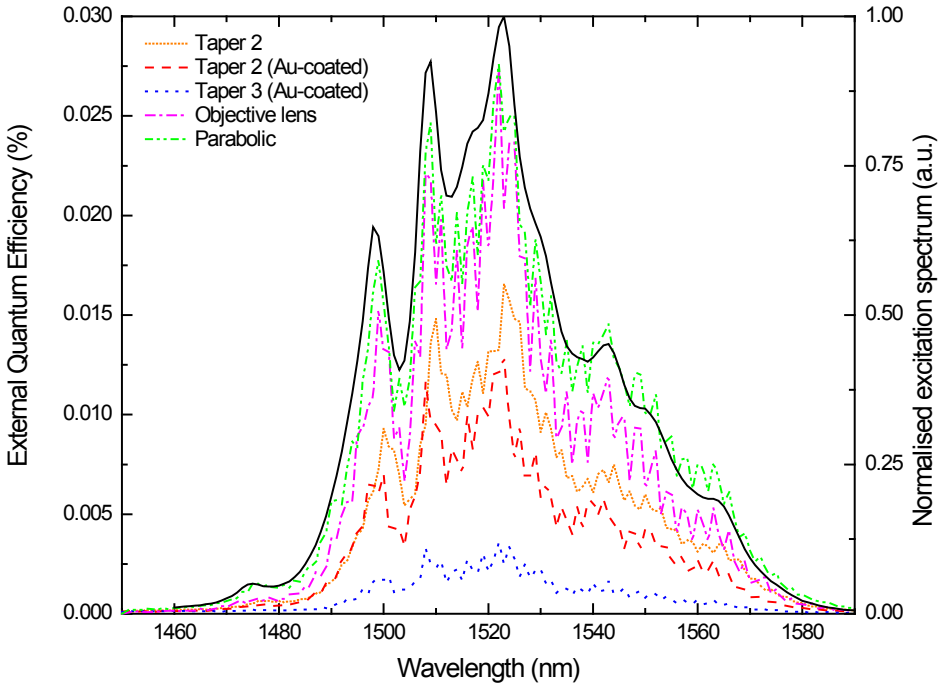

Figure 6.5: EQE of UC-SC device characterised between 1450-1590 nm at 0.007 W/cm^2 with five different secondary concentrator elements. The EQE closely resembles the $^4I_{15/2}$ to $^4I_{13/2}$ excitation spectrum of Er^{3+} shown on the secondary axis with main resonant peaks at 1497, 1508, 1522 nm.

The highest EQE was measured with the parabolic concentrator, while a lower EQE was obtained with the objective lens despite its higher concentration ratio and entry aperture matching the area of the solar cell. An even lower EQE was measured with taper 2 due to optical losses associated with disruption of total internal reflection (TIR). The EQE did not improve even when the tapers were coated with Au. On the contrary, as demonstrated in Figure 6.5, a reduced EQE response was observed after coating taper 2. The reflectivity of Au at ±5^o angle of incidence for both the excitation (1450-1590 nm) and emission (940-1050 nm) wavelengths is greater than 99% [274], however this value would be multiplied for every reflection resulting in a factor of R^{n+m}, where R the reflectivity at the interface, n and m the number of reflections for the excitation and emission respectively. This is expected to affect the excitation at normal incidence, but especially the internal reflection of the isotropic UC emission. The EQE of the device with taper 2 shows a higher response than with taper 3. As taper 3 has a higher angle of acceptance than taper 2, a progressively higher angle of reflection and consequently a higher number of reflections n, before the excitation reaches the β-$NaYF_4$:25%Er^{3+} up-converter.

6.6 Optical efficiency (forward) of the integrated optics

The response of each device is described on the one hand by the optical losses due to transmission of the excitation (named here also forward transmission), and on the other hand by losses due to transmission of the UC emission back to the solar cell (named backwards transmission). To estimate the losses due to excitation, each optical element was characterised for forward transmission between wavelengths of 900 nm and 1600 nm (*cf.* Figure 6.6). As mentioned in the section of materials and methods, the exit aperture of the optical elements was positioned flush with the entrance port of an integrating sphere to make possible measurement over a solid angle of 2π sr. The transmission is constant within 1% for this wavelength range as expected for the material of the optical elements (fused silica). A reduced transmission is observed between elements with 82% for the parabolic concentrator, 77% for the objective lens and 65% for the Au-coated taper 2 at 1522 nm; the wavelength where the highest EQE was obtained. For comparison, the transmission of the bifacial solar cell is also plotted in Figure 6.6, with 42% at 1522 nm.

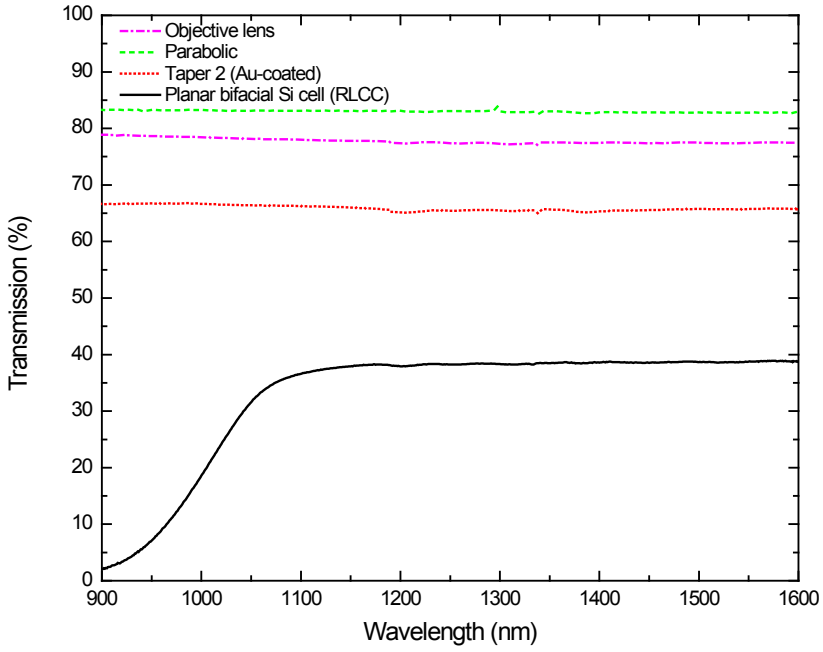

Figure 6.6: Transmission of the concentrating elements of the UC-SC device as a function of wavelength between 900-1600 nm. The transmission of the bifacial solar cell is also plotted for comparison.

The transmission between optical elements follows the same trend as the EQE of each UC-SC device, which suggests that a significant portion of the optical losses in the UC-SC device originates from reduced transmission of the excitation.

6.7 Optical efficiency (backwards) of the integrated optics

The losses due to backwards transmission T_b can be estimated based on the light collection properties of the optical elements. For an objective lens this collection over a solid angle 2π is described by the *NA* and the refractive index of the immersion medium *n* from the following equation,

$$T_b = \left(1 - \sqrt{1 - \left(\frac{NA}{n}\right)^2}\right) \qquad (6.1).$$

For the parabolic and tapered optics the backwards transmission was determined by Monte Carlo simulations. The isotropic emission at the main wavelength of 980 nm was modelled as a Lambertian source extending over 2π. These results are shown in Figure 6.7 for source diameters between fully covering the exit aperture of the optics (7.69 mm for the parabolic and 2 mm for the tapered optics) and down to 1μm.

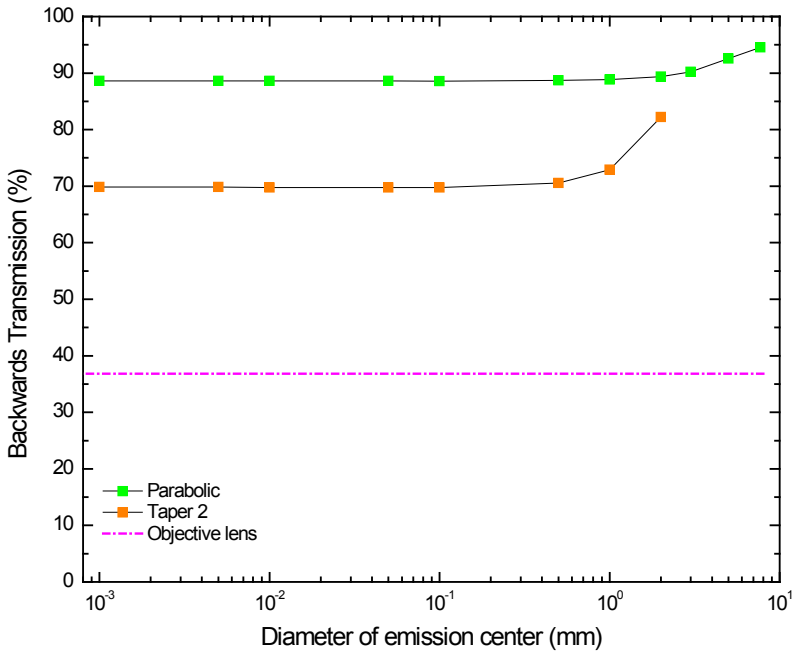

Figure 6.7: Backwards transmission of the concentrating elements of the UC-SC device as a function of the diameter of an isotropic emission centre. The lines act as a guide to the eye. The transmission of the objective lens, estimated from Equation (6.1), is plotted for comparison.

A backwards transmission higher than 88% is revealed for the parabolic optics, while 69% is given for taper 2. The transmission of both parabolic and tapered optics is displayed to be higher as the diameter of the emission centre approaches the diameter of the aperture of the optics. As the diameter of the source increases, the angle of reflection traced from the Lambertian emitter to the edge of the optic is smaller, resulting in progressively higher backwards transmission. While the parabolic concentrator displays high collection properties for the emission, the collection efficiency of the objective lens is limited by its geometry to only 47%. This efficiency is multiplied by the forward transmission to result to a 36% backwards transmission. While this value might appear low compared to the parabolic and tapered optics, it agrees well with dedicated studies on objective lenses [275], where collection and transmission of fluorescence is crucial for multi-photon microscopy.

6.8 External quantum efficiency vs power density on the UC-SC

The forward transmission is expected to affect the population rates of β-$NaYF_4$:25%Er^{3+} in the up-conversion layer, while the backwards transmission is expected to affect the collection of the UC emission, and consequently the EQE of the UC-SC device. Therefore a power dependent characterisation of the UC-SC is needed to further investigate this effect. As the highest EQE was observed for an excitation wavelength of 1522 nm, the incident power at this wavelength was varied to obtain the EQE as a function of excitation power. These results are displayed in Figure 6.8 for all UC-SC devices.

An EQE of 0.038% was obtained with uncoated taper 2, while this value was reduced by half following Au deposition. As expected the EQE of the device with the parabolic optics performed best with a maximum EQE of 0.075% under excitation of 0.022 W/cm^2, while under the same excitation power, the EQE of the UC-SC with the objective lens was 0.039%. A lower EQE of 0.006% was obtained for the Au-coated taper 3 as expected due to the optical losses described previously.

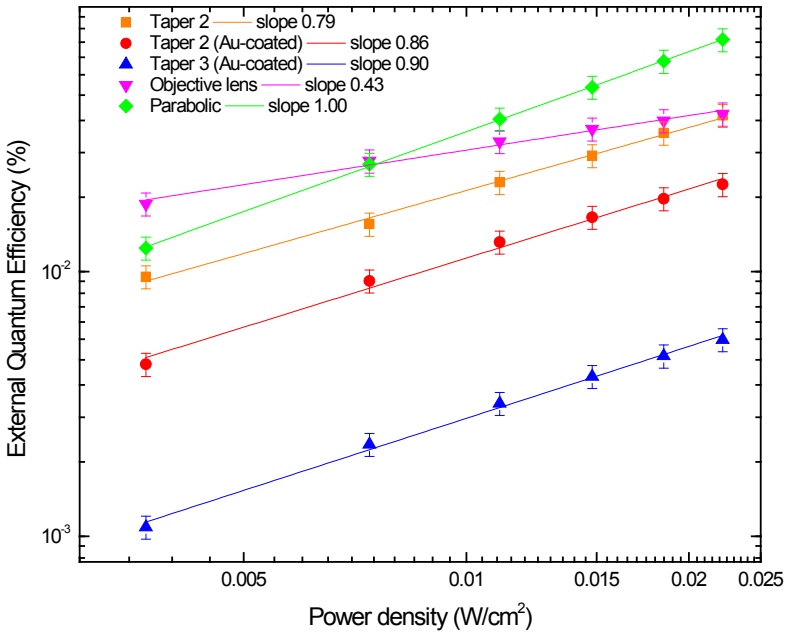

Figure 6.8: Power dependent EQE of the UC-SC device for the strongest resonant peak at 1522 nm. The slope of each least square fit indicates the order of the luminescence process involved on each device.

The power dependence of non-linear optical processes is commonly plotted on double logarithmic scales to extract information about the number of excitation photons involved in UC emission and consequently the order of up-conversion. In an UC-SC device, the up-conversion emitted photons are measured directly by the solar cell and follow a quadratic relation between I_{sc} and power density [165]. Therefore, the EQE follows a relation with power density expressed by Equation (2.22).

As shown in Figure 6.8, the slope of the least square fit is 1.00 for the UC-SC device with parabolic concentrator which agrees with Eq. (3) for $n = 2$, i.e. two-photon up-conversion. For the UC-SC devices with taper 2, Au-coated taper 2 and Au-coated taper 3, the slope is 0.79, 0.86 and 0.90 respectively which suggests that mechanisms such as excitation of higher energy levels, cross relaxation or amplified spontaneous emission are more probable and are competing with ETU and ESA [148]. The slope is reduced further from the theoretical down to 0.43 for the UC-SC system with objective lens with the highest concentration ratio of all devices in the study.

6.9 External quantum efficiency vs power density on the up-conversion phosphor

Although the EQE of each UC-SC device has been displayed in Figure 6.8 for equal incident power densities, the power density on the up-conversion layer should be quantified to indicate the achievable concentration that actually excites the up-converter. As shown in Figure 6.9, where the EQE is plotted as a function of the power density on the up-conversion layer (measured after the solar cell and the concentrating optics), the power density is adjusted for the lower and high-pump regimes. In particular, the power density achieved with the parabolic optics remains in the low-pump regime with slope 1.13 while the objective lens is at the high-pump regime with a slope of 0.53. It is noted that the output of the parabolic concentrator wasn't totally illuminated; therefore the power density is expected to be higher in the case of full illumination. Despite this, the EQE resulting from the parabolic concentrator indicates the suitability of the optics for collection of the emission back to the solar cell. Although the tapered optics achieve power densities as high as the objective lens, the slope remains on the low-pump regime with slope of 1.02 which can be explained by poor collection of the emission with a backwards transmission of 70% back to the solar cell.

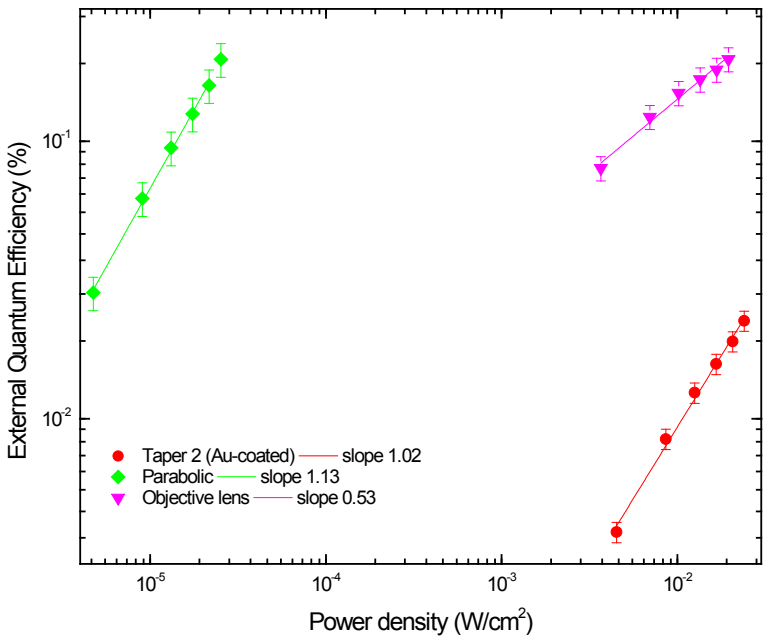

Figure 6.9: EQE of the UC-SC device for the resonant peak at 1522 nm at the up-conversion layer. The power density on the up-conversion layer and the respective regime, achieved by each concentrator, is indicated by the slope.

6.10 Irradiance profile exciting the up-conversion phosphor

By comparing the power density in Figure 6.9 with the power density from independent measurements [151] of the up-conversion quantum yield for the same up-conversion phosphor, it is shown that the slopes leading to saturation at the high-pump regime observed here appear in lower powers. While this power is an average of the achieved concentration at the up-conversion layer, the geometry of each concentrating optic is known to have a non-uniform profile [276] that may lead to much higher local power densities. This effect was investigated further by Monte Carlo simulations for the parabolic and tapered optics and is displayed in Figure 6.10.

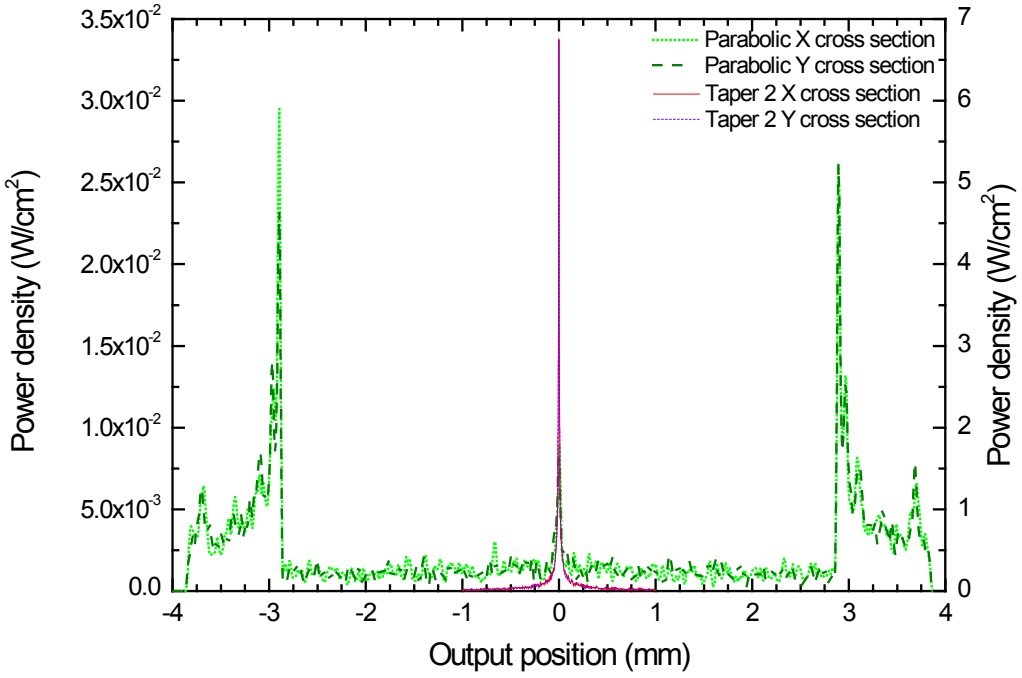

Figure 6.10: Irradiance profile at the output of the parabolic and the tapered optics. Localised peak concentrations are observed for both, that are responsible for the gradient of the least square fits in Figure 6.8 and Figure 6.9.

As shown in Figure 6.10, the irradiance profile at the output of the parabolic concentrator is uniform at the centre, but exhibits local concentration towards the edges of the aperture that reach power densities as high as $3x10^{-2}$ W/cm^2. Highly local concentration is also displayed for the tapered concentrator, at the centre of the exit aperture with values as high as 6.50 W/cm^2. An experimental demonstration wasn't

allowed, due to distortion of the output profile measured with an IR camera, originating from the optics used to expand the laser beam. An irradiance profile similar to the taper is expected also for the objective lens. Again, this could not be verified experimentally due to the aforementioned reasons and additionally due to the high *NA* of the objective lens.

6.11 Discussion

For increasing power density at the up-conversion layer, an inverse relation is observed for the slope, *i.e.* the order of up-conversion. It is known that for incident power densities in the high-pump regime (1000 W/m^2,) the slope of the relationship between power density and the UC emission is 0.35 [169]. Thus, for a given system, the EQE can saturate at a certain high value of power density. These findings agree very well with my results. Higher power densities at the up-conversion layer, are also associated with a higher up-conversion quantum yield [151, 183]. Therefore, where lower slopes do not correlate with a higher EQE (as is the case for tapered optics) this is a sign of optical losses in backward transmission. However, the results confirm the initial hypothesis for independent optimisation of the sub-band-gap photons, since for a constant power density incident on the UC-SC device, the concentration on the up-conversion layer can be optimised to levels that maximize up-conversion.

The normalised EQE (NEQE) for the highest power density of 0.022 W/cm^2 is listed in Table 6.1 for the five devices of the study along with the UC-SC devices based on Er^{3+} found in literature for comparison. A value of 3.38×10^{-2} cm^2/W was calculated for the device using the parabolic concentrator. The NEQE of the device in this work is comparable with the other devices found in literature [164-166, 169, 182, 277]. The NEQE of the device without any concentrating optics was 13.15×10^{-2} cm^2/W, higher than the NEQE of the best UC-SC device of the study with the parabolic concentrator, which reflects the optical losses discussed previously.

The EQE values reported in this study are low for a functional UC-SC device, however they were acquired with integrated optics that have not been optimised for forward and backward transmission. Despite this, the proof-of-principle experiments have shown that the presented devices enhance the sub-band-gap response of a silicon solar cell without prior concentration.

Table 6.1: Comparison of UC-SC devices based on Er^{3+} with absolute and normalised EQE.

	UC phosphor	λ (nm)	EQE (%)	W/cm^2	NEQE (cm^2/W)	Reference
	$NaYF_4$:20%Er^{3+}	1523	2.500	-	-	[165]
	$NaYF_4$:20%Er^{3+}	1523	3.400	2.400	1.400×10^{-2}	[166]
	$NaYF_4$:20%Er^{3+}	1522	0.340	0.109	3.000×10^{-2}	[169]
	CaF_2YF_3:5%Er^{3+}	1540	2.400	100	0.024×10^{-2}	[277]
	BaY_2F_8:30%Er^{3+}	1557	5.100	2.400	2.100×10^{-2}	[164]
	$NaYF_4$:20%Er^{3+}	1508	1.790	0.100	17.900×10^{-2}	[182]
$NaYF_4$:Er^{3+}	Taper 2	1522	0.038	0.022	1.750×10^{-2}	This study
	Taper 2 (Au-coated)	1522	0.021	0.022	0.960×10^{-2}	
	Taper 3 (Au-coated)	1522	0.005	0.022	0.240×10^{-2}	
	Objective lens	1522	0.039	0.022	1.770×10^{-2}	
	Parabolic	1522	0.075	0.022	3.380×10^{-2}	

There are several points signified by the results of this work that can be indicated for further optimisation of the UC-SC device:

- Transmission of the solar cell: The bifacial solar cell used in this study has exhibited poor spectral response at 980 nm and 42% transmission at 1522 nm. It is clear that with the current progress in solar cells for UC-SC devices with optimised reflection and transmission at the wavelength of excitation [272] and a reported NEQE of 17.9×10^{-2} cm^2/W [182], a significant enhancement of the NEQE is expected for the proposed UC-SC devices.

- Optics for excitation: The transmission of the concentrating optics in this study exhibited a direct effect on the EQE of the UC-SC devices. However, the optical elements used in this study were selected according to their concentrating properties and not the absolute transmission. Refracting and TIR optics displayed better performance to coated reflecting optics in this study, although the incident excitation reaching the up-converter depends on the irradiance profile and the localised concentration.

- Optics for UC emission: Concentrating optics are in general designed for forward transmission. In the case of the proposed UC-SC device the exit aperture of the optics is also the entry aperture for a source with isotropic emission (the up-conversion layer). Optics that fulfil the last property have been extensively studied [61] and lessons can be learned from the optics of light-emitting-diodes [278]. However, the backwards transmission of the parabolic optics was shown to be

superior to the other optics of the study, exhibiting efficient collection of the extended isotropic emission.

- Concentration ratio: It has been shown that the concentration ratio of the secondary integrated optics plays a significant role on the EQE of the UC-SC. Although low to moderate concentration levels can be adequate to maximize UC emission, higher concentration will populate higher energy levels and competing processes that lead to reduced up-conversion. In addition, the irradiance profile at the output of the concentrator can vary significantly from the geometric concentration and exhibits localised peaks that further enhance saturation effects. Finally this secondary concentration should be matched with adequate primary concentration at levels that maximize the efficiency of the PV layer. It is therefore envisaged that the elements that assemble the UC-SC device are optimised concurrently in order for this technology to have a direct effect.

6.12 Conclusion

In this chapter, concentrating optics were integrated in UC-SC devices to investigate the effect of independent solar concentration of sub-band-gap photons. The concentration was achieved by dielectric tapered, parabolic and imaging optics. The Au-coated tapers exhibit lower response compared to the uncoated as a result of the multiple reflections of the excitation before reaching the up-conversion layer. The UC-SC device with parabolic concentrators, results in the highest EQE of the study of 0.075%. This corresponds to a normalised EQE of 3.38×10^{-2} cm^2/W, achieved without prior concentration of the excitation incident on the device. This result indicates that solar concentration of the sub-band-gap photons can be independently optimised and represents a significant step for UC-SC devices towards integration in CPV systems.

Chapter 7 : Enhanced energy conversion of up-conversion solar cells by the integration of compound parabolic concentrating optics – influence of the excitation profile

7.1 Introduction

The comparative study [279] between imaging and non-imaging optics was presented in Chapter 6. This analysed the limitations of the former and identified the advantages of the latter for integration in UC-SC which are three-fold: i) concentration of transmitted photons through the solar cell to excite the up-conversion phosphor, ii) high transmission of the excitation over a broad range in the NIR, and iii) high collection efficiency of the isotropic emission from the up-conversion phosphor back to the solar cell. It is highlighted that the collection of the isotropic emission shares common traits with the restriction in the angle of emission. This has been conceptualised as another approach to overcome the limiting efficiency of solar cells [280, 281] by taking advantage of the external radiative emission of a solar cell [282, 283].

In this chapter the focus is brought on the properties of the best performing non-imaging optics as mentioned above and particularly in dielectric-filled compound parabolic concentrators (CPC). An artistic impression of the concept utilizing CPC in UC-SC is depicted in Figure 6.1(a). I proceed by investigating the questions of how the angle of acceptance of the CPC – and therefore the angle for the collection of the emitted luminescence – can enhance the EQE of an UC-SC in section 7.4 and how the EQE is affected by the incident power in section 7.5. Finally, the performance of an UC-SC is quantified *via* current-voltage (*I-V*) characteristics presented in section 7.6, the first ever reported for UC-SC based on c-Si to the best of the authors' knowledge.

This chapter expands on material from the following publications: **G.E. Arnaoutakis,** J. Marques-Hueso, A. Ivaturi, K.W. Krämer, S. Fischer, J.C. Goldschmidt, B.S. Richards, Enhanced energy conversion of up-conversion solar cells by the integration of compound parabolic concentrating optics. *Solar Energy Materials & Solar Cells,* 140, (2015), 217-223. **G.E. Arnaoutakis**, J. Marques-Hueso, K.W. Krämer, J.C. Goldschmidt, B.S. Richards, (2014, September). Up-conversion enhancement in photovoltaic devices *via* non-imaging optics. In *29th European Photovoltaic Solar Energy Conference and Exhibition*. Amsterdam, the Netherlands.

7.2 Experimental details

7.2.1 Monte Carlo simulations and ray-tracing

A three-dimensional model based on ray optics and Monte Carlo simulations (Optis, Optisworks) was used for spatially resolved considerations, where the entry aperture of the CPC was illuminated with the maximum power available in the experimental configuration transmitted through the solar cell. The up-conversion phosphor coupled at the exit aperture of the CPC was also modelled with optical properties taken from references [237, 284].

7.2.2 Current-Voltage (I-V) characteristic measurements

A schematic of the UC-SC and the optical setup used for characterisation is shown in Figure 7.1. Illumination between 1450-1590 nm from a NIR tuneable laser (HP-Agilent, 8168-F, 6 mW at 1523 nm) was used, fibre-coupled, and collimated. This resulted in a beam of second moment width (*d4σ)* 4.2 mm and divergence of 0.02°, spatially characterised by a NIR camera (Electrophysics, Micronviewer 7290A), and the power measured with a calibrated germanium photodiode (Newport, 818-IR). A source-meter (Keithley Instruments, 2440-C) was used to measure the *I-V* characteristics of the UC-SC, as well as the photo-generated short circuit current (I_{sc}) to determine the EQE.

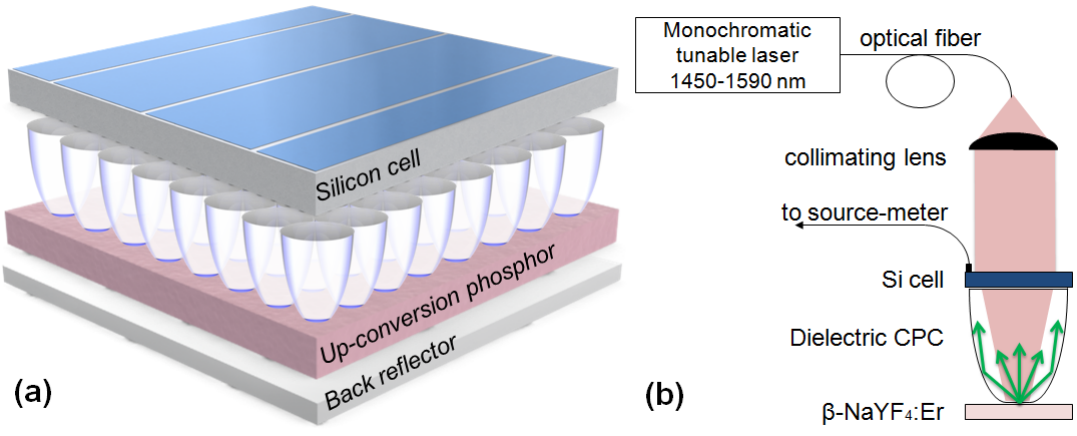

Figure 7.1: (a) Artistic impression of the UC-SC with a regular two-dimensional array of integrated CPC optics. The gaps between the layers are only for illustrative reasons. (b) Schematic and optical setup used for characterisation. The three-fold role of the optics – concentration, broadband transmission of the excitation (light red beam) and coupling of the isotropic emission (green arrows) – is depicted.

7.2.3 Bifacial planar solar cells optimised for up-conversion

The UC-SC were based on planar bifacial solar cells fabricated on silicon wafers (1 Ωcm, 200 µm-thick, *n*-type float zone) with aluminium oxide (Al_2O_3) surface passivation on both front and rear surfaces. The solar cells feature anti-reflection coatings (ARC) optimised for high transmittance of sub-band-gap photons, with a double layer ARC (110 nm hydrogenated silicon nitride (a-SiN_x:H) and 110 nm magnesium fluoride (MgF_2) on the front and a single layer ARC (120 nm a-SiN_x:H) on the rear. This yielded a solar cell that exhibited an excellent EQE for rear-side illumination with 980 nm. A detailed description of the solar cells, their performance and optimisation is beyond the scope of this chapter and can be found elsewhere [272].

7.2.4 Compound Parabolic Concentrating Optics

Two geometries of CPC (Edmund Optics) were used with acceptance angles of 25° and 45°, denoted as CPC-25° and CPC-45° henceforth, with entry apertures of 9.01 mm and 5.39 mm, lengths of 19.93 mm and 7.52 mm, respectively, and an exit aperture of 2.5 mm for both. The dielectric used for both CPC was B270 borosilicate glass, without ARC deposited on any of the apertures other than a refractive index matching liquid (Cargille, L-RIA-766, n=1.53 at 589.2 nm) for optical coupling between the elements.

Although it has already been suggested that the CPC may be combined with a lens of positive focal length as a primary optic on the solar cell [61, 279], this aspect is part of further system integration [188, 285] and will not be considered in this chapter. Therefore, all experiments in this chapter are performed with the illumination at normal incidence despite the wider acceptance angle of the optics.

7.3 Spatial distribution of power

The irradiance profile at the exit aperture of the two CPC geometries is displayed in Figure 7.2, as obtained by Monte Carlo simulations. The average power density at the input and output is 0.019 W/cm^2 and 0.053 W/cm^2, respectively, for both CPC. This corresponds to a geometrical concentration C_{geo} of 2.79× and an optical transmission above 98%.

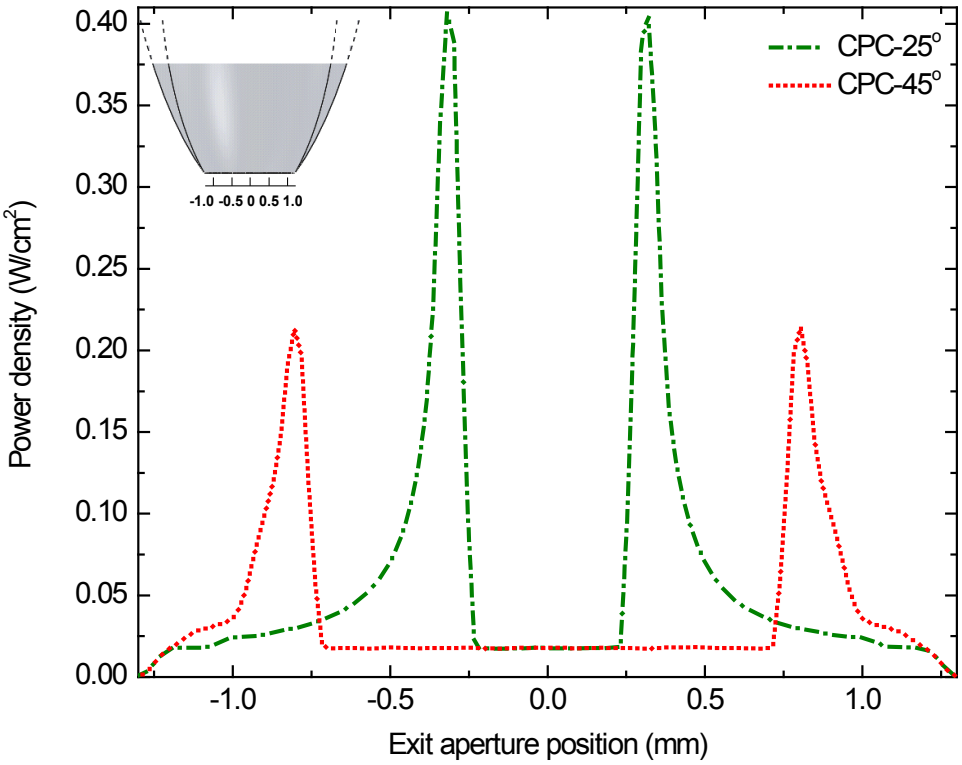

Figure 7.2: Distribution of the power density at the exit aperture of each CPC under normal incidence. The CPC are illuminated with light of 1523 nm and at the maximum power available in the experiment after transmission through the solar cell (0.019 W/m^2 or 7 suns). The cross section of the two CPC, indicating the exit aperture at the x-axis, is shown in the inset.

It can be seen that for both CPC the profile is uniform around the centre of the exit aperture, as expected for rays transmitted without reflection on the side of the parabola. Localised peaks that maximize towards the edges of the exit aperture are also observed due to the characteristic concentration profile of the parabolas. For the CPC-45^o the local maxima of 0.21 W/cm^2 are at ±0.80 mm from the centre, while for the CPC-25^o the maxima of 0.41 W/cm^2 are observed at ±0.32 mm.

The CPC-25^o exhibits higher maxima than the CPC-45^o as a result of the curvature of the 45^o parabola reflecting more rays towards the edges of the aperture. To explain this aspect it is informative to mention that the CPC is designed according to the edge-ray principle. Subsequently, all the incident rays at the maximum (designed) acceptance angle are being reflected at the parabola and focused at the edge of the exit aperture. For a given design, as the condition for acceptance is relaxed and the angle is approaching normal incidence, the distribution of rays is deviating from the edge towards the centre

of the exit aperture. In other words, the parabola of the CPC-45° is more abrupt in relation to the exit aperture than the CPC-25° (see inset in Figure 2). Therefore, for rays perpendicularly incident on the parabola of the CPC-25°, the angle of reflection would be higher, consequently concentrating more rays towards the centre of the exit aperture compared to the CPC-45°.

An example of this behaviour can be seen in Figure 7.3 where (a) CPC-45° and (b) CPC-25° are illuminated from a source with the same number of rays and angular distribution.

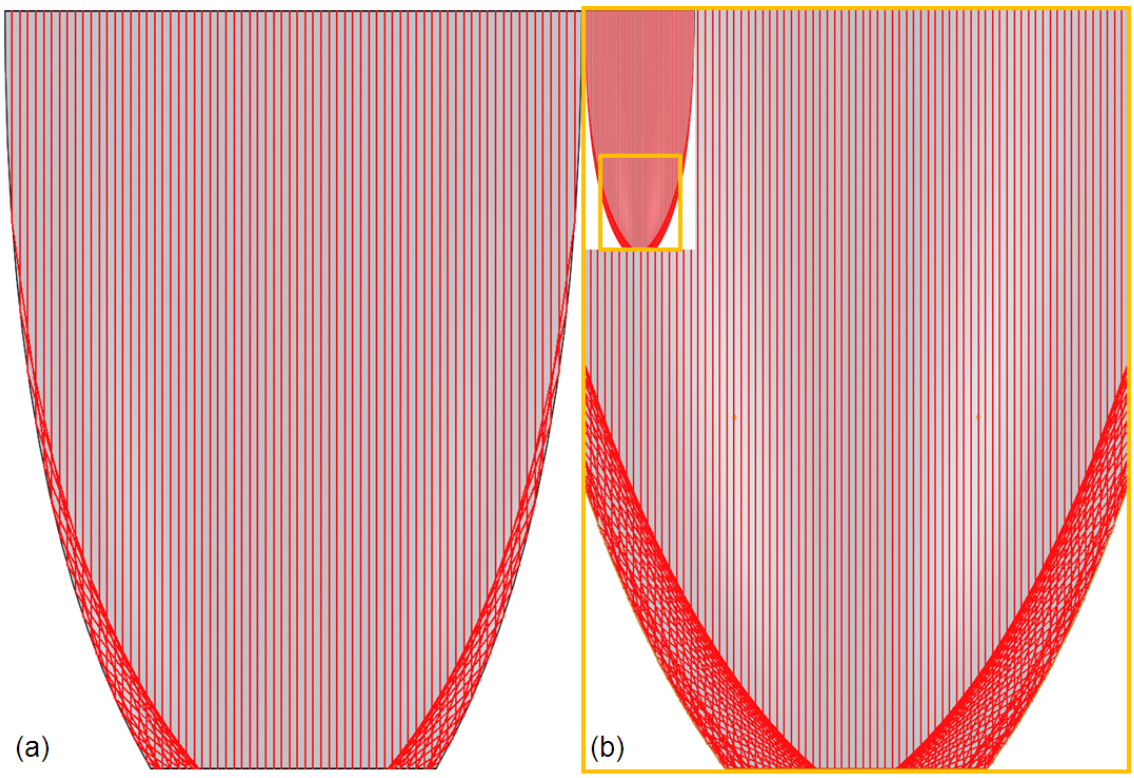

Figure 7.3: Ray-tracing diagrams of the (a) CPC-45° and the (b) CPC-25°. A higher distribution of the light in the centre of the aperture can be seen for the CPC-25° compared to the CPC-45° as a result of higher angle of reflection on the parabola of the former optics.

Following this notion, the acceptance angle can be further reduced to result in even higher local concentration. Additionally, the exit aperture is further reduced, while keeping the entry aperture constant to allow for comparison with experimental data in this configuration. It is noted that smaller angles and exit apertures will result in longer optics that can be further optimised *via* truncation, however to illustrate the purposes of

the current design these will not be considered here. Figure 7.4 shows the irradiance profile at the exit apertures of two CPC with acceptance angles of 4° and 2°, and exit apertures of 200 μm and 100 μm, respectively (CPC-4° and CPC-2°). The localised peaks are observed at the centre of the exit aperture for both CPC as expected. Output peak power densities of 530 W/cm^2 and 3,240 W/cm^2 are obtained while the average power densities are 11.92 W/cm^2 and 41.95 W/cm^2 from the CPC-4° and CPC-2°, respectively. From Equation (2.24) this would result in solar concentration C_{exc} of 4,250 suns for the CPC-4° and 14,980 suns for the CPC-2°. Although, this solar concentration is more than 200× higher compared to the power density of the CPC-25° and CPC-45°, additional factors will affect the performance of the UC-SC. This aspect is analysed in the following sections along with the expected enhancement in EQE.

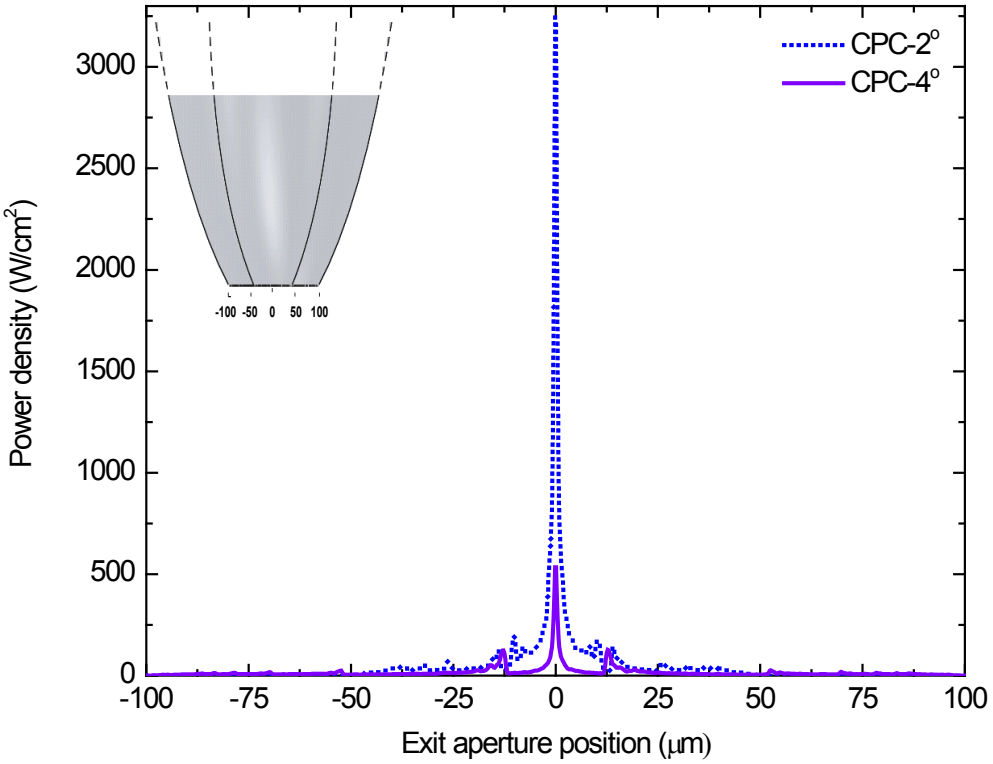

Figure 7.4: Distribution of the power density at the exit aperture of CPC-4° and CPC-2° with apertures 200 μm and 100 μm, respectively. The illumination and modelling conditions are identical to these of Figure 7.2 to allow for direct comparisons. The cross section of the two CPC, indicating the exit aperture at the x-axis, is shown in the inset.

The resultant spatial distribution with the assigned localised peaks will excite the up-conversion phosphor non-uniformly, subsequently altering the rate of transitions

between energy levels and more importantly the energy transfer between Er^{3+} ions. However, it has been analytically and numerically confirmed [286] that even for non-linear processes such as up-conversion, a good approximation can be derived for a Gaussian beam with a uniform beam of cylindrical radius and equal beam waist. The latter was also validated in respect to the incident pump power with insignificant effect on the UC emission [148]. This can be determined *via* power dependent characterisation of the UC-SC and is discussed further in section 7.5.

7.4 External Quantum Efficiency

Figure 7.5 shows the EQE of the UC-SC without any optics and with concentrating optics of two different geometries as function of wavelength between 1450-1590 nm and power density of 0.01 W/cm^2.

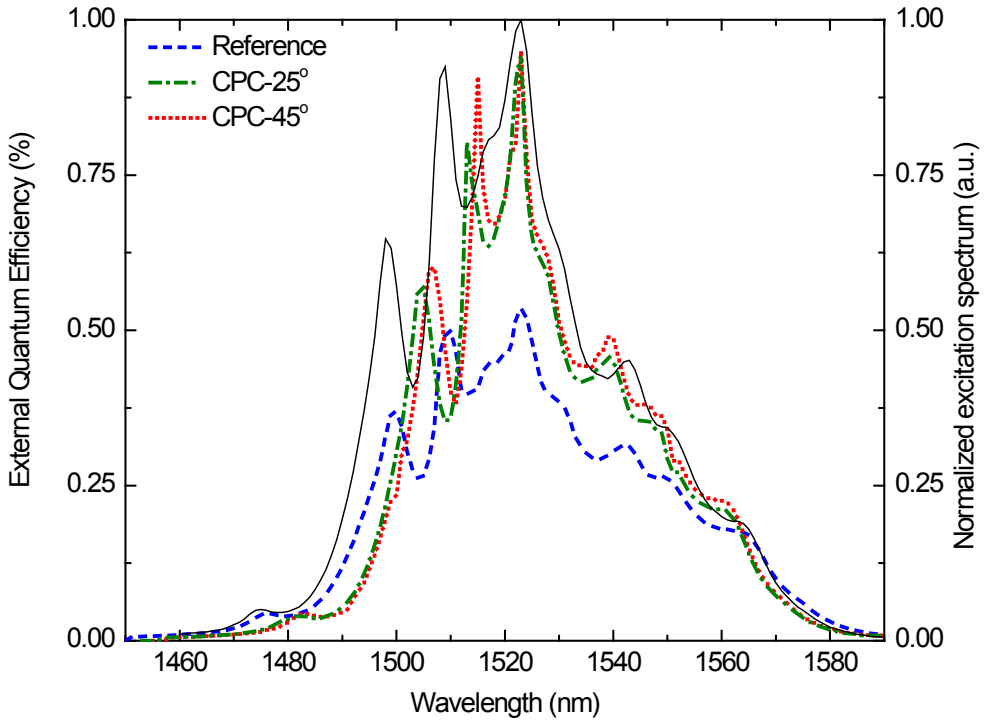

Figure 7.5: EQE of the UC-SC without (reference) and with two different CPC geometries characterised at 0.01 W/cm^2. The shift of the peaks between the UC-SC is an artefact of the software used for acquisition of the spectra. The excitation spectrum of the $^4I_{11/2}$ to $^4I_{15/2}$ UC emission for $^4I_{15/2}$ to $^4I_{13/2}$ excitation of β-$NaYF_4$:25%Er^{3+} is also plotted for comparison.

The highest EQE is obtained at the peak wavelength of the $^4I_{15/2}$ to $^4I_{13/2}$ excitation of β-$NaYF_4$:25%Er^{3+} at 1523 nm. For all measured solar cells the EQE agrees with the $^4I_{11/2}$ to $^4I_{15/2}$ UC emission spectrum of β-$NaYF_4$:25%Er^{3+} also plotted in Figure 4 for comparison. This can be one of the indications that the dominant mechanism for depopulation of $^4I_{13/2}$ is ETU between Er^{3+} ions. For the main peak at 1523 nm the CPC devices exhibit similar EQE, while for the weaker peaks the solar cell with CPC-45° has higher EQE than the CPC-25°.

Spectral narrowing of the weaker peaks is observed for the UC-SC with CPC. This suggests that the concentrating effect of the optics effectively alters the macroscopic excitation profile (shown in Figure 7.2) and affects the probability of ETU on the microscopic level. Shifting is observed for the UC-SC with CPC-45° (3-8 nm) and smaller for the UC-SC with CPC-25° (1-6 nm) which is an experimental artefact of the software used for acquisition of the spectra. The spectral shape of the up-conversion excitation spectrum varies with increasing excitation power since excited state populations increase and also higher lying Stark levels are populated due to a rising sample temperature [287]. Accordingly, UC emissions from the higher lying $^4F_{9/2}$, $^4S_{3/2}$, and $^2H_{11/2}$ states, populated by more than two photon processes [133], contribute to the photocurrent of the silicon solar cell. Intense green luminescence due to the $^2H_{11/2}$ and $^4S_{3/2}$ to $^4I_{15/2}$ transitions was observed by naked eye under the characterisation conditions of 0.01 W/cm^2 reported here, which corroborates the latter hypothesis.

Although the EQE of the UC-SC in Figure 7.5 was obtained at a constant incident power density of 0.01 W/cm^2, the power density exciting the up-conversion phosphor varies locally according to the concentration achieved by the CPC optics, see Figure 7.2. As discussed in the previous section, despite that the average power density is equal for both CPC, the maximum local power density for the UC-SC with the CPC-25° is significantly higher than this of the CPC-45°. Consequently, a higher EQE was expected for the UC-SC with CPC-25°. For increasing power density however, saturation of the EQE is also expected [165, 169], which is evidenced by the observed response at the abovementioned power density. Nevertheless, due to the non-linear nature of up-conversion and hence UC-SC, a power dependent characterisation is required to investigate for lower and higher pump regimes. This follows in the next section.

7.5 Power dependence

The EQE as a function of incident power is displayed in Figure 7.6 as open symbols for the reference and the UC-SC with integrated CPC. In the low power regime (0.0047-0.028 W/cm^2) the EQE is enhanced for both CPC devices by a factor of 2.7× from 0.13% to 0.37% and 0.35% for the reference UC-SC compared to the CPC-25^o and CPC-45^o, respectively. The enhancement is lower for the high power regime (0.028-0.057 W/cm^2) from 1.33% to 1.58% and 1.80%, respectively. Due to the additional power density on the up-conversion material from the concentration of the integrated optics, the EQE saturates faster at high pump power for the UC-SC with CPC. A stronger pump power populates higher energy levels of erbium and increases the probability of processes competing with ETU [148].

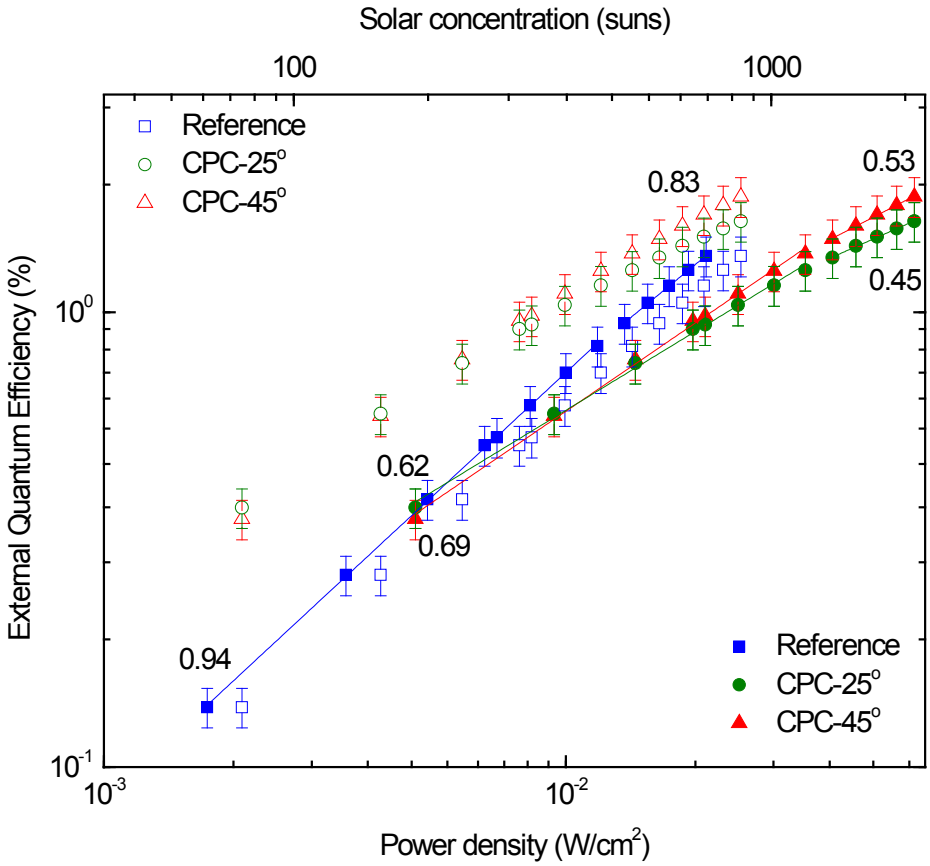

Figure 7.6: EQE of the UC-SC for the strongest excitation peak at 1523 nm as a function of incident power and monochromatic solar concentration on logarithmic scales. Open symbols correspond to values of power incident on the UC-SC, while solid symbols to power incident on the up-converter. Enhancements of 2.7× are observed in the low power regime and 1.3× in the high power regime of the UC-SC. The slopes of the curves for the various power regimes are given for the three experimental configurations.

To further analyze this effect, the power density incident on the UC-SC needs to be normalised to the power concentrated by the optics, consequently exciting the up-converter. This is displayed in Figure 5 as solid symbols. The maximum equivalent solar concentrations from Equation (2.24) are 740 suns and 2090 suns for the reference and the CPC devices, respectively. These C_{exc} are high because the monochromatic irradiance $P_{AM1.5D}$ was used at 1523 nm. After normalisation of the power density the high power regime of the reference overlaps with the low power regime of the UC-SC with integrated optics. A lower EQE is observed at the low-pump regime of the CPC devices that at this excitation power overlaps with the high-pump regime of the reference.

According to Equation (2.23) for a purely two-photon process an exponent equal to 1 is expected. But the slope for the reference starts from 0.94 in the low power regime and decreases to 0.83 in the high power regime, while even lower slopes are observed for the CPC devices. In particular, in the low power regime the slopes are 0.62 and 0.69 for CPC-25^{o} and CPC-45^{o} and change to 0.45 and 0.53 in the high power regime, respectively. The reduced slopes relate to the change in population at the high-pump regime, involving higher order processes and cross relaxation, which compete with ETU and excited state absorption.

For the same incident power on the UC-SC, the power exciting the up-conversion material depends on the concentration achieved by the CPC. Since the beam size and exit aperture for both CPC are equal, the geometrical concentration factor is 2.79×; a value that agrees well with the observed enhancement of the EQE in the low power regime. However, the CPC-25^{o} locally concentrates the excitation beam up to 0.41 W/cm^2 which is twice the value obtained for the CPC-45^{o}, see Figure 2. This can explain the lower slope of CPC-45^{o} in the high power regime of Figure 5.

An equation of the form EQE = $a + b\,P^n$, where a and b are fitting parameters, was used to fit the experimentally obtained EQE of the CPC-25^{o} UC-SC which exhibits the highest saturation. Furthermore, the expected EQE by extrapolating to power densities of 11.92 W/cm^2 (4,250 suns) and 41.95 W/cm^2 (14,980 suns) for the CPC-4^{o} and CPC-2^{o} presented in section 7.3 could be estimated. An enhancement in EQE of 5.4% and 8.9% is obtained, respectively. This shows not only that levels of concentration C_{exc} of 10^4 suns, corresponding to C_{inc} of 6.78 suns from Equation (2.26) are required, but also

that substantial improvements can be achieved by the blending of concentrating systems with UC-SC.

The normalised EQE (NEQE) is usually calculated for comparison with UC-SC in the literature. It has to be mentioned, however, that the NEQE is not totally independent from the excitation power density. For the highest incident power of 0.024 W/cm^2 the NEQE were 0.55 cm^2/W for the reference UC-SC, 0.75 cm^2/W for CPC-45^o, and 0.66 cm^2/W for the CPC-25^o device. These values are in the range of the normalised ePLQY of the up-conversion material for which a value of 0.67 cm^2/W was determined from photoluminescence measurements [151], albeit three times higher than the NEQE values from the recent work by S. Fischer *et al.* [182], the highest reported NEQE so far to the best of the authors' knowledge. The latter NEQE was obtained for an UC-SC utilizing the same up-conversion phosphor but a lower phosphor to polymer ratio (75.7 w/w%) and an excitation at 1508 nm with 0.1 W/cm^2. Thus the values cannot be compared directly with our results. Nevertheless, it underlines the substantial improvements that can be obtained by concentration and photonic management.

7.6 Current-Voltage characteristic

For a more comprehensive characterisation of the performance of a solar cell, the *I-V* characteristic is required to indicate equilibrium conditions between photons and carriers as well as the origin of losses in the device [288]. This was measured for the aforementioned UC-SC and is displayed in Figure 7.7 with the performance parameters short-circuit current (I_{sc}), open-circuit voltage (V_{oc}), fill factor (FF), and efficiency (η) summarised in Table 7.1. For all the presented UC-SC, the I-V characteristics were measured under dark conditions, and only 1523 nm illumination at incident irradiance of 0.024 W/cm^2 was used.

The current from the un-doped reference solar cell with an undoped β-$NaYF_4$ sample is shown to be negligible. Under sub-band-gap illumination, the I_{sc} is mainly affected by dark current. The additional I_{sc} resulting from UC photons is 0.054 mA for the reference UC-SC, and 0.065 mA and 0.066 mA for the UC-SC with CPC-25^o and CPC-45^o optics, respectively. The difference between I_{sc} and dark current confirms the origin of the increased I_{sc} from up-conversion in Er^{3+}.

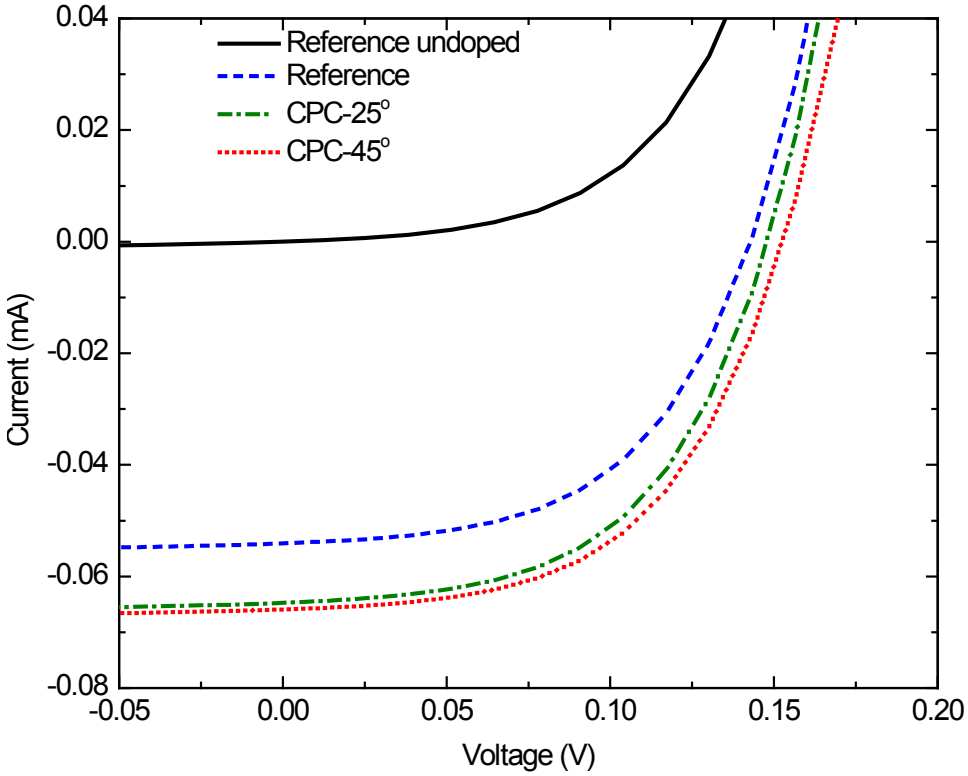

Figure 7.7: Current-voltage characteristics of the UC-SC under illumination of 1523 nm at 0.024 W/cm^2. The additional I_{sc} for the UC-SC with concentrating optics is displayed over the reference, while the negligible I_{sc} from the undoped reference solar cell is also displayed.

The V_{oc} are 0.136 V, 0.145 V, and 0.153 V for the reference, CPC-25°, and CPC-45° UC-SC, respectively. Albeit quite lower than the expected V_{oc} of a good silicon solar cell under AM1.5G illumination (approx. 0.7 V), these values of V_{oc} result from the low I_{sc} of the UC emission. The reference, CPC-25°, and CPC-45° UC-SC exhibit *FF* of 55.38%, 54.35%, and 53.21%, respectively. Since the same silicon cell is used for all UC-SC configurations, losses due to series and shunt resistance between silicon and contacts as well as the *p-n* junction [289] are not expected to contribute to the reduced *FF*. Moreover, the *FF* of the silicon cell was independently measured under AM1.5G conditions and was determined to be as high as 80% [272]. The low *FF* of the UC-SC presented here are thus attributed to the low illumination conditions. Accordingly, under the conditions of the intended solar application, the solar cell would perform at a V_{oc} as high as 0.7 V. An increased V_{oc} can be expected therefore from the UC-SC, given the contribution of the I_{sc} from the up-conversion additionally to the I_{sc} from photons above the band-gap.

Table 7.1: Performance parameters of the UC-SC corresponding to the *I-V* curves in Figure 7.7 characterised in the dark, under illumination of 1523 nm at an irradiance of 0.024 W/cm^2.

UC-SC	I_{sc} (mA)	V_{oc} (V)	*FF* (%)	η (%)
Reference	0.054	0.136	55.38	0.123
CPC-25^o	0.065	0.145	54.35	0.154
CPC-45^o	0.066	0.153	53.21	0.163

The efficiency, also displayed in Table 7.1, is extracted from the I-V characteristics and translates to 0.123% for the reference while for the CPC-45^o and CPC-25^o it is 0.163% and 0.154%, respectively. It has to be mentioned however that the presented efficiencies should be considered in relation to the absolute efficiency of the overlying silicon solar cell. Since this efficiency under one sun AM1.5G conditions is 17.6% [182], the presented UC-SC efficiencies display clearly the contribution of the up-converter alone and after the enhancement of the concentrating optics. The efficiency improvement achieved by the concentrating optics is marginal compared to the improvement in EQE. This again indicates that the UC-SC is operating at low illumination conditions, *i.e.* the emission from the up-conversion phosphor. At these conditions the additional I_{sc} from the concentrating optics affects only marginally the *FF*, the V_{oc} and therefore the efficiency. This performance aspect is made apparent by characterizing the UC-SC under open circuit conditions. In fact, characterisation so far has been mainly limited to short-circuit conditions, consequently limiting a complete evaluation of the performance of UC-SC. Although another step towards a comprehensive characterisation of UC-SC was presented here, additional steps can be foreseen. The effect of sub-band-gap photons along with the photons above the band-gap should be considered in these steps, to exhibit the higher V_{oc}, *FF* and η. Such steps may comprise of characterisation under the standard AM1.5G conditions where solar cells are commonly characterised, and finally under the ambient solar spectrum.

Nonetheless, these results are quite encouraging for UC-SC and highlight that considerable improvement can be gained via concentration and photonic management. Further improvements are expected by optimisation of the collecting properties of the CPC and merit further investigation to indicate the limits of the current design. In

addition, advances in two-photon lithography enable three-dimensional fabrication of CPC structures in the micro-scale [290] opening routes for thin-film UC-SC [158].

7.7 Conclusion

It can be concluded that integration of CPC optics in UC-SC can significantly enhance the EQE. An increase is reported from 1.33% to 1.80% under an excitation of 1523 nm at an irradiance of 0.024 W/cm^2. This improvement is achieved by the concentration of the excitation on the up-conversion phosphor and also efficient collection of the UC emission. Due to the non-linear relation of up-conversion with power, the concentration has an optimum regime where up-conversion luminescence is maximised and competing processes are minimised. This has been exhibited for the UC-SC without and with concentrating optics presented in this paper. Saturation of the EQE is displayed in power dependent measurements and underlines the requirements for photonic management in UC-SC. Increased I_{sc} and V_{oc} of the CPC enhanced UC-SC were also obtained from I-V characteristics. The effect of concentration after the solar cell in addition to the effect of the up-conversion phosphor in UC-SC was specified via this characterisation. This also indicates the performance parameters and the affecting factors that should be considered for further improvements. Additionally to the quantification of the EQE and I_{sc} being widely used in characterisation of UC-SC, the V_{oc}, FF and finally η provide a comprehensive performance rating. It can finally be suggested, that these performance characteristics should accompany future schemes, to identify routes for improvements and make UC-SC as competitive as other emerging solar cell technologies.

Chapter 8 : Up-conversion concentrating solar cells based on BaY_2F_8:30%Er^{3+} – influence of scattering

8.1 Introduction

In this chapter, concentrating UC-SC are investigated with BaY_2F_8:30%Er^{3+} as the up-conversion material. The two geometries of the compound parabolic concentrators presented in Chapter 7, with acceptance angles 25° and 45°, are utilised. As seen in Chapter 2, another promising up-conversion material for photovoltaic applications and c-Si is the BaY_2F_8:30%Er^{3+}. In this material system, Er^{3+} is again the rare earth of interest embedded in a fluoride host. What differs from the most efficient up-conversion materials, β-$NaYF_4$ and Gd_2O_2S presented in section 3.4.6, is its crystalline state. Its monoclinic structure results in a crystal of high purity that can be grown into long boules and minimum scattering due to the size of the crystal. When doped with Er^{3+}, this additionally results in a higher absorption coefficient and PLQY compared to the β-$NaYF_4$ and the Gd_2O_2S, as seen in section 2.10. For UC-SC, reduced scattering would increase transmission of the emission in the up-converter and the back reflector. Although the excitation has mainly been at a normal incidence, the conditions of the application are quite different. That is, either by the diurnal position between the sun and the solar cell, or the dilute irradiance profile of the concentrating optics. The question rises then on how would this irradiance affect the performance of the UC-SC at incident angles other than the normal. In this chapter, the effect of the back reflector in the I_{SC} of an UC-SC is assessed in section 8.3 and how the EQE is affected by the incident power density in sections 8.4 and 8.5. The conversion efficiency of an UC-SC is also quantified *via* current-voltage (*I-V*) characteristics presented in section 8.6 and the analysis of the identified geometrical losses is presented in section 8.7.

This chapter expands on material from the following publications: **G.E. Arnaoutakis** *et al.*, Up-conversion concentrating solar cells based on BaY_2F_8:30%Er^{3+}. *In preparation*.

8.2 Experimental details

A schematic of the studied UC-SC configurations is depicted in Figure 8.1. The geometrical losses were calculated *via* ray optics and Monte Carlo simulations (Optis, Optisworks) in three-dimensional models of the UC-SC configurations. This includes the optical properties of the CPC optics made of B270 and the up-conversion material from references [164, 239] that were incorporated in the model. The maximum power density available in the experimental configuration P_{exp} transmitted through the solar cell was used as the excitation at the peak absorption wavelength that is 1493 nm as,

$$P_{exc}(\lambda) = P_{exp}(\lambda) * T_{SC}(\lambda)$$

For the emission, the power P_{em} was calculated by considering the iPLQY of the up-conversion material at the main radiative up-conversion emissions 970 nm and 517 nm as,

$$P_{em}(\lambda) = P_{exc}(\lambda) * iPLQY(\lambda)$$

Ideal Lambertian scattering was considered for the isotropic emission in the up-conversion material, while the back reflectors were modelled as ideal specular and Lambertian.

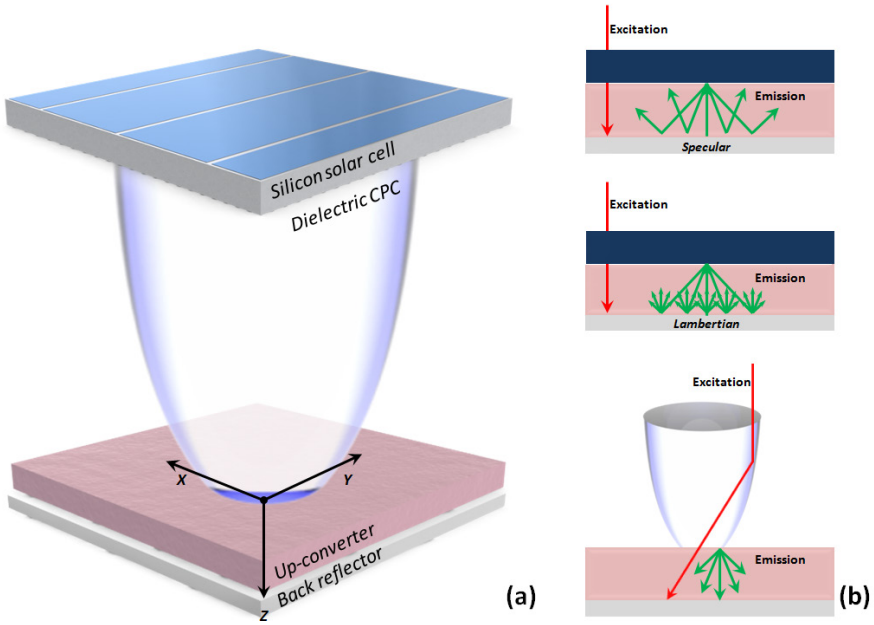

Figure 8.1: (a) Isometric view of a concentrating UC-SC. (b) Schematics of the UC-SC configurations investigated in this chapter. For the two top schematics the excitation is at normal incidence and the emission is reflected either by a specular or a Lambertian back reflector. For the bottom schematic, the up-converter is excited at oblique angles as a result of the concentrating optics.

8.3 Preliminary assessment of the back reflector

In an UC-SC, minimum scattering of the material should result in higher transmission, and hence longer propagation length, for the excitation and the emission. This makes the role of the back reflector more crucial compared to highly scattering material systems based *e.g.* on β-$NaYF_4$ and Gd_2O_2S. In fact, one of the initial investigations on UC-SC utilised evaporated silver as a specular and white paint as a diffuse reflector. The total absolute reflectance of silver was higher than that of the white paint. That is 99% for the silver, but only 90% and between 30-60% for the white paint [145], at the emission and excitation wavelengths, respectively. Despite the lower reflectance, diffuse reflectors such as PTFE were mainly utilised in UC-SC with up-conversion phosphors [291]. In particular, the diffusely back-reflected emission was expected to result in a minor contribution to the photocurrent. However, the additional photocurrent or the optical losses have not been quantified.

Besides the absolute reflectance of the back reflector, the directional reflectance is expected to affect the performance of an UC-SC. Diffuse Lambertian reflectors have been shown to enhance the EQE of TTA-UC solar cells [292, 293]. A two-fold enhancement was demonstrated with a back reflector consisting of 100 µm Ag-coated beads in comparison to a reflector-free configuration. Furthermore, a 3.6× possible enhancement was estimated with an ideal Lambertian layer, while only an enhancement of 2.6× was estimated with a specular reflector. The effect of the back reflector in the up-conversion material is governed by two aspects. The first relates to the probability of absorption connected to the path length, while the second relates to the power density of the excitation connected to the PLQY of the up-conversion material.

To investigate these aspects, in addition to PTFE back reflectors used previously, thin films of at least 100 nm Au and Cr, as an inexpensive alternative to Au, evaporated on fused silica slides were also used in this chapter. The back reflectors were applied directly at the back of the UC-SC with index matching liquid, without any concentrating optics. For the same illumination conditions at the highest power density of 0.021 W/cm^2 at 1493 nm the Au back reflector resulted in the highest photocurrent of 109 µA. The current of the UC-SC with PTFE and Cr was 106 µA and 88 µA, respectively. Therefore, Au and PTFE were further used for characterisation of the EQE and I-V.

8.4 External quantum efficiency

In Figure 8.2 the EQE of UC-SC was characterised in the range 1450 – 1590 nm with a resolution of 2 nm at 0.01 W/cm^2. Bifacial planar c-Si solar cells, as described in section 7.2.3, were also utilised here. Three UC-SC are displayed, the reference without concentrating optics, with the CPC-25^o and the CPC-45^o optics. In all configurations, Au was used as a back reflector. The EQE follows the line shape of the absorption coefficient of BaY_2F_8:30%Er^{3+}, with the main peak at 1493 nm for all three UC-SC configurations.

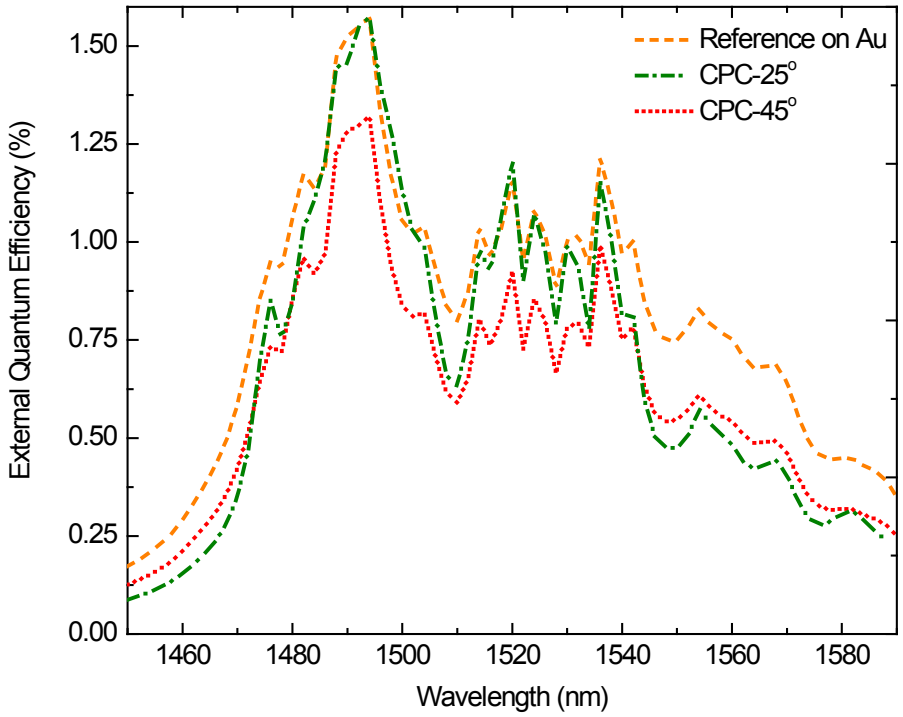

Figure 8.2: EQE of the UC-SC without (reference on Au) and with two different CPC geometries characterised at 0.01 W/cm^2. The EQE agrees with the absorption spectrum of the $^4I_{11/2}$ to $^4I_{15/2}$ UC emission for $^4I_{15/2}$ to $^4I_{13/2}$ excitation of BaY_2F_8:Er^{3+}.

It can be seen that at the main peak of 1493 nm the reference and CPC-25^o have an EQE of 1.57%, while the EQE of the CPC-45^o is 1.32%. Lower EQE of the CPC-45^o compared to the reference and the CPC-25^o can be also seen for the peaks at 1520, 1524, 1532 and 1536 nm. On the contrary, a different trend is observed for wavelengths between 1450-1472 nm and 1544-1590 nm. These bands match with the absorption tails

of the up-conversion crystal. At this range, the UC-SC with CPC-45^{o} performs better than the CPC-25^{o}.

On the one hand, this is a result of a higher absorbance in the reference UC-SC, 99% compared to 95% for the CPC-enhanced, see section 8.7. On the other hand, the higher localised power density of the CPC-25^{o}, *cf.* Figure 7.2, induces a higher PLQY on the up-converter equally across the excitation spectrum than the CPC-45^{o}. This is the case for the EQE at the abovementioned absorption peaks.

At the absorption tails, however, the excitation propagates a longer path length in the material. The propagation is retro-reflected back towards the solar cell, followed by emission and resulting in the high EQE of the reference UC-SC. But for the CPC-25^{o} with wider cone at the exit aperture than the CPC-45^{o} this further results in propagation towards the peripheral facets. Since the emission transmitted through these facets is not coupled back to the solar cell, a reduced EQE is measured.

In other words, the EQE of the UC-SC is a trade-off between the localised power density, the absorption path length in the material and the geometrical loss from the solid cone at the exit of the concentrating optic. This is clearly demonstrated for the CPC-25^{o}, the higher localised power density results in an EQE higher than the CPC-45^{o} only at the main peaks, where a short absorption path length does not lead to further geometrical losses. The path length and the geometrical losses of the configurations are quantified in section 8.7. For the same configuration, one could consider that there is one wavelength where the power density of the excitation is optimised. Equivalently, for the same wavelength there would be a single power density that the UC emission towards the solar cell is optimised. To further investigate this consideration, the power dependence of the UC-SC was analysed and presented in the following section.

8.5 Power dependence

The EQE of the three UC-SC is presented in Figure 8.3(a), where the UC-SC were excited by 1493 nm illumination. Additionally, the reference UC-SC with a back reflector of PTFE is displayed. The EQE of the configurations is presented as open symbols for the power density on the SC and as solid symbols for the power density concentrated by the CPC optics and exciting the up-conversion material.

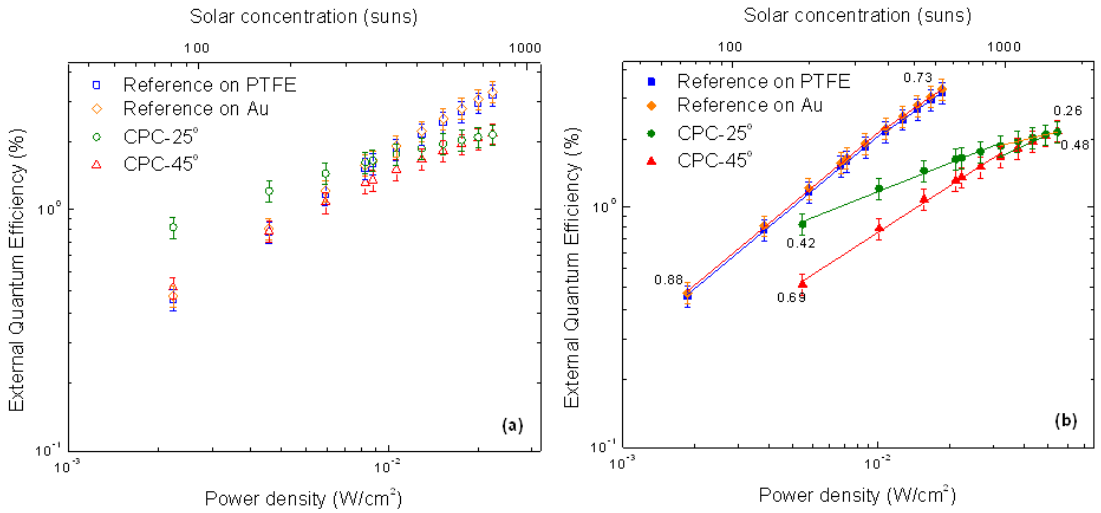

Figure 8.3: EQE of the UC-SC for the strongest excitation peak at 1493 nm as a function of incident power and equivalent solar concentration on logarithmic scales. (a) The EQE (open symbols) for the incident power on the UC-SC. While in the low power regime enhancements of 1.95× are observed with the concentrating optics, in the high power regime the EQE of the reference UC-SC is higher by 1.5×. (b) The EQE for power incident on the up-converter (solid symbols). The slopes of the curves for the various power regimes are given for the four configurations.

The reference UC-SC with PTFE and Au back reflectors have similar EQE within the experimental error along the power density regimes investigated herein. This is an EQE of 1.55% and 1.60% for the reference on PTFE and Au, respectively, in the low pump regime. A maximum EQE of 2.98% and 3.08% was measured respectively at a power density of 0.021 W/cm^2. The PTFE and Au back reflectors have two main differences. The former has a higher absolute reflectance over the investigated wavelengths in comparison to the latter. However, the directional content of this reflectance is mostly diffuse and spread over a full hemisphere, while for Au this reflectance is mainly specular. This could explain the relatively higher EQE of the reference UC-SC with Au back reflector over the PTFE.

The EQE is quite different for the UC-SC with concentrating optics. For both configurations an Au back reflector was used, while the EQE with a PTFE reflector, not shown in Figure 8.3 for clarity, was similar. The CPC-25^o has 1.2× higher EQE than the CPC-45^o in the low pump regime, 1.60% and 1.33% respectively. But for the CPC-25^o the EQE saturates to 2.04% in the high pump regime, similar to the latter UC-SC with 2.06%.

It is clear that at this excitation wavelength, the EQE of the UC-SC is enhanced by the CPC-25^{o} concentrating optics only at the low pump regime, until 0.009 W/cm^2. Beyond this power density the additional concentration does not result in additional photocurrent in the overlying solar cell. This could be attributed to a loss of photons, on one hand from population of higher energy levels and subsequent depopulation through non-radiative processes. The population can be in part investigated by the power dependence on the up-conversion crystal. On the other hand, a reduced photocurrent may originate from loss of photons towards directions other than the SC. For the CPC-enhanced UC-SC, where the excitation and the emission are reflected at other than normal incidence, optical losses may occur through the peripheral facets of the crystal. The effect of these losses would be analysed and quantified in section 8.6.

The power dependence of the UC-SC, after normalising to the power density on the up-conversion crystal, is displayed in Figure 8.3(b) by the least square fits of the solid symbols. From Equation (2.24), this power density relates to a maximum equivalent solar concentration of 657 suns and 1853 suns for the reference and the CPC devices, respectively. The theoretical slope for a two-photon process from Equation (2.22) is equal to 1. At the low pump regime a slope of 0.88 is calculated for the reference UC-SC. This slope is decreased to 0.73 at the high pump regime, indicating the increasing influence of processes competing with ETU and ESA by population of higher energy levels.

The slope of the CPC-25^{o} is 0.42 at the low pump regime and 0.26 at the high pump regime. For the CPC-45^{o} the slopes are 0.69 and 0.48 at the low and high pump regimes, respectively. As analysed in section 7.3, the CPC-25^{o} has a local concentration of 0.41 W/cm^2 when the respective value for the CPC-45^{o} is 0.21 W/cm^2, see Figure 7.2. This consequently results in the difference in EQE between the two UC-SC and the slopes. However, the slopes for the concentrating devices, relating to the order of the up-conversion process, are quite lower than the reference UC-SC. This indicates that a loss of emission occurs towards other directions, further analysed in the next section 8.6.

The highest EQE of the reference on PTFE, on Au, the CPC-25^{o} and the CPC-45^{o} UC-SC are 2.98%, 3.08%, 2.05% and 2.07% at 0.021 W/cm^2. The NEQE of the UC-SC is 1.40 cm^2/W, 1.45 cm^2/W, 0.96 cm^2/W and 0.97 cm^2/W, respectively. For UC-SC based on the same up-conversion crystal, the NEQE was reported as 0.021 cm^2/W at 1557 nm

[164] and 0.177±0.010 cm^2/W at 1520 nm [171]. The NEQE values reported here are among the highest in literature for up-conversion solar cells and were characterised at a wavelength of the peak absorption coefficient of the UC material in the 1400-1650 nm range. However, the power density of the characterisation was lower than in other reports in the literature and it is known [169, 285], *cf.* Figure 3.16, that the relation of the NEQE with the excitation is not linear.

8.6 Current-Voltage characteristic

The I-V characteristics of the UC-SC were characterised under excitation of 1493 nm at 0.021 W/cm^2. These are displayed in Figure 8.4 with the I_{SC} and the V_{OC} extracted, the *FF* and the η calculated in Table 8.1.

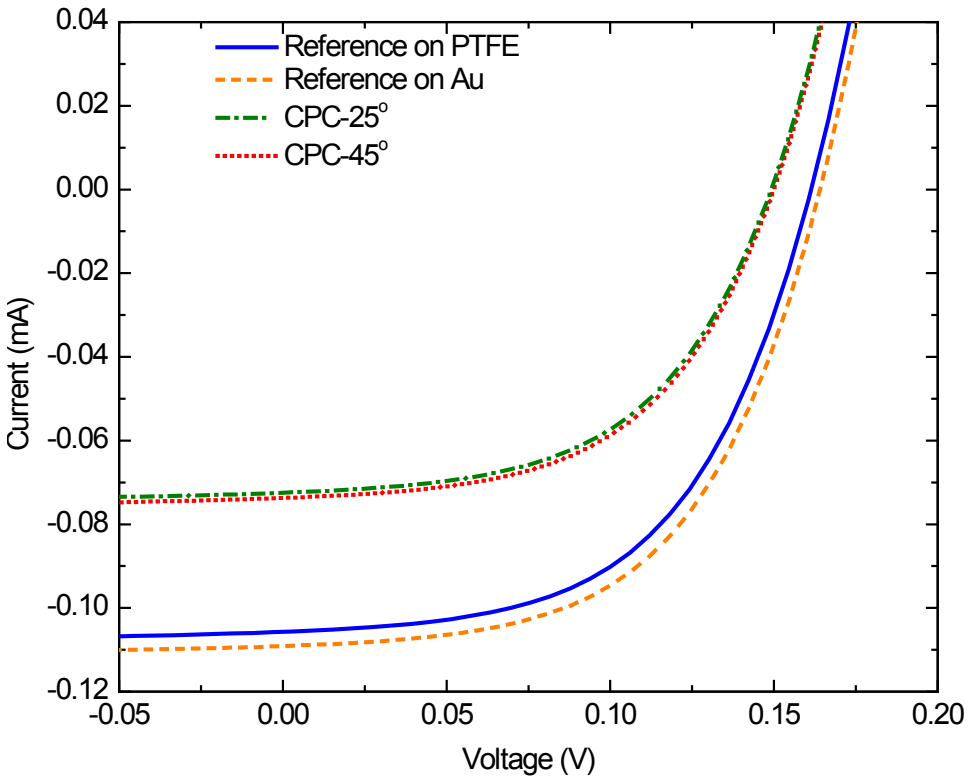

Figure 8.4: Current-voltage characteristics of the UC-SC under illumination of 1493 nm at 0.021 W/cm^2.

The two reference UC-SC perform best with η of 0.315% and 0.333% with PTFE and Au reflectors, respectively. The trend discussed for the EQE in the previous section, is also observed for the η of the UC-SC, with the lower η of the CPC devices as 0.195%

and 0.199% for CPC-25° and CPC-45°, respectively. The *FF* of all UC-SC is similar in the region of 54%, which is expected from the low I_{SC} and V_{OC} at these illumination conditions.

Table 8.1: Performance parameters of the UC-SC corresponding to the *I-V* curves in Figure 8.3 characterised, under illumination of 1493 nm at an irradiance of 0.021 W/cm^2.

UC-SC	I_{sc} (mA)	V_{oc} (V)	*FF* (%)	η (%)
Ref. PTFE	0.106	0.161	54.42	0.315
Ref. Au	0.109	0.164	54.85	0.333
CPC-25°	0.072	0.149	53.12	0.195
CPC-45°	0.074	0.149	53.57	0.199

8.7 Geometrical losses

As discussed in section 8.1, the monocrystalline structure of the up-conversion crystal results in minimum scattering. The emission towards the concentrating optics and the solar cell will be directly coupled out of the up-conversion crystal, see Figure 8.5. But for other directions it will propagate towards the up-converter.

Depending on the wavelength, the power density and the path length in the crystal, this emission will be, i) re-absorbed and re-emitted in the up-conversion crystal, ii) reflected at the back reflector with subsequent re-absorption and re-emission, iii) transmitted through the peripheral facets out of the up-conversion crystal as shown in Figure 8.5.

In the two former cases the emission can propagate back to the concentrating optics and finally the solar cell to result in a photocurrent. In the third case, however, a proportion of this isotropic emission will exit the crystal and may end up in the solar cell, while the remaining is reflected through TIR inside the crystal. Finally, this will induce propagation towards the peripheral facets of the up-conversion crystal and additional geometrical losses, associated with a lower EQE.

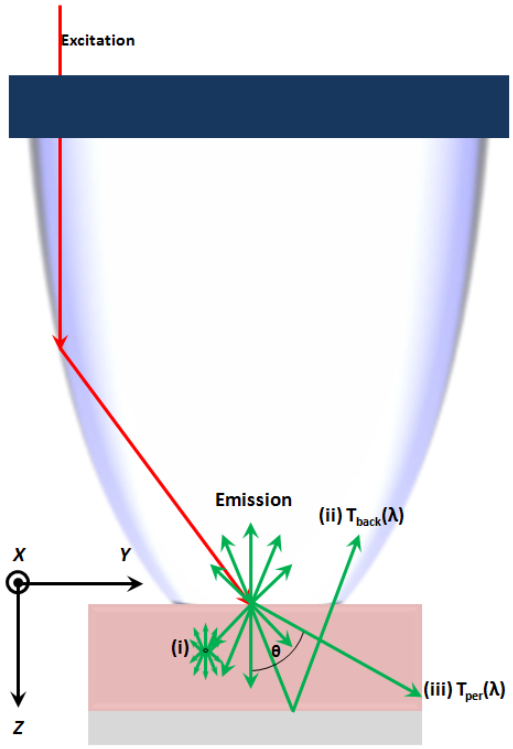

Figure 8.5: Ray-paths of emission in an up-conversion crystal. Externally, the isotropic emission is collected by the CPC and coupled to an overlying solar cell. Internally, the emission may be: i) re-absorbed and re-emitted, ii) reflected at the back reflector and transmitted towards the solar cell, or iii) transmitted from the peripheral facets.

The back reflector of the UC-SC doubles the path length of the emission and any unabsorbed excitation. This effectively reduces the optimal thickness of the up-conversion material for maximum ePLQY [185] in comparison to the case of a measurement configuration with an integrating sphere. An integrating sphere is universally the accepted method in the measurement of the PLQY. In this configuration the emission undergoes a single pass before being transmitted out of the up-conversion material. For the UC-SC however, the ePLQY of the up-conversion material is maximised at a higher path length for increasing power density, *cf.* Figure 3 [185]. Equally, for an up-conversion material of defined thickness, the ePLQY would be maximised at a single power density. This indicates the additional excitation photons from a higher power density that would require additional path length to be absorbed.

The additional path length would be required for the emitted photons. This is demonstrated in Figure 8.6(a-e), where the up-conversion crystal was excited at 1493 nm for increasing power density. Green emissions from the $^4S_{3/2}$ and the $^2H_{11/2}$ to the $^4I_{15/2}$ energy level are clearly visible. The emission is shown to occur in longer path lengths as the power density increases.

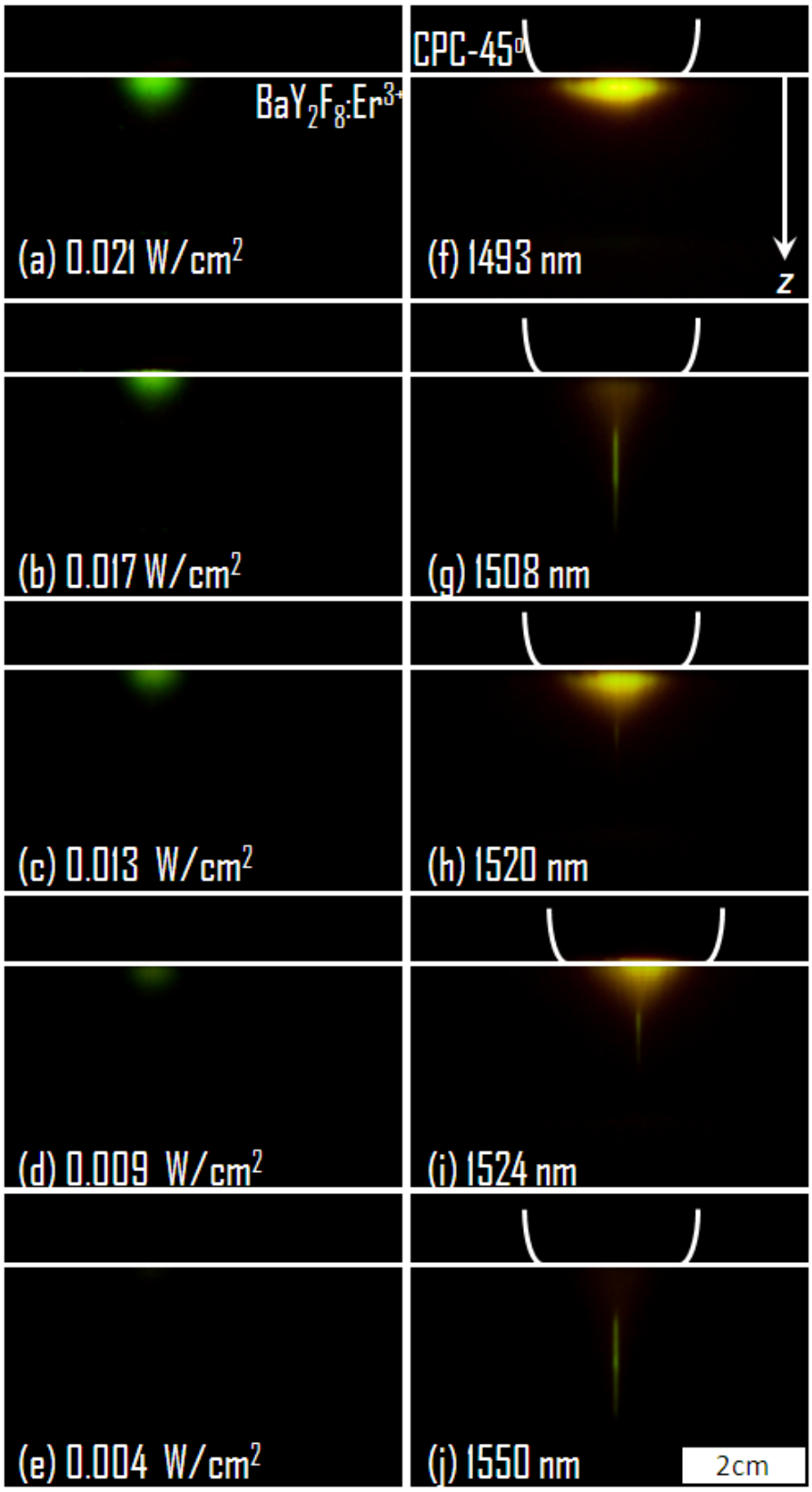

Figure 8.6: Photographs of the up-conversion crystal, from a) to e) the excitation power density is varied at a fixed wavelength of 1493 nm. From f) to j) the up-conversion crystal coupled with the CPC-45^o is excited at wavelengths corresponding to the peaks of various absorption coefficients at 0.01 W/cm^2. The propagation of the emission in longer path lengths can be seen for decreasing absorption coefficients and increasing power density.

A similar behaviour can be seen when the CPC-45° is coupled with the up-conversion crystal at different excitation wavelengths and a constant power density of 0.01 W/cm^2. In Figure 8.6(f-j) the same configuration is excited at 1493, 1508, 1520, 1524 and 1550 nm. The absorption coefficient of BaY_2F_8:30%Er^{3+} at these wavelengths is 57, 9, 13, 15 and 6 cm^{-1}, respectively [164]. The emission is shown to spread further inside the up-conversion crystal at 1508 and 1550 nm, the wavelengths of the lowest absorption coefficient. On the other hand, at 1493, 1520 and 1524 nm the emission is accumulated near the CPC-crystal interface. This is in agreement with the Beer-Lambert relation between the absorption coefficient and the path length in a medium. The different colour compared to (a-e) is possibly a saturation effect of the Si detector in the camera used to take the images.

In Figure 8.7 the cross-section along the axis of the emission intensity from Figure 8.6(a-e) is shown. The intensity follows a log-normal distribution with the path length. The mean deviation of the emission intensity in respect to the path length could be calculated from the log-normal fit. That is 0.316, 0.309 and 0.291 mm at a power density of 0.05-0.03 W/cm^2, respectively, where the signal-to-noise ratio was above 0.5.

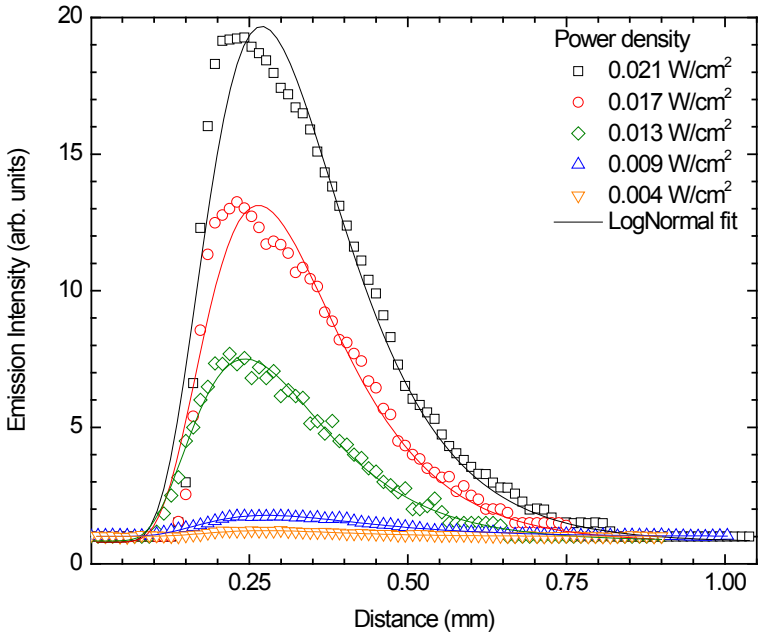

Figure 8.7: Cross-section of the emission intensity along the direction Z in the up-conversion crystal from Figure 8.6(a-e). The distance at the horizontal axis is equally offset by approximately 0.15 mm for all cross-sections.

The emission from the $^4S_{3/2}$ and the $^2H_{11/2}$ to the $^4I_{15/2}$ energy level was shown to propagate in longer path lengths in the previous section. However, the emission from the $^4I_{11/2}$ to $^4I_{15/2}$ level is more crucial for the performance of the UC-SC and is investigated *via* ray-tracing in this section. The ray-tracing results of the reference, CPC-25° and CPC-45° configurations with ideal specular and Lambertian back reflectors are summarised in Table 8.2.

For the reference UC-SC, where illumination and excitation are at normal incidence, the back reflector would reflect the emission enabling a double pass which results in a near unity absorbance. Even for isotropic emission near the crystal-solar cell interface and a Lambertian back reflector, with the refractive indices of 1.59 for BaY_2F_8 [239] and 3.5 for silicon [294], nearly all the emission will be out-coupled from the crystal towards the solar cell.

Table 8.2: Absorbance, back-reflected and peripheral transmittance at the excitation and the main emission wavelengths of the reference, CPC-25° and CPC-45° UC-SC configurations.

	Specular back reflector			*Lambertian back reflector*		
λ (nm)	**A (%)**	**T_{back} (%)**	**T_{per} (%)**	**A (%)**	**T_{back} (%)**	**T_{per} (%)**
	Reference					
1493	99.99	1.30×10^{-8}	0	99.99	7.12×10^{-9}	0
970	99.99	4.06×10^{-3}	6.29×10^{-3}	99.99	1.96×10^{-3}	5.54×10^{-3}
517	99.99	6.12×10^{-9}	0	99.99	1.33×10^{-9}	0
	CPC-25°					
1493	96.27	6.11×10^{-9}	3.72	96.27	1.34×10^{-9}	3.72
970	96.11	4.45×10^{-3}	3.88	96.11	2.32×10^{-3}	3.88
517	95.95	5.88×10^{-9}	4.04	95.95	1.28×10^{-9}	4.04
	CPC-45°					
1493	96.26	6.11×10^{-9}	3.73	96.27	1.37×10^{-9}	3.72
970	96.11	4.59×10^{-3}	3.88	96.11	2.45×10^{-3}	3.88
517	95.95	5.87×10^{-9}	4.04	95.95	1.28×10^{-9}	4.04

The probability of coupling this emission from the UC-SC with concentrating optics would be quite different, since the concentrated excitation deviates from the normal. Even under normal incidence, this could extend over the full hemisphere, however, the near and far field irradiance profiles of the two CPC exhibited a higher probability at a specific angle. The half-angle θ was calculated from the simulated irradiance profiles, as 66.85° for the CPC-25° and 35.30° for the CPC-45°. In this UC-SC configuration the half-angle did not change with the wavelength, that is for the excitation at 1493 nm and the main emission wavelengths, at 970 and 517 nm.

An absorbance higher than 95% is obtained in all the configurations, which is by 1-2% higher than the measured absorbance [171] from a single pass. A Lambertian back reflector is expected to induce a longer path length in the crystal than a specular reflector. Interestingly, equal absorbance is obtained for both specular and Lambertian back reflectors at this power density. For the concentrating UC-SC, approximately 3-4% is transmitted through the peripheral facets of the material associated with the decreased slopes and EQE at the high pump regime.

Less than 0.01% is transmitted towards the solar cell. Specifically, the backwards transmission T_{back} is by six orders of magnitude lower at 1493 and 517 nm in comparison to the T_{back} at 970 nm due to the lower absorption coefficient at this wavelength that is 17.97 cm^{-1}. For all UC-SC the transmission at this wavelength, however, is too low and indicates the significant effect of re-absorption.

To mitigate for losses due to the peripheral transmission, information of the irradiance of the out-coupled emission at 970 nm is required. It was seen in section 7.3 that for the excitation profile the CPC-25° attains a higher local irradiance than the CPC-45°. This explains why the CPC-25° exhibits the highest irradiance of the emission at the CPC-crystal interface in Figure 8.8. Within the up-conversion sample, *i.e.* at ±5 mm, it can be seen that the emission at 970 nm is transmitted from the crystal towards the CPC with an integrated irradiance of 3.06×10^{-7} W/cm^2. As indicated with vertical lines in the Figure only 1.76×10^{-7} W/cm^2 is coupled in the CPC and finally the solar cell. However, the remaining may still be absorbed subject to at least one reflection at the air-solar cell interface.

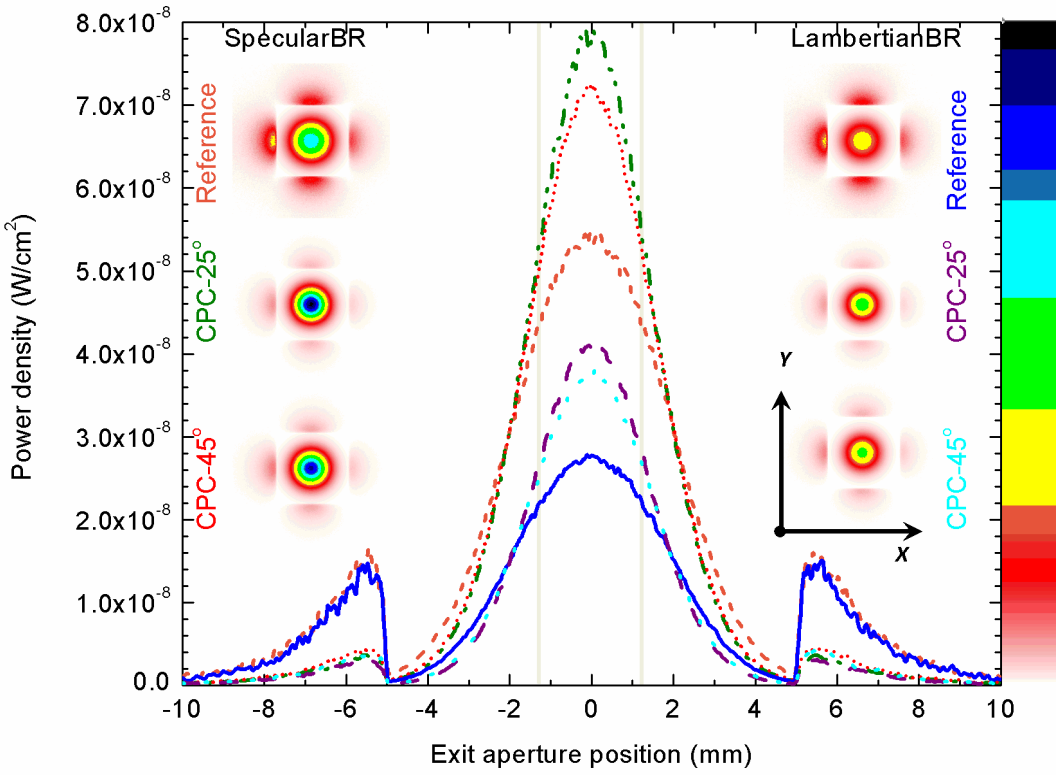

Figure 8.8: Irradiance profiles of the 970 nm emission at the CPC-crystal interface after reflection at the back. Six UC-SC are displayed for the reference, CPC-25° and CPC-45° with specular and Lambertian back reflectors. The insets expose the spatial distribution of the irradiance transmitted out of the up-conversion crystal, with corresponding colours on the right axis.

Clearly, the transmitted emission T_{per} can be coupled back to the system with an appropriate optimisation of the configuration. An apparent solution could include reflectors attached to the peripheral facets. The reflectors should ideally guide the 970 nm emission directly towards the solar cell, thus avoiding re-absorption in the crystal. Alternatively, concentrating optics with excitation profile approximating the normal incidence, *cf.* Figure 7.4, seem more suitable for reduced peripheral losses and a less complex device.

8.8 Discussion

It is interesting to compare the performance of UC-SC for the up-converters, β-$NaYF_4$:25%Er^{3+} and BaY_2F_8:30%Er^{3+}. For the reference UC-SC, it is clear from the EQE and NEQE that the UC-SC utilising the BaY_2F_8:30%Er^{3+} performs better than the

β-$NaYF_4$:25%Er^{3+}. That is, from an EQE of 1.33% at 0.024 W/cm^2 and NEQE of 0.55 cm^2/W, the EQE of the former is 3.08% at 0.021 W/cm^2 and NEQE of 1.40 cm^2/W. The enhancement can be also seen for the η which is almost tripled. Considering that all else remains constant for both UC-SC, that is the solar cell, the back reflector and the other coupling parameters, the improvement in EQE reflects the ePLQY of the up-conversion material. A comparison can be made at a power density of 500 W/m^2, where the influence of ETU is dominant. For the BaY_2F_8:30%Er^{3+} this is 2% [171] compared to 1% [151], under excitation of 1520 nm and 1523 nm, respectively.

It is also interesting that the ePLQY of β-$NaYF_4$:25%Er^{3+} is quite different from the iPLQY. A large difference between iPLQY and ePLQY relates to absorption of the excitation in the up-conversion material that does not result in emission. This is the case for β-$NaYF_4$:25%Er^{3+} with 8.4% iPLQY and 6.5% ePLQY. The difference can be attributed to an absorbance of 53% at 1523 nm, of which approximately 75% is absorbed by Er^{3+} [151]. The remaining absorbance occurs in the host, evident from the scatter spectra of the un-doped phosphor sample, *cf*. Figure 2(c) in reference [151]. This can be attributed to absorption in β-$NaYF_4$, but also parasitic absorption in the polymer, PFCB, since a higher PLQY was measured for the up-converter in powder form [291]. For BaY_2F_8:30%Er^{3+} with 10.1% iPLQY and 9.5% ePLQY, the difference was quite lower and the corresponding absorbance from Er^{3+} was 94% [171]. This suggests that scattering affects the ePLQY considerably, by inhibiting the emission to be out-coupled from the up-conversion material. This is also reflected in the absorption coefficients of the up-conversion materials. At the peak wavelengths these are 45.1 cm^{-1} [164] and 5.5 cm^{-1} [284] for the BaY_2F_8:30%Er^{3+} and the β-$NaYF_4$:25%Er^{3+}, respectively.

Comparing the reference with the CPC-enhanced UC-SC, it can be seen that the geometrical losses discussed in section 8.7 deteriorate significantly the performance of the UC-SC with BaY_2F_8:30%Er^{3+}. Instead of enhancing the reference devices, they result in decreased EQE, NEQE and η, at the highest power density of 0.021 W/cm^2. On the contrary, the enhancement of the reference UC-SC based on β-$NaYF_4$:25%Er^{3+} is clear. In fact, in the low-pump regime, the enhancement in EQE is equal to the geometrical concentration. This proves that the optical losses by integration of the CPC optics in the UC-SC are minimal and the potential of a two-photon up-conversion is maximised. For a highly scattering material, it is expected that the absorption of the excitation takes place near the surface and the emission is scattered towards the external

surface. Consequently, for a highly scattering up-conversion phosphor such as the β-$NaYF_4$:25%Er^{3+}, an additional thickness of the material would not contribute to the ePLQY. On the other hand, for a non-scattering up-conversion material such as the BaY_2F_8:30%Er^{3+}, the excitation and the emission propagates further into the material. Since the UC luminescence of the material is non-linear in relation to the excitation power, the absorption length depends on the power density of the excitation. This was demonstrated for the UC-SC with CPC-25^o with the highest local excitation between the optics. For this UC-SC, saturation of the EQE occurred at a lower power density than the CPC-45^o and the reference UC-SC.

8.9 Conclusions

In this chapter, concentrating UC-SC based on the up-conversion material BaY_2F_8:30%Er^{3+} were investigated. The reference UC-SC exhibited an EQE of 3.08% under 1493 nm excitation at 0.021 W/cm^2, relating to a NEQE of 1.45 cm^2/W. This corresponds to a conversion efficiency of 0.315% at this illumination condition. The UC-SC with concentrating optics displayed a maximum enhancement of 1.95× in EQE compared to the reference UC-SC at low power density. At a higher power density, above 0.009 W/cm^2, the emission was shown to propagate further into the up-conversion crystal. This lead to further geometrical losses towards the peripheral facets of the up-conversion material, due to the excitation profile of the concentrating UC-SC as was investigated in this chapter. However, these exhibited an EQE of 2.06% and a conversion efficiency of 0.199% under the abovementioned illumination conditions. These values are among the highest in literature and highlight on the one hand the potential of this up-conversion material and on the other of the concentrating concept in UC-SC.

Chapter 9 : Overall conclusions and outlook

In this thesis approaches to enhance the sub-band-gap response of silicon solar cells *via* up-conversion and solar concentration were presented. Enhancement of the EQE and consequently the conversion efficiency was achieved by improving the short circuit current in novel designs either by increasing the up-conversion emission or the concentration ratio of the device. The approaches that lead to the most exceptional results of this thesis will be reviewed, as well as the potential for future work will be highlighted in this chapter.

9.1 Tapered and rare earth-doped optical fibres

On the first investigated approach, a solar concentration of 2000 suns was demonstrated at the end of a single optical fibre. This was obtained in a simple optical system comprising of spherical plano-convex lenses and dielectric tapers, directly attached to optical fibres. For longer *f*-numbers and shorter acceptance angles for the lenses and tapers, respectively, a maximum experimental coupling efficiency of 29% for broadband and 72% for monochromatic light was achieved. An upper broadband coupling efficiency over 85% was calculated for this optical system, which is limited merely by the alignment between primary and secondary optics.

The solar concentration was also characterised as a function of wavelength, an insightful method that is rarely applied in concentrating systems. For solar energy devices such as photovoltaics, with reduced conversion efficiency at high solar concentrations, characterisation of spectral effects at the solar cell and the concentrating optics becomes imperative. At high solar concentration, solar cells are characterised under the reference solar spectra with integrated spectral irradiance. In the investigated system, the effect and magnitude of the chromatic aberration of the primary optics was revealed through the wavelength dependent method. The solar concentration was spectrally characterised as broadband, whereas it maximised at specific bands. The maxima were shown to have an inverse relation to the *f*-number of the lens, or otherwise proportional to the focal length.

In regard to the Er^{3+}-doped optical fibres, the effect of the length was investigated in a double-clad silicate fibre of low doping concentration. The up-conversion emission at

980 nm was characterised under 1523 nm excitation and was maximised for a fibre length of 20 mm. The emission power dependence was found to agree with the literature as ESA being the dominant up-conversion mechanism.

9.2 Future research on tapered and rare earth-doped optical fibres

Improvements in coupling efficiency are expected with improved optical design. As presented in Chapter 2, optics such as the DCPC and the DTIRC have a better angular transmission compared to the tapered. The *NA* of the optical fibre still restricts the wave guiding of sunlight in the optical fibre. However, the sharper cut-off of the transmission at the acceptance angle of the optic will enable a higher coupling efficiency. As has been demonstrated for the DCPC optics [295], this would be accompanied by a more uniform irradiance profile at the end of the fibre which is desired in high irradiance applications such as solar cells and laser beam shaping.

In doped fibres, the emission from the investigated type of fibre was low to provide a significant enhancement by further incorporation in photovoltaic systems, due to its design for minimum up-conversion. Of course, other material systems based on fluorides were shown to be more suitable for up-conversion. Further limitations however exist, to transfer the optical fibre platform in up-conversion photovoltaics. The incomplete absorption of sub-band-gap photons is the main. An advantage of this design is that optical fibres doped with different rare earths, such as Tm^{3+} and Ho^{3+}, can be incorporated into a fibre bundle receiving sunlight *via* a concentrating coupler. This way, the absorption spectrum is broadened and the up-conversion emission can be independently optimised in each optical fibre.

9.3 Up-conversion solar cells

On the second investigated approach, concentrating optics were integrated in UC-SC. This way, the solar concentration required to excite the up-converter need not be limited by the concentration at the overlying solar cell. For silicon, this limit is approximately 100 suns, whereas a solar concentration above 350 suns results in increased PLQY of the up-converter and EQE of the UC-SC. A systematic study of imaging and non-imaging optics ranging from 2 to 100× concentration was conveyed. The non-imaging

optics investigated in this thesis, exhibited higher EQE in comparison to the imaging counterparts. This was associated with the better optical properties of the non-imaging optics for this application. In particular, the forward and backward transmission of the non-imaging, the parabolic and the tapered optics, were superior to that of the imaging objective lens.

This further led to a significant enhancement in EQE and η that was first ever demonstrated upon the integration of CPC optics in UC-SC with β-$NaYF_4$:25%Er^{3+}. In this demonstration an enhancement equal to the concentration factor of 2.79× was obtained in the low pump regime with a quadratic relation to power. An enhancement of 1.95× was obtained for UC-SC with BaY_2F_8:30%Er^{3+} at the same pump regime for the same non-optimised design. The enhancement was lower than the concentration factor despite the higher PLQY of the material, due to optical losses of the emission through the up-conversion crystal.

The integration of concentrating optics enabled the transition of the UC-SC from quadratic to linear in the high pump regime, at a rate faster than a non-concentrating device. Expectedly, the enhancement was lower in the high pump regime for both investigated up-conversion materials. On the one hand, this probed the non-linear behaviour of the up-conversion material, where higher order and non-radiative processes become more probable. On the other hand, the abovementioned optical losses associated with increased transmission through the up-conversion material were shown as a higher saturation of the EQE. The latter was clearly the case for the BaY_2F_8:30%Er^{3+} where the transmission was shown to increase further inside the crystal for higher power density. For the β-$NaYF_4$:25%Er^{3+} the saturation in EQE was shown to be lower at the high pump regime, possibly due to higher scattering in this system.

The EQE was 1.80% under 1523 nm illumination while for BaY_2F_8:30%Er^{3+} was 2.07% under 1493 nm illumination. This resulted to a high normalised EQE to the incident irradiance, a figure of merit usually calculated to compare the performance between up-conversion materials and photovoltaic devices. This result was obtained for UC-SC with CPC-45^o optics and was 0.97 cm^2/W for BaY_2F_8:30%Er^{3+} and 0.75 cm^2/W for β-$NaYF_4$:25%Er^{3+}, which is nearly two times higher than the highest normalised EQE for UC-SC to-date. Both results were obtained at an irradiance of 0.02 W/cm^2, corresponding to a monochromatic solar concentration in the range of 2000 suns. By

further optimising the geometrical parameters of the CPC to over 10^4 suns concentration, an EQE higher than 8% was estimated with the presented up-conversion materials. Although this solar concentration is incident on the up-converter, the presented concentrating concept required only a concentration in the range of 7 suns on the solar cell.

The I-V characteristics of the UC-SC were also characterised under the same illumination conditions. This enabled the quantification of the conversion efficiency under sub-band-gap illumination, first ever reported for UC-SC based on c-Si. The relative efficiency was determined as 0.163% for the UC-SC with β-$NaYF_4$:25%Er^{3+} and 0.199% for the UC-SC with BaY_2F_8:30%Er^{3+} at 1523 nm and 1493 nm, respectively. Since these values were measured under sub-band-gap illumination they are relative to the 17.6% efficiency of the silicon solar cell under standard AM1.5G conditions.

9.4 Future research on up-conversion solar cells

The EQE and efficiency results presented in this thesis are among the highest for UC-SC and can highlight some of the directions for further improvement:

i) Improvements can be achieved *via* concentration of the sub-band-gap photons transmitted by the overlying solar cell before these excite the up-conversion material. If the concentration is at an irradiance corresponding to the low pump regime of the up-conversion material, the maximum from the quadratic behaviour of a two photon up-conversion is gained. The coupling of the up-conversion emission with the solar cell must also be considered. Since this emission is isotropic, optics designed for collection over a solid angle 2π are required. An additional advantage of the concentrating optics is the shaping of the localised irradiance. This is important especially in other than the standard characterisation conditions. For example, the irradiance during the course of a day can be quite different than the AM1.5G spectrum. Hence, a way of adjusting this irradiance at levels that maximise the up-conversion emission can be in the form of suitable concentrating optics.

ii) The importance of an up-conversion material of high PLQY. This was shown for both up-conversion materials in this thesis, and particularly for

BaY_2F_8:30%Er^{3+}. On the one hand, the monoclinic structure of the crystal and the excellent absorbance resulted in the better performance of the UC-SC compared to β-$NaYF_4$:25%Er^{3+}. On the other hand, the importance of this result can be recognised especially in view of the fact that an amount of up-conversion emission in the device escaped in the peripheral sides of the crystal.

iii) The high transmission of the solar cell at sub-band-gap wavelengths and the excellent EQE at the emission wavelength of the up-conversion materials, *i.e.* 980 nm. Ultimately, a high transmission relates to more sub-band-gap photons available to excite the up-conversion material. The c-Si solar cells utilised in this thesis enabled a greater portion of the incident illumination to reach the up-converter. However, the transmission for other than the normal incidence angle, *e.g.* when concentrating optics are used, is expected to be different. In this case, TIR due to the high refractive index of the solar cell would result in reduced transmission. Equally, the up-conversion emission has to be coupled with the solar cell. To this end, an optimised antireflective coating proved to play a significant role by reducing the reflectance at the respective emission wavelengths.

While this thesis focused on the up-conversion improvement *via* concentration, other approaches are required for extending the sub-band-gap response of solar cells. The restricted absorption spectrum of the up-converters remains the main challenge for UC-SC. Spectral concentration is currently the main approach to extend the absorption, however several challenges still remain. To this end, optical designs could direct the downshifted emission from the quantum dots only towards Er^{3+}, and the emission from Er^{3+} directly to the solar cell, thereby avoiding any re-absorption. Such designs could comprise of spectrum splitting or photonic structures that permit this one-way coupling, but also non-imaging optics to permit omni-directional collection of the emission.

To conclude, promising concepts were demonstrated towards up-conversion and solar concentration during the course of this thesis. Novel system and UC-SC device designs with available semiconductor and up-conversion materials were reviewed and studied throughout this thesis. To this end, the response of UC-SC with concentrating optics integrated in the device was shown to improve significantly. In conjunction with the investigated concentrating concepts, they present important future directions for photovoltaics and a wider exploitation of the solar resource.

Appendix

Selection rules for optical transitions

Here, I provide further details on the mechanisms that allow the optical transitions in a rare earth which controls the shape of the spectral lines. An overview of relevant literature is also given that can be traced into more details for the interested reader.

Generally, *f-f* transitions in free ions are parity forbidden according to the Laporte selection rule. Accordingly, states and consequently wave-functions are by convention divided between odd and even parity. Empirical observations on iron [296], later formulated into the parity conservation law [297, 298], led to the conclusion that electric dipole transitions were not allowed between like states, *i.e.* only transitions between even and odd parity states were allowed. Equally, the orbital angular momentum of electrons in the initial l_i and final states l_f can only be connected if,

$$\Delta l = l_i - l_f = \pm 1 \qquad \text{(A.1)},$$

However, it was later suggested [299, 300] that the observed spectral lines of the rare earths occur due to the mixing of parity states by the crystal field of the solid surrounding the ion. In fact, as the active ion is screened by the electron shell, when incorporated in a solid host, it is further surrounded by a crystal lattice. Therefore, the electronic transitions will be consequently coupled to the lattice before being externally observed. The energy of these transitions will be affected by the coupling of the forces described by the interaction Hamiltonian of the lattice H_L and the crystal field H_{CF} in addition to the free ion interaction Hamiltonians. The latter consist of the central field between the nucleus and the valence electrons H_0, the Coulomb (electrostatic) interaction H_{ee} and the spin-orbit interaction H_{SO} between the valence electrons. The complete interaction Hamiltonian H would then be [140],

$$H = H_0 + H_{ee} + H_{SO} + H_{CF} + H_L \qquad \text{(A.2)},$$

The crystal field forces in rare earth ions are weaker than the spin-orbit and the electrostatic forces. Nevertheless, they lead to the Stark splitting of the energy levels into an extended manifold (*cf.* Figure A.1), consequently allowing transitions in the 4*f* shell that are observed as a distinctive broadened spectrum depending on the surrounding lattice.

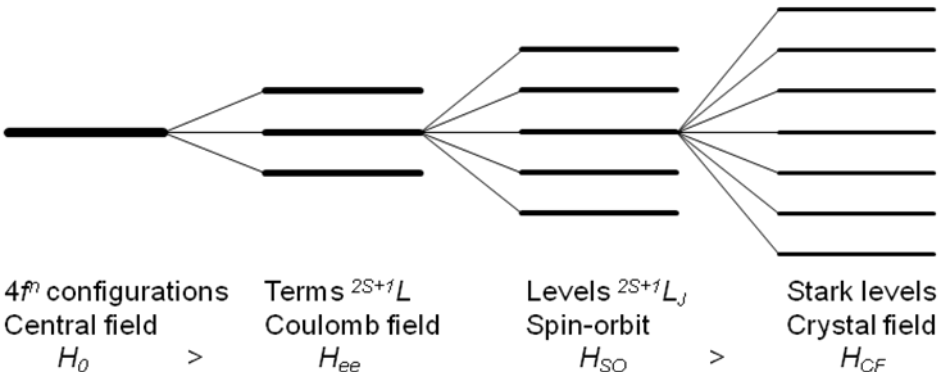

Figure A.1: Forces and interactions leading to crystal field splitting. An equidistant energy splitting is shown only for illustration purposes (adapted from [301]).

The probabilities of the optical transitions can be determined owing to the theory derived independently by B.R. Judd [302] and G.S. Ofelt [303]. Accordingly, either by calculating *ab-initio* or by obtaining experimentally a set of phenomenological parameters, the line-strength S_m of a transition can be expressed as [301],

$$S_m = \frac{3ch(2J+1)}{8\pi^3 e^2 \bar{\lambda}} n\left(\frac{3}{n^2+2}\right)^2 \int \sigma(\lambda)\partial\lambda \qquad \text{(A.3)},$$

from the absorption cross section $\sigma(\lambda)$ over the wavelength range of a respective manifold, the angular momentum number J, the refractive index n of the host at the mean wavelength λ. The line-strength depends on the oscillator strengths S_{ED} and S_{MD} of the electric magnetic dipoles, respectively. The oscillator strengths though, are independent of the host and have been extensively tabulated for several lanthanoids [304-306]. From these, the so-called Judd-Ofelt intensity parameters can be determined and the radiative transition probabilities A_{fi} for all excited states are given by,

$$A_{fi} = \frac{64\pi^4 e^2}{3h(2J'+1)\bar{\lambda}^3}\left[n\left(\frac{n^2+2}{3}\right)^2 S_{ED} + n^2 S_{MD}\right] \qquad \text{(A.4)}.$$

Finally, the radiative lifetime τ_r and the branching ratio β_{fi} between states f and i, especially useful in the case of excited states where experimental data cannot be obtained, are given by,

$$1/\tau_r = \Sigma A_{fi} \qquad \text{(A.5)},$$

$$\beta_{fi} = \tau_f A_{fi} \qquad \text{(A.6)}.$$

Absorption and emission

In a simplified system of two distinct energy levels, initial (i) and final (f), the probabilities of stimulated (induced) absorption Wa_{if}, stimulated emission $Wste_{fi}$ and spontaneous emission $Wspe_{fi}$ are connected by the Einstein coefficients A and B as,

$$dWa_{if} = B_{if}\,\rho_{\omega}\,N_i\,dt \qquad \text{(A.7)},$$

$$dWste_{fi} = B_{fi}\,\rho_{\omega}\,N_f\,dt \qquad \text{(A.8)},$$

$$dWspe_{fi} = A_{fi}\,N_f\,dt \qquad \text{(A.9)},$$

with N being the population density of either i or f level, and ρ_{ω} the energy density per unit angular frequency. The energy density is described by Planck's law of radiation as,

$$\rho_{\omega} = \frac{\hbar\omega^3}{4\pi^3 c^2 e^{\hbar\omega/(kT)} - 1} \qquad \text{(A.10)},$$

with $\hbar$ the Planck constant h divided by 2π, c the speed of light, k the Boltzmann constant and T the absolute temperature. It has been shown [307, 308] that for monochromatic transitions the Einstein coefficients are connected as follows,

$$g_i\,B_{if} = g_f\,B_{fi} \qquad \text{(A.11)},$$

$$A_{fi} = 16\pi^2\hbar(\omega/2\pi c)^3\,B_{fi} \qquad \text{(A.12)},$$

where g_i and g_f the degeneracy of each level. It has later been shown that for broadband transitions the emission cross section σ_{ε} is reciprocally connected with the absorption cross section σ_{α} by [309, 310],

$$\sigma_{\alpha} = \sigma_{\varepsilon}\,e^{[\hbar(\omega-\omega_{fi})/kT]} \qquad \text{(A.13)},$$

where ω the zero line frequency at room temperature and ω_{fi} the angular frequency interval between states f and i. The angular frequencies ω and ω_{fi} are measured from the lowest Stark levels of each manifold [301, 311]. Conveniently, owing to this relation the unknown emission cross section can be derived from the known absorption cross section as has been applied for example in Er^{3+}-doped optical fibres [312]. However, if the energy levels can be matched *via* phonons, the spectra are affected by vibronic transitions and deviation from this relation occurs, as has been observed in Nd^{3+}-doped yttrium aluminium garnet (YAG) [313].

References

1. Birol F, "World Energy Outlook 2010," (2010).
2. Birol F. World Energy Outlook. *IX Congreso of the Spanish Association for Energy Economics (AEEE),* Madrid, Spain, 2014;
3. Cook J, Nuccitelli D, Green SA, Richardson M, Winkler B, Painting R, Way R, Jacobs P, Skuce A. Quantifying the consensus on anthropogenic global warming in the scientific literature. *Environmental Research Letters* 2013; **8**(2): 024024. doi: 10.1088/1748-9326/8/2/024024.
4. Hermann WA. Quantifying global exergy resources. *Energy* 2006; **31**(12): 1685-1702. doi: 10.1016/j.energy.2005.09.006.
5. Kopp G, Lean JL. A new, lower value of total solar irradiance: Evidence and climate significance. *Geophysical Research Letters* 2011; **38**(1): 10.1029/2010GL045777.
6. Morton O. Solar energy: a new day dawning?: silicon valley sunrise. *Nature* 2006; **443**(7107): 19-22. doi: 10.1038/443019a.
7. MacKay D. *Sustainable Energy-without the hot air*. UIT Cambridge: 2008;
8. Mints P, Donnelly J, "Photovoltaic Manufacturer Shipments, Capacity & Competitive Analysis 2011/2012," (2012).
9. Ardani K, Margolis R, "Solar technologies market report," (2011).
10. Council NR. *Optics and Photonics: Essential Technologies for Our Nation*. The National Academies Press: Washington, DC, 2013; 360.
11. Dale M, Benson SM. Energy Balance of the Global Photovoltaic (PV) Industry-Is the PV Industry a Net Electricity Producer? *Environmental science & technology* 2013; **47**(7): 3482-3489. doi: 10.1021/es3038824.
12. Green MA, Emery K, Hishikawa Y, Warta W, Dunlop ED. Solar cell efficiency tables (version 43). *Progress in Photovoltaics: Research and Applications* 2014; **22**(1): 1-9. doi: 10.1002/pip.2452.
13. Stauffer PH, Hendley II JW, Haxel GB, Hedrick JB, Orris GJ, "Rare earth elements–critical resources for high technology," in *Fact Sheet 087-02,* U. S. D. o. t. I.-U. S. G. Survey, ed. (2002), pp. 087-002.
14. Bloembergen N. Solid state infrared quantum counters. *Physical Review Letters* 1959; **2**(3): 84. doi: 10.1103/PhysRevLett.2.84.
15. Esterowitz L, Schnitzler A, Noonan J, Bahler J. Rare earth infrared quantum counter. *Applied Optics* 1968; **7**(10): 2053-2070. doi: 10.1364/AO.7.002053.
16. Gurski TR, Epps HW, Maran SP. Astronomical demonstration of an infrared upconverter. *Nature* 1974; **249**(638 - 639. doi: 10.1038/249638a0.
17. Gueymard C, Myers D, Emery K. Proposed reference irradiance spectra for solar energy systems testing. *Solar Energy* 2002; **73**(6): 443-467. doi: 10.1016/s0038-092x(03)00005-7.
18. ASTM, "Standard Tables for Reference Solar Spectral Irradiances: Direct Normal and Hemispherical on 37^{o} Tilted Surface," in *Annual Book of ASTM Standards,* (American Society for Testing and Materials International, West Conshohocken, PA, 2012).
19. Becquerel A-E. Mémoire sur les effets électriques produits sous l'influence des rayons solaires. *Comptes Rendus de l'Académie des sciences* 1839; **9**(561-567. doi:
20. Becquerel A-E. *Mémoire sur le rayonnement chimique qui accompagne la lumière solaire et la lumière électrique*. Imprimerie Royale: Paris, 1842;
21. Smith W. The action of light on selenium. *Journal of the Society of Telegraph Engineers* 1873; **2**(4): 31-33. doi: 10.1049/jste-1.1873.0023.

22. Adams WG. The Action of Light on Selenium. *Proceedings of the Royal Society of London* 1874; **23**(156-163): 535-539. doi: 10.1098/rspl.1874.0087.
23. Fritts CE. On a new form of selenium cell, and some electrical discoveries made by its use. *American Journal of Science* 1883; **26**(156): 465-472. doi: 10.2475/ajs.s3-26.156.465.
24. Stoletow A. Sur une sorte de courants électriques, provoqués par les rayons ultra-violets. *Comptes Rendus de l'Académie des sciences* 1888; **CVI**(1149. doi:
25. Stoletow M. On a kind of electrical current produced by ultra-violet rays. *Philosophical Magazine Series 5* 1888; **26**(160): 10.1080/14786448808628270.
26. Einstein A. Über einen die Erzeugung und Verwandlung des Lichtes betreffenden heuristischen Gesichtspunkt. *Annalen der Physik* 1905; **322**(6): 132-148. doi: 10.1002/andp.19053220607.
27. Ohl RS, "Light-sensitive electric device," 2,402,662 (1946).
28. Ohl RS, "Light-sensitive electric device including silicon," 2,443,542 (1948).
29. Shockley W. *Electrons and holes in semiconductors, with applications to transistor electronics*. Krieger: Toronto, Van Nostrand, 1953;
30. Shockley W, Sparks M, Teal G. *p-n* Junction Transistors. *Physical Review* 1951; **83**(1): 151. doi: 10.1103/PhysRev.83.151.
31. Chapin D, Fuller C, Pearson G. A new silicon *p-n* junction photocell for converting solar radiation into electrical power. *Journal of Applied Physics* 1954; **25**(5): 676-677. doi: 10.1063/1.1721711.
32. Chapin DM, "Solar energy converting apparatus," US2780765 A (1957).
33. Whipple F, Hynek J, "Standby for satellite take-off," Popular Mechanics, 1957, pp. 65-71.
34. Kazmerski LL. Photovoltaics: a review of cell and module technologies. *Renewable & Sustainable Energy Reviews* 1997; **1**(1): 71-170. doi: 10.1016/S1364-0321(97)00002-6.
35. Green MA. The path to 25% silicon solar cell efficiency: History of silicon cell evolution. *Progress in Photovoltaics: Research and Applications* 2009; **17**(3): 183-189. doi: 10.1002/pip.892.
36. Green MA. Photovoltaics: technology overview. *Energy Policy* 2000; **28**(14): 989-998. doi: 10.1016/S0301-4215(00)00086-0.
37. Green MA. Third generation photovoltaics: Ultra-high conversion efficiency at low cost. *Progress in Photovoltaics: Research and Applications* 2001; **9**(2): 123-135. doi: 10.1002/pip.360.
38. Tanabe K. A review of ultrahigh efficiency III-V semiconductor compound solar cells: multijunction tandem, lower dimensional, photonic up/down conversion and plasmonic nanometallic structures. *Energies* 2009; **2**(3): 504-530. doi: 10.3390/en20300504.
39. Ekins-Daukes N, Barnham K, Connolly J, Roberts J, Clark J, Hill G, Mazzer M. Strain-balanced GaAsP/InGaAs quantum well solar cells. *Applied Physics Letters* 1999; **75**(26): 4195-4197. doi: 10.1063/1.125580.
40. Dhomkar S, Manna U, Peng L, Moug R, Noyan I, Tamargo M, Kuskovsky I. Feasibility of submonolayer ZnTe/ZnCdSe quantum dots as intermediate band solar cell material system. *Solar Energy Materials and Solar Cells* 2013; **117**(604-609. doi: 10.1016/j.solmat.2013.07.037.
41. Sullivan JT, Simmons CB, Buonassisi T, Krich JJ. Targeted Search for Effective Intermediate Band Solar Cell Materials. *IEEE Journal of Photovoltaics* 2014; **PP**(9): 1 - 7. doi: 10.1109/jphotov.2014.2363560.
42. Conibeer G, Patterson R, Huang L, Guillemoles J-F, Kőnig D, Shrestha S, Green MA. Modelling of hot carrier solar cell absorbers. *Solar Energy Materials and Solar Cells* 2010; **94**(9): 1516-1521. doi: 10.1016/j.solmat.2010.01.018.

43. Hirst L, Walters R, Führer M, Ekins-Daukes N. Experimental demonstration of hot-carrier photo-current in an InGaAs quantum well solar cell. *Applied Physics Letters* 2014; **104**(23): 231115. doi: 10.1063/1.4883648.
44. Swanson RM. The promise of concentrators. *Progress in Photovoltaics: Research and Applications* 2000; **8**(1): 93-111. doi: 10.1002/(sici)1099-159x(200001/02)8:1<93::aid-pip303>3.0.co;2-s.
45. Imenes A, Mills D. Spectral beam splitting technology for increased conversion efficiency in solar concentrating systems: a review. *Solar Energy Materials and Solar Cells* 2004; **84**(1): 19-69. doi: 10.1016/j.solmat.2004.01.038.
46. Barnett A, Kirkpatrick D, Honsberg C, Moore D, Wanlass M, Emery K, Schwartz R, Carlson D, Bowden S, Aiken D. Very high efficiency solar cell modules. *Progress in Photovoltaics: Research and Applications* 2009; **17**(1): 75-83. doi: 10.1002/pip.852.
47. Mitchell B, Peharz G, Siefer G, Peters M, Gandy T, Goldschmidt JC, Benick J, Glunz SW, Bett AW, Dimroth F. Four-junction spectral beam-splitting photovoltaic receiver with high optical efficiency. *Progress in Photovoltaics: Research and Applications* 2011; **19**(1): 61-72. doi: 10.1002/pip.988.
48. Richards B. Enhancing the performance of silicon solar cells *via* the application of passive luminescence conversion layers. *Solar Energy Materials and Solar Cells* 2006; **90**(15): 2329-2337. doi: 10.1016/j.solmat.2006.03.035.
49. Grätzel M. Photoelectrochemical cells. *Nature* 2001; **414**(6861): 338-344. doi: 10.1038/35104607.
50. Grätzel M. The light and shade of perovskite solar cells. *Nature Materials* 2014; **13**(9): 838-842. doi: 10.1038/nmat4065.
51. Shockley W, Queisser HJ. Detailed balance limit of efficiency of *p-n* junction solar cells. *Journal of Applied Physics* 1961; **32**(3): 510-519. doi: 10.1063/1.1736034.
52. Tiedje T, Yablonovitch E, Cody GD, Brooks BG. Limiting efficiency of silicon solar cells. *IEEE Transactions on Electron Devices* 1984; **31**(5): 711-716. doi: 10.1109/T-ED.1984.21594.
53. Richter A, Hermle M, Glunz SW. Reassessment of the Limiting Efficiency for Crystalline Silicon Solar Cells. *IEEE Journal of Photovoltaics* 2013; **3**(4): 1184-1191. doi: 10.1109/jphotov.2013.2270351.
54. Strümpel C, McCann M, Beaucarne G, Arkhipov V, Slaoui A, Švrček V, Del Cañizo C, Tobias I. Modifying the solar spectrum to enhance silicon solar cell efficiency—An overview of available materials. *Solar Energy Materials and Solar Cells* 2007; **91**(4): 238-249. doi: 10.1016/j.solmat.2006.09.003.
55. Klampaftis E, Ross D, McIntosh KR, Richards BS. Enhancing the performance of solar cells *via* luminescent down-shifting of the incident spectrum: A review. *Solar Energy Materials and Solar Cells* 2009; **93**(8): 1182-1194. doi: 10.1016/j.solmat.2009.02.020.
56. Trupke T, Green M, Würfel P. Improving solar cell efficiencies by up-conversion of sub-band-gap light. *Journal of Applied Physics* 2002; **92**(7): 4117-4122. doi: 10.1063/1.1505677.
57. Atre AC, Dionne JA. Realistic upconverter-enhanced solar cells with non-ideal absorption and recombination efficiencies. *Journal of Applied Physics* 2011; **110**(3): 034505. doi: 10.1063/1.3610522.
58. Johnson CM, Conibeer GJ. Limiting efficiency of generalized realistic c-Si solar cells coupled to ideal up-converters. *Journal of Applied Physics* 2012; **112**(10): 103108. doi: 10.1063/1.4766386.
59. Badescu V. An extended model for upconversion in solar cells. *Journal of Applied Physics* 2008; **104**(11): 113120. doi: 10.1063/1.3040692.

60. Würfel P, Würfel U. *Physics of Solar Cells: From Basic Principles to Advanced Concepts*. John Wiley & Sons: Weinheim, Germany, 2009;
61. Winston R, Miñano JC, Benitez PG. *Nonimaging Optics*. Academic Press: Amsterdam; Boston, Mass., 2005;
62. Friedman E, Miller JL. *Photonics Rules of Thumb: Optics, Electro-Optics, Fiber Optics, and Lasers*. SPIE, The McGraw-Hill Companies, Inc.: 2004;
63. Kurtz S, "Opportunities and Challenges for Development of a Mature Concentrating Photovoltaic Power Industry (Revision)," DOE Contract No. DE-AC36-08GO28308 (National Renewable Energy Laboratory, Golden, CO., 2010).
64. Kotsidas P, Modi V, Gordon JM. Gradient-index lenses for near-ideal imaging and concentration with realistic materials. *Optics Express* 2011; **19**(16): 15584-15595. doi: 10.1364/OE.19.015584.
65. Kotsidas P, Modi V, Gordon JM. Nominally stationary high-concentration solar optics by gradient-index lenses. *Optics Express* 2011; **19**(3): 2325-2334. doi: 10.1364/OE.19.002325.
66. Karp JH, Tremblay EJ, Ford JE. Planar micro-optic solar concentrator. *Optics Express* 2010; **18**(2): 1122-1133. doi: 10.1364/OE.18.001122.
67. Karp JH, Tremblay EJ, Hallas JM, Ford JE. Orthogonal and secondary concentration in planar micro-optic solar collectors. *Optics Express* 2011; **19**(104): A673-A685. doi: 10.1364/OE.19.00A673.
68. Duerr F, Meuret Y, Thienpont H. Tracking integration in concentrating photovoltaics using laterally moving optics. *Optics Express* 2011; **19**(103): A207-A218. doi: 10.1364/OE.19.00A207.
69. Hallas JM, Baker KA, Karp JH, Tremblay EJ, Ford JE. Two-axis solar tracking accomplished through small lateral translations. *Applied Optics* 2012; **51**(25): 6117-6124. doi: 10.1364/AO.51.006117.
70. Cotal H, Sherif R. The effects of chromatic aberration on the performance of GaInP/GaAs/Ge concentrator solar cells from Fresnel optics. *Conference Record of the Thirty-first IEEE Photovoltaic Specialists Conference,* 2005; 747-750. doi: 10.1109/PVSC.2005.1488240.
71. Victoria M, Herrero R, Domínguez C, Antón I, Askins S, Sala G. Characterization of the spatial distribution of irradiance and spectrum in concentrating photovoltaic systems and their effect on multi-junction solar cells. *Progress in Photovoltaics: Research and Applications* 2013; **21**(3): 308-318. doi: 10.1002/pip.1183.
72. Leutz R, Suzuki A. *Nonimaging Fresnel lenses: design and performance of solar concentrators*. Springer: 2001;
73. Stefancich M, Zayan A, Chiesa M, Rampino S, Roncati D, Kimerling L, Michel J. Single element spectral splitting solar concentrator for multiple cells CPV system. *Optics Express* 2012; **20**(8): 9004-9018. doi: 10.1364/OE.20.009004.
74. Wang C-M, Huang H-I, Pan J, Kuo H-Z, Hong H-F, Shin H-Y, Chang J-Y. Single stage transmission type broadband solar concentrator. *Optics Express* 2010; **18**(102): A118-A125. doi: 10.1364/OE.18.00A118.
75. Cassarly W, "Nonimaging optics: concentration and illumination," in *Handbook of Optics,* 2nd ed., M. Bass, ed. (McGraw-Hill, 2000), pp. 71-123.
76. Rabl A. Comparison of solar concentrators. *Solar Energy* 1976; **18**(2): 93-111. doi: 10.1016/0038-092X%2876%2990043-8.
77. Chaves J. *Introduction to nonimaging optics*. CRC Press: 2008;
78. Hecht E. *Optics*. 4th ed. Addison-Wesley: San Francisco, CA 94111, 2002; 122-127.

79. Garwin R. The design of liquid scintillation cells. *Review of Scientific Instruments* 1952; **23**(12): 755-757. doi: 10.1063/1.1746152.
80. Powell WR. Transmission characteristics of specularly reflecting light pipes uniformly irradiated by obliquely inclined rays. *Applied Optics* 1974; **13**(4): 952-954. doi: 10.1364/AO.13.000952.
81. Myer J. Collimated radiation in conical light guides. *Applied Optics* 1980; **19**(18): 3121-3124. doi: 10.1364/AO.19.003121.
82. Williamson DE. Cone Channel Condenser Optics. *Journal of the Optical Society of America* 1952; **42**(10): 712-714. doi: 10.1364/josa.42.000712.
83. Keck P, Redmann J, White C, DeKinder Jr R. A New Condenser for a Sun-Powered Continuous Laser. *Applied Optics* 1963; **2**(8): 827-831. doi: 10.1364/AO.2.000827.
84. Winston R. Dielectric compound parabolic concentrators. *Applied Optics* 1976; **15**(2): 291-292. doi: 10.1364/AO.15.000291.
85. Hinterberger H, Winston R. Use of a solid light funnel to increase phototube aperture without restricting angular acceptance. *Review of Scientific Instruments* 1968; **39**(8): 1217-1218. doi: 10.1063/1.1683629.
86. Scharlack R. All-dielectric compound parabolic concentrator. *Applied Optics* 1977; **16**(10): 2601-2602. doi: 10.1364/AO.16.002601.
87. Winston R, Zhang W. Pushing concentration of stationary solar concentrators to the limit. *Optics Express* 2010; **18**(101): A64-A72. doi: 10.1364/OE.18.000A64.
88. Hull JR. Dielectric compound parabolic concentrating solar collector with a frustrated total internal reflection absorber. *Applied Optics* 1989; **28**(1): 157-162. doi: 10.1364/AO.28.000157.
89. Ali IMS, O'Donovan TS, Reddy K, Mallick TK. An optical analysis of a static 3-D solar concentrator. *Solar Energy* 2013; **88**(57-70. doi: 10.1016/j.solener.2012.11.004.
90. Winston R. Light collection within the framework of geometrical optics. *Journal of the Optical Society of America* 1970; **60**(2): 245-247. doi: 10.1364/JOSA.60.000245.
91. Edmonds I. Prism-coupled compound parabola: a new ideal and optimal solar concentrator. *Optics Letters* 1986; **11**(8): 490-492. doi: 10.1364/OL.11.000490.
92. O'Gallagher J, Winston R, Welford WT. Axially symmetric nonimaging flux concentrators with the maximum theoretical concentration ratio. *Journal of the Optical Society of America* 1987; **4**(1): 66-68. doi: 10.1364/JOSAA.4.000066.
93. Ning X, Winston R, O'Gallagher J. Dielectric totally internally reflecting concentrators. *Applied Optics* 1987; **26**(2): 300-305. doi: 10.1364/AO.26.000300.
94. Miñano JC, Ruiz JM, Luque A. Design of optimal and ideal 2-D concentrators with the collector immersed in a dielectric tube. *Applied Optics* 1983; **22**(24): 3960-3965. doi: 10.1364/AO.22.003960.
95. Edmonds I. The performance of bifacial solar cells in static solar concentrators. *Solar Energy Materials* 1990; **21**(2): 173-190. doi: 10.1016/0165-1633(90)90052-3.
96. Rabl A. Prisms with total internal reflection as solar reflectors. *Solar Energy* 1977; **19**(5): 555-565. doi: 10.1016/0038-092X(77)90112-8.
97. Sellami N, Mallick TK. Optical characterisation and optimisation of a static Window Integrated Concentrating Photovoltaic system. *Solar Energy* 2013; **91**(273-282. doi: 10.1016/j.solener.2013.02.012.
98. Sarmah N, Richards BS, Mallick TK. Design, development and indoor performance analysis of a low concentrating dielectric photovoltaic module. *Solar Energy* 2014; **103**(390-401. doi: 10.1016/j.solener.2014.02.029.

99. Baig H, Sellami N, Chemisana D, Rosell J, Mallick TK. Performance analysis of a dielectric based 3D building integrated concentrating photovoltaic system. *Solar Energy* 2014; **103**(525-540. doi: 10.1016/j.solener.2014.03.002.
100. Spigulis J. Compact dielectric reflective elements. I. Half-sphere concentrators of radially emitted light. *Applied Optics* 1994; **33**(25): 5970-5974. doi: 10.1364/AO.33.005970.
101. Lassila E, Alahautala T, Hernberg R. Focusing diode laser light with a truncated dielectric paraboloid. *Optical Engineering* 2005; **44**(10): 103001-103001-103007. doi: 10.1117/1.2083207.
102. Lassila E, Hernberg R, Alahautala T. Focusing diode lasers using a truncated paraboloid with spherical output surface. *Optical Engineering* 2007; **46**(5): 054301-054301-054305. doi: 10.1117/1.2734993.
103. Sansoni P, Francini F, Fontani D, Mercatelli L, Jafrancesco D. Indoor illumination by solar light collectors. *Lighting Research & Technology* 2008; **40**(4): 323-332. doi: 10.1177/1477153508095128.
104. Liang DW, Monteiro LF, Teixeira MR, Monteiro MLF, Collares-Pereira M. Fiber-optic solar energy transmission and concentration. *Solar Energy Materials and Solar Cells* 1998; **54**(1-4): 323-331. doi: 10.1016/S0927-0248(98)00083-X.
105. Cariou JM, Dugas J, Martin L. Transport of Solar Energy with Optical Fibers. *Solar Energy* 1982; **29**(5): 397-406. doi: 10.1016/0038-092x(82)90076-7.
106. Jaramillo OA, del Rio JA. Optical fibres for a mini-dish/Stirling system: thermodynamic optimization. *Journal of Physics D-Applied Physics* 2002; **35**(11): 1241-1250. doi: 10.1088/0022-3727/35/11/322.
107. Peill NJ, Hoffmann MR. Solar-powered photocatalytic fiber-optic cable reactor for waste stream remediation. *Journal of Solar Energy Engineering* 1997; **119**(3): 229-236. doi: 10.1115/1.2888024.
108. Roger M, Bottger G, Dreschmann M, Klamouris C, Huebner M, Bett AW, Becker J, Freude W, Leuthold J. Optically powered fiber networks. *Optics Express* 2008; **16**(26): 21821-21834. doi: 10.1364/OE.16.021821.
109. Gordon JM, Katz EA, Feuermann D, Huleihil M. Toward ultrahigh-flux photovoltaic concentration. *Applied Physics Letters* 2004; **84**(18): 3642-3644. doi: 10.1063/1.1723690.
110. Anton I, Silva D, Sala G, Bett AW, Siefer G, Luque-Heredia I, Trebst T. The PV-FIBRE concentrator: A system for indoor operation of 1000× MJ solar cells. *Progress in Photovoltaics: Research and Applications* 2007; **15**(5): 431-447. doi: 10.1002/pip.745.
111. Kandilli C, Ulgen K. Review and modelling the systems of transmission concentrated solar energy *via* optical fibres. *Renewable & Sustainable Energy Reviews* 2009; **13**(1): 67-84. doi: 10.1016/j.rser.2007.05.005.
112. Cutolo A, Rendina I, Reale F. Coupling efficiency of non-uniform optical fibers for solar energy applications. *Solar Energy Materials* 1989; **18**(3-4): 191-200. doi: 10.1016/0165-1633(89)90053-1.
113. Cutolo A, Carlomusto L, Reale F, Rendina I. Tapered and inhomogeneous dielectric light concentrators. *Applied Optics* 1990; **29**(9): 1353-1364. doi: 10.1364/AO.29.001353.
114. Fang YP, Feuermann D, Gordon JM. Maximum-performance fiber-optic irradiation with nonimaging designs. *Applied Optics* 1997; **36**(28): 7107-7113. doi: 10.1364/AO.36.007107.
115. Ning XH. Three-dimensional ideal θ_1/θ_2 angular transformer and its uses in fiber optics. *Applied Optics* 1988; **27**(19): 4126-4130. doi: 10.1364/AO.27.004126.

116. Moslehi B, Ng J, Kasimoff I, Jannson T. Fiber-optic coupling based on nonimaging expanded-beam optics. *Optics Letters* 1989; **14**(23): 1327-1329. doi: 10.1364/OL.14.001327.
117. Nakamura T, Smith BK. Solar Thermal System for Lunar ISRU Applications: Development and Field Operation at Mauna Kea, HI. *SPIE Nonimaging Optics: Efficient Design for Illumination and Solar Concentration VIII,* San Diego, California, USA, 2011; 10.1117/12.892810.
118. Arecchi AV, Koshel RJ, Messadi T. *Field guide to illumination*. SPIE: Bellingham, Washington, 2007; xiv, 137 p.
119. Feuermann D, Gordon JM, Huleihil M. Solar fiber-optic mini-dish concentrators: first experimental results and field experience. *Solar Energy* 2002; **72**(6): 459-472. doi: 10.1016/S0038-092x(02)00025-7.
120. Feuermann D, Gordon JM, Huleihil M. Erratum to 'Solar fiber-optic mini-dish concentrators: first experimental results and field experience': [Solar Energy 72(6) (2002) 459–472]. *Solar Energy* 2002; **73**(1): 73-73. doi: 10.1016/S0038-092x(02)00061-0.
121. Connelly NG, Damhus T, Hartshorn RM, Hutton AT. *Nomenclature of inorganic chemistry: IUPAC recommendations 2005*. Royal Society of Chemistry: King's Lynn, Norfolk, UK, 2005; 51-52.
122. Bünzli J-CG, Piguet C. Taking advantage of luminescent lanthanide ions. *Chemical Society Reviews* 2005; **34**(12): 1048-1077. doi: 10.1039/b406082m.
123. Resch-Genger U, DeRose PC. Fluorescence standards: Classification, terminology, and recommendations on their selection, use, and production (IUPAC Technical Report). *Pure and Applied Chemistry* 2010; **82**(12): 2315-2335. doi: 10.1351/pac-rep-09-09-02.
124. Polman A. Erbium as a probe of everything? *Physica B: Condensed Matter* 2001; **300**(1): 78-90. doi: 10.1016/S0921-4526(01)00573-7.
125. Hollas JM. *Modern spectroscopy*. John Wiley & Sons: 2004; 270, 349.
126. Dieke GH, Crosswhite H. The spectra of the doubly and triply ionized rare earths. *Applied Optics* 1963; **2**(7): 675-686. doi: 10.1364/AO.2.000675.
127. Dieke GH, Crosswhite HM, Crosswhite H. *Spectra and energy levels of rare earth ions in crystals*. Interscience Publishers: New York, 1968; 128-143.
128. Wegh RT, Meijerink A, Lamminmäki R-J, Hölsä J. Extending Dieke's diagram. *Journal of Luminescence* 2000; **87-89**(1002-1004. doi: 10.1016/S0022-2313(99)00506-2.
129. Peijzel P, Meijerink A, Wegh R, Reid M, Burdick GW. A complete $4f^n$ energy level diagram for all trivalent lanthanide ions. *Journal of Solid State Chemistry* 2005; **178**(2): 448-453. doi: 10.1016/j.jssc.2004.07.046.
130. Kano T, "Principal phosphor materials & their optical properties," in *Phosphor Handbook*, W. M. Yen, S. Shionoya, and H. Yamamoto, eds. (CRC press, 2012), pp. 19-211.
131. Werts MH. Making sense of lanthanide luminescence. *Science Progress* 2005; **88**(2): 101-131. doi: 10.3184/003685005783238435.
132. Suijver JF, "Upconversion Phosphors," in *Luminescence: From Theory to Applications*, C. Ronda, ed. (Wiley-VCH Verlag GmbH & Co. KGaA, Weinheim, Germany, 2007), pp. 133-177.
133. Auzel F. Upconversion and anti-Stokes processes with f and d ions in solids. *Chemical Reviews* 2004; **104**(1): 139-174. doi: 10.1021/cr020357g.
134. Blasse G. Energy transfer in oxidic phosphors. *Physics Letters A* 1968; **28**(6): 444-445. doi: 10.1016/0375-9601(68)90486-6.
135. Förster T. Zwischenmolekulare energiewanderung und fluoreszenz. *Annalen der Physik* 1948; **437**(1-2): 55-75. doi: 10.1002/andp.19484370105.

136. Dexter DL. A theory of sensitized luminescence in solids. *The Journal of Chemical Physics* 1953; **21**(5): 836-850. doi: 10.1063/1.1699044.
137. Blasse G. The physics of new luminescent materials. *Materials Chemistry and Physics* 1987; **16**(3): 201-236. doi: 10.1016/0254-0584(87)90100-3.
138. Steinkemper H, Fischer S, Hermle M, Goldschmidt JC. Stark level analysis of the spectral line shape of electronic transitions in rare earth ions embedded in host crystals. *New Journal of Physics* 2013; **15**(5): 053033. doi: 10.1088/1367-2630/15/5/053033.
139. Becker PM, Olsson AA, Simpson JR. *Erbium-doped fiber amplifiers: fundamentals and technology*. Academic press: 1999; 105.
140. Solé J, Bausa L, Jaque D. *An introduction to the optical spectroscopy of inorganic solids*. John Wiley & Sons: 2005; 183, 200, 206.
141. Weber M. Radiative and multiphonon relaxation of rare-earth ions in Y_2O_3. *Physical Review* 1968; **171**(2): 283. doi: 10.1103/PhysRev.171.283.
142. Riseberg LA, Moos HW. Multiphonon orbit-lattice relaxation of excited states of rare-earth ions in crystals. *Physical Review* 1968; **174**(2): 429. doi: 10.1103/PhysRev.174.429.
143. Suyver J, Aebischer A, Biner D, Gerner P, Grimm J, Heer S, Krämer KW, Reinhard C, Güdel H. Novel materials doped with trivalent lanthanides and transition metal ions showing near-infrared to visible photon upconversion. *Optical Materials* 2005; **27**(6): 1111-1130. doi: 10.1016/j.optmat.2004.10.021.
144. Suyver J, Grimm J, Krämer KW, Güdel H. Highly efficient near-infrared to visible up-conversion process in $NaYF_4:Er^{3+},Yb^{3+}$. *Journal of Luminescence* 2005; **114**(1): 53-59. doi: 10.1016/j.jlumin.2004.11.012.
145. Shalav A. *Rare-earth doped up-converting phosphors for an enhanced silicon solar cell response*. Doctoral Thesis. University of New South Wales: Sydney, New South Wales, Australia, 2006;
146. Gamelin DR, Güdel HU, "Upconversion processes in transition metal and rare earth metal systems," in *Transition Metal and Rare Earth Compounds: Excited States, Transitions, Interactions II*, H. Yersin, ed. (Springer, Heidelberg, Berlin, 2001), pp. 1-56.
147. Johnson C. *Up-conversion for Crystalline Silicon Photovoltaics: Realistic Efficiency Limits and Enhancement in Photonic Structures*. Doctoral Thesis. University of New South Wales: Sydney, New South Wales, Australia, 2012;
148. Pollnau M, Gamelin D, Lüthi S, Güdel H, Hehlen M. Power dependence of upconversion luminescence in lanthanide and transition-metal-ion systems. *Physical Review B* 2000; **61**(5): 3337. doi: 10.1103/PhysRevB.61.3337.
149. Suyver J, Aebischer A, García-Revilla S, Gerner P, Güdel H. Anomalous power dependence of sensitized upconversion luminescence. *Physical Review B* 2005; **71**(12): 125123. doi: 10.1103/PhysRevB.71.125123.
150. Riedener T, Güdel HU. Up-Conversion Dynamics of Er^{3+} Doped $RbGd_2Br_7$. *The Journal of Chemical Physics* 1997; **107**(7): 2169-2174. doi: 10.1063/1.474597.
151. Ivaturi A, MacDougall SKW, Martín-Rodríguez R, Quintanilla M, Marques-Hueso J, Krämer KW, Meijerink A, Richards BS. Optimizing infrared to near infrared upconversion quantum yield of β-$NaYF_4:Er^{3+}$ in fluoropolymer matrix for photovoltaic devices. *Journal of Applied Physics* 2013; **114**(1): 013505-013505-013509. doi: 10.1063/1.4812578.
152. Munz P, Bucher E, "The use of rare earths in photovoltaics," in *The Rare Earths in Modern Science and Technology* (Springer, 1982), pp. 547-556.
153. Saxena V. Phosphors for solar-cells: Tb doped lanthanum fluoride and Th-doped calcium tungstate. *Indian Journal of Applied Physics* 1983; **21**(5): 306-307. doi:

154. Huang X, Han S, Huang W, Liu X. Enhancing solar cell efficiency: the search for luminescent materials as spectral converters. *Chemical Society Reviews* 2013; **42**(1): 173-201. doi: 10.1039/c2cs35288e.
155. Ramasamy P, Manivasakan P, Kim J. Upconversion nanophosphors for solar cell applications. *Royal Society of Chemistry Advances* 2014; **4**(66): 34873-34895. doi: 10.1039/C4RA03919J
156. Gibart P, Auzel F, Guillaume J-C, Zahraman K. Below brand-gap IR response of substrate-free GaAs solar cells using two-photon up-conversion. *Japanese Journal of Applied Physics* 1996; **35**(8): 4401-4402. doi: 10.1143/JJAP.35.4401.
157. Lin HY, Chen HN, Wu TH, Wu CS, Su YK, Chu SY. Investigation of Green Up-Conversion Behavior in $Y_6W_2O_{15}$:Yb^{3+},Er^{3+} Phosphor and its Verification in 973-nm Laser-Driven GaAs Solar Cell. *Journal of the American Ceramic Society* 2012; **95**(10): 3172-3179. doi: 10.1111/j.1551-2916.2012.05281.x.
158. De Wild J, Rath JK, Meijerink A, Van Sark WGJHM, Schropp REI. Enhanced near-infrared response of a-Si: H solar cells with β-$NaYF_4$:Yb^{3+}(18%), Er^{3+}(2%) upconversion phosphors. *Solar Energy Materials and Solar Cells* 2010; **94**(12): 2395-2398. doi: 10.1016/j.solmat.2010.08.024.
159. Li Z, Li X, Liu Q, Chen X, Sun Z, Liu C, Ye X, Huang SM. Core/shell structured $NaYF_4$:Yb^{3+}/Er^{3+}/Gd^{3+} nanorods with Au nanoparticles or shells for flexible amorphous silicon solar cells. *Nanotechnology* 2012; **23**(2): 025402. doi: 10.1088/0957-4484/23/2/025402.
160. Schulze TF, Schmidt TW. Photochemical upconversion: present status and prospects for its application to solar energy conversion. *Energy & Environmental Science* 2015; 10.1039/C4EE02481H.
161. Baluschev S, Miteva T, Yakutkin V, Nelles G, Yasuda A, Wegner G. Up-conversion fluorescence: noncoherent excitation by sunlight. *Physical Review Letters* 2006; **97**(14): 143903. doi: 10.1103/PhysRevLett.97.143903.
162. Ekins-Daukes N, Schmidt T. A molecular approach to the intermediate band solar cell: The symmetric case. *Applied Physics Letters* 2008; **93**(6): 063507. doi: 10.1063/1.2970157.
163. Sansonetti JE, Martin WC, Young S. Handbook of basic atomic spectroscopic data. *Journal of Physical and Chemical Reference Data* 2005; **34**(4): 1559-2260. doi: 10.1063/1.1800011.
164. Boccolini A, Faoro R, Favilla E, Veronesi S, Tonelli M. BaY_2F_8 doped with Er^{3+}: An upconverter material for photovoltaic application. *Journal of Applied Physics* 2013; **114**(6): 064904. doi: 10.1063/1.4817171.
165. Shalav A, Richards BS, Trupke T, Krämer KW, Güdel HU. Application of $NaYF_4$:Er^{3+} up-converting phosphors for enhanced near-infrared silicon solar cell response. *Applied Physics Letters* 2005; **86**(1): 013505. doi: 10.1063/1.1844592.
166. Richards BS, Shalav A. Enhancing the near-infrared spectral response of silicon optoelectronic devices *via* up-conversion. *IEEE Transactions on Electron Devices* 2007; **54**(10): 2679-2684. doi: 10.1109/TED.2007.903197.
167. MacDougall SK, Ivaturi A, Marques-Hueso J, Richards BS. Measurement procedure for absolute broadband infrared up-conversion photoluminescent quantum yields: Correcting for absorption/re-emission. *Review of Scientific Instruments* 2014; **85**(6): 063109. doi: 10.1063/1.4881537.
168. Fischer S, Fröhlich B, Steinkemper H, Krämer KW, Goldschmidt J. Absolute upconversion quantum yield of β-$NaYF_4$ doped with Er^{3+} and external quantum efficiency of upconverter solar cell devices under broad-band excitation considering spectral mismatch corrections. *Solar Energy Materials and Solar Cells* 2014; **122**(197-207. doi: 10.1016/j.solmat.2013.12.001.

169. Fischer S, Goldschmidt JC, Löper P, Bauer GH, Brüggemann R, Krämer KW, Biner D, Hermle M, Glunz SW. Enhancement of silicon solar cell efficiency by upconversion: Optical and electrical characterization. *Journal of Applied Physics* 2010; **108**(4): 044912. doi: 10.1063/1.3478742.
170. Martín-Rodríguez R, Fischer S, Ivaturi A, Froehlich B, Krämer KW, Goldschmidt JC, Richards BS, Meijerink A. Highly Efficient IR to NIR Upconversion in $Gd_2O_2S:Er^{3+}$ for Photovoltaic Applications. *Chemistry of Materials* 2013; **25**(9): 1912-1921. doi: 10.1021/cm4005745.
171. Fischer S, Goldschmidt JC, Favilla E, Tonelli M. Record Efficient Upconverter Solar Cell Devices with Optimized Bifacial Silicon Solar Cells and Monocrystalline BaY_2F_8:30%Er^{3+} Upconverter. *Solar Energy Materials and Solar Cells* 2015; **136**(0): 127–134. doi: 10.1016/j.solmat.2014.12.023.
172. Ahrens B, Löper P, Goldschmidt JC, Glunz S, Henke B, Miclea PT, Schweizer S. Neodymium-doped fluorochlorozirconate glasses as an upconversion model system for high efficiency solar cells. *physica status solidi (a)* 2008; **205**(12): 2822-2830. doi: 10.1002/pssa.200880452.
173. Lin H, Marqués-Hueso J, Chen D, Wang Y, Richards BS. Tm^{3+}-sensitized up- and down-conversions in nano-structured oxyfluoride glass ceramics. *Materials Research Bulletin* 2012; **47**(12): 4433-4437. doi: 10.1016/j.materresbull.2012.09.048.
174. Ball D, Shalav A, Conibeer G, "Investigation of $NaYF_4$: Er co-doped phosphors for the up-conversion of sub-bandgap photons in silicon solar cells," in *Australian & New Zealand Solar Energy Society: Destination Renewables,* (The Australian National University, Canberra, Australia, 2006).
175. Strümpel C, McCann M, Del Cañizo C, Tobias I, Fath P. Erbium-doped up-converters on silicon solar cells: assessment of the potential. *Proceedings of the 20th European Photovoltaic Solar Energy Conference,* 2005; 43-46. doi:
176. Lahoz F. Ho^{3+}-doped nanophase glass ceramics for efficiency enhancement in silicon solar cells. *Optics Letters* 2008; **33**(24): 2982-2984. doi: 10.1364/OL.33.002982.
177. Hernández-Rodríguez M, Imanieh M, Martín L, Martín I. Experimental enhancement of the photocurrent in a solar cell using upconversion process in fluoroindate glasses exciting at 1480nm. *Solar Energy Materials and Solar Cells* 2013; **116**(171-175. doi: 10.1016/j.solmat.2013.04.023.
178. Strümpel C. *Application of erbium-doped up-converters to silicon solar cells*. Doctoral Thesis. Universität Konstanz: Konstanz, Germany, 2007; 119-122. doi:
179. Goldschmidt JC, Loper P, Fischer S, Janz S, Peters M, Glunz SW, Willeke G, Lifshitz E, Krämer KW, Biner D. Advanced upconverter systems with spectral and geometric concentration for high upconversion efficiencies. *IEEE Conference on Optoelectronic and Microelectronic Materials and Devices,* Sydney, SA, 2008; 307-311. doi: 10.1109/commad.2008.4802153.
180. Pan AC, Del Cañizo C, Cánovas E, Santos N, Leitão J, Luque A. Enhancement of up-conversion efficiency by combining rare earth-doped phosphors with PbS quantum dots. *Solar Energy Materials and Solar Cells* 2010; **94**(11): 1923-1926. doi: 10.1016/j.solmat.2010.06.028.
181. Marques-Hueso J, Peretti R, Abargues R, Richards BS, Seassal C, Martínez-Pastor JP. Photonic Crystal-Driven Spectral Concentration for Upconversion Photovoltaics. *Advanced Optical Materials* 2014; 10.1002/adom.201400402.
182. Fischer S, Ivaturi A, Fröhlich B, Rudiger M, Richter A, Krämer KW, Richards BS, Goldschmidt JC. Upconverter silicon solar cell devices for efficient utilization of sub-band-gap photons under concentrated solar radiation. *IEEE*

Journal of Photovoltaics 2014; **4**(1): 183-189. doi: 10.1109/jphotov.2013.2282744.

183. MacDougall SKW, Ivaturi A, Marques-Hueso J, Krämer KW, Richards BS. Ultra-high photoluminescent quantum yield of β-$NaYF_4$:10% Er^{3+} *via* broadband excitation of upconversion for photovoltaic devices. *Optics Express* 2012; **20**(23): A879-887. doi: 10.1364/OE.20.00A879.
184. MacDougall SKW, Ivaturi A, Marques-Hueso J, Krämer KW, Richards BS. Broadband photoluminescent quantum yield optimisation of Er^{3+}-doped β-$NaYF_4$ for upconversion in silicon solar cells. *Solar Energy Materials and Solar Cells* 2014; **128**(0): 18-26. doi: 10.1016/j.solmat.2014.05.004.
185. Boccolini A, Marques-Hueso J, Richards BS. Self-absorption in upconverter luminescent layers: impact on quantum yield measurements and on designing optimized photovoltaic devices. *Optics Letters* 2014; **39**(10): 2904-2907. doi: 10.1364/OL.39.002904.
186. Handy J, Peterson T. Concentrating PV survey: an unbiased overview. *SPIE High and Low Concentrator Systems for Solar Electric Applications VI,* San Diego, California, 2011; 810808-810808-810811. doi: 10.1117/12.897957.
187. Cooke D, Gleckman P, Krebs H, O'Gallagher J, Sagie D, Winston R. Sunlight brighter than the sun. *Nature* 1990; **346**(802. doi: 10.1038/346802a0.
188. Arnaoutakis GE, Marques-Hueso J, Mallick TK, Richards BS. Coupling of sunlight into optical fibres and spectral dependence for solar energy applications. *Solar Energy* 2013; **93**(0): 235-243. doi: 10.1016/j.solener.2013.04.008.
189. Sinton R, Kwark Y, Gan J, Swanson RM. 27.5-percent silicon concentrator solar cells. *IEEE Electron Device Letters* 1986; **7**(10): 567-569. doi: 10.1109/EDL.1986.26476.
190. Mohr A, Roth T, Glunz SW. BICON: high concentration PV using one axis tracking and silicon concentrator cells. *Progress in Photovoltaics: Research and Applications* 2006; **14**(7): 663-674. doi: 10.1002/pip.691.
191. Sinton RA, Swanson RM. Recombination in highly injected silicon. *IEEE Transactions on Electron Devices* 1987; **34**(6): 1380-1389. doi: 10.1109/T-ED.1987.23095.
192. Algora C, Diaz V. Influence of series resistance on guidelines for manufacture of concentrator p-on-n GaAs solar cells. *Progress in Photovoltaics: Research and Applications* 2000; **8**(2): 211-225. doi: 10.1002/(SICI)1099-159X(200003/04)8:2<211::AID-PIP291>3.0.CO;2-D.
193. Galiana B, Algora C, Rey-Stolle I, Vara IG. A 3-D model for concentrator solar cells based on distributed circuit units. *IEEE Transactions on Electron Devices* 2005; **52**(12): 2552-2558. doi: 10.1109/TED.2005.859620.
194. Katz EA, Gordon JM, Feuermann D. Effects of ultra high flux and intensity distribution in multi junction solar cells. *Progress in Photovoltaics: Research and Applications* 2006; **14**(4): 297-303. doi: 10.1002/pip.670.
195. Slade A, Garboushian V. 27.6% efficient silicon concentrator solar cells for mass production. *Technical Digest of the 15th International Photovoltaic Science and Engineering Conference,* Beijing, 2005;
196. Algora C, Ortiz E, Rey-Stolle I, Diaz V, Pena R, Andreev VM, Khvostikov VP, Rumyantsev VD. A GaAs solar cell with an efficiency of 26.2% at 1000 suns and 25.0% at 2000 suns. *IEEE Transactions on Electron Devices* 2001; **48**(5): 840-844. doi: 10.1109/16.918225.
197. Baluschev S, Yu F, Miteva T, Ahl S, Yasuda A, Nelles G, Knoll W, Wegner G. Metal-enhanced up-conversion fluorescence: effective triplet-triplet annihilation

near silver surface. *Nano letters* 2005; **5**(12): 2482-2484. doi: 10.1021/nl0517969.
198. Mertens H, Polman A. Plasmon-enhanced erbium luminescence. *Applied Physics Letters* 2006; **89**(21): 211107. doi: 10.1063/1.2392827.
199. Aisaka T, Fujii M, Hayashi S. Enhancement of upconversion luminescence of Er doped Al_2 O_3 films by Ag island films. *Applied Physics Letters* 2008; **92**(13): 132105-132105-132103. doi: 10.1063/1.2896303.
200. Verhagen E, Kuipers L, Polman A. Field enhancement in metallic subwavelength aperture arrays probed by erbium upconversion luminescence. *Optics Express* 2009; **17**(17): 14586-14598. doi: 10.1364/OE.17.014586.
201. Fischer S, Hallermann F, Eichelkraut T, von Plessen G, Krämer KW, Biner D, Steinkemper H, Hermle M, Goldschmidt JC. Plasmon enhanced upconversion luminescence near gold nanoparticles–simulation and analysis of the interactions. *Optics Express* 2012; **20**(1): 271-282. doi: 10.1364/OE.20.000271.
202. Fischer S, Hallermann F, Eichelkraut T, von Plessen G, Krämer KW, Biner D, Steinkemper H, Hermle M, Goldschmidt JC. Plasmon enhanced upconversion luminescence near gold nanoparticles–simulation and analysis of the interactions: Errata. *Optics Express* 2013; **21**(9): 10606-10611. doi: 10.1364/OE.21.010606.
203. Atre AC, García-Etxarri A, Alaeian H, Dionne JA. Toward high-efficiency solar upconversion with plasmonic nanostructures. *Journal of Optics* 2012; **14**(2): 024008. doi: 10.1088/2040-8978/14/2/024008.
204. Johnson C, Reece P, Conibeer G. Theoretical and experimental evaluation of silicon photonic structures for enhanced erbium up-conversion luminescence. *Solar Energy Materials and Solar Cells* 2013; **112**(0): 168-181. doi: 10.1016/j.solmat.2013.01.026.
205. Herter B, Wolf S, Fischer S, Gutmann J, Bläsi B, Goldschmidt JC. Increased upconversion quantum yield in photonic structures due to local field enhancement and modification of the local density of states–a simulation-based analysis. *Optics Express* 2013; **21**(105): A883-A900. doi: 10.1364/OE.21.00A883.
206. Morton J, Marques-Hueso J, Richards BS. Enhanced Up-conversion for Photovoltaics using 2D Photonic Crystals. *OSA Renewable Energy and the Environment Congress - Optical Instrumentation for Energy and Environmental Applications,* Tucson, Arizona United States, 2013; JM3A. 19. doi: 10.1364/freeform.2013.jm3a.19.
207. Le KQ, John S. Synergistic plasmonic and photonic crystal light-trapping: Architectures for optical up-conversion in thin-film solar cells. *Optics Express* 2014; **22**(101): A1-A12. doi: 10.1364/OE.22.0000A1.
208. Schulze TF, Cheng YY, Khoury T, Crossley MJ, Stannowski B, Lips K, Schmidt TW. Micro-optical design of photochemical upconverters for thin-film solar cells. *Journal of Photonics for Energy* 2013; **3**(1): 034598-034598. doi: 10.1117/1.JPE.3.034598.
209. Strümpel C, Hahn G, McCann M. Influence of hygroscopy on the optical properties of the up-converter $BaCl_2$: Er^{3+}. *Proceedings of the 23rd European Photovoltaic Solar Energy Conference,* 2008; 10.4229/23rdEUPVSEC2008-1DV.2.17.
210. Kik P, De Dood M, Kikoin K, Polman A. Excitation and deexcitation of Er^{3+} in crystalline silicon. *Applied Physics Letters* 1997; **70**(13): 1721-1723. doi: 10.1063/1.118680.
211. Hamelin N, Kik P, Suyver J, Kikoin K, Polman A, Schönecker A, Saris F. Energy backtransfer and infrared photoresponse in erbium-doped silicon p–n

diodes. *Journal of Applied Physics* 2000; **88**(9): 5381-5387. doi: 10.1063/1.1310188.
212. Kenyon A. Erbium in silicon. *Semiconductor Science and Technology* 2005; **20**(12): R65. doi: 10.1088/0268-1242/20/12/R02.
213. Zanatta A, Nunes L. Green photoluminescence from Er-containing amorphous SiN thin films. *Applied Physics Letters* 1998; **72**(24): 3127-3129. doi: 10.1063/1.121568.
214. Heikenfeld J, Garter M, Lee D, Birkhahn R, Steckl A. Red light emission by photoluminescence and electroluminescence from Eu-doped GaN. *Applied Physics Letters* 1999; **75**(9): 1189-1191. doi: 10.1063/1.124686.
215. Kudryavtsev K, Kryzhkov D, Antonov A, Shengurov D, Shmagin V, Krasilnik Z. Specific features of the nonradiative relaxation of Er^{3+} ions in epitaxial Si structures. *Semiconductors* 2014; **48**(12): 1586-1591. doi: 10.1134/S1063782614120112.
216. Lang M, Milster TD. Investigation of Optics in the 10–200μm Size Regime. *Optical Review* 2007; **14**(4): 189-193. doi: 10.1007/s10043-007-0189-8.
217. Stevenson MA. *Human Skin and Tissue Phantoms in Optical Software: Engineering Design and Future Medical Applications*. University of Arizona: Tucson, AZ , 85715, 2009;
218. Oskooi AF, Roundy D, Ibanescu M, Bermel P, Joannopoulos JD, Johnson SG. MEEP: A flexible free-software package for electromagnetic simulations by the FDTD method. *Computer Physics Communications* 2010; **181**(3): 687-702. doi: 10.1016/j.cpc.2009.11.008.
219. Sellmeier. Zur erklärung der abnormen Farbenfolge im Spectrum einiger Substanzen. *Annalen der Physik und Chemie* 1871; **219**(6): 272-282. doi: 10.1002/andp.18712190612.
220. Fleming J. Material dispersion in lightguide glasses. *Electronics Letters* 1978; **14**(11): 326-328. doi: 10.1049/el:19780222.
221. Fleming J. Erratum: Material dispersion in lightguide glasses. *Electronics Letters* 1979; **15**(16): 507. doi: 10.1049/el:19790367.
222. Malitson IH. Interspecimen Comparison of the Refractive Index of Fused Silica. *Journal of the Optical Society of America* 1965; **55**(10): 1205-1208. doi: 10.1364/josa.55.001205.
223. Schott North America I, "Optical Glass Data Sheets," S. A. Optics, ed. (400 York Avenue, Duryea, PA18642, USA, 2012).
224. Zorabedian P, "Tunable external-cavity semiconductor lasers," in *Tunable Lasers Handbook*, F. J. Duarte, ed. (Academic Press Ltd., 24-28 Oval Road, London, NW1 7DX, 1995), pp. 349-442.
225. Müller E, Reichert W, Rück C, Steiner R. External-cavity laser design and wavelength calibration. *Hewlett-Packard Journal* 1993; **44**(1): 20-27. doi:
226. Siegman A. How to (Maybe) Measure Laser Beam Quality. *OSA Diode Pumped Solid State Lasers: Applications and Issues - M^2 Laser Beam Quality and Characterization (MQ),* Washington D.C. United States, 1998; 10.1364/dlai.1998.mq1.
227. Weimer PK, Forgue SV, Goodrich RR. The vidicon photoconductive camera tube. *Electronics* 1950; 70-73. doi:
228. Redington R, "Introduction to the Vidicon Family of Tubes," in *Photoelectronic Imaging Devices*, L. M. Biberman and S. Nudelman, eds. (Springer, US, 1971), pp. 263-273.
229. Siegman AE. *Lasers*. University Science Books: Mill Valley, California, 1986; 675-679.

230. Walker JH, Saunders RD, Jackson J, McSparron D. The NBS scale of spectral irradiance. *Journal of Research of the National Institute of Standards and Technology* 1988; **93**(1): 7. doi: 10.6028/jres.093.003.
231. Zhou C, Verlinden P, Crane R, Swanson R, Sinton R, "21.9% efficient silicon bifacial solar cells," in *Conference Record of the 26th IEEE Photovoltaic Specialists Conference,* (IEEE, Anaheim, CA, 1997), pp. 287-290.
232. Krämer KW, Biner D, Frei G, Güdel HU, Hehlen MP, Luthi SR. Hexagonal sodium yttrium fluoride based green and blue emitting upconversion phosphors. *Chemistry of Materials* 2004; **16**(7): 1244-1251. doi: 10.1021/cm031124o.
233. Thoma R, Insley H, Hebert G. The sodium fluoride-lanthanide trifluoride systems. *Inorganic chemistry* 1966; **5**(7): 1222-1229. doi: 10.1021/ic50041a032.
234. Suyver J, Grimm J, Van Veen M, Biner D, Krämer KW, Güdel H. Upconversion spectroscopy and properties of $NaYF_4$ doped with Er^{3+}, Tm^{3+} and/or Yb^{3+}. *Journal of Luminescence* 2006; **117**(1): 1-12. doi: 10.1016/j.jlumin.2005.03.011.
235. Smith DW, Chen S, Kumar SM, Ballato J, Topping C, Shah HV, Foulger SH. Perfluorocyclobutyl copolymers for microphotonics. *Advanced Materials* 2002; **14**(21): 1585-1589. doi:
236. Ballato J, Foulger SH, Smith Jr DW. Optical properties of perfluorocyclobutyl polymers. II. Theoretical and experimental attenuation. *Journal of the Optical Society of America B* 2004; **21**(5): 958-967. doi: 10.1364/JOSAB.21.000958.
237. Gordon J, Ballato J, Smith Jr DW, Jin J. Optical properties of perfluorocyclobutyl polymers. III. Spectroscopic characterization of rare-earth-doped perfluorocyclobutyl polymers. *Journal of the Optical Society of America B* 2005; **22**(8): 1654-1659. doi: 10.1364/josab.22.001654.
238. Guilbert L, Gesland J, Bulou A, Retoux R. Structure and Raman spectroscopy of Czochralski-grown barium yttrium and barium ytterbium fluorides crystals. *Materials Research Bulletin* 1993; **28**(9): 923-930. doi: 10.1016/0025-5408(93)90039-G.
239. Kaminskii A, Lux O, Hanuza J, Rhee H, Eichler H, Zhang J, Tang D, Shen D, Yu H, Wang J. Monoclinic β-BaY_2F_8—a novel crystal simultaneously active for SRS and Ln^{3+}-ion lasing. *Laser Physics* 2015; **25**(1): 015801. doi: 10.1088/1054-660X/25/1/015801.
240. Kaminskii AA. *Laser Crystals: Their Physics and Properties*. Springer-Verlag: Berlin, Heidelberg, 1981;
241. Mendez A, Morse TF. *Specialty Optical Fibers Handbook*. Academic Press: Amsterdam ; Boston, 2007; xlii, 798 p.
242. French R, Rodríguez-Parada J, Yang M, Derryberry R, Pfeiffenberger N. Optical properties of polymeric materials for concentrator photovoltaic systems. *Solar Energy Materials and Solar Cells* 2011; **95**(8): 2077-2086. doi: 10.1016/j.solmat.2011.02.025.
243. Qu Y, Puttitwong E, Howell JR, Ezekoye OA. Errors associated with light-pipe radiation thermometer temperature measurements. *IEEE Transactions on Semiconductor Manufacturing* 2007; **20**(1): 26-38. doi: 10.1109/TSM.2007.890772.
244. Liang DW, Nunes Y, Monteiro LF, Monteiro MLF, CollaresPereira M. 200-W solar energy delivery with optical fiber bundles. *SPIE Nonimaging Optics: Maximum Efficiency Light Transfer IV,* San Diego, CA, 1997; 217-224. doi: 10.1117/12.279217.
245. Nakamura T, Comaskey B, Bell M. Development of Optical Components for Space-Based Solar Power System for ISRU and Regenerative Life Support. *40th AIAA Aerospace Sciences Meeting and Exhibit,* Reno, NV, 2002; 2002-0462. doi: 10.2514/6.2002-462.

246. Feuermann D, Gordon JM, Huleihil M. Light leakage in optical fibers: Experimental results, modeling and the consequences for solar concentrators. *Solar Energy* 2002; **72**(3): 195-204. doi: 10.1016/s0038-092x(01)00100-1.
247. Garcia-Botella A, Fernandez-Balbuena AA, Vázquez D, Bernabeu E. Ideal 3D asymmetric concentrator. *Solar Energy* 2009; **83**(1): 113-117. doi: 10.1016/j.solener.2008.07.004.
248. Rabl A. *Active solar collectors and their applications*. Oxford University Press, USA: 200 Madison Avenue, New York, New York 10016, 1985; 182.
249. Limpert J, Liem A, Zellmer H, Tünnermann A. 500 W continuous-wave fibre laser with excellent beam quality. *Electronics Letters* 2003; **39**(8): 645-647. doi: 10.1049/el:20030447.
250. Myslinski P, Nguyen D, Chrostowski J. Effects of concentration on the performance of erbium-doped fiber amplifiers. *Journal of Lightwave Technology* 1997; **15**(1): 112-120. doi: 10.1109/50.552118.
251. Snitzer E, Po H, Hakimi F, Tumminelli R, McCollum B. Double clad, offset core Nd fiber laser. *OSA Optical Fiber Sensors,* New Orleans, LA, 1988; PD5. doi:
252. Nilsson J, Clarkson W, Selvas R, Sahu J, Turner P, Alam S-U, Grudinin A. High-power wavelength-tunable cladding-pumped rare-earth-doped silica fiber lasers. *Optical Fiber Technology* 2004; **10**(1): 5-30. doi: 10.1016/j.yofte.2003.07.001.
253. Kouznetsov D, Moloney JV, Wright EM. Efficiency of pump absorption in double-clad fiber amplifiers. I. Fiber with circular symmetry. *Journal of the Optical Society of America B* 2001; **18**(6): 743-749. doi: 10.1364/josab.18.000743.
254. Kouznetsov D, Moloney JV. Efficiency of pump absorption in double-clad fiber amplifiers. II. Broken circular symmetry. *Journal of the Optical Society of America B* 2002; **19**(6): 1259-1263. doi: 10.1364/josab.19.001259.
255. Kouznetsov D, Moloney JV. Efficiency of pump absorption in double-clad fiber amplifiers. III. Calculation of modes. *Journal of the Optical Society of America B* 2002; **19**(6): 1304-1309. doi: 10.1364/josab.19.001304.
256. Klocek P, Sigel GH. *Infrared Fiber Optics*. SPIE Press: Bellingham, Washington, 1989; 12.
257. Boccolini A, Marques-Hueso J, Chen D, Wang Y, Richards B. Physical performance limitations of luminescent down-conversion layers for photovoltaic applications. *Solar Energy Materials and Solar Cells* 2014; **122**(8-14. doi: 10.1016/j.solmat.2013.11.005.
258. Dubinskii M, Zhang J, Kudryashov I. Single-frequency, Yb-free, resonantly cladding-pumped large mode area Er fiber amplifier for power scaling. *Applied Physics Letters* 2008; **93**(3): 031111. doi: 10.1063/1.2964189.
259. Guzman-Chavez A, Barmenkov YO, Kiryanov A. Spectral dependence of the excited-state absorption of erbium in silica fiber within the 1.48–1.59 μm range. *Applied Physics Letters* 2008; **92**(19): 191111-191111-191113. doi: 10.1063/1.2926671.
260. Blixt P, Nilsson J, Carlnäs T, Jaskorzynska B. Concentration-dependent upconversion in Er^{3+}-doped fiber amplifiers: Experiments and modeling. *IEEE Photonics Technology Letters* 1991; **3**(11): 996-998. doi: 10.1109/68.97839.
261. Nilsson J, Blixt P, Jaskorzynska B, Babonas J. Evaluation of parasitic upconversion mechanisms in Er^{3+}-doped silica-glass fibers by analysis of fluorescence at 980 nm. *Journal of Lightwave Technology* 1995; **13**(3): 341-349. doi: 10.1109/50.372427.

262. Ainslie BJ. A review of the fabrication and properties of erbium-doped fibers for optical amplifiers. *Journal of Lightwave Technology* 1991; **9**(2): 220-227. doi: 10.1109/50.65880.
263. Khoptyar D, Jaskorzynska B. Experimental determination of the energy-transfer parameters for homogeneous upconversion in Er-doped silica. *Journal of the Optical Society of America B* 2005; **22**(10): 2091-2098. doi: 10.1364/josab.22.002091.
264. Khoptyar D, Sergeyev S, Jaskorzynska B. Homogeneous upconversion in Er-doped fibers under steady state excitation: analytical model and its Monte Carlo verification. *Journal of the Optical Society of America B* 2005; **22**(3): 582-590. doi: 10.1364/josab.22.000582.
265. Delevaque E, Georges T, Monerie M, Lamouler P, Bayon J. Modeling of pair-induced quenching in erbium-doped silicate fibers. *IEEE Photonics Technology Letters* 1993; **5**(1): 73-75. doi: 10.1109/68.185065.
266. Ye C, Morkel P, Taylor E, Payne D. Direct observation of cooperative upconversion mechanisms in Erbium-doped fiber amplifiers. *19th European Conference on Optical Communication (ECOC),* Montreux, Switzerland, 1993; 73-76. doi:
267. Di Pasquale F, Federighi M. Modelling of uniform and pair-induced upconversion mechanisms in high-concentration erbium-doped silica waveguides. *Journal of Lightwave Technology* 1995; **13**(9): 1858-1864. doi: 10.1109/50.464735.
268. Auzel F, Chen Y. Multiphonon pumping in Er^{3+} ZBLAN bulk and fibre, the first step for the photon avalanche process. *Journal of Non-Crystalline Solids* 1995; **184**(57-60. doi: 10.1016/0022-3093(94)00595-8.
269. Goldner P, Auzel FE. Propagation modes and avalanche spatial domains in Er-doped ZBLAN fiber. *SPIE Infrared Glass Optical Fibers and Their Applications,* Quebec, Canada, 1998; 157-164. doi: 10.1117/12.323385.
270. Mohr A, Steuder M, Bett A, Glunz S. Silicon concentrator cells designed for a direct mounting on compound parabolic concentrator. *IEEE Proceedings of the 3rd World Conference on Photovoltaic Energy Conversion,* Osaka, Japan, 2003; 841-844. doi:
271. Mohr A. *Silicon concentrator cells in a two-stage photovoltaic system with a concentration factor of 300*×. Doctoral Thesis. Albert-Ludwigs-Universität: Freiburg im Breisgau, Germany, 2005;
272. Rüdiger M, Fischer S, Frank J, Ivaturi A, Richards BS, Krämer KW, Hermle M, Goldschmidt JC. Bifacial n-type silicon solar cells for upconversion applications. *Solar Energy Materials and Solar Cells* 2014; **128**(0): 57-68. doi: 10.1016/j.solmat.2014.05.014.
273. Welford W, Winston R. *High Collection Nonimaging Optics*. Academic Press: San Diego, 1989;
274. Bennett JM, Ashley E. Infrared reflectance and emittance of silver and gold evaporated in ultrahigh vacuum. *Applied Optics* 1965; **4**(2): 221-224. doi: 10.1364/AO.4.000221.
275. Zinter JP, Levene MJ. Maximizing fluorescence collection efficiency in multiphoton microscopy. *Optics Express* 2011; **19**(16): 15348. doi: 10.1364/OE.19.015348.
276. Rice JP, Zong Y, Dummer DJ. Spatial uniformity comparison of two nonimaging concentrators. *Optical Engineering* 1997; **36**(11): 2943-2947. doi: 10.1117/1.601534.
277. Pellé F, Ivanova S, Guillemoles J-F. Upconversion of 1.54 μm radiation in Er^{3+} doped fluoride-based materials for c-Si solar cell with improved efficiency. *The*

European Physical Journal Photovoltaics 2011; **2**(20601. doi: 10.1051/epjpv/2011002.
278. Abram R, Allen R, Goodfellow R. The coupling of light emitting diodes to optical fibers using sphere lenses. *Journal of Applied Physics* 1975; **46**(8): 3468-3474. doi: 10.1063/1.322072.
279. Arnaoutakis GE, Marques-Hueso J, Ivaturi A, Krämer KW, Fischer S, Goldschmidt JC, Richards BS. Enhanced up-conversion for photovoltaics *via* concentrating integrated optics. *Optics Express* 2014; **22**(102): A452-A464. doi: 10.1364/OE.22.00A452.
280. Peters M, Goldschmidt JC, Bläsi B. Angular confinement and concentration in photovoltaic converters. *Solar Energy Materials and Solar Cells* 2010; **94**(8): 1393-1398. doi: 10.1016/j.solmat.2010.04.009.
281. Kosten ED, Atwater JH, Parsons J, Polman A, Atwater HA. Highly efficient GaAs solar cells by limiting light emission angle. *Light: Science & Applications* 2013; **2**(1): e45. doi: 10.1038/lsa.2013.1.
282. Green MA. Radiative efficiency of state-of-the-art photovoltaic cells. *Progress in Photovoltaics: Research and Applications* 2012; **20**(4): 472-476. doi: 10.1002/pip.1147.
283. Miller OD, Yablonovitch E, Kurtz SR. Strong internal and external luminescence as solar cells approach the Shockley–Queisser limit. *IEEE Journal of Photovoltaics* 2012; **2**(3): 303-311. doi: 10.1109/jphotov.2012.2198434.
284. Fischer S, Steinkemper H, Löper P, Hermle M, Goldschmidt JC. Modeling upconversion of erbium doped microcrystals based on experimentally determined Einstein coefficients. *Journal of Applied Physics* 2012; **111**(1): 013109. doi: 10.1063/1.3674319.
285. Arnaoutakis GE, Marques-Hueso J, Ivaturi A, Krämer KW, Mallick TK, Richards BS. Enhancement of Upconversion for Photovoltaics with *β*-$NaYF_4$:Er^{3+} and Concentrating Integrated Optics. *OSA Renewable Energy and the Environment Congress - Optical Nanostructures and Advanced Materials for Photovoltaics,* Tucson, Arizona United States, 2013; PT3C. 4. doi: 10.1364/pv.2013.pt3c.4.
286. Pollnau M, Hardman P, Clarkson W, Hanna D. Upconversion, lifetime quenching, and ground-state bleaching in Nd^{3+}:$LiYF_4$. *Optics Communications* 1998; **147**(1): 203-211. doi: 10.1016/s0030-4018(97)00524-5.
287. Blasse G, Grabmaier B. *Luminescent materials*. Springer-Verlag: Berlin; New York;, 1994; 16-19, 95-102.
288. Hirst LC, Ekins-Daukes NJ. Fundamental losses in solar cells. *Progress in Photovoltaics: Research and Applications* 2011; **19**(3): 286-293. doi: 10.1002/pip.1024.
289. Green MA. *Solar cells: operating principles, technology, and system applications*. Prentice-Hall, Inc.: Englewood Cliffs, NJ, 1982; 96-98.
290. Atwater JH, Spinelli P, Kosten E, Parsons J, Van Lare C, Van de Groep J, de Abajo JG, Polman A, Atwater HA. Microphotonic parabolic light directors fabricated by two-photon lithography. *Applied Physics Letters* 2011; **99**(15): 151113. doi: 10.1063/1.3648115.
291. Fischer S. *Upconversion of sub-band-gap photons for silicon solar cells*. Albert-Ludwigs-Universität Freiburg: Freiburg, Germany, 2014; ISBN 978-3-8396-0785-5.
292. Cheng YY, Fückel B, MacQueen RW, Khoury T, Clady RG, Schulze TF, Ekins-Daukes N, Crossley MJ, Stannowski B, Lips K. Improving the light-harvesting of amorphous silicon solar cells with photochemical upconversion. *Energy & Environmental Science* 2012; **5**(5): 6953-6959. doi: 10.1039/C2EE21136J

293. Schulze TF, Cheng YY, Fückel B, MacQueen RW, Danos A, Davis NJ, Tayebjee MJ, Khoury T, Clady RG, Ekins-Daukes N. Photochemical upconversion enhanced solar cells: Effect of a back reflector. *Australian Journal of Chemistry* 2012; **65**(5): 480-485. doi: 10.1071/CH12117.
294. Green MA. Self-consistent optical parameters of intrinsic silicon at 300K including temperature coefficients. *Solar Energy Materials and Solar Cells* 2008; **92**(11): 1305-1310. doi: 10.1016/j.solmat.2008.06.009.
295. Arnaoutakis GE, Marques-Hueso J, Richards BS, Mallick TK. Propagation of white light through optical fibres for CPV systems. *SPIE Photonics Europe - Photonics for Solar Energy Systems IV,* Brussels, Belgium, 2012; 843811-843811-843816. doi: 10.1117/12.922134.
296. Laporte O. Die Struktur des Eisenspektrums. *Zeitschrift für Physik* 1924; **23**(1): 135-175. doi: 10.1007/bf01327582.
297. Wigner EP. *Gruppentheorie und ihre Anwendung auf die Quantenmechanik der Atomspektren*. 1931;
298. Wigner EP. *Group theory and its Application to the Quantum Mechanics of Atomic Spectra*. Academic Press: New York, 1959;
299. Vleck Jv. The Puzzle of Rare-earth Spectra in Solids. *Journal of Physical Chemistry* 1937; **41**(1): 67-80. doi: 10.1021/j150379a006.
300. Broer L, Gorter C, Hoogschagen J. On the intensities and the multipole character in the spectra of the rare earth ions. *Physica* 1945; **11**(4): 231-250. doi: 10.1016/S0031-8914(45)80009-5.
301. Walsh BM. *Judd-Ofelt theory: Principles and Practices*. Springer: 2006; 418.
302. Judd B. Optical absorption intensities of rare-earth ions. *Physical Review* 1962; **127**(3): 750. doi: 10.1103/PhysRev.127.750.
303. Ofelt G. Intensities of crystal spectra of rare-earth ions. *The Journal of Chemical Physics* 1962; **37**(3): 511-520. doi: 10.1063/1.1701366.
304. Carnall W, Crosswhite H, Crosswhite HM, "Energy level structure and transition probabilities in the spectra of the trivalent lanthanides in LaF_3," ANL-78-XX-95 (Argonne National Lab., IL (USA), 1978).
305. Carnall W, Fields P, Rajnak K. Electronic energy levels in the trivalent lanthanide aquo ions. I. Pr^{3+}, Nd^{3+}, Pm^{3+}, Sm^{3+}, Dy^{3+}, Ho^{3+}, Er^{3+}, and Tm^{3+}. *The Journal of Chemical Physics* 1968; **49**(10): 4424-4442. doi: 10.1063/1.1669893.
306. Görller-Walrand C, Binnemans K, "Spectral intensities of *f-f* transitions," in *Handbook on the Physics and Chemistry of Rare Earths*, K. A. Gschneider and L. Eyring, eds. (Elsevier Science B.V., 1998).
307. Einstein A. Zur quantentheorie der strahlung. *Physikalische Zeitschrift* 1917; **18**(121-128. doi:
308. Einstein A, Ehrenfest P. Zur quantentheorie des strahlungsgleichgewichts. *Zeitschrift für Physik A Hadrons and Nuclei* 1923; **19**(1): 301-306. doi:
309. McCumber D. Einstein relations connecting broadband emission and absorption spectra. *Physical Review* 1964; **136**(4A): A954. doi: 10.1103/PhysRev.136.A954.
310. Payne SA, Chase L, Smith LK, Kway WL, Krupke WF. Infrared cross-section measurements for crystals doped with Er^{3+}, Tm^{3+}, and Ho^{3+}. *IEEE Journal of Quantum Electronics* 1992; **28**(11): 2619-2630. doi: 10.1109/3.161321.
311. Cornacchia F, Toncelli A, Tonelli M. 2-μm lasers with fluoride crystals: Research and development. *Progress in Quantum Electronics* 2009; **33**(2): 61-109. doi: 10.1016/j.pquantelec.2009.04.001.
312. Miniscalco WJ, Quimby RS. General procedure for the analysis of Er^{3+} cross sections. *Optics Letters* 1991; **16**(4): 258-260. doi: 10.1364/OL.16.000258.

313. Aull BF, Jenssen H. Vibronic interactions in Nd: YAG resulting in nonreciprocity of absorption and stimulated emission cross sections. *IEEE Journal of Quantum Electronics* 1982; **18**(5): 925-930. doi: 10.1109/JQE.1982.1071611.